Probing circuits for spinal motor control

Timothy Aloysius Machado

Submitted in partial fulfillment of the
requirements for the degree of
Doctor of Philosophy
under the Executive Committee
of the Graduate School of Arts and Sciences

COLUMBIA UNIVERSITY

2015

©2015
Timothy Aloysius Machado
All Rights Reserved

ABSTRACT

Probing circuits for spinal motor control

Timothy Aloysius Machado

Spinal circuits can generate locomotor output in the absence of sensory or descending input, but the principles of locomotor circuit organization remain unclear. We sought insight into these principles by considering the elaboration of locomotor circuits across evolution. The identity of limb-innervating motor neurons was reverted to a state resembling that of motor neurons that direct undulatory swimming in primitive aquatic vertebrates, permitting assessment of the role of motor neuron identity in determining locomotor pattern. Two-photon imaging was coupled with spike inference to measure locomotor firing in hundreds of motor neurons in isolated mouse spinal cords. In wild type preparations we observed sequential recruitment of motor neurons innervating flexor muscles controlling progressively more distal joints. Strikingly, after reversion of motor neuron identity virtually all firing patterns became distinctly flexor-like.

Our interneuron imaging experiments demonstrate a new approach for functionally mapping the types of inputs that motor neurons might receive during locomotor firing. These data revealed that En1-derived inhibitory spinal interneuron activity appears to be dominated by a flexor-like pattern across the ventrolateral extent of the lumbar spinal cord–even in the regions surrounding flexor and extensor motor pools. Together, these findings show that motor neuron identity directs locomotor circuit wiring, and indicate the evolutionary primacy of flexor pattern generation.

Table of Contents

List of Figures

ACKNOWLEDGEMENTS

This work would not have been possible without the support, guidance, and generosity of a number of mentors, colleagues, and friends.

In particular, I owe a great debt to my advisor Thomas Jessell who afforded me the opportunity to conduct this work. Over the last few years, I have grown greatly as a scientist and much of this I owe to his scientific rigor, advice, and constructive feedback. I have been privileged to work with him and with the talented members of his laboratory.

I was also fortunate to work with my co-advisor, Liam Paninski. I have interacted with him at each stage of my scientific career beginning as an undergraduate student in E.J. Chichilnisky's lab who wanted to learn about Bayesian methods for data analysis, through my rotation projects, and into the thesis work described here. At each step, I have benefitted greatly from his advice, ideas, and support.

My thesis committee, Charles Zuker, Attila Losonczy, and Mark Churchland, generously gave me their time and advice. Their guidance has certainly had a positive impact on my project and development as a scientist. I am also grateful to my external committee member, Ron Harris-Warrick, for being willing to read my thesis and take part in the defense.

Andrew Miri played an instrumental role in this project, from early conversations

that we had while I was conducting experiments, to later collaborative work with some of the data analysis and with interpreting experimental findings. His involvement in the writing and construction of the paper certainly had a positive impact on the final product. I learned much about how to frame a scientific story from working with him and am grateful to have had his involvement.

Eftychios Pnevmatikakis contributed his new and improved spike inference algorithms and provided advice about how to best employ them on my data. I was also lucky to work with Lars Buesing and Kamiar Rahnama Rad, who developed and tested their respective computational modeling frameworks on data from this thesis.

I received constant support from Barbara Han (and more recently, Erica Famojure), with developing the infrastructure necessary to do my experiments, building my experimental apparatus, and making sure I had everything I needed in order to succeed. Susan Morton was a good neighbor in room 1024 and provided me with helpful advice and guidance. Kathy MacArthur provided crucial organizational assistance and support. Monica Mendelsohn and Nataliya Zabello helped me manage my mouse colony and taught me about mouse husbandry. David Wu assisted me with genotyping.

My ability to perform electrophysiological and imaging experiments is a consequence of the time that a number of people invested in teaching me. In particular, George Mentis taught me all about the isolated spinal cord preparation. He instructed me about how to perform ventral root recordings and fills, how to properly assemble a rig, and talked with me at length about experimental design. I am very grateful for his advice and assistance. Prior to joining the Jessell lab, I rotated in Rafael Yuste's lab where I was fortunate to learn about intracellular recordings and two-photon microscopy from Darcy Peterka, Elodie Fino, Adam Packer, and Tanya Sippy.

The program directors of the Neurobiology and Behavior program: Darcy Kelley, Carol Mason, and Ken Miller were a source of guidance. And our departmental administrators Alla Kerzhner and Cecil Oberbeck ensured that I continued in the program as a paid, consistently enrolled, student.

Each member of the Jessell lab played an important role in my project at some point and I am grateful for each of my interactions with them. In particular, Andy Murray taught me about cloning, cell culture, and viruses. Jay Bikoff taught me about genetics and immunohistochemistry. Turgay Akay taught me about EMG. Eiman Azim was always a source of good feedback. Laskaro Zagoraiou introduced me to spinal cord circuits as my mentor during my rotation in the lab. Finally, Andrew Fink showed me how to do surgery and provided me with a great deal of advice on how to succeed as a graduate student in the lab.

I would also like to thank my friends, in particular, Matt Lovett-Barron, Shobhit Singla, Thomas Reardon, Amy Norovich, Alana Mendelsohn, Patrick Kaifosh, Mariano Gabitto, Armen Enikolopov, Martin Vignovich, and especially my girlfriend Myra Laird. They were a constant source of feedback and support. Finally, I would like to thank my parents for everything over the years.

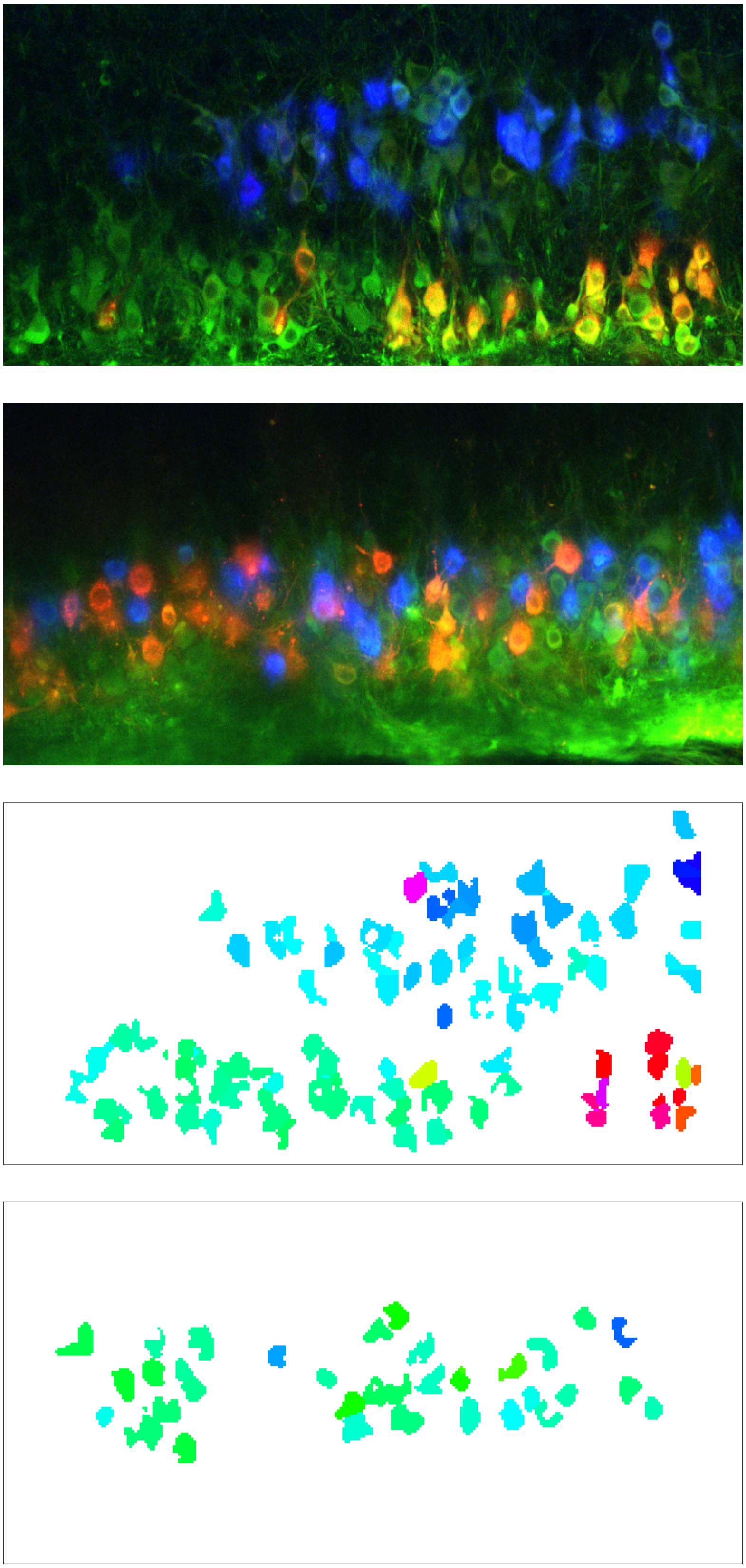

1

Introduction: The functional organization of pattern generating circuits

1.1 Understanding recurrent dynamics in neural circuits

A primary computational goal of the central nervous system is to transform sensory input into motor output. For reflexive actions, the mapping between sensory input and behavior may appear clear and nearly deterministic. But during more complex behaviors, the relationship between stimulus and response may not be apparent at all. Indeed, a key feature of many neural circuits is that they are capable of persistent sustained activity, even in the absence of any external input. Such recurrent dynamics are thought to underlie some forms of short-term memory [Seung et al., 2000], evidence integration during decision making [Mante et al., 2013], and also movement planning [Churchland et al., 2012]. Despite the ubiquity of persistent activity in neural networks, the network mechanisms responsible are comparatively poorly understood.

In this thesis, we will focus on elucidating the organization of a specific type of recurrent network: the spinal interneuron circuits involved in producing patterned motor neuron activity. Because these circuits are capable of producing stereotyped, locomotor-like patterns of output in the absence of external drive, we can use them as a model for understanding how neuronal ensembles can autonomously produce specific patterns of activity. To constrain this problem, we will first measure the patterns produced by spinal interneuron networks and their manifestation across space by comprehensively monitoring locomotor firing across motor neurons at cellular resolution. We will then use this approach to examine how spinal interneurons find appropriate motor neuron targets during development in order to achieve appropriate patterns of muscle recruitment during locomotor behavior. Finally, we will consider the logic of interneuron circuits themselves, by directly measuring the activity of genetically defined subsets of neurons that are rhythmically active during locomotion.

One advantage of our focus on locomotor circuits is that the activity and output of these networks must be relatively stereotyped and predictable both to ensure smooth movement but also to simplify the kinds of descending and sensory commands that are necessary to modulate spinal network dynamics. This means the activity of individual neurons is often fairly stereotyped and interpretable with respect to network output. For this reason, a number of experimentally tractable motor systems composed of small numbers of neurons have been developed. Perhaps the simplest of these model circuits is the crab somatogastric ganglion (STG) [Marder & Bucher, 2007]. This neural circuit drives stomach muscles in the crustacean foregut to contract in a precise sequence in order to grind food. Unlike many other recurrent networks that contain large populations of interneurons whose activity is often not clearly related to behavior, the motor neurons in the STG that innervate stomach muscles are also directly connected to one another. As a result, intracellular recordings from motor neurons provide a readout of network output, as well as of the dynamics in the recurrent network itself. Because this network consists of only approximately thirty neurons that require no external input to function, and because the connectivity of the entire circuit has been reconstructed using electron microscopy [Bargmann & Marder, 2013], the precise mechanisms by which rhythmic activity can be produced in each neuron are mostly understood.

The use of a similar strategy for untangling the origins of rhythmic activity in mammalian neural circuits has been more problematic, in part because they are hundreds of times larger, suggesting that these larger circuits have many components serving redundant functions during simple motor behaviors. Importantly, even the small neural circuits in the STG appear to be highly redundant and robust. In practice, this redundancy means that many experimental perturbations to the STG have no apparent effect (owing to homeostatic network mechanisms; [Marder, 2011]), or have identical effects (owing to redundant mechanisms for controlling network output; [Gutierrez et al., 2013]). These lessons are likely to hold in larger circuits as well, but have been difficult to test, largely as a consequence of technical limitations.

In the past decade, new large-scale optical imaging and recording methods have finally made it possible to apply network analyses previously restricted to small circuits like the STG to the mammalian CNS [Ohki et al., 2005; Harvey et al., 2012]. However, these methods can only currently scale to the analysis of local regions consisting of approximately 1,000 neurons—not an entire mammalian brain. As a result, this appears to be a uniquely appropriate time for studying mammalian spinal locomotor networks, as these central pattern generating (CPG) circuits can also function in isolation to produce locomotor-like activity and therefore be used as a model in a similar manner as the STG. But more importantly, locomotor circuits appear to consist of similar microcircuit building blocks as other parts of the CNS, like those in the neocortex [Yuste et al., 2005], and are thus likely to teach us about the basic principles of neural computation.

1.2 The organization of spinal interneuron circuits

1.2.1 Spinal circuits for processing sensory information and producing motor output

In contrast with most other structures in the CNS, the spinal cord is involved in both the processing of sensory input as well as the production of motor output (Figure 1.1A-C; [Rexed, 1952]). Cutaneous, proprioceptive, and nociceptive sensory neurons residing in dorsal root ganglia directly send afferents onto many central neuron targets residing in the spinal cord. Most of these sensory projections receive input from their corresponding sensory organs in the periphery and then terminate onto interneurons residing in the first five laminae that comprise the dorsal horn (Figure 1.1C; [Lallemend & Ernfors, 2012]). In contrast, motor neurons residing in the ventral horn (Lamina IX) most prominently receive local inputs from interneurons positioned in the ventral spinal cord [Tripodi et al., 2011; Kjaerulff & Kiehn, 1996] and only receive monosynaptic sensory input from proprioceptive afferents that convey muscle stretch information from muscle spindles (Figure 1.1C). Importantly, most other sensory pathways and descending tracts indirectly relay their inputs to motor neurons through the ventral spinal interneuron networks [Brownstone & Bui, 2010].

But even though some sensory and descending afferents directly contact motor neurons, copies of those same signals are usually sent redundantly to ventral spinal interneuron networks that relay the same information to motor neurons at longer latencies. The presence of such feedback loops across different spatial scales is a common theme throughout the CNS [Azim et al., 2014; Swanson, 2012]. Also, different types of feedback are biased towards different components of motor circuits. For example, the vestibulospinal tract selectively excites extensor versus flexor motor pools [Grillner et al., 1970]. As a consequence of this organization, it is important to think about the production of motor pattern as a flexible process that is usually being modulated by diverse feedback signals during behavior. To better understand how these different kinds of feedback might influence motor output, we need to understand the intrinsic dynamics of spinal circuits in the absence of such input.

In the subsequent chapters, we will focus on elucidating the features of motor neuron pattern produced in the absence of input from these disparate sensory sources such that the most basic dynamical activity in ventral spinal circuits that is capable of producing locomotor-like motor neuron firing might become more clear.

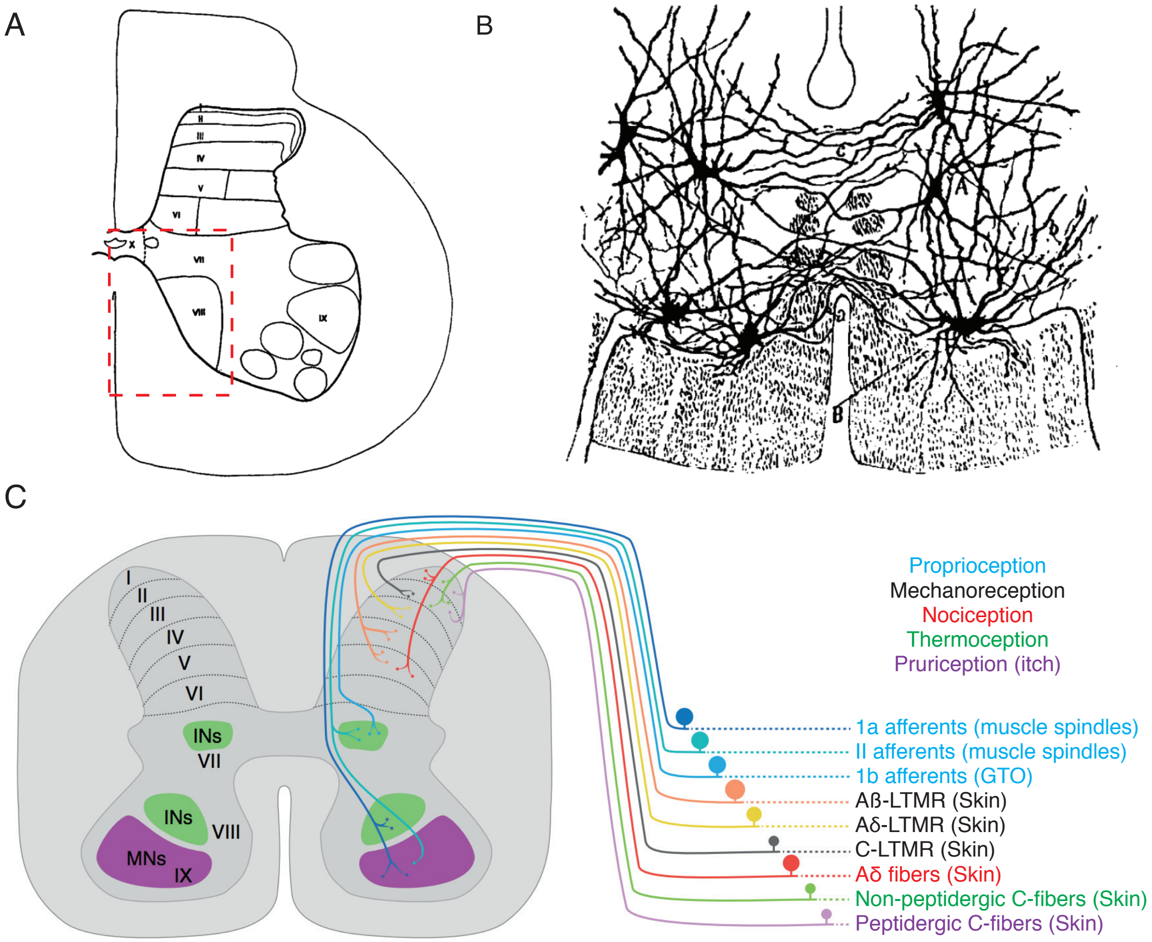

Figure 1.1: **The cytoarchitectural organization of spinal circuits**

(A) The laminar organization of a lumbar segment from the cat, as proposed by [Rexed, 1952]. (B) Red boxed region from (A) as drawn five decades earlier by Santiago Ramón y Cajal [Cajal, 1909]. Dorsally, commissural interneurons can be seen. Ventrally, motor neurons innervating epaxial musculature send their axons out through ventral roots. (C) Trajectories of sensory afferent inputs onto the different spinal laminae. Panels A and B adapted from [Rexed, 1952]. Panel C adapted from [Lallemend & Ernfors, 2012].

1.2.2 The physiology of premotor interneuron networks

Elements of contemporary spinal network models date back to the work of Thomas Graham Brown in the years before the First World War [Jones et al., 2011]. Brown's experiments in decerebrate cats revealed that even in the absence of descending input from the brain, or peripheral sensory feedback from the limb, the spinal cord was capable of producing a rhythmic alternating pattern between pairs of flexor and extensor muscles (Figure 1.2A). In order to explain these observations, Brown developed the "half-center" model shown in Figure 1.2B. Although inhibition had only recently been suggested as a feature of central circuits [Sherrington, 1913], his model predicted that flexor-extensor alternation might be mediated by a mutual antagonism between flexor and extensor subnetworks. At the time, this idea that spinal networks could function in isolation to produce motor output was largely discounted, as sensory input was thought to be necessary. Lord Adrian even argued that while Brown's work added to the "general store of information on the spinal reflexes…it cannot be said to have had much influence on the progress of physiology" [Adrian, 1966; Jones et al., 2011].

This sentiment was largely a consequence of the experimental methods available at the time: a candidate cellular basis for these half-centers was not found for decades. Finally in the 1940s, [Lloyd, 1943] showed that stimulation of a motor neuron evoked monosynaptic excitation of other motor neurons that shared the same muscle target, but also evoked inhibition in antagonist motor neurons. In the subsequent decades, this reciprocal inhibition was found to be mediated by a set of inhibitory interneurons that receive 1a afferent input [Hultborn, 1972], now referred to as 1a inhibitory interneurons. Intracellular recordings from these putative 1a inhibitory interneurons showed that they tend to fire in phase with their homonymous motor neurons—presumably then inhibiting antagonist motor neurons during each step cycle to ensure that co-contraction of muscles on opposite sides of a joint does not occur (Figure

1.2C; [Pratt & Jordan, 1987]). These discoveries led to a new appreciation for Graham Brown's early work and to the incorporation of half-center like circuits in contemporary spinal circuit models [Alstermark et al., 2010].

In the subsequent decades, a number of generalizations have been made to the basic half-center model. For example, to expand a half-center like circuit to control an entire limb, the unit burst generator model was proposed. This model assumes that the hindlimb might be controlled by a collection of many half-centers: one for each joint [Grillner, 1981]. Other work by Grillner and others has shown half-center like circuits to mediate more than just flexor-extensor alternation. Reciprocal inhibition has been shown to underlie left-right alternation in animals ranging from lamprey [Grillner et al., 1995] and frogs [Moult et al., 2013] to mammals [Talpalar et al., 2013].

A modern spinal network model for controlling alternation at a joint, based around a half-center like microcircuit, can be seen in (Figure 1.2D; [McCrea & Rybak, 2008]). A key difference versus earlier models is that there is a two-layer network providing input to the half-center that in turn provides monosynaptic input to the motor neurons. These upstream networks are themselves driven to fire by a combination of reciprocal interactions between flexor and extensor-firing interneurons and proprioceptive sensory feedback. The presence of persistent conductances and other cell-intrinsic mechanisms is also thought to play a role in driving firing in these neurons in conjunction with network activity [Zhong et al., 2007; Brocard et al., 2013].

In contrast to the model shown, some have argued that these top level "rhythm generating" circuits involved might be asymmetric and mostly consist of neurons firing in a single flexor-like pattern (Figure 1.3; [Pearson & Duysens, 1976; Brownstone & Wilson, 2008; Kwan et al., 2009]). Such models do not, however, argue that such asymmetries are present at the final half-center layer that is monosynaptic to each motor neuron.

Independent of the architecture of the rhythm generating circuits, most contemporary spinal circuit models argue that there are at least two layers in the premotor network. This conclusion has been reached as a consequence of analysis into how motor neuron and interneuron activity changes when motor neurons skip a rhythmic burst (so-called "deletions"; [Zhong et al., 2012]). Most of these deletions are "non-resetting" meaning that the next motor burst will occur at the time expected had it not failed on the previous cycle. Interestingly, there is an inherent asymmetry in these deletions: if a flexor motor neuron fails to fire a burst, tonic activity in extensor motor neurons is always seen. But if an extensor motor neuron fails to fire a burst, flexor motor neurons continue their activity unabated. Similarly, deletions in motor neuron activity do not affect all interneurons. Some interneurons display missed bursts, just like the motor neurons, while others continue to fire unperturbed. Based on this evidence, it has been suggested that spinal circuits consist of interneurons that propagate a core rhythm (and thus when they miss a burst, a "resetting" deletion is observed across the whole network), while missed bursts in downstream pattern formation interneurons will only perturb a subset of the network and thus cause "non-resetting" deletions.

A significant caveat in much of this work is that there is much evidence that locomotor circuits are very distributed and redundant [Guzulaitis et al., 2014; Kjaerulff & Kiehn, 1996], and that cell-intrinsic mechanisms may play a dominant role in the generation and maintenance of locomotor pattern. For instance, flexor-extensor alternation can persist in the absence of all excitatory interneurons [Talpalar et al., 2011], and rhythmic motor neuron activity that is locally coordinated will continue even in the presence of TTX to block action potential firing [Tresch & Kiehn, 2000].

Moreover, our knowledge of spinal interneurons is largely defined with respect to the periphery: the 1a inhibitory interneuron is defined in part due to its sensory inputs, and the Renshaw cell was located because it is inhibitory and post-synaptic to motor neurons—and therefore the effects of its recurrent feedback onto motor neurons could be observed when motor neurons are antidromically activated [Renshaw, 1941]. The idea that these two microcircuits are the only ones involved in mediating inhibition directly onto motor neurons seems unlikely. Instead, they are simply two microcircuits that were amenable to observation with the recording techniques available in past decades. The use of new methods that have different measurement biases are likely to reveal new circuits that might have similar functions during locomotion.

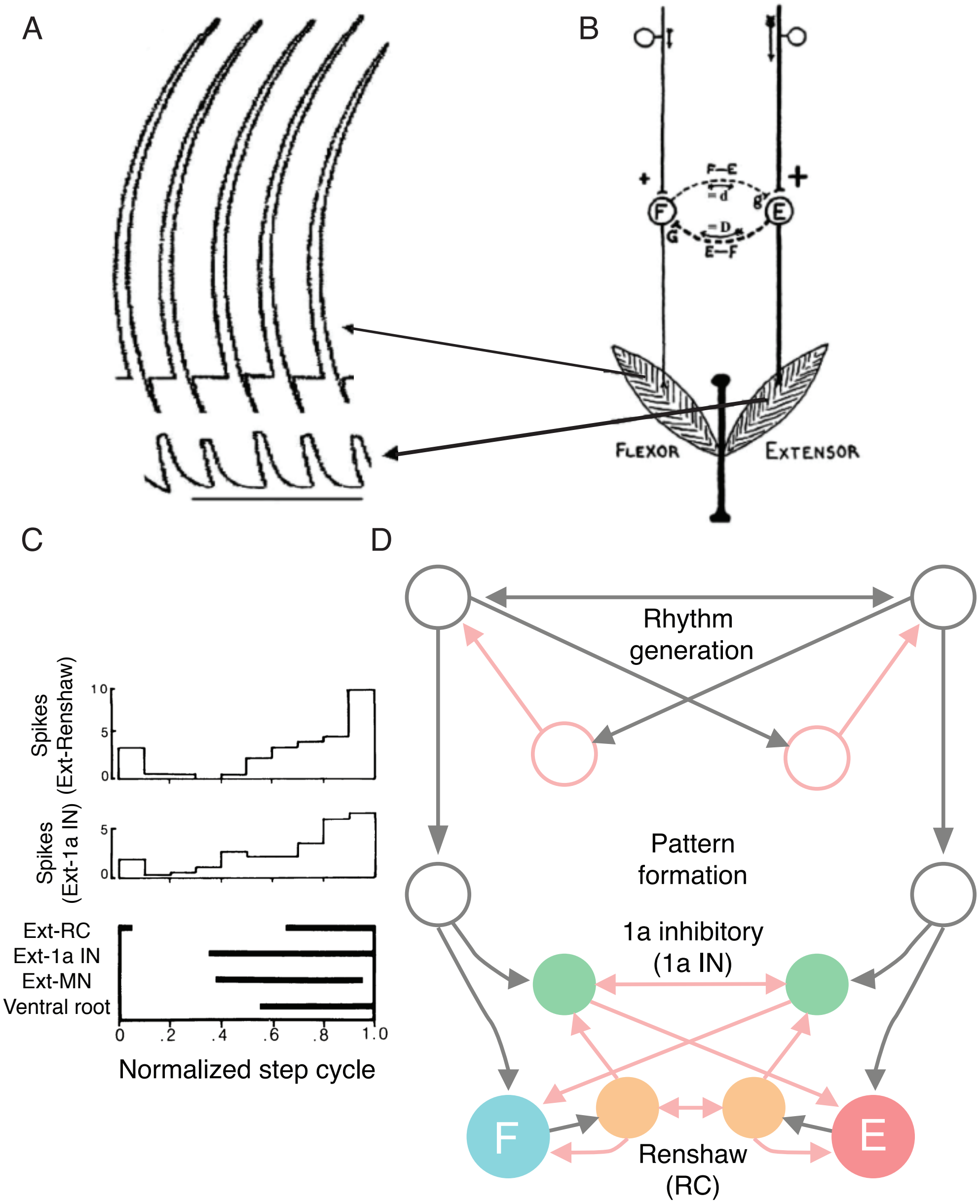
A
B
+
F—E
=d
g
F
E
+
G
=D
E—F
FLEXOR
EXTENSOR
C
Spikes (Ext-Renshaw)
10
5
0
Spikes (Ext-1a IN)
5
0
Ext-RC
Ext-1a IN
Ext-MN
Ventral root
0
.2
.4
.6
.8
1.0
Normalized step cycle
D
Rhythm generation
Pattern formation
1a inhibitory (1a IN)
F
E
Renshaw (RC)

Figure 1.2 *(preceding page)*: **Models of spinal locomotor circuits**

(A) Measurements of flexor and extensor nerve activity in a spinalized, deafferented cat obtained by Thomas Graham Brown in 1911. (B) A schematic of Graham Brown's half-center model, published in [Brown, 1916]. (C) Illustration of a contemporary multi-layer model for the control of a flexor-extensor pair of muscles. (D) Phase tuning of an extensor-related (quadriceps in this case) Renshaw cell and 1a inhibitory interneuron (1aIN) over a normalized step cycle. The step cycle was discretized into ten bins, the first five during flexor activation, and the second five during extensor activation. Panels A and B are from [Jones et al., 2011]. Panel C was adapted from [McCrea & Rybak, 2008]. Panel D was adapted from [Pratt & Jordan, 1987].

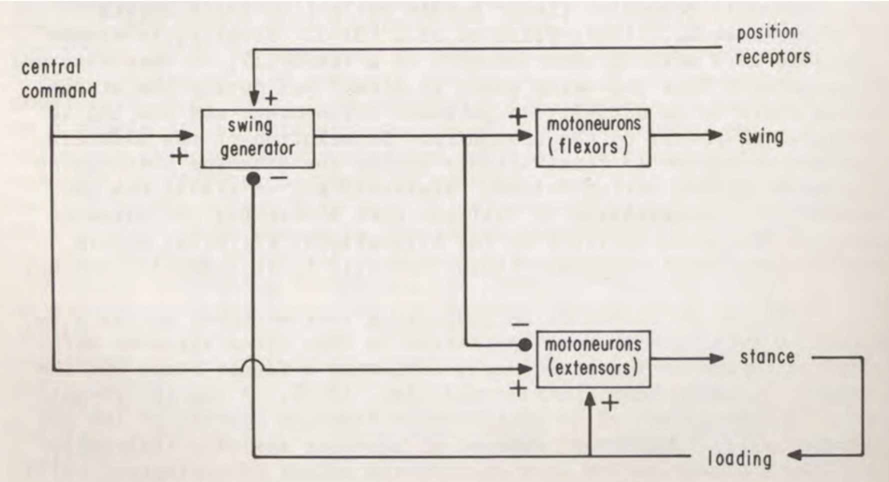

Figure 1.3: **An asymmetric, flexor-biased model for limb control**

Block diagram from [Pearson & Duysens, 1976] showing a schematic circuit for controlling the limb of a cat or cockroach based on a "swing generator" circuit that produces a flexor-like pattern by integrating descending and sensory inputs. During stance phase, extensor motor neurons are activated by post-inhibitory rebound, excitatory central commands, and sensory feedback.

1.2.3 The sufficiency of spinal networks for motor behavior

The ventral spinal cord consists of a heterogeneous set of motor neurons and interneurons. Impinging upon this region is a diverse array of descending and sensory inputs, but despite suggestions that some of this sensory feedback might be necessary for generating appropriate patterns of motor output *in vivo* [Pearson, 2004], ventral spinal circuits alone are sufficient to produce robust locomotor-like network activity [Dai et al., 2005; Kjaerulff & Kiehn, 1996; Cowley & Schmidt, 1997]. As we discussed above, this feature of spinal circuits was first explored in decerebrate cat preparations that had also had sensory inputs blocked using pharmacological agents, or physically cut [Grillner & Zangger, 1979; Grillner & Wallen, 1985; Jones et al., 2011]. However, because it is technically difficult to obtain intracellular recordings from interneurons in these semi-intact cat preparations and to perturb circuit activity. As a consequence, new model systems needed to be developed.

In more recent years, the study of locomotor circuits has mostly focused on rodents instead of cats [Kudo & Yamada, 1987b] owing in part to its genetic tractability [Lanuza et al., 2004; Gosgnach et al., 2006; Crone et al., 2008; Zhang et al., 2008]. In contrast to the decerebrate, deafferented cat preparation, rodent spinal circuits are typically studied *in vitro* by isolating the the spinal cords of neonatal rats and mice under oxygenated artificial cerebrospinal fluid (ACSF). In this controlled setting, the activity of motor neurons can be monitored by obtaining recordings from ventral roots or peripheral nerves. These experiments have shown that periodic locomotor-like firing can be induced by either the application of drugs, or by electrical stimulation of sensory or descending projections [Kiehn & Kjaerulff, 1996; Cowley & Schmidt, 1997; Talpalar et al., 2011; Beliez et al., 2014].

The work in this thesis will rely on this isolated neonatal rodent spinal cord preparation to study locomotor circuits. But before we can generalize any findings from such experiments to our understanding of motor networks in general, we must go beyond previous work [Kiehn & Kjaerulff, 1996; Kjaerulff & Kiehn, 1996] to determine how similar the activity of a spinal cord in a dish can actually come to recapitulating *in vivo* locomotor behavior. With that information in hand, we will be able to use our knowledge of spinal cord circuit development to better take advantage of the genetic tractability of the *in vitro* preparation.

1.3 Understanding recurrent network activity in spinal locomotor circuits

As recurrent spinal interneuron circuits are sufficient for producing patterned locomotor output, and because they can be modulated by sensory inputs and descending commands, they represent an ideal system for considering how recurrent neural networks generally solve computational tasks. But they are more than a model: in order to approach the problem of how upstream circuits in the brainstem and cortex sculpt motor output during behavior, we must first understand the types of dynamics that these descending commands must engage with in spinal circuits themselves.

Unfortunately, spinal locomotor circuits are difficult to study for many of the same reasons that other recurrent neural networks are difficult to decipher. Until recently, the field of neuroscience has generally lacked the experimental and theoretical means of functionally dissecting large, redundant, and recurrent networks. In recent years, the development of new large-scale recording and data analytical techniques has permitted significant advances. Our hope is that these new experimental and analytical approaches that have become recently available will permit us to gain new insight into longstanding questions about the neural control of movement.

1.3.1 The molecular logic of spinal interneuron circuits

To constrain our investigation into the intrinsic activity of local spinal circuits, let us review what is known about the development of locomotor networks, which are predominantly located in the ventral spinal cord [Dai et al., 2005]. The identity of different types of ventral spinal interneurons and motor neurons is specified by a combination of environmental signals and cell-intrinsic gene expression patterns (Figure 1.4A-B; [Jessell, 2000; Dasen & Jessell, 2009; Goulding, 2009]). In particular, a dorsoventral gradient of Sonic hedgehog (Shh) plays a key role. Shh is secreted ventrally by the notochord and floor plate and acts by controlling the expression of certain transcription factors in progenitor cells (Figure 1.4C; [Jessell, 2000]). This Shh gradient induces the expression of Class I transcription factors while simultaneously repressing the expression of Class II transcription factors. Bone morphogenetic proteins (BMPs) play a similar in defining transcription factor expression in dorsal progenitor cells [Lee & Jessell, 1999].

Once distinct subsets of progenitor cells have been induced to express different sets of these transcription factors, cross-repressive interactions between Class I and Class II transcription factors further refine the spatial boundaries between different progenitor domains along the dorsoventral axis. The resultant bands of progenitor cells can then be observed to each express a distinct cohort of transcription factors. On this basis, there are known to be six ventral progenitor domains (pV0-V3, pMN, and the pdI6 interneurons that arise from the dorsal neural tube; shown in yellow in Figure 1.4A). These domains in turn give rise to V0-V3 and dI6 interneurons as well as motor neurons.

Based on immunohistochemical and anatomical studies of neurons that were lineage traced from each of the ventral interneuron populations, the neurotransmitter phenotype of each of these different domains is known, as well as the laterality of their axonal projection patterns [Stepien & Arber, 2008; Goulding, 2009]. Further work studying the what is known about their functional roles during behavior will be described in 1.3.2. These studies have provided the field with clues to begin the process of defining the genetic identity and developmental provenance of functionally distinct sets of interneurons that are necessary for controlling motor neuron activity during behavior.

A different set of regulatory mechanisms drives cell type diversity along the rostrocaudal axis of the spinal cord (Figure 1.4B; [Dasen & Jessell, 2009]). In particular, the genetic identity of motor neurons that innervate limb muscles (residing at brachial and lumbar segmental levels) must be different from that of motor neurons at thoracic levels that instead target axial musculature. These segmental-specific genetic identities are achieved through the differential expression of Hox transcription factors at different spinal segments [Dasen et al., 2005; Dasen & Jessell, 2009]. As can be seen in Figure 1.4D, the segmental expression of *Hox* genes is driven by rostrocaudal gradients of fibroblast growth factors (FGF), retinoic acid (RA), and Gdf11. Expression of the first genes in the *Hox* gene cluster are induced most rostrally, while the last genes are expressed most caudally. In a similar manner to how cross-repressive interactions achieve spatial stratification between progenitor domain populations, similar interactions between different Hox proteins enforce the development of sharp segmental boundaries that have different Hox expression profiles.

Importantly, the action of the Hox regulatory network in defining motor neuron identity is dependent on the presence of FoxP1, a Hox accessory factor. In mice lacking FoxP1, limb innervating motor neurons (that together comprise the lateral motor column, or LMC) are reverted to an ancestral-like state resembling that seen innervating the axial musculature of primitive aquatic vertebrates [Kusakabe & Kuratani, 2005; Dasen et al., 2008]. The importance of the Hox network for defining interneuron identity is not currently well-understood but is also plausibly controlled by similar mechanisms. Together the both the Shh and Hox pathways provide a system by which the molecular identity of a spinal neuron can be defined by its position along the dorsoventral and rostrocaudal axes.

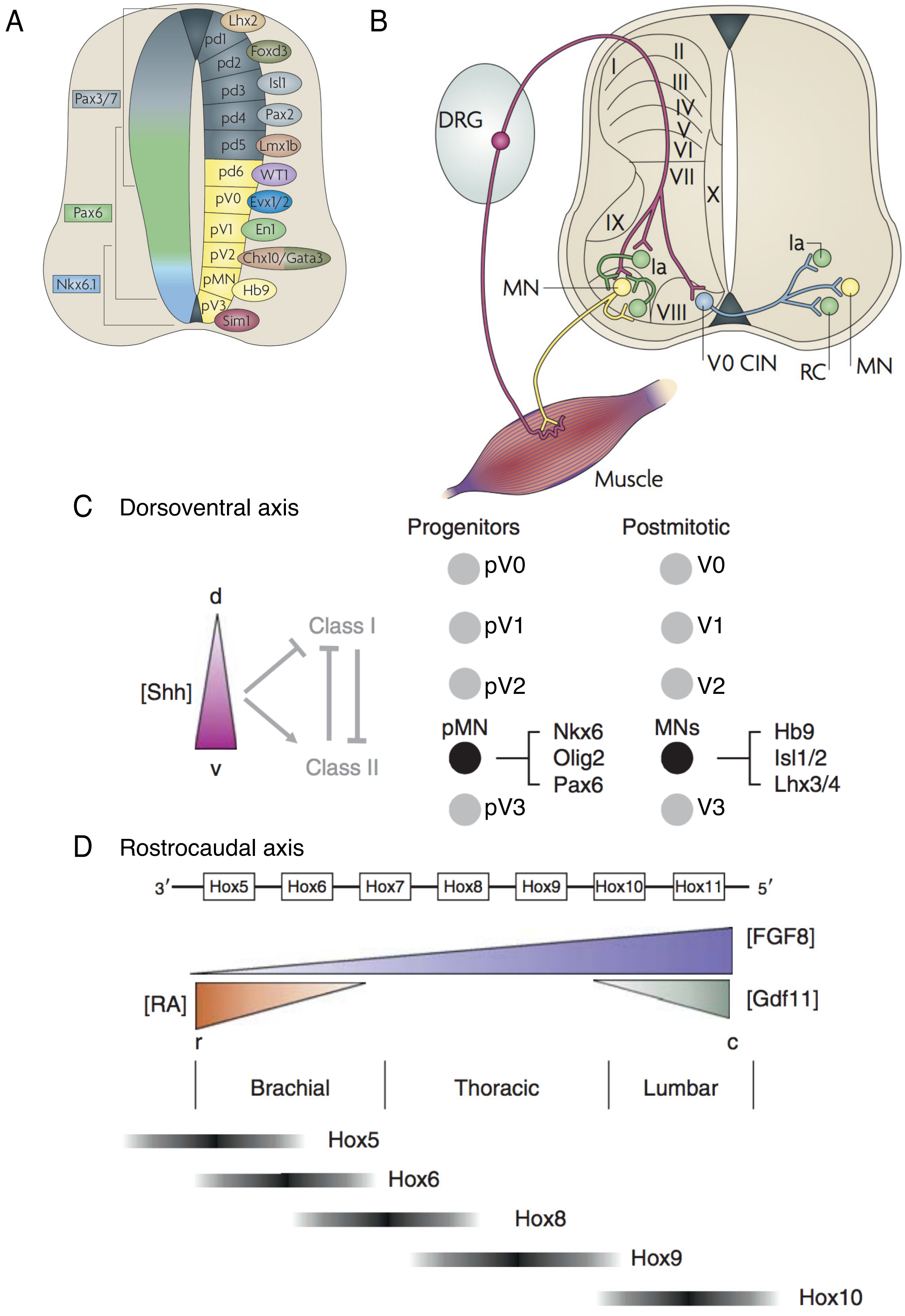
A
Pax3/7
Pax6
Nkx6.1
pd1
pd2
pd3
pd4
pd5
pd6
pV0
pV1
pV2
pMN
pV3
Lhx2
Foxd3
Isl1
Pax2
Lmx1b
WT1
Evx1/2
En1
Chx10/Gata3
Hb9
Sim1
B
DRG
I
II
III
IV
V
VI
VII
VIII
IX
X
MN
Ia
Ia
V0 CIN
RC
MN
Muscle
C
Dorsoventral axis
d
[Shh]
v
Class I
Class II
Progenitors
pV0
pV1
pV2
pMN
Nkx6
Olig2
Pax6
pV3
Postmitotic
V0
V1
V2
MNs
Hb9
Isl1/2
Lhx3/4
V3
D
Rostrocaudal axis
3′
Hox5
Hox6
Hox7
Hox8
Hox9
Hox10
Hox11
5′
[FGF8]
[RA]
[Gdf11]
r
c
Brachial
Thoracic
Lumbar
Hox5
Hox6
Hox8
Hox9
Hox10

Figure 1.4 *(preceding page)*: **Locomotor circuits consist of four cardinal subtypes of interneurons**

(A) At embryonic day 11, there are eleven classes of postmitotic neuron in the spinal cord: dorsal progenitors DI1-DI5 (gray), and classes DI6, V0-V3, and MN residing ventrally (yellow). Different transcription factors expressed by each class are also indicated. (B) At postnatal stages the ventral progenitor classes (DI6, V0-V3, and MN) collectively give rise to locomotor circuits. In the schematized spinal cord, motor neurons (MN; yellow) innervate muscles and inhibitory Renshaw cells (RC, from the V1 domain; green) while they receive input from sensory afferents (purple) and inhibitory interneurons (1a and RC, from the V1 domain; green). Excitatory V0 interneurons project contralaterally (blue). The position of spinal laminae are shown as Roman numerals. (C) Along the dorsoventral axis of the spinal cord, a gradient Sonic hedgehog (Shh) controls the expression of Class I and Class II transcription factors to define different progenitor domains of ventral interneuron. (D) Similarly, along the rostrocaudal axis, gradients of retinoic acid (RA) and fibroblast growth factors (FGFs), can induce the expression of *Hox* genes along the extent of the spinal cord. Panels A and B were adapted from [Goulding, 2009]. Panels C and D are from [Dasen & Jessell, 2009].

1.3.2 Enumerating elements of locomotor circuits in the spinal cord

Over the last decade, a body of work has attempted to relate our knowledge of spinal cord development to physiological data and locomotor circuit modeling studies. Much of this work has focused on defining a functional role for each of the four cardinal domains of spinal interneurons during locomotor firing. Based on histological and genetic tracing studies, we know the neurotransmitter phenotype of each domain and whether it contains only ipsilaterally projecting neurons or a mixture of ipsilateral and contralaterally projecting neurons [Stepien & Arber, 2008]. In contrast, much less is known about how physiological subtypes of interneuron like the 1a inhibitory interneuron, or different layers of the pattern generating network, might relate to our understanding of how interneurons diversify into genetically-distinct subpopulations during development.

In many of the studies (e.g. [Lanuza et al., 2004; Gosgnach et al., 2006; Crone et al., 2008; Zhang et al., 2008]), a popular approach was to pair methods for acute genetic ablation with ventral root recordings obtained from isolated spinal cord preparations. For example, in [Gosgnach et al., 2006], interneurons from the En1-derived V1 domain were acutely ablated using various genetic methods (e.g. by using En1::Cre; ROSA::DTA mice). These strains of mice were then characterized using an isolated neonatal mouse spinal cord preparation induced to fire in a locomotor-like pattern by the application of rhythmogenic drugs: NMDA, 5-HT, and/or DA. Following drug application, suction electrode recordings obtained from multiple ventral roots revealed rhythmic bursting activity at each lumbar segment (Figure 1.5A). As ventral roots consist of the axons of the motor neurons present at their homonymous segment, and because motor neurons sharing common muscle targets reside in stereotyped, spatially coherent, positions called motor pools [Romanes, 1964], clear temporal structure can be resolved from comparing the ventral root recordings obtained from different spinal segments. For example, alternation can be observed between the left and the right side of the spinal cord preparation.

As can be seen from Figure 1.5, the genetic ablation of each cardinal domain of interneurons appears to have had an effect on locomotor firing—causing changes to either pattern frequency, deficits in burst robustness, or deficits in left-right alternation. These results are certainly interesting to consider, and perhaps most strikingly in the case of the V0 domain which is involved in left-right alternation, they have also provided a map forward for future studies [Talpalar et al., 2013]. However, this ventral root recording assay is also insufficient for more detailed studies as its readout is far too low dimensional. Ablation experiments affected each parameter that could be quantified from this assay: burst shape, rhythm frequency, and alternation. It seems unreasonable to assume that all possible phenotypes can be encompassed by one of those three features.

In the subsequent chapters, we will discuss new approaches for moving beyond this simple ventral root recording assay. For instance, a cellular-resolution motor neuron assay would permit us to better understand how the isolated preparation is similar and dissimilar from *in vivo* rodent preparations that are less amenable to large-scale physiological measurements. If we understood the fundamental grain of locomotor activity, in the absence of sensory or descending inputs, we would also be afforded much greater resolution to assess subtle perturbations to the interneuron network.

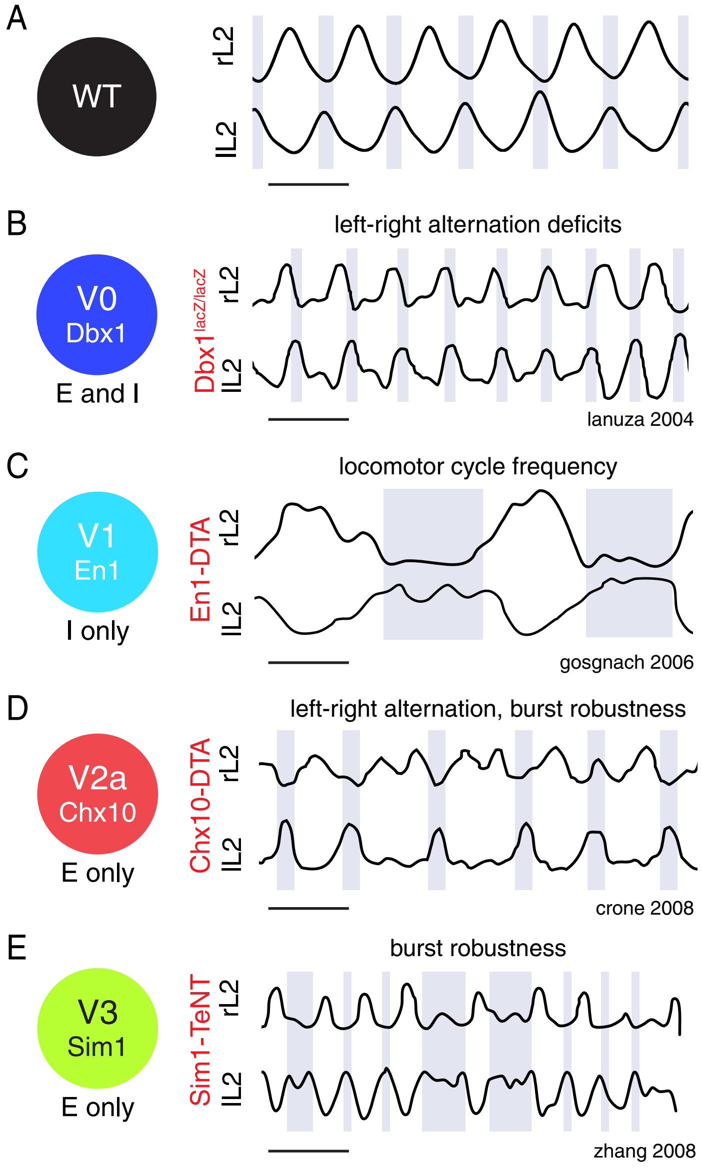

Figure 1.5: **Summary of locomotor phenotypes after perturbations to interneurons**

(A) Filtered ventral root recordings obtained from ipsilateral ventral roots L2 and L5 showing characteristic antiphase alternation. (B-E) Filtered ventral root recording data adapted from [Lanuza et al., 2004; Gosgnach et al., 2006; Crone et al., 2008; Zhang et al., 2008], respectively. The scale bar in all panels denotes 5 seconds of time.

1.3.3 The modulation of intrinsic activity via sensory and descending inputs

Understanding how *in vivo* and isolated locomotor patterns differ for the sake of building a better experimental assay for studying recurrent interneuron circuits is an important goal in itself, but it is also significant for another reason. Upstream circuits in the cortex and brainstem must structure their descending commands to interface with the ongoing dynamics of spinal motor circuits in order to successfully control movement. This is especially true in the rodent, where monosynaptic connections from motor cortex onto motor neurons might not exist at all [Lemon & Griffiths, 2005]. Given our lack of mechanistic understanding of how even the simplest periodic locomotor activities are produced by spinal circuits, we hope that the results presented here might inform future studies in the spinal cord, and in other premotor circuits.

While comparatively little is known about the structure of descending commands onto the spinal cord, much work has examined the role of cutaneous and proprioceptive feedback onto spinal motor circuits during behavior. For example, the sequential activation of flexor muscles during walking, and limb kinematics during swimming, are selectively perturbed after proprioceptive muscle spindle afferents are ablated (Figure 1.6; [Akay et al., 2014; Takeoka et al., 2014]. Similarly, severing nerves carrying cutaneous sensory information from the foot appears to selectively impair foot placement during locomotor tasks—but most strikingly during walking on inclined surfaces [Bouyer & Rossignol, 2003]. These studies illustrate how sensory feedback can play a significant role in modulating organizing features of motor neuron recruitment during locomotion.

In this context of modulation, a number of previous studies have examined the effects of different pharmocological agents and stimulation protocols on spinal network activity [Beliez et al., 2014; Taccola, 2011]. In [Frigon & Gossard, 2009], the authors compared different mechanisms for inducing locomotor-like activity in a decerebrate cat that lacked peripheral sensory feedback. When they compared the length of flexor bursts to extensor bursts, they found that extensor bursting lasted longer than flexor bursting across a range of gait speeds. This observation of “extensor dominance” was seen during both spontaneous and drug-induced bouts of locomotor activity and matches activity patterns seen in intact animals. In contrast, when locomotor activity was induced with electrical stimulation to the mesencephalic locomotor region, aberrant “flexor dominant” activity was seen. These results reveal an apparent asymmetry in the default, spontaneously generated, pattern of activity in spinal networks that can be reshaped by descending commands. Understanding more details like this about what the default pattern of motor circuit activity looks like and how it is maintained will likely be critical for deciphering the logic of descending control signals in premotor regions of the brain.

In this thesis, we will quantify the amount of variance in motor neuron firing patterns that we observe across dozens of preparations and retrogradely labeled motor neuron pools, during a drug-induced locomotor-like network state. After comparing these activity patterns to those seen in knockout animals where the network structure has been perturbed, we will return to this idea of a “default” locomotor state to consider what the fundamental grain of motor neuron firing might be: is it organized at the level of single neurons, spinal segments, or muscle groups? Next, we will use these data to examine how the interneuron networks responsible for producing different patterns of motor neuron firing during locomotion might find their appropriate motor neuron targets during development. This line of inquiry will lead us towards the final chapter where we will present data suggesting how inhibitory interneurons might be differentially recruited by functionally distinct groups of motor neurons.

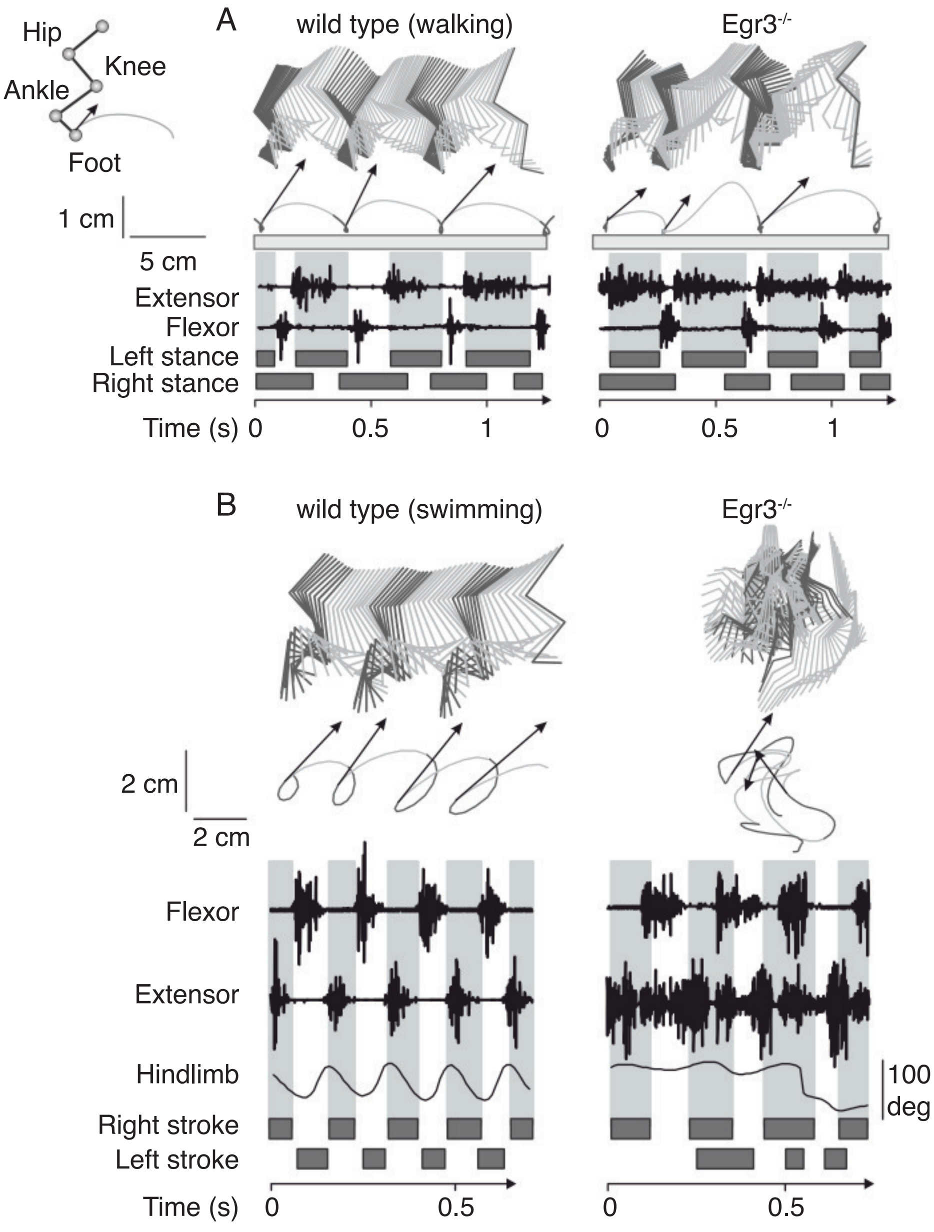

Figure 1.6: **Perturbation to proprioceptive feedback selectively causes deficits in certain locomotor tasks**

(A) Kinematic and EMG data obtained from a wild type (left) and an $Egr3^{-/-}$ mouse (right) that lacks proprioceptive muscle spindle afferents during treadmill walking. (B) Format matches (A), but data was taken during swimming behavior. Figure adapted from [Takeoka et al., 2014].

2

Optical imaging of neuronal firing in locomotor circuits

2.1 Introduction

2.1.1 Limitations of conventional methods in understanding motor neuron activity

The sequence of muscle activation during locomotor behavior has been studied with various methods for more than 100 years [Sherrington, 1906; Brown, 1914][1]. In particular, electromyography (EMG), peripheral nerve recordings, and intracellular recording techniques have been applied to great effect in describing the principles guiding motor neuron recruitment under muscle load [Henneman et al., 1965], the circuits underlying different spinal reflexes [Brown, 1914; Creed et al., 1932], the sequence of muscle activation during varied gaits [Grillner, 1981; Krouchev et al., 2006], and that isolated spinal circuits are sufficient to drive patterned motor neuron activity [Grillner & Zangger, 1979].

---

[1] Portions of this chapter were derived from work in [Machado et al., 2015].

However, none of these electrical recording methods permits the detailed measurement of motor neuron pattern across space [Yakovenko et al., 2002]. Since the discovery that motor neurons sharing common muscle targets are spatially segregated into defined clusters called pools [Romanes, 1964], the question of whether spinal circuits use motor neuron position as a guide during development has remained a persistent question [Jessell et al., 2011]. To resolve this issue, we decided to take advantage of recent advances in optical imaging methods for measuring neural activity. Such methods permit the direct observation of motor neuron and interneuron activation across space, as fluorescence fluctuations related to neuronal firing can be directly observed in neuronal somata and processes.

2.1.2 Interrogating spinal circuits with Ca^{2+}-based imaging techniques

Ca^{2+} imaging has been used in neuroscience for decades. While the usage of Ca^{2+} sensors gained widespread popularity after the development of the first synthetic small-molecule Ca^{2+} indicators [Tsien, 1988], the first reports of optical measurement of Ca^{2+} flux during action potential firing date nearly as far back as the discovery of the Ca^{2+}-activated photoprotein aequorin [Ridgway & Ashley, 1967; Shimomura et al., 1962; Llinas et al., 1972; Shimomura, 1995]. In the years following the initial development of this methodology, it was successfully applied towards the study of spinal circuits [O'Donovan et al., 1993]. However, due to a reliance on widefield epifluorescence microscopy, these first imaging measurements lacked cellular resolution. As a consequence these imaging studies in isolated spinal cord preparations could not discern whether motor neuron pools fired as discrete units or rather as participants in a larger wave-like pattern during rhythmic network activity [Bonnot et al., 2005; O'Donovan et al., 2008] (see Figure 2.1).

Therefore, while Ca^{2+} imaging techniques have been applied towards the analysis of spinal circuits for nearly as long as synthetic Ca^{2+} indicators have existed, only recently has it become possible to resolve the activation patterns of individual neurons at high temporal fidelity. Recent advances have emerged due to the development and application of two-photon laser scanning microscopy (reviewed in [Svoboda & Yasuda, 2006]). This approach has been successfully used to measure the rhythmic activity of genetically defined subpopulations of spinal interneurons that expressed fluorescent markers like GFP [Kwan et al., 2009; Kwan et al., 2010].

In addition, over the last six years genetically encoded Ca^{2+} indicators (GECIs) have improved to the point that they have surpassed synthetic Ca^{2+} indicators in both signal sensitivity and strength [Chen et al., 2013; Horikawa et al., 2010]. In particular, the GCaMP family of GECIs [Nakai et al., 2001] has been improved tremendously. The third-generation variant of GCaMP, called GCaMP3 [Tian et al., 2009], represented an important milestone in the development of GECIs because it was finally adequate to perform many experiments. It remained insensitive to small Ca^{2+} fluxes associated with small bursts of spikes (less than 5 Hz), but importantly exhibited large fluorescence transients after larger bursts of neural activity that could be detected robustly even under *in vivo* conditions. More recently, the GCaMP6 series of indicators was developed—enabling the optical measurement of single action potentials from individual neurons [Chen et al., 2013].

In this work, we took advantage of both the high spatial resolution afforded by two-photon microscopy as well as recent advances in the development of GECIs. This allowed us to achieve high signal-to-noise measurements at high temporal resolution with genetic specificity.

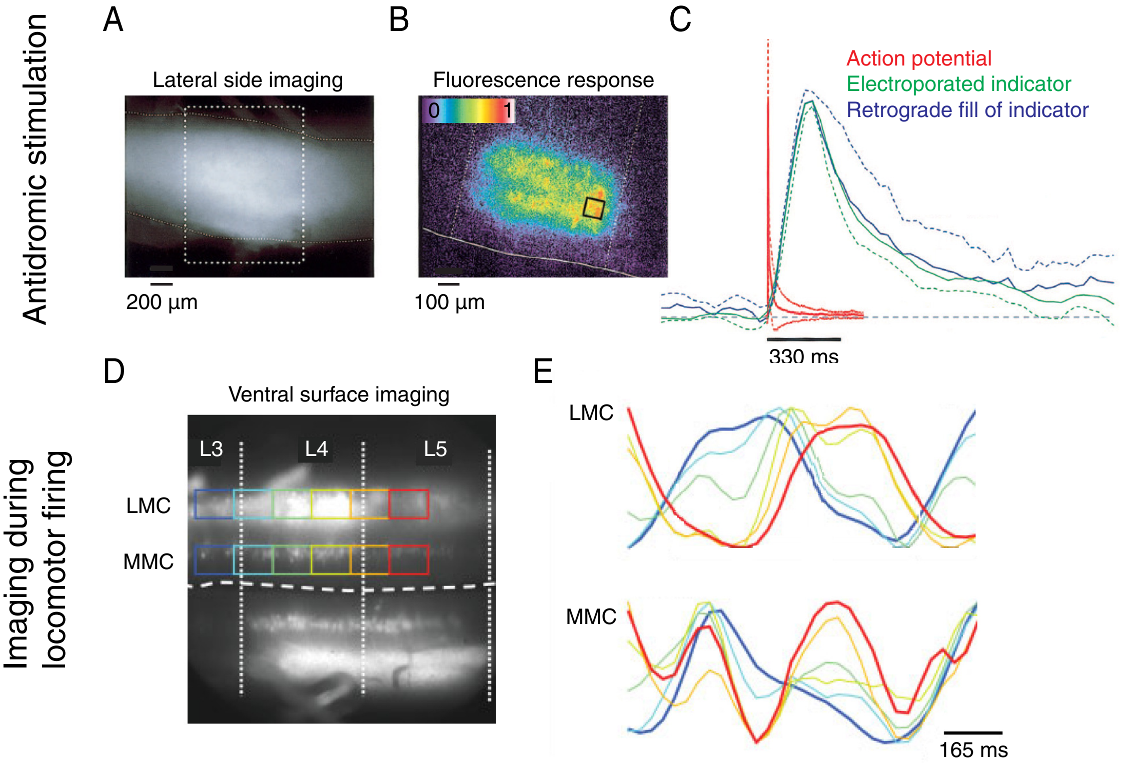

Figure 2.1: **Optical characterization of motor neuron activity using fluorescence microscopy**

(A) Lateral view of lumbar segments L4-L6 in a neonatal mouse spinal cord preparation after electroporation with Calcium Green. (B) Normalized mean fluorescence response during sustained ventral root L5 stimulation at 20 Hz. (C) Comparison of responses to a single antidromic stimulus pulse. Mean fluorescence for electroporated preparations was averaged across 5 preparations (green trace) and across 4 retrogradely labeled preparations (blue trace). Electrical responses were averaged across 7 neurons taken from 6 preparations. All means shown ± s.d. (D) Ventral view of lumbar segments L3-L5 after retrogradely loading of motor neurons with Calcium Green dextran via ventral roots. Colored boxes represent regions of interest (ROIs) drawn over the lateral and median motor columns (LMC and MMC, respectively). (E) Mean fluorescence traces taken from colored ROIs in (D). Panels (A-C) were adapted from [Bonnot et al., 2005]. Panels (D-E) were adapted from [O'Donovan et al., 2008].

2.1.3 Difficulties in quantifying burst timing using optical imaging data

Measurements of Ca^{2+}-sensitive fluorescence transients are intrinsically noisy, especially when made at cellular resolution. Furthermore, the relationship between fluorescence and neuronal spiking is complex. As a consequence, many of the most successful early experimental results to arise from the use of Ca^{2+} imaging methods relied on experimental paradigms where the precise timing and strength of neuronal responses did not need to be known. For example, one of the first papers to demonstrate *in vivo* Ca^{2+} imaging presented moving grating stimuli at different orientations to cats and mice in order to deduce the orientation selectivity of layer 2/3 neurons in primary visual cortex ([Ohki et al., 2005], also see more recent data from [Chen et al., 2013] demonstrating this assay in Figure 2.2A-B). Since each grating stimulus could be displayed for $\sim$10 s, and because most neurons in layer 2/3 were already known to selectively respond to a subset of orientations, data analysis in this experimental setting was straightforward: it merely required thresholding fluorescence data to decide whether a neuron was active or not during a given stimulus presentation. This approach yielded spatial maps of orientation tuning, at cellular resolution.

In contrast, more recent work where layer 2/3 neurons were imaged in posterior parietal cortex (PPC) [Harvey et al., 2012], provides an example of an imaging context where the timing of neuronal activity was much more important to discern. In this work, Harvey and colleagues trained mice to choose to turn left or right in a virtual reality environment containing a T-maze, depending on the color of the walls (i.e. white walls denoted “turn left” and green walls denoted “turn right”). They found that some neurons in PPC seemed to encode the choice that the mouse would choose. Quantifying this result was simple, the raw data during a trial could be thresholded as in the drifting grating task (note the similarity in raw data between Figure 2.2B to Figure 2.2C). However, when they examined their trial-averaged data, they noticed a subtle but robust trend: the collection of all left or right-preferring neurons spanned the duration of the trial, with individual neurons active at distinct moments in time. In order to more clearly understand this result, more complex state-space analyses were necessary, and certain features of this timing result were not quantified owing in part to a lack of knowledge of the relationship between neuronal firing and fluorescence.

This second experimental example bears many similarities with our assay for measuring locomotor-firing from an isolated spinal cord preparation. Because we obtained detailed measurements of the relationship between firing and fluorescence in each experiment, we were able to effectively leverage spike inference methods (described in this chapter as well as Chapter 3). We found that the firing properties of motor neurons during locomotor-firing were also well suited for characterization with optical methods: bursts were big, the frequency of locomotor firing is slow relative to the imaging rate (0.2 Hz bursting verses a 15 Hz imaging rate), and there is rich structure that can be extracted from the timing of motor neuron activity. Indeed, with each subsequent improvement to the experimental preparation and methods described here, we observed additional spatial structure in locomotor firing. This richness in neuronal firing will be described in more detail in the subsequent chapters.

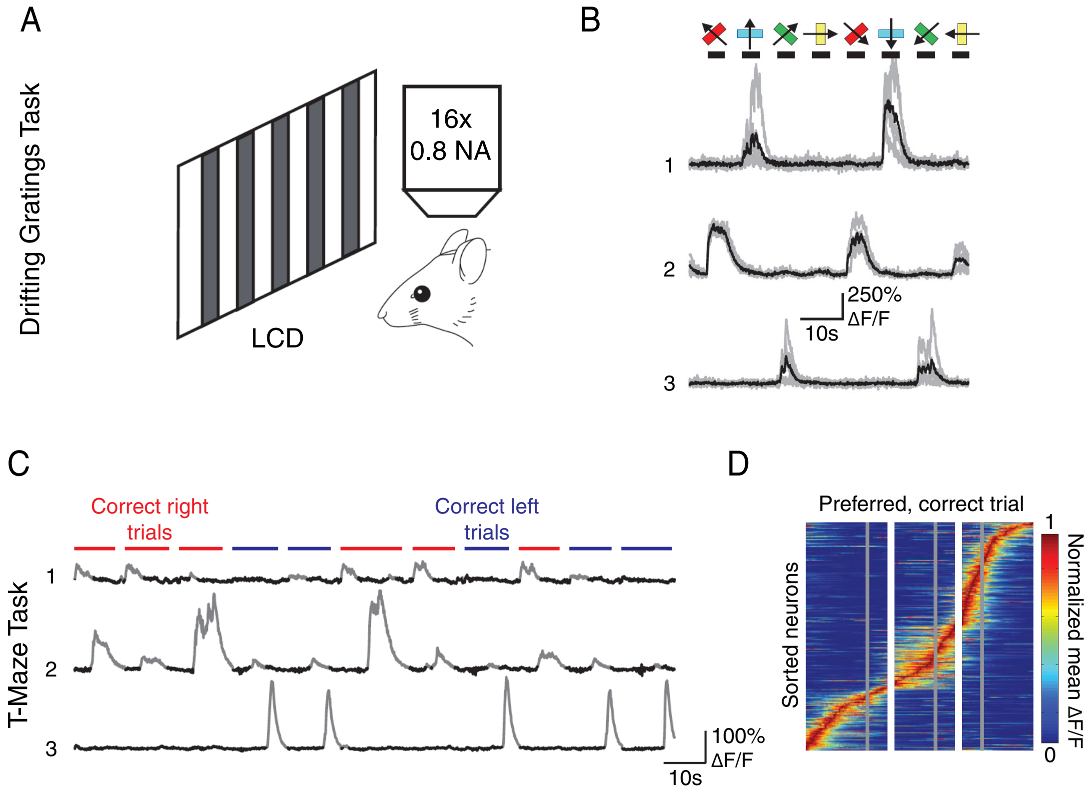

Figure 2.2: **Estimating the timing of neuronal firing is necessary in some experimental contexts**

(A) *In vivo* fluorescence imaging data obtained from [Chen et al., 2013] demonstrating the drifting gratings task. Data analysis only requires determining whether or not a neuron was active or not during a given grating stimulus. (B) Example GCaMP6s fluorescence responses from three neurons in response to eight different grating stimuli. (C) Example GCaMP3 data taken from three neurons imaged during a T-maze exploration task [Harvey et al., 2012]. (D) Individual neurons were found to exhibit activity peaks at each point during all three epochs of a trial (cue, delay, and end)—structure that would have been missed by simply classifying neurons as responders or non-responders. Panels A-B were adapted from [Chen et al., 2013]. Panels C-D were adapted from [Harvey et al., 2012].

2.2 Results

To measure the firing of motor neurons during locomotor-like network activity using optical methods, two technical concerns must be first considered. First, Ca^{2+} indicator (synthetic or genetic) must be selectively introduced into motor neurons. The concentration of indicator within an individual neuron must be determined appropriately. If too little indicator is present in a neuron, Ca^{2+}-sensitive fluorescence transients will be too small to detect. If too much is present, then endogenous Ca^{2+} buffering properties will be perturbed and fluorescence transients will also be undetectable—despite bright baseline fluorescence [Helmchen & Tank, 2005; Garaschuk et al., 2006]. Second, because we are concerned with action potential firing rather than Ca^{2+} concentration per se, each measured Ca^{2+}-sensitive fluorescence transient must be quantitatively related to neuronal firing [Vogelstein et al., 2010; Pnevmatikakis et al., 2015].

In this chapter, we describe our optical imaging setup, our means of delivering indicator selectively to motor neurons, and methods for reliably relating Ca^{2+}-sensitive fluorescence to action potential firing in the face of indicator concentration variability and imaging noise. Then we describe our methods for validating the relationship between spiking and fluorescence for dozens of neurons in each experimental preparation.

2.2.1 Using high-speed two-photon microscopy to characterize motor neuron activity

In widefield fluorescence microscopy, a large fraction of the sample below the microscope objective lens is bathed in excitation light produced by a high-intensity light source and resulting fluorescence emission is captured by a camera. Owing to the light scattering properties of neural tissues, and the fact that excitation light cannot be restricted to the focal plane of the microscope, this approach lacks cellular resolution.

Instead, we must use a microscope that iteratively collects fluorescence from a single point and focal plane at each moment in time by scanning an excitation laser across space. There are two common types of laser scanning microscopes (LSM): confocal and two-photon. In confocal microscopy, the laser sequentially excites a cone of light at a each X,Y position that extends far above and below the focal plane. However, because the current X,Y,Z location is known to the microscope, fluorescence emitted from the sample can be collected through a pinhole positioned to reject emitted fluorescence that did not originate from the current focal plane. Unfortunately, this approach to light collection is highly inefficient in tissues that are ensheathed in white matter which scatters the emitted fluorescence such that it does not pass through the pinhole. This is the case in neonatal mouse spinal cords: even the most superficial motor neurons are more than 100 μm deep relative to the lateral surface.

An alternative approach to is to simply restrict the excitation beam to only illuminate a single spot in X,Y and Z. In such a scheme, a pinhole is no longer needed to block potentially out-of-focus fluorescence, because nearly all excited fluorescence must have originated from the location of interest (Figure 2.3A). This type of microscope requires the use of a pulsed, long-wavelength, femtosecond laser to evoke "two-photon" fluorescence. In this setting, two photons of excitation light are needed to excite a single fluorophore instead of one. As a consequence, fluorophore excitation probability diminishes quadratically above and below the focal point, effectively creating a spatially restricted point of excitation, instead of an elongated cone of light that extends broadly in the Z dimension [Svoboda & Yasuda, 2006]. In addition to spatially restricting the area of excitation at each moment in time, the use of longer wavelengths of excitation light that are not absorbed well by molecules and proteins that are intrinsic to neurons themselves results in reduced photodamage and therefore permits imaging data to be acquired from the same neurons for longer temporal periods. For these reasons, we found two-photon LSM to be well-suited for use in imaging isolated spinal cord preparations.

Unfortunately, one significant disadvantage of LSM is that the laser source must be physically scanned across the tissue of interest by moving two galvanometer mirrors, one on each the X and Y axes. Depending on the size of the galvanometer mirrors themselves and the area to be scanned this process of scanning a whole imaging frame can be quite slow ($\sim$ 1 Hz). Since we want to describe the patterns of neural activity at much faster time scales (ideally closer to 100 Hz), we solved this problem in two ways. First, instead of scanning the X galvanometer mirror in successive lines we jointly scanned the two mirrors in a spiral trajectory. This approach permits image acquisition at speeds up to $\sim$8 Hz. Another solution takes advantage of the fact that when an imaging field is scanned one line at a time, the X galvanometer must scan quickly across each line while the Y galvanometer only needs to slowly step after each line on the X axis has been acquired. Therefore we replaced the X axis galvanometer with a "resonant" galvanometer capable of scanning across each line at a single high resonant frequency: 8 kHz. This approach allowed us to acquire 256 x 256 pixel imaging frames at 60 Hz. In practice we averaged across frames in these image sequences to improve signal-to-noise, achieving an effective frame rate of 15 Hz. Scanning at a high frame rate and then downsampling further reduced photodamage due to the greatly reduced dwell time at each point in space [Varga et al., 2011].

We used this resonant-scanning LSM approach to characterize isolated neonatal mouse spinal cords (aged 2-5 days) while suction electrode recordings were simultaneously obtained from multiple ventral roots (Figure 2.3B). We found that scanning each preparation in the sagittal plane was more effective than imaging from the ventral surface. Sagittal imaging obviated the need to remove ventral roots, which would otherwise occlude the imaging path and also allowed us to simultaneously view multiple motor neuron pools that were arranged along the dorsoventral axis of the spinal cord. Owing to the size and position of the white matter tracts surrounding the spinal cord, pools that were too deep to image from the sagittal plane were also too deep to see from the ventral surface.

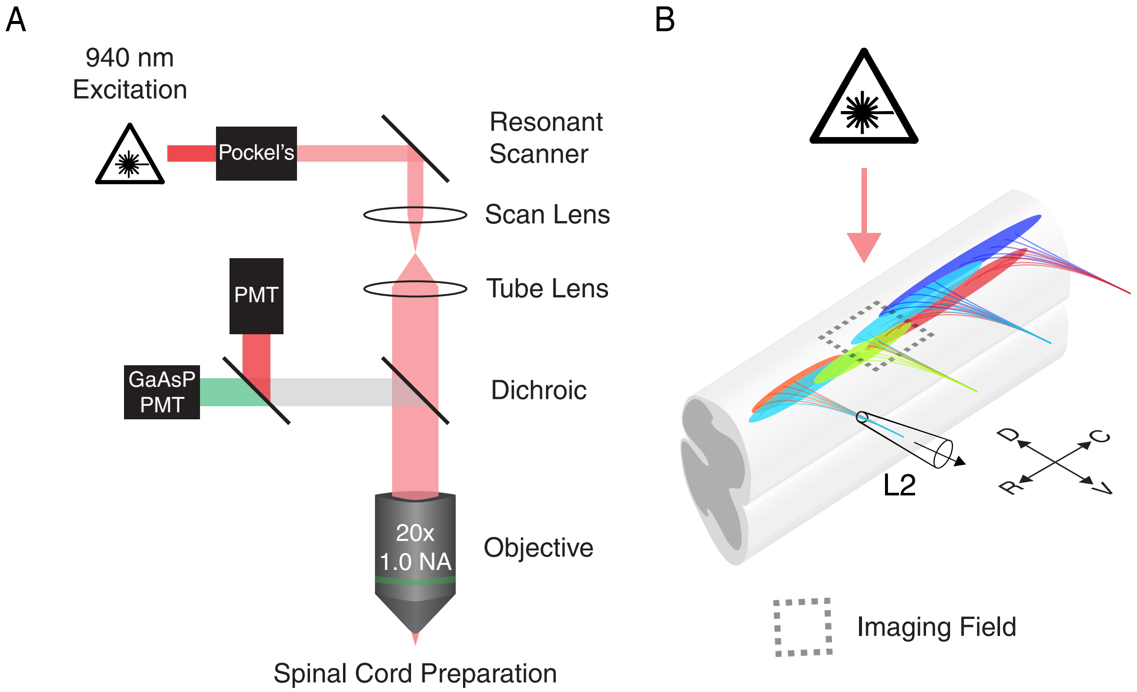

Figure 2.3: **Experimental preparation for optical imaging of locomotor activity**

(A) Diagram of optical layout of resonant galvanometer-equipped two-photon laser scanning microscope used in experiments. (B) Schematic illustrating isolated neonatal mouse spinal cord preparation with a suction electrode positioned on ventral root L2 and the laser scanning microscope positioned over the lateral white matter.

2.2.2 Driving expression of genetically encoded Ca^{2+} indicator in defined neuronal subtypes

We next turn our attention towards the task of selecting an appropriate Ca^{2+} indicator and driving its expression selectively in motor neurons.

Over the course of this project, we evaluated three approaches for selectively delivering indicator to motor neurons. First, we tried direct application of Calcium Green (Calcium Green-1 dextran 10,000 MW; Life Technologies) to ventral roots via suction electrodes (Figure 2.4A). While this approach yielded nice dye filling, it required 8-10 hours of time. This required the experimental preparation to be isolated and held under cold artificial cerebrospinal fluid (ACSF) overnight before an imaging experiment could be conducted, resulting in diminished preparation viability once the experiment could actually begin. The amplitude of fluorescence transients was also highly variable from neuron to neuron, owing to variability in dye uptake by each axon in the ventral root. This issue, combined with the fact that each ventral root had to be independently filled with dye if we desired to label multiple spinal segments with indicator, made this method inappropriate for our experimental needs. Consequently, we were left with two remaining options: drive the expression of GCaMP (the best GECI family available to us, we were unable to obtain useful data through the use of GECOs [Zhao et al., 2011]) using either a viral vector or a transgenic mouse.

We evaluated both of these options. First, we attempted to use *Cre* dependent adeno-associated virus (AAV) vectors. Either via muscle injection, or by direct spinal cord injection into the neonatal mouse, we found that this approach was ineffective due to the >1 week latency between initial viral infection and robust GECI expression (Figure 2.4B). Instead, we found that glyocoprotein-deficient SAD-B19 rabies viruses expressing GCaMP variants were able to drive robust levels of expression in just 2-3 days following muscle or spinal cord injection (collaboration with TR Reardon; protocol for production based on [Osakada et al., 2011]). Unfortunately, this approach had two significant downsides: at 4-5 days post-infection, $GCaMP^+$ motor neurons became non-responsive and exhibited unusual morphological characteristics, suggesting that rabies (or high levels of GCaMP) eventually had toxic effects on the neurons. Additionally, rabies yielded sparse labeling of neuronal tissues after spinal injection, and only a few infected neurons per muscle injection. Consequently, in order to drive robust indicator expression at young postnatal ages across all motor neurons, we decided to use conditional Rosa::GCaMP3 mice generated by the Allen Institute (line Ai38; Figure 2.4C; [Zariwala et al., 2012]).

We also tested three different types of Ca^{2+} indicator: the synthetic indicator Calcium Green and two GECIs: GCaMP3 and GCaMP6 (both the *s* and *f* variants). To evaluate the relationship between fluorescence and spiking for each of these probes, three motor neurons (expressing Calcium Green, GCaMP3, and GCaMP6S, respectively in panels D-F of Figure 2.4) were driven to fire in a sequence of different sized bursts (burst count indicated in numbers above each orange stimulus). In response, clear fluorescence transients of varying magnitudes were observed (red lines; spike inference appears as black bars; note variable scale bar size in each panel). In the examples shown, both Calcium Green and GCaMP6S show clear fluorescence transients to single spikes while the GCaMP3 expressing neuron only shows clear responses above 10 Hz. In most of the experimental data in this thesis, we elected to use GCaMP3 (since a conditional mouse was available) despite its insensitivity to small numbers of action potentials because we were able to resolve bursting activity during each cycle of locomotor firing in our data using this sensor. This is consistent with published intracellular recording data obtained from motor neurons during the same network state that shows bursting activity at high firing rates during each burst—with nearly no activity out-of-cycle (e.g. in [Zhong et al., 2007; Beliez et al., 2015]).

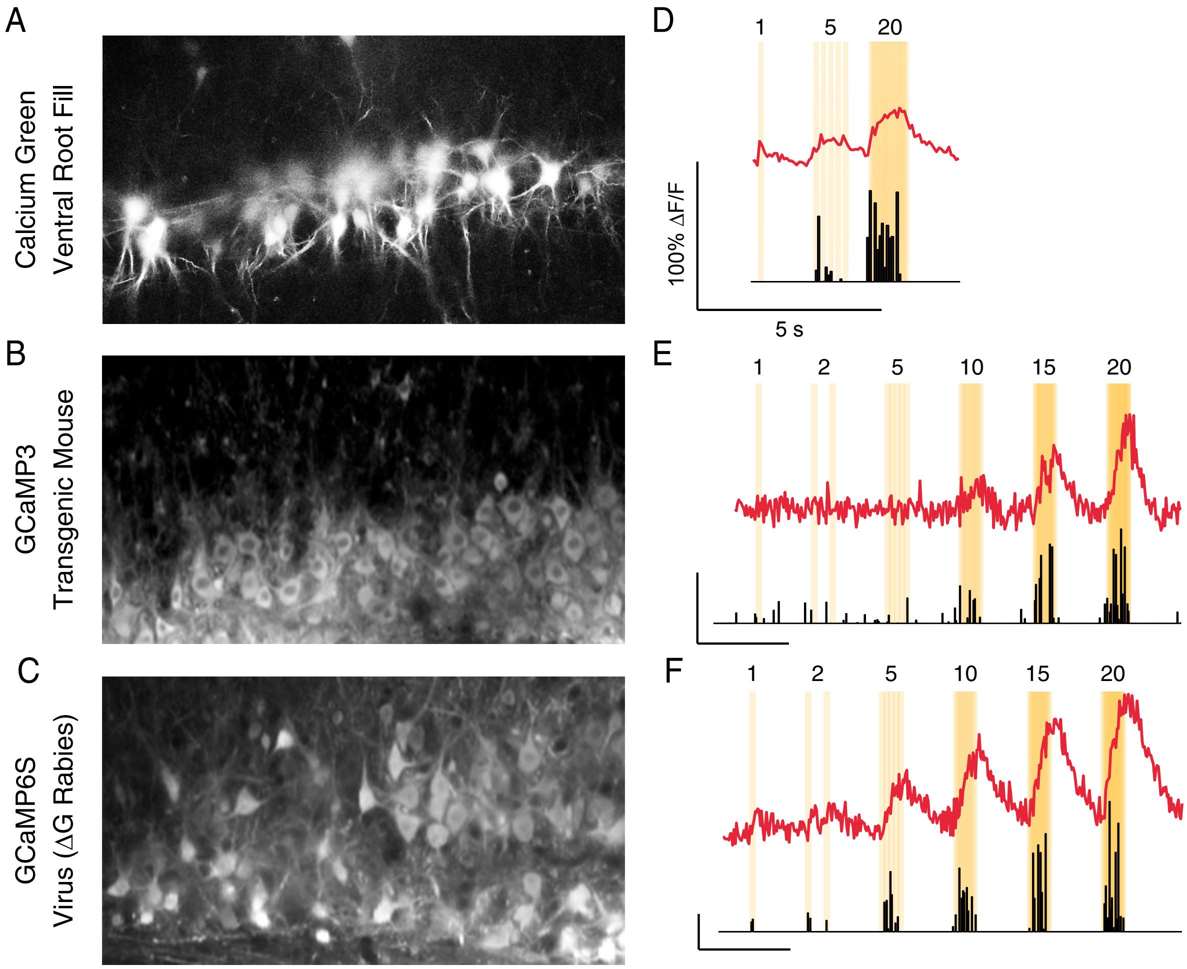

Figure 2.4: **Optical readout of action potential firing in motor neurons** (A-C) Ca^{2+} indicator was loaded into motor neurons, either via ventral root fill of Ca^{2+} green (A), use of conditional transgenic mice ($Olig2 :: Cre; Rosa :: GCaMP3$; B), or via viral injections ($\Delta G - Rabies - GCaMP6S$; C). (D-F) Action potential firing was reflected in single-trial Ca^{2+}-sensitive fluorescence time series data acquired from single motor neuron somata (red traces) during antidromic stimulation of ventral roots (orange bars) at different frequencies (numbers above orange bars). Inferred action potential firing is shown below each red trace (black bars; amplitude is arbitrarily scaled). Note different scale bar sizes on fluorescence measurements between panels D-F.

2.2.3 Quantifying features of motor neuron firing using Ca^{2+} imaging

As is shown in Figure 2.5A-D, and in [Helmchen & Tank, 2005; Vogelstein et al., 2010; Pnevmatikakis et al., 2015], the relationship between fluorescence and the spiking of a single neuron can be approximated by convolving a spike train (simulated data in Figure 2.5A) with a exponentially-decaying kernel with sharp rise and slow decay, where the decay time constant is related to the concentration of Ca^{2+} indicator (left panels of Figure 2.5B-C). Independent, Gaussian noise, can then be added at each time step in the simulated calcium time series to generate simulated data that approximates that measured from real motor neurons that were induced to fire in rhythmic bursting activity (Figure 2.5E, red fluorescence time series data aligned to a simultaneous recording from ventral root L2).

In this context it is straightforward to see that while the onset of neuronal spiking (seen in Figure 2.5A) aligns clearly with a rise in fluorescence, neither burst peak or burst duration (red and blue lines, respectively in Figure 2.5B-D) can be easily inferred. There are two possible solutions to this problem. First, we could restrict our analyses of neuronal firing to detecting burst onset and simply detect fluorescence rise times [Kwan et al., 2009]. Alternative, we could try to estimate the decay rate of the Ca^{2+} indicator and try to estimate the timing of burst peaks and offsets, either through the use of spectral methods [Kwan et al., 2010] or using spike inference algorithms to estimate the timing of neuronal spiking [Vogelstein et al., 2010; Pnevmatikakis et al., 2015].

In this work, we chose to apply spike inference methods (as described in Chapter 3 and schematized in Figure 2.6A) to estimate the onset, offset, and duration of motor bursting from Ca^{2+} fluorescence data. However, we worried whether our simple model of Ca^{2+} dynamics was adequate for describing our data. In particular, it is known that certain nonlinearities may exist in calmodulin-based sensors owing to the structure of calmodulin itself [Crivici & Ikura, 1995]. Calmodulin can bind up to four Ca^{2+} at two high-affinity binding sites and two low-affinity binding sites, plausibly generating nonlinearities in the relationship between spiking and fluorescence when using GCaMPs vs. other sensors that are not based on calmodulin [Greenberg, 2015].

Therefore, we explicitly validated the three assumptions that underlie the spike inference model we used. First, we assume that the relationship between spiking and fluorescence is linear, and can be modeled by simply convolving a spike train with a kernel with instantaneous rise (relative to the imaging frame rate) and exponential decay (red 1 in Figure 2.6A). We tested this assumption in Figure 2.6C-D by fitting a nonlinear model to the data and observing that it did not produce appreciably better fits to the data.

Second, we assume that the noise in our imaging measurements can be modeled as a normally distributed random variable added to each fluorescence observation (red 2 in Figure 2.6A). We validated this assumption on fluorescence measurements when the actual spiking behavior of the neuron was known. By convolving the true spike train of the neuron with an appropriate exponential kernel, we could create a predicted noiseless calcium trace (Figure 2.7A-D). Testing this assumption, we found that histograms of the difference between this "linear prediction" and the actual fluorescence observations (i.e. the residual error) clearly resembled normal distributions (Figure 2.7D; as in [Vogelstein et al., 2010]).

Third, we needed to determine whether the actual output from the spike inference algorithm closely matched the actual firing of the neuron (red 3 in Figure 2.6A). If it did not, that could either be due to the fact that our inference algorithm has failed, or because the sensitivity of our chosen Ca^{2+} indicator, GCaMP3, was inadequate to resolve features of the underlying neural activity. In the next section, we will provide validation for this third assumption. A detailed description of the development and implementation of the spike inference algorithm is provided in Chapters 3 and 8.6.

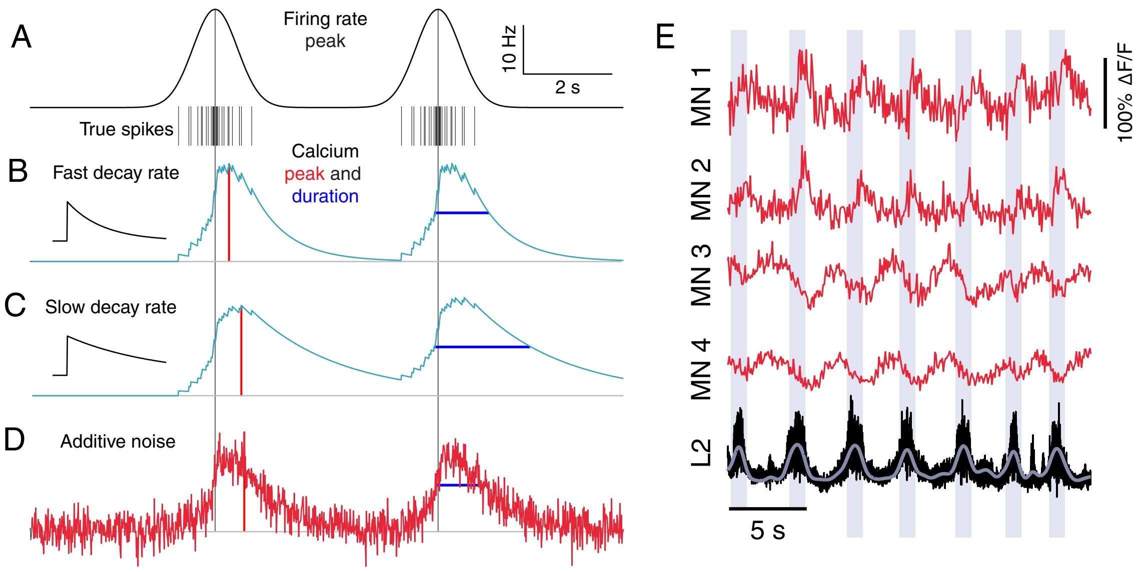

Figure 2.5: **Quantifying features of motor neuron firing using Ca^{2+} imaging** (A-D) Schematic depicting the relationship between firing and Ca^{2+}. (A) Model firing rate with bursts peaking at 20 Hz (top) and underlying Poisson spike train (bottom). The spike train is identical during both bursts. Extended vertical black lines indicate the time of peak firing rate during each burst. (B) Convolving a fast-decaying Ca^{2+} kernel (black; left) with the spike train shown in (A) results in a Ca^{2+} time series (cyan; right). Red bars denote the time of the Ca^{2+} peak. Blue lines indicate burst duration as measured from the Ca^{2+} signal (defined as full width at half maximum amplitude). (C) The convolution of the spike train from (A) with a slower-decaying kernel (black; left) results in the time series shown (cyan; right). Variability in the Ca^{2+} indicator decay rate makes the comparison of burst duration measurements taken from different preparations difficult. (D) Gaussian noise was added to the Ca^{2+} time series from (B) in order to simulate noisy fluorescence measurements, in which both the Ca^{2+} peak and duration are obscured. (E) Ca^{2+} sensitive fluorescence time series data acquired from four motor neurons during locomotor firing (MN1-MN4) aligned to a simultaneous electrical recording from ventral root L2.

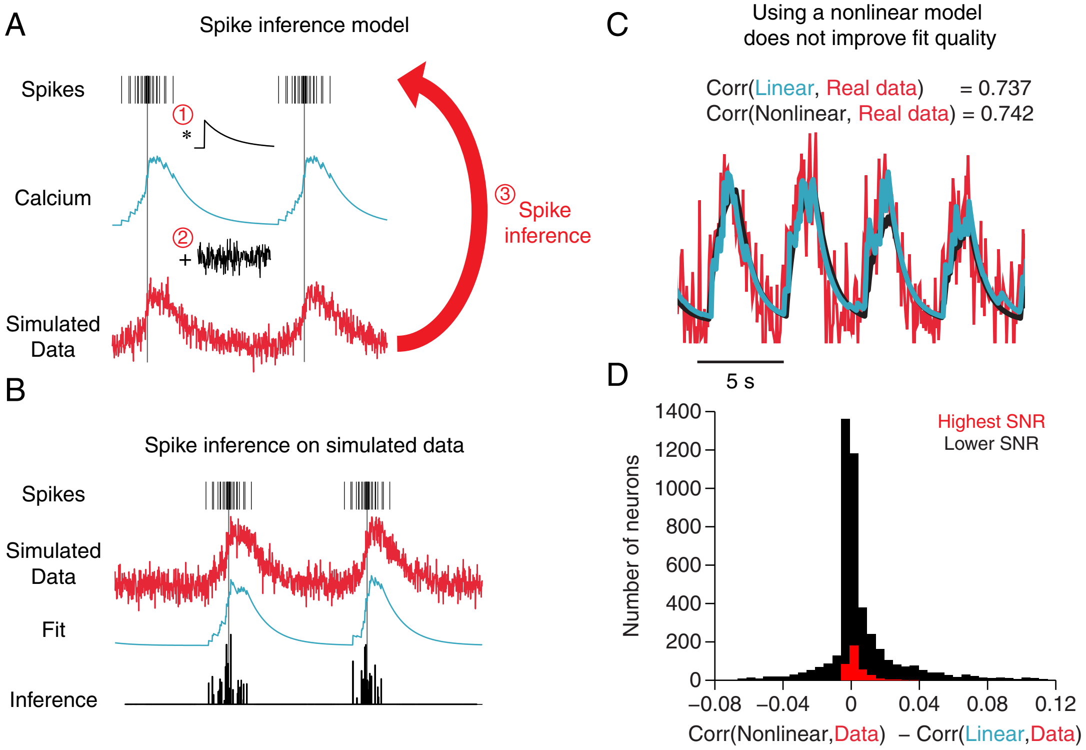

Figure 2.6: **Spike inference permits estimation of motor neuron firing**
(A) Our spike inference algorithm used a simple model that assumed fluorescence measurements arose from a spike train convolved with a single-exponential kernel (red 1; validated in panels C-D), with additive Gaussian noise (red 2; validated in Figure 2.7D-E). The algorithm inverted this model (3; validated in Figure 2.8) to find the most likely spike histogram underlying each fluorescence time series. (B) Example showing performance of spike inference on simulated data (red) plotted above the spike inference model fit (cyan) and inferred spikes (black bars). (C) A fluorescence time series measured from a motor neuron (red), together with the predicted Ca^{2+} signal derived from either a linear model of Ca^{2+} (cyan) or a nonlinear model (black). (D) Histogram comparing the differences between linear and nonlinear model fit quality, as measured using the Pearson correlation (Corr) between measured fluorescence and model prediction. This difference, Corr(linear prediction, data) - Corr(nonlinear prediction, data), is shown for 4944 neurons that were driven to fire in defined patterns (see Figure 2.7D-E). Red bars show a subset of high SNR neurons (n = 367) that were used to estimate the fluorescence transient decay rate.

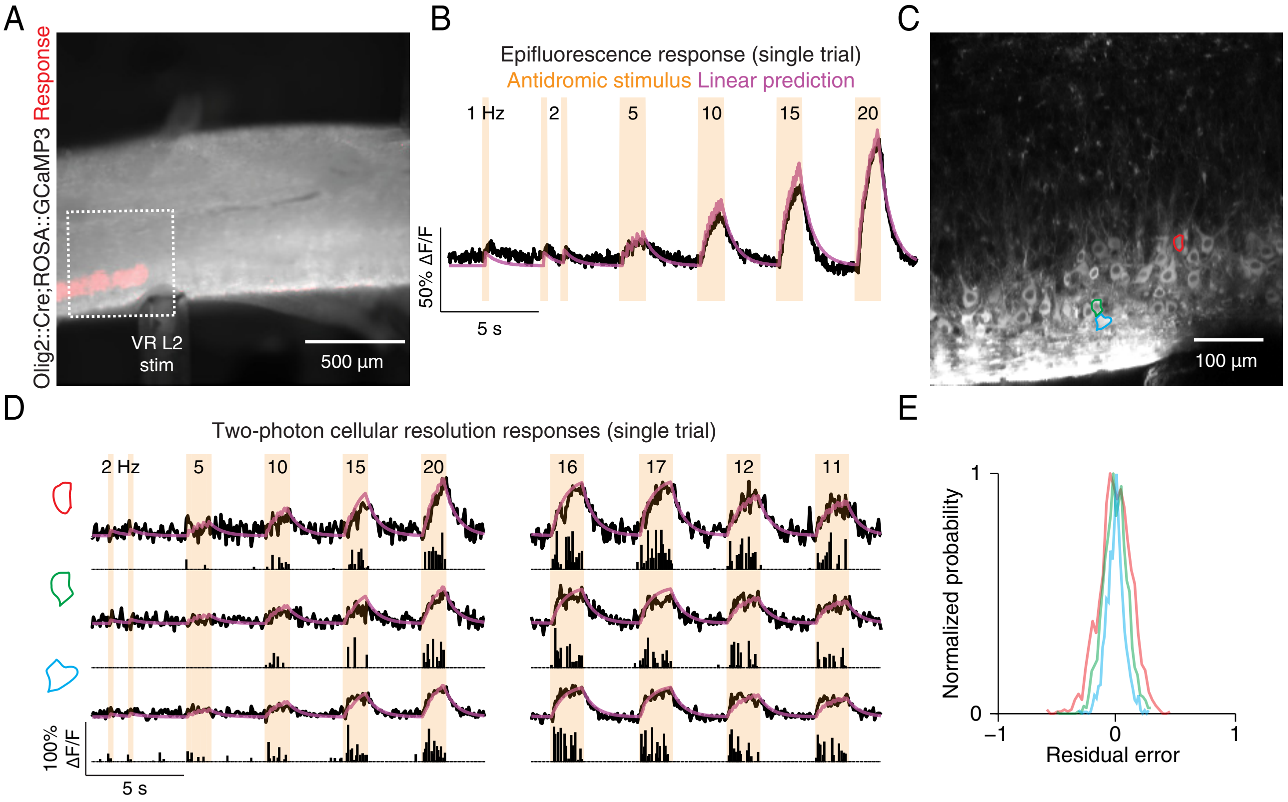

Figure 2.7: **Antidromic calibration to relate fluorescence to neuronal spiking** (A) Sagittal view of L2 during antidromic stimulation taken under epifluorescence illumination. The region responsive to antidromic stimulation is shown in red. (B) Average response to the antidromic stimulus (orange; numbers show stimulation rate during each stimulus train in Hz) across the red region shown in (A). The convolution of the antidromic stimulus and an exponentially decaying kernel is superimposed upon the average fluorescence time series (purple), and represents the predicted Ca^{2+} response to the antidromic stimulus under our Ca^{2+} model. (C) Two-photon imaging field (dotted region in (A)) containing example motor neurons that were responsive to antidromic stimulation (colored ROIs). (D) Fluorescence time series (black) from three ROIs in (C) during antidromic stimulation (orange; numbers show stimulation rate during each stimulus in Hz). The predicted Ca^{2+} response is shown in purple and the inferred spikes underlying each fluorescence time series are shown as black bars. (E) Histograms of the residual error between the fluorescence time series and predicted Ca^{2+} response for each of the three responses shown in (D).

2.2.4 Antidromic calibration to relate fluorescence to neuronal spiking

The validity of our quantification neuronal activity depends on the ability of the spike inference model to capture the relationship between firing and fluorescence. The model was calibrated and its applicability evaluated by exploiting the fact that motor neurons activated antidromically by ventral root stimulation fire in patterns that match stimulus timing (Figure 2.7; see example data from [Bonnot et al., 2005] in Figure 2.1A-C). For each experimental preparation, a fluorescence transient decay time constant was computed using fluorescence measurements obtained during patterned antidromic stimulation that mimic locomotor-like rhythmic burst firing.

Use of these time constant values corrected for decay time variation between preparations (Figure 2.8). Importantly, we noted a systematic bias in observed time constant values as a function of *Cre* driver line (Figure 2.8A). Use of $Olig2 :: Cre$ reliably yielded preparations with average time constant values between 0.65-0.85 seconds. In contrast, $ChAT :: Cre$ preparations typically had time constant values closer to 1.0 seconds. This discrepancy likely results in part from the fact that *ChAT* expression in motor neurons begins at embryonic day 12, while expression of *Olig2* begins earlier at embryonic day 11 (Nikolaos Balaskas, personal communication). Whatever the mechanism, our ability to detect this difference underscores the importance of being able to accurately estimate this time constant value in each preparation. Not accounting for this variance results in apparent variance in phase tuning between different experimental preparations (Figure 2.8B-C; in particular compare the spread of datapoints in 2.8C between peak detection and spike inference).

To assess the accuracy of spike inference, we examined phase tuning estimates for individual motor neurons during antidromic stimulation (Figure 2.7D). Tuning measurements derived from spike inference were nearly identical to values computed directly from antidromic stimuli (mean difference ± standard deviation (s.d.) = -2.0 ± 10.7°, n = 367 neurons; Figure 2.8B,C). Thus, spike inference permits accurate estimation of motor neuron phase tuning.

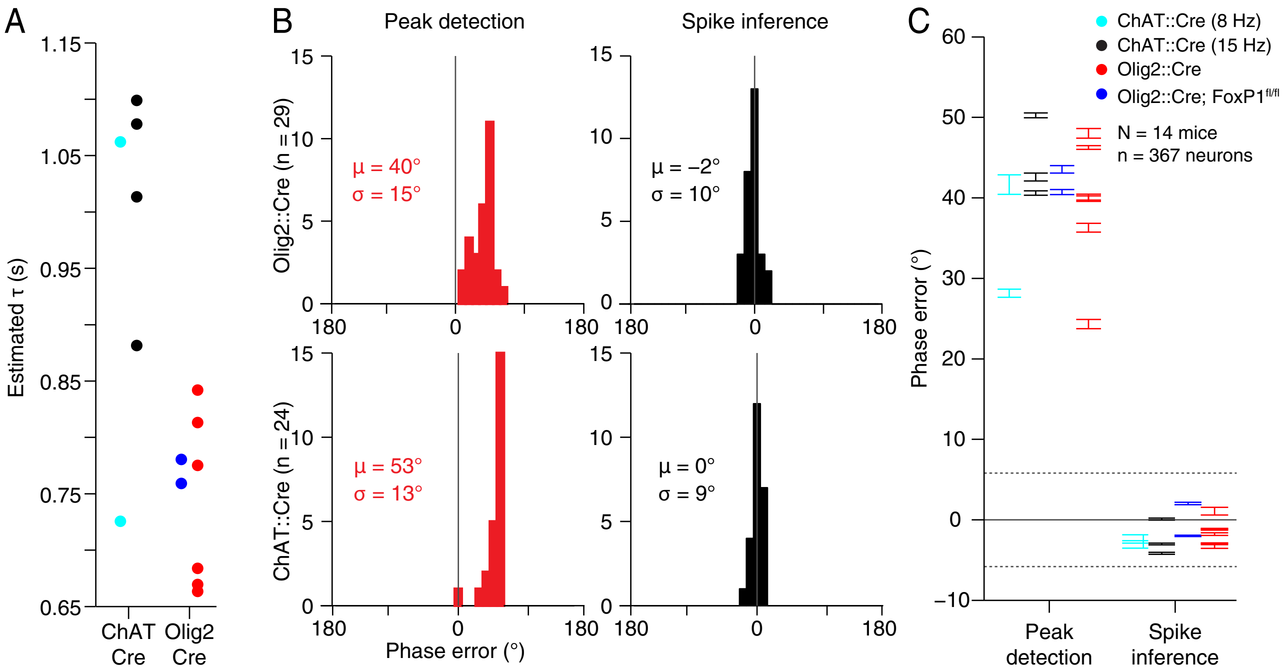

Figure 2.8: **Variation in Ca^{2+} transient decay rates between preparations** (A) Estimated decay time constants in seconds for each dataset plotted in (C). Colors correspond to different experimental conditions (legend in (C)). (B) Comparison of peak detection and spike inference approaches to phase tuning estimation. Phase tuning was estimated using a simple peak detection method (left), or using spike inference (right). Phase tuning was estimated using fluorescence data taken from four antidromic bursts (shown in the left panel of (Figure 2.7D)). The midpoint of each burst was defined as 0°. Histograms showing phase tuning estimation error from n = 29 motor neurons from a single $Olig2 :: Cre$ mouse (top) and n = 24 motor neurons from a single $ChAT :: Cre$ mouse (bottom). (C) Error distributions for each mouse preparation calibrated during antidromic stimulation using peak detection (left) or spike inference (right) to estimate phase. Error bars span the mean ± s.e.m. This analysis reveals that spike inference successfully reduces phase error that arises due to the temporal delay between peak Ca^{2+} and peak firing rate, and due to variation in Ca^{2+} decay rates between preparations.

2.3 Discussion

2.3.1 Necessity of large-scale calibration methods

Many previous studies have examined the relationship between fluorescence and spiking for individual neurons [Smetters et al., 1999; Bonnot et al., 2005; Kwan et al., 2009; Vogelstein et al., 2010; Smith & Häusser, 2010]. However, this work is the first to our knowledge to use antidromic stimulation or a similar method to measure the distribution of fluorescence responses after inducing dozens of neurons of a single cell type to fire in a particular pattern and then use that information to calibrate and evaluate quantitative data analysis procedures. Because we repeated this calibration process in each one of our experimental datasets, we were able to compensate for changes in indicator expression level between preparations. The isolated neonatal mouse spinal cord imaging preparation that we developed here represents a good test case for the development of these methods because there is a significant amount of structure to be uncovered in the timing of motor neuron recruitment.

In the future, antidromic calibration of Ca^{2+}-sensitive fluorescence measurements via electrical [Bonnot et al., 2005] or optogenetic [Li et al., 2015] stimulation of axons might represent an important tool for assessing the relationship between fluorescence and neuronal activity. Recently, a number of papers have presented experimental schemes for "all-optical" recording and stimulation of individual neurons within neural circuits [Packer et al., 2014; Grosenick et al., 2015]. However, we will never have truly reached this goal while we are still reliant on electrical recording methods to calibrate our measurements. Calibration experiments where spiking is measured with an electrode during simultaneous imaging is always labor intensive and often impossible in many deep *in vivo* imaging settings. Therefore, an important must be to develop both experimental and theoretical methods for relating spiking to fluorescence that can make use of even imperfect or incomplete calibration data. For example, direct optogenetic activation of a population of neurons using a sequence of light pulses with increasing intensity would not deterministically evoke a specific spike train in all neurons, but it could certainly be used to produce fluorescence imaging data where strong prior information about the relative firing of the population is known–especially if this procedure was repeated multiple times to permit averaging.

2.3.2 New computational and genetic tools make large-scale imaging possible

Approximately 2,000 motor neurons innervate each hindlimb of the mouse [McHanwell & Biscoe, 1981], yet the precise number of activation patterns produced by this set of neurons during locomotion is unknown. In order to constrain the types of neural computations that spinal locomotor circuits might need to perform to control a limb, detailed measurements of neural activity during behavior would be ideally collected from all of the motor neurons that control a limb. In this chapter, we discussed the technical obstacles that needed to be first resolved before such measurements could be obtained. With this combined genetic and computational approach in hand, we can now generate nearly comprehensive maps of motor neuron activity during locomotor firing.

2.3.3 A population readout of motor pattern

Earlier optical measurements of motor neuron activity across space lacked cellular resolution and therefore were unable to determine whether individual motor neuron pools had distinct firing patterns, or if all motor neurons participated in a single wave-like pattern of activation [Bonnot et al., 2005; O'Donovan et al., 2008] (Figure 2.1).We obtained similar epifluorescence measurements from a mouse spinal cord preparation positioned on its lateral side that expressed GCaMP3 in all motor neurons (30 Hz acquisition rate). Figure 2.9 shows phase tuning estimates, relative to peak L2 ventral root activity, that were computed for individual pixels that are each likely to contain many motor neurons.

This first experiment reveals clear, reproducible, spatial structure in the phase tuning of motor neurons across space. Colored patches that represent groups of motor neurons that are activated at similar times are strikingly present. However, a gradient in phase tuning along the rostrocaudal axis is also apparent: light green pixels that represent early-firing neurons can only be found rostrally, while dark blue pixels representing later firing neurons predominate at more caudal segments. These results seem to reproduce those reported in [O'Donovan et al., 2008] (where imaging was conducted from the ventral surface). But how do these maps actually appear at cellular resolution? Is there a wave of activity, or is such a pattern simply a consequence of the spatial organization of motor neurons into pools? In the next chapters, we will consider these questions in detail.

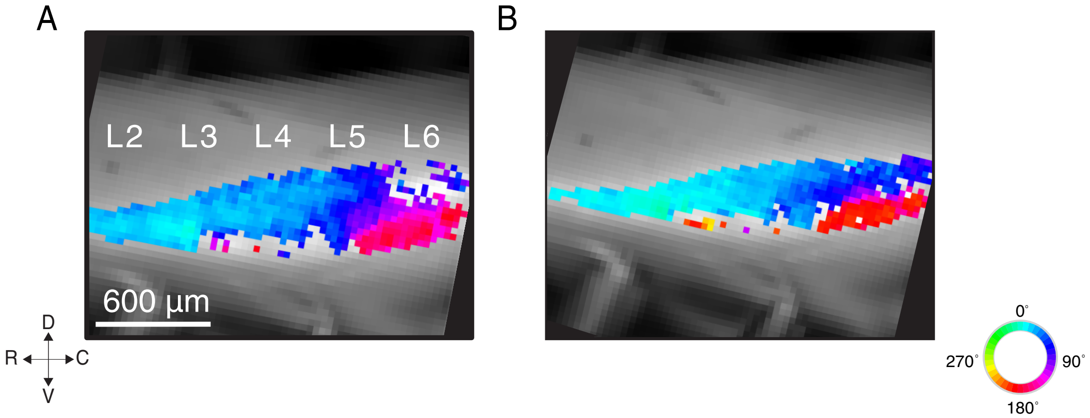

Figure 2.9: **Motor neuron phase tuning is organized across space**

(A-B) Phase of locomotor firing was inferred pixelwise with respect to ventral root L2 for two 90s-long epifluorescence time series datasets taken from a single spinal cord that expressed GCaMP3 solely in motor neurons ($Olig2 :: Cre$; $Rosa :: GCaMP3$). Each panel shows a sagittal view of the spinal cord preparation (gray). The phase tuning of the subset of all pixels with the brightest mean intensity is shown in colors (see legend on bottom right).

3

Analysis of large-scale optical imaging datasets

3.1 Introduction

Before we consider the structure of locomotor firing at cellular resolution, we will first examine problems inherent in the analysis of large datasets containing measurements from hundreds of neurons.[1] Methods suitable for the analysis of recordings obtained from individual neurons are inappropriate for understanding the aggregate activity of thousands of neurons. We therefore present our approach towards the automated analysis of large-scale imaging datasets as well as our contributions to other work that developed statistical models to explain our high-dimensional data in a more intuitive manner.

3.1.1 Understanding firing dynamics across large neuronal ensembles

Since the 1960s, the number of transistors that can be fabricated per square inch has doubled roughly every eighteen months [Moore, 1965]. This trend, known as

---

[1] This chapter in part details contributions made to: [Buesing et al., 2014], [Pnevmatikakis et al., 2015], [Rad et al., 2015], and the SIMA toolbox introduced in [Kaifosh et al., 2014].

Moore's Law, has become somewhat self-fulfilling as semiconductor manufacturers actually structure their hardware development plans such that this trend will continue. Indeed, because this trend has held for so long that software developers can practically assume that it will continue for years into the future, and therefore design new systems and algorithms of increasing complexity under the assumption that the necessary hardware to run their software will exist soon. This expectation of exponential gain over time has led to transformational changes in the manner in which we interact with and use computational tools in our daily lives.

A similar trend of exponential growth can also be seen in the development of new methods for simultaneously recording neurons (Figure 3.1; [Stevenson & Kording, 2011]). Our capability for measuring from neuronal populations roughly doubles every 7.4 years. In contrast to Moore's law, this trend is dictated mostly by experimental need, rather than by market forces. Nevertheless, we have now approached a point along this doubling curve that demands new approaches for data analysis. Simply computing tuning curves, peri-stimulus time histograms, or other summary statistics for each neuron is inadequate when you have simultaneous measurements from 1,000+ cells for a simple reason: neurons exist in circuits and therefore their activity patterns are often interdependent.

If an experimentalist only has access to the activity of a single neuron and a stimulus or behavioral readout, there is not much to be done analytically beyond relating the observed firing pattern to the provided stimulus. In contrast, if the experimentalist is recording from nearly all neurons in a local circuit, they can now ask questions about which parts of the activity are driven by external input vs. recurrent interactions between the observed neurons. Unfortunately, asking such questions about recurrent interactions quickly becomes computationally infeasible: instead of computing a single summary statistic per neuron (which scales $O(n)$), examining just pairwise interactions scales quadratically and exponentially if higher order correlations are considered. Simply interpreting large pairwise correlation matrices consisting of hundreds of entries has become difficult. In this chapter, we will examine new approaches for grappling with this sort of complexity both computationally and intuitively.

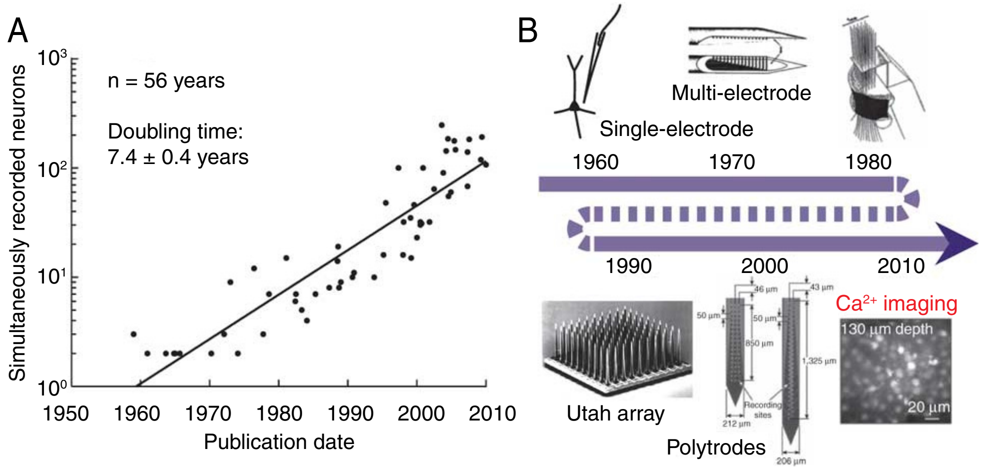

Figure 3.1: **The scale of neural data is growing exponentially**

(A) Measurements from simultaneously recorded neuronal populations plotted on a logarithmic scale as a function of publication date. (B) The growth shown in (A) can be attributed to the development of new recording methods over the past half-century. In this work, we focus on large-scale data obtained from Ca^{2+} imaging methods (red). Adapted from [Stevenson & Kording, 2011].

3.1.2 Difficulties in analyzing large-scale imaging datasets

Aside from the choice of appropriate analysis techniques for understanding population dynamics, large-scale imaging datasets also present a more practical problem: manually processing each piece of data becomes infeasible. In this work, we typically recorded more than 50 image sequences each containing ~ 50 neurons from each mouse. Each of these image sequences then must be decomposed into groups of pixels that contain individual neurons. Additionally, each image sequence had associated ventral root recording data that needed to be filtered, processed, and aligned. Manually tracing 2,500 neurons and aligning associated electrophysiology data is not only labor intensive, but it is error-prone and non-quantitative. In this chapter, we present our methods for automatically processing our data.

3.1.3 New methods for measuring and analyzing population dynamics

Ideally, the process of locating neurons within image sequences, extracting activity events, and relating that collection of information towards the testing of hypotheses about circuit function would all occur simultaneously in a single model fitting process. While the bulk of our analysis resulted from the chaining of simple analysis procedures into a single workflow, other approaches exist (e.g. [Pnevmatikakis et al., 2015]) that combine these steps. This approach will be applied towards the analysis of axonal imaging data in Chapter 6. Additionally, we will consider the question of whether tuning functions (in this case phase tuning estimates, relative to ventral root activity) should be computed for neurons individually, or whether we can take advantage of the fact that adjacent neurons might have similar tuning preferences to achieve more accurate measurements of phase tuning—using less data.

3.2 Results

3.2.1 Automated processing of large-scale imaging datasets

In order to process our imaging data with minimal user intervention, we wrote a series of scripts to implement each step of the analysis workflow shown in Figure 3.2. First, we took ran our semi-automated source extraction algorithm on each fluorescence image sequence to identify the set of pixels within each imaging frame that corresponded to each neuron (Figure 3.3A). To initialize this algorithm, we manually identified the centroid of each motor neuron cell body in ImageJ and then automatically extracted a "block" around each centroid of size 15 x 15 pixels x T images (30 x 30 μm; Figure 3.3B). After this process, we were left with a single block for each user-defined neuron. The set of pixels corresponding to each neuron were then extracted by running a sparse PCA algorithm on each block, defining the positively weighted-pixels in the first principal component as the initial spatial filter, and then smoothing the resultant object with a morphological filter to remove noncontiguous pixels. This process yielded well-defined spatial filters for each neuron and required no manual modification of results—since each filter was "seeded" by the user's decision to define that region as containing a neuron. At the end of this process, pixels that were shared between neurons were assigned to belong to only a single neuron based on whichever centroid was closest to that pixel. This process is described in more detail in Chapter 8.5.

While various algorithms exist for automatically identifying the location and cardinality of cell bodies within an image, these algorithms typically require some amount of user intervention to validate and refine (e.g. [Kaifosh et al., 2014]). Additionally, locating motor neurons within the spinal cord was somewhat difficult relative to other brain structures, owing to the fact that the sagittal surface of the spinal cord is not flat, nor is the thickness of the white matter along the dorsoventral axis.

As a consequence, the effective depth of imaging (and therefore mean fluorescence intensity) will vary considerably across a single sagittal imaging field. We found that our approach of quickly identifying cell centroids by hand and then automatically processing individual blocks robustly solved these problems. Imposing quality thresholds on the extracted neuronal signals proved adequate for culling the subset of neurons where this approach failed. Finally, because our approach for neuronal identification relies on independently processing small blocks of fluorescence data before a later merge and de-duplication operation, this scheme is well-suited for parallelization and thus integration into distributed computing frameworks such as Spark/Thunder [Freeman et al., 2014]. Other groups have independently converged upon similar semi-automated approaches wherein neuron locations are manually identified to seed spatial filters [Chen et al., 2013], further suggesting the merits of this approach.

Once a single fluorescence time series had been successfully extracted from each neuron, we then aligned each time series to simultaneously recorded ventral root recording data and performed spike inference using methods described in the next section (additional technical details can be found in Chapter 8.8).

While methods exist for jointly extracting sources and performing spike inference [Pnevmatikakis et al., 2015], they are currently also much more computationally intensive than performing each step separately. Therefore, we only employed them for analysis of axonal imaging datasets that could not be processed using the method described here (see Chapter 6).

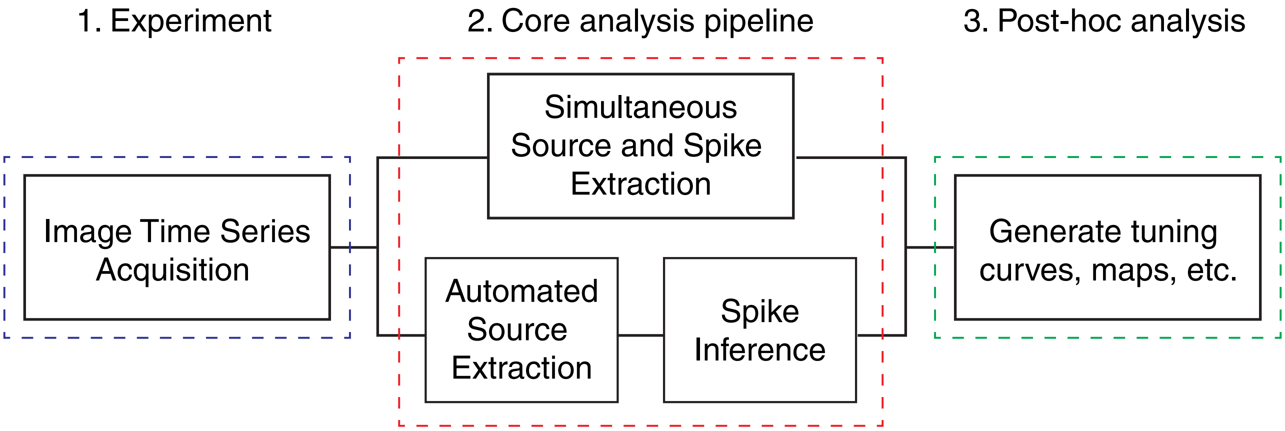

Figure 3.2: **Data analysis workflow for large-scale spinal cord imaging data** (1) Sequences of fluorescence images are acquired from our isolated neonatal mouse spinal cord preparations with simultaneous ventral root measurements. (2, bottom) Individual neurons are identified within each image sequence and their locations are used to extract a one-dimensional fluorescence time series for each cell. These fluorescence time series data are then further processed using spike inference algorithms to estimate the spiking activity of each neuron. (2, top) Alternatively, both cell extraction and spike inference can be solved in a single step, using more advanced computational methods (e.g. [Pnevmatikakis et al., 2015]). (3) Finally, a variety of post-hoc analyses to examine the structure of neuronal firing, from the generation of tuning curves, to state-space analyses, can be performed on the spike inference obtained from each neuron with respect to the ventral root recording data.

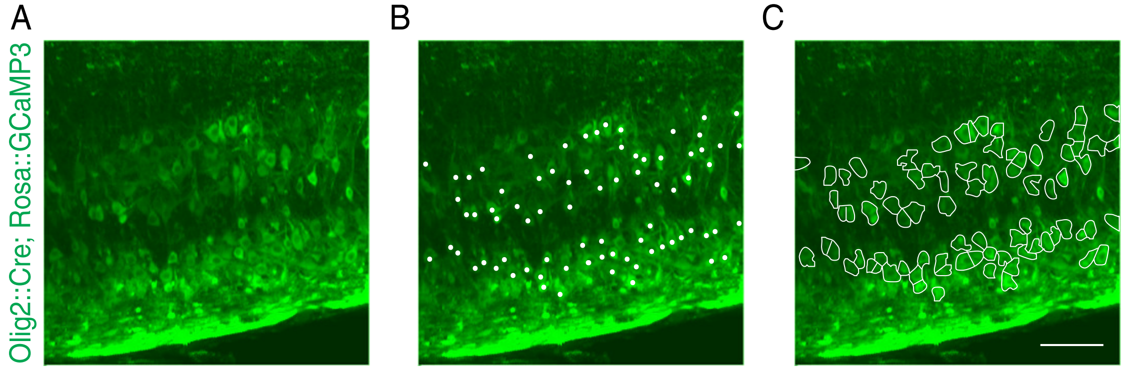

Figure 3.3: **Semi-automatic neuron identification and image segmentation** (A) Example imaging field from an isolated spinal cord preparation expressing the Ca^{2+} sensor GCaMP3 in all motor neurons. (B) Centroids of fluorescent motor neurons were manually identified (denoted as dots). (C) Sparse PCA, followed by a sequence of morphological operations (see text), was automatically applied to a block of pixels surrounding each centroid to extract spatial regions encircling motor neuron somata. Scale bar is 100 μm.

3.2.2 Improved algorithms for spike inference

In Chapter 2, we described how spike inference algorithms can be used to precisely quantify features of neuronal firing from Ca^{2+} imaging data and how to experimentally validate these algorithms[2]. However, we did not discuss the implementation of these algorithms, computational costs to consider, or justify the simple mathematical structure of our model for relating fluorescence to spiking. We will address each of these issues in this section.

The problem of deconvolving the neural activity from an one-dimensional fluorescence time series is achievable at high image acquisition rates, that is, when the time between two consecutive measurements is small compared to the Ca^{2+} indicator decay time constant. Modern resonant scanning [Rochefort et al., 2008], random access microscopy [Reddy et al., 2008], and scanless imaging [Nikolenko et al., 2008] protocols can allow for this by recording from neural ensembles at high temporal resolution.

Under this regime, we take a completely unsupervised approach for performing deconvolution that can be summarized as follows. First, we estimate a parametric model for the Ca^{2+} concentration transient response evoked by a single spike. Instead of fitting a parametric model to isolated calcium transients evoked by single spikes (often only available from dual recording and imaging experiments, as in [Grewe et al., 2010]), we characterize the Ca^{2+} transient as the impulse response of an autoregressive (AR) process of general order p (as schematized in the previous chapter), that models the rise and decay time constants, and estimate it by adapting standard AR estimation methods. After determining the shape of the Ca^{2+} transient we estimate the spiking signal by solving a constrained, non-negative, sparse deconvolution problem. This approach finds the sparsest non-negative neural activity signal that will fit the data up to a desired noise level of the observed fluorescence trace (implementation

---

[2] Portions of section 3.2.2 are derived from [Pnevmatikakis et al., 2015]

details and methods for parameter estimation can be found in Chapter 8.6). Importantly, the noise level, and indicator decay rate can be robustly estimated from the autocovariance and power spectral density (PSD) of each fluorescence time series (see Chapter 8.6). Given these two parameters, the optimal spike inference solution can be found using a convex optimization framework [Boyd & Vandenberghe, 2004]. This computational approach is efficient, as its runtime scales linearly with the number of observed time steps.

Using the antidromic stimulation protocol described in the previous chapter, we tested the deconvolution method using an in vitro dataset of $n = 63$ spinal motor neurons obtained from 7 sequentially acquired imaging fields in a single preparation. The neurons expressed the GCaMP6s indicator (via a rabies vector provided by TR Reardon) and were antidromically stimulated to reliably fire in patterns that matched the stimulus pulses (as in GCaMP3 data presented in [Machado et al., 2015]); we treat the antidromic stimulus spike times as ground truth in this setting. The imaging rate was 14.6 Hz and a first order AR model ($p = 1$) was found to be sufficient to model the Ca^{2+} dynamics in this case (see 2.6C-D in the previous chapter). To quantify the performance we used a correlation measure between the true spiking signal (as is defined by the stimulus timing) and the inferred spiking signal, binned at the resolution defined by the imaging rate or coarser. We compared our methods with a computationally more intensive Markov Chain Monte Carlo (MCMC) method that was first presented in [Pnevmatikakis et al., 2013].

As can be seen in Figure 1A, both methods have largely similar performance: the reconstructed Ca^{2+} time series for the constrained deconvolution algorithm (blue) and the mean Ca^{2+} time series obtained with 500 samples from the MCMC algorithm (green) superimposed on the raw data (black dashed). The MCMC method produces samples of spike trains with continuous time resolution, and thus it can provide further insight into the number of spikes produced at every time bin and the uncertainty of these estimates due to noise and finite imaging rate. This is shown in Figure 3.4B where the marginal posterior of the number of spikes at each time bin is plotted and the true number of spikes is also shown (purple dots). This uncertainty quantification is not available with the constrained deconvolution algorithm, which is based on a convex optimization framework and thus provides just a single estimate of the neural activity (up to a scaling constant and with no quantification of uncertainty), binned at the imaging rate resolution. Nevertheless, the performance of the two methods is largely equivalent (Figure 3.4C,E).

However, at native resolution (bin width = 1Δ), significant dispersion is apparent around the 45° degree line. This dispersion comes from the fact that the correlation metric is sensitive to spike jitter, since it only compares the signal between identical time bins and does not depend on the ordering. If the true spike train is smoothed, this dispersion reduces significantly, and thus the quantified performance increases, indicating that our constrained deconvolution method generally infers the correct number of spikes at approximately the correct times in order to explain the observed fluorescence data. Figure 3.4D displays the recovered traces and true antidromic stimulus spikes in more detail, and finally a plot of the correlation values at multiple bin widths for all cells is shown in Figure 3.4F. Therefore, we conclude that our constrained deconvolution method is scalable and delivers quantitatively similar spike inference output to more computationally intensive techniques like the MCMC algorithm.

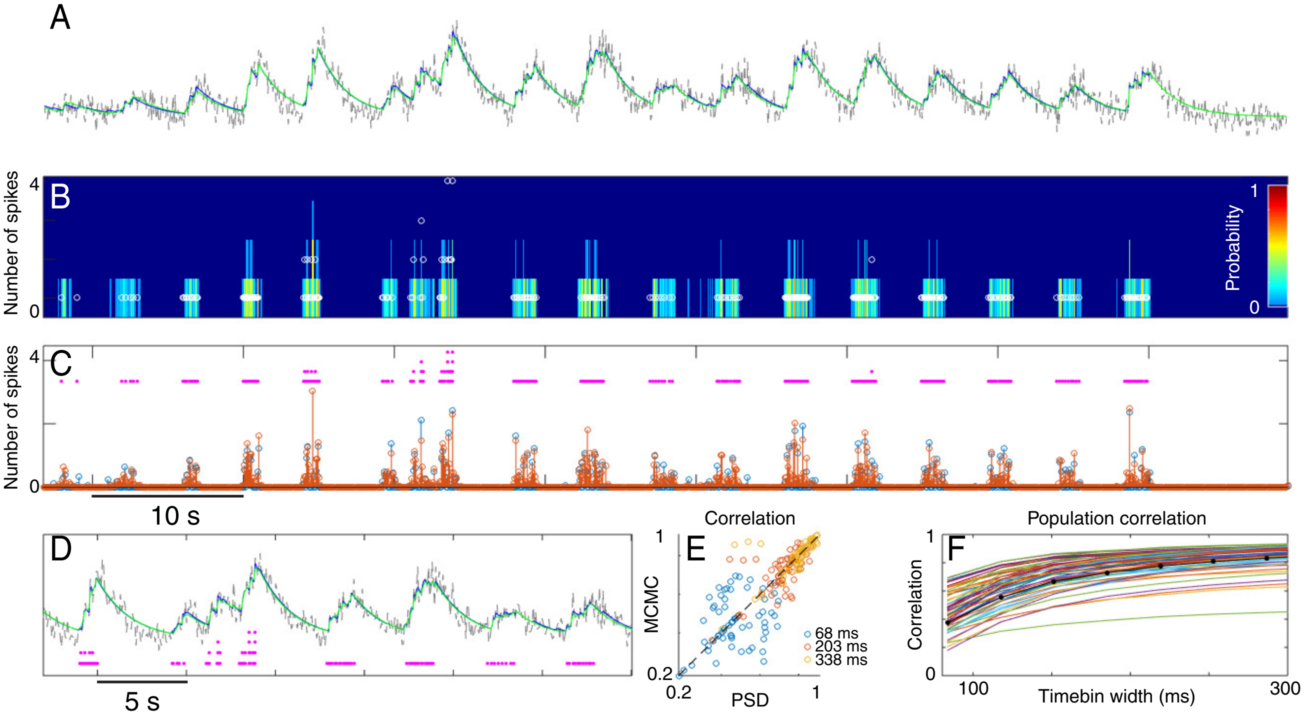
A
B
Number of spikes
4
0
1
Probability
0
C
Number of spikes
4
0
10 s
D
5 s
Correlation
E
1
MCMC
0.2
0.2
PSD
1
68 ms
203 ms
338 ms
Population correlation
F
1
Correlation
0
100
Timebin width (ms)
300

Figure 3.4 *(preceding page)*: **Application of the constrained deconvolution algorithm to *in vitro* spinal cord data**

(A) Raw fluorescence data from a motor neuron (black) and reconstructed fluorescence time series fit by the constrained deconvolution method (blue) and the MCMC method (green) [Pnevmatikakis et al., 2013]. (B) Histogram of spike train samples obtained from the MCMC method (plotted in color) verses the true number of antidromic spikes during each time bin (open circles). Colors indicate the probability of a certain number of spikes within a given time bin, illustrating the ability of the MCMC method to quantify uncertainty and identify multiple spikes within a single time bin. (C) Estimated neural activity (normalized) from the constrained deconvolution method (blue) and mean of the posterior marginal per time bin with the MCMC method (red) verses the true number of antidromic spikes during each time bin (purple dots). (D) Zoomed in version of panel A. (E) Correlation values between true antidromic spike times and the constrained deconvolution estimate using two different methods to estimate the noise power: a method based on computing the power spectral density (PSD; x-axis) and the MCMC approach (y-axis). Neural activity is binned at 3 different resolutions (Δ, 3Δ, and 5Δ, where $\Delta = 68.5$ ms, the duration of a single imaging frame at 14.6 Hz). (F) Correlation values for all 63 cells at various time bin widths. The neuron used in panels A-D is highlighted with black markers.

3.2.3 Clustered factor analysis of multi-neuronal spike data

Recent progress in large-scale techniques for recording neural activity has made it possible to study the joint firing statistics of up to 10^5 cells at single-neuron resolution.[3] Such data sets grant unprecedented insight into the temporal and spatial structure of neural activity and will hopefully lead to an improved understanding of neural coding and computation.

These recording techniques have spurred the development of statistical analysis tools which help to make accessible the information contained in simultaneously recorded activity time series. Amongst these tools, latent variable models prove to be particularly useful for analyzing such datasets [Smith & Brown, 2003; Jones et al., 2007; Macke et al., 2011; Byron et al., 2009]. They aim to capture shared structure in activity across different neurons and therefore provide valuable summary statistics of high dimensional data that can be used for exploratory data analysis as well as for visualization purposes. The majority of latent variable models, however, being relatively general purpose tools, are not designed to extract additional structure from the data. This leads to latent variables that can be hard to interpret biologically. Furthermore, additional information from other sources, such as spatial structure or genetic cell type information, cannot be readily integrated into these models.

An approach to leveraging simultaneous activity recordings that is complementary to applying unstructured factor models, is to infer detailed circuit properties from the data. By modeling the detailed interactions between neurons in a local microcircuit, multiple tools aim at inferring the existence, type, and strength of synaptic connections between neurons [Okatan et al., 2005; Mishchenko et al., 2011]. In spite of algorithmic progress [Keshri et al., 2013], the feasibility of this approach has only

---

[3] Section 3.2.3 is derived from [Buesing et al., 2014]

been demonstrated in circuits of up to three neurons [Gerhard et al., 2013], as large scale data with ground truth connectivity is currently only rarely available. This lack of validation data sets also makes it difficult to asses the impact of model mismatch and unobserved, highly correlated noise sources ("common input").

We therefore propose here a statistical tool for analyzing multi-cell recordings that offers a middle ground between unstructured latent variable models and models for inferring detailed network connectivity. The basic goal of the model is to cluster neurons into groups based on their joint activity statistics. Clustering is a ubiquitous and valuable tool in statistics and machine learning as it often yields interpretable structure (a partitioning of the data), and is of particular relevance in neuroscience because neurons often can be categorized into distinct groups based on their morphology, physiology, genetic identity or stimulus-response properties. In many experimental setups, side information allowing for a reliable supervised partitioning of the recorded neurons is not available. Hence, the main goal of this section is to develop a method for clustering neurons based on their activity recordings.

We model the firing time series of a cluster of neurons using latent factors, assuming that different clusters are described by disjoint sets of factors. The resulting model is similar to a mixture of factor analyzers [Tipping & Bishop, 1999; Ghahramani et al., 1996] with Poisson observations, where each mixture component describes a subpopulation of neurons. In contrast to a mixture of factor analyzers model which assumes independent factors, we put a Markovian prior over the factors, capturing temporal dependencies of neural activity as well as interactions between different clusters over time. The resulting model, which we call mixture of Poisson linear dynamical systems (mixPLDS) model, is able to capture more structure using the cluster assignments compared to latent variable models previously applied to neural recordings, while at the same time still providing low-dimensional latent trajectories for each cluster for exploratory data analysis and visualization. In contrast to the lack of connectivity ground truth for neurons from large-scale recordings, there are indeed large-scale activity recordings available that exhibit rich and biologically interpretable clustering structure, allowing for a validation of the mixPLDS model in practice.

MixPLDS model definition

Let y_{kt} denote the observed spike count of neuron $k = 1, \dots, K$ in time bin $t = 1, \dots, T$. For the mixture of Poisson linear dynamical systems (mixPLDS) model, we assume that each neuron k belongs to exactly one of M groups (subpopulations, clusters), indicated by the discrete (categorical) variable $s_k \in \{1, \dots, M\}$.

The s_k are modeled as i.i.d.:

$$p(\mathbf{s}) \;=\; \prod_{k=1}^{K} p(s_k) = \prod_{k=1}^{K} \mathrm{Disc}(s_k|\phi_0), \tag{3.1}$$

where $\phi_0 := (\phi_0^1, \dots, \phi_0^M)$ are the natural parameters of the categorical distribution. In the remainder of the paper we use the convention that the group index $m = 1, \dots, M$ is written as superscript. The activity of each subpopulation m at time t is modeled by a latent variable $\mathbf{x}_t^m \in R^{d^m}$.

We assume that these latent variables (we will also call them factors) are jointly normal and we model interactions between different groups by a linear dynamical system (LDS) prior:

$$\mathbf{x}_t = \begin{pmatrix} \mathbf{x}_t^1 \\ \vdots \\ \mathbf{x}_t^M \end{pmatrix} \;=\; A\mathbf{x}_{t-1} + \eta_t = \begin{pmatrix} A^{11} & \cdots & A^{1M} \\ \vdots & & \vdots \\ A^{M1} & \cdots & A^{MM} \end{pmatrix} \begin{pmatrix} \mathbf{x}_{t-1}^1 \\ \vdots \\ \mathbf{x}_{t-1}^M \end{pmatrix} + \eta_t, \tag{3.2}$$

where the block matrices $A^{ml} \in R^{d^m \times d^l}$ capture the interactions between groups m and l. The innovations η_t are i.i.d. from $\mathcal{N}(0, Q)$ and the starting distribution is given by $\mathbf{x}_1 \sim \mathcal{N}(\mu_1, Q_1)$.

If neuron k belongs to group m, i.e. $s_k = m$, we model its activity y_{kt} at time t as Poisson distributed spike count with a log-rate given by an affine combination of the factors of group m:

$$\begin{aligned} z_{kt} \mid s_k = m &= C^m_{k:}\mathbf{x}^m_t & (3.3) \\ y_{kt} \mid z_{kt},\ s_k &\sim \text{Poisson}(\exp(z_{kt} + b_k)), & (3.4) \end{aligned}$$

where $\mathbf{b} \in R^K$ captures the baseline of the firing rates.

We denote with $C^m \in R^{K \times d^m}$ the group loading matrix with rows $C^m_{k:}$ for neurons k in group m and fill in the remaining rows with 0s for all neurons not in group m. We concatenate these into the total loading matrix $C := (C^1 \ \cdots \ C^M) \in R^{K \times d}$, where $d := \sum_{m=1}^M d^m$ is the total latent dimension. If the neurons are sorted with respect to their group membership, then the total loading C has block diagonal structure. Further, we denote with $\mathbf{y}_{k:} := (y_{k,1} \ \cdots \ y_{k,T})$ the activity time series of neuron k and use an analogous notation for $\mathbf{x}^m_n := (\mathbf{x}^m_{n,1} \ \cdots \ \mathbf{x}^m_{n,T}) \in R^{1 \times T}$ for $n = 1, \dots, d^m$. The model parameters are $\theta := (A, Q, Q_1, \mu_1, C, \mathbf{b})$; we consider the hyperparameters ϕ_0 to be given and fixed.

For known clusters $\mathbf{s}$, the mixPLDS model can be regarded as a special case of the Poisson linear dynamical system (PLDS) model [Macke et al., 2011], where the loading C is block diagonal.

For unknown group memberships $\mathbf{s}$, the mixPLDS model defined above is similar to a mixture of factor analyzers (e.g. see [Tipping & Bishop, 1999; Ghahramani et al., 1996]) with Poisson observations over neurons $k = 1, \dots, K$. In the mixPLDS model however, we do not restrict the factors of the mixture components to be independent but allow for interactions over time which are modeled by a LDS.

When applying the mixPLDS model to data $\mathbf{y}$, we are interested in inferring the group memberships $\mathbf{s}$ and the latent trajectories $\mathbf{x}$ as well as estimating the parameters θ. For known parameters θ, the posterior $p(\mathbf{x}, \mathbf{s}|\mathbf{y}, \theta)$ (even in the special case of a single mixture component $M = 1$) is not available in closed form and needs approximating. Here we propose to approximate the posterior using variational inference with the following factorization assumption:

$$p(\mathbf{x}, \mathbf{s}|\mathbf{y}, \theta) \approx q(\mathbf{x})q(\mathbf{s}). \tag{3.5}$$

Further details about methods used for approximating this posterior distribution (using variational inference techniques), as well as how to estimate the parameters of the mixPLDS model, are contained in [Buesing et al., 2014].

MixPLDS application I: Artificial data

Here we validate the parameter estimation procedure for the mixPLDS model on artificial data. We generate 35 random ground truth mixPLDS models with $M = 3$, $d^1 = d^2 = d^3 = 2$ and 20 observed neurons per cluster. We sampled from each ground truth model a data set consisting of 4 i.i.d. trials with $T = 250$ time steps each. Ground truth parameters were generated such that the resulting data was sparse (12% of the bins non empty). We compared the ability of different clustering methods to recover the 3 clusters from each data set. We report the results in Figure 3.5A in terms of the fraction of misclassified neurons (class labels were determined by majority vote in each cluster). We applied k-means with careful initialization of the cluster centers [Arthur & Vassilvitskii, 2007] to the data. For k-means, we preprocessed the data in a standard way by smoothing (Gaussian kernel, standard deviation 10 time steps), mean centering and scaling (such that each dimension $k = 1,\ldots,k$ has variance 1). We found k-means yielded reasonable clusters when all populations are one-dimensional (i.e. $\forall m \; d^m = 1$, data not shown) but it fails when clustering multi-dimensional groups of neurons.

An alternative approach is to cluster the cross correlation matrix of neurons (computed from preprocessed data as above) with standard spectral clustering [Ng et al., 2002]. We found that this approach works well when all the factors have small variances, as in this case the link function of the observation model is only mildly nonlinear. However, with growing variances of the factors (larger dynamic ranges of neurons) spectral clustering performance quickly degrades. Standard sparse subspace clustering [Elhamifar & Vidal, 2013] on the spike trains (preprocessed as above) yielded very similar results to spectral clustering. We found our novel Poisson subspace clustering algorithm detailed in [Buesing et al., 2014] to robustly outperform the other approaches, as long as reasonable amounts of data were available (roughly $T > 100$ for the above system).

The mixPLDS model initialized with Poisson subspace clustering consistently yielded the best results, as it is able to integrate information over time and denoise the observations. One advantage of the mixPLDS model is that it not only returns cluster assignments for neurons but also provides a measure of uncertainty over these assignments. However, variational inference tends to return overconfident posteriors in general and the factorization approximation (Equation 3.5) might yield posterior uncertainty that is uninformative.

To show that the variational posterior uncertainty is well-calibrated we computed the entropy of the posterior cluster assignment $q(s_k)$ for all neurons as a measure for assignment uncertainty. We binned the neurons according to their assignment uncertainty and report the misclassification rate for each bin in Figure 3.5B. 89% of the neurons have low posterior uncertainty and reside in the first bin having a low misclassification rate of ≈ 0.1, whereas few neurons (5%) have an assignment uncertainty larger than 0.3 nats and they are misclassified with a rate of ≈ 0.4.

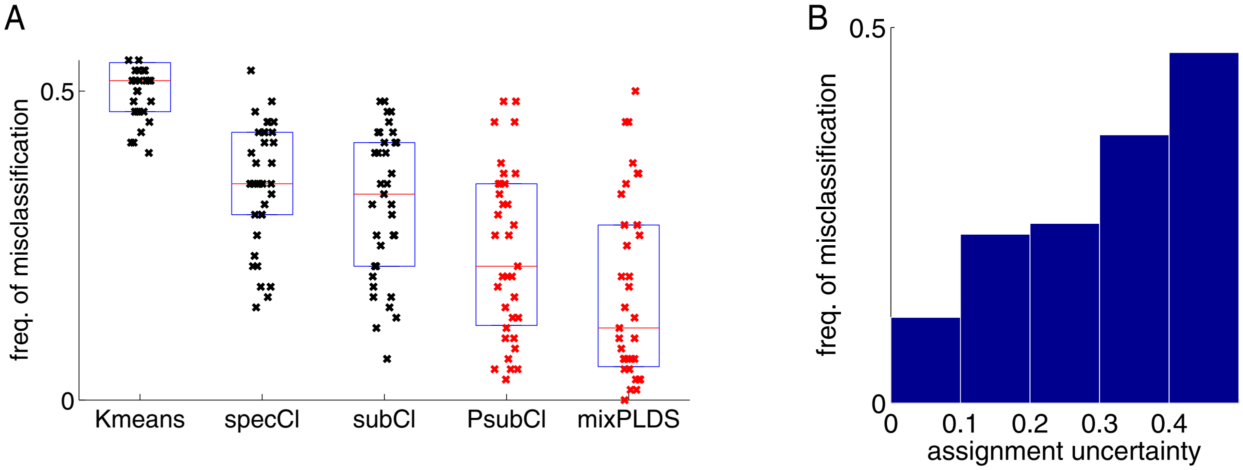

Figure 3.5: **Finding clusters of neurons in simulated data**

(A) Performance of different clustering algorithms, reported in terms of frequency of misclassified neurons, on artificial data sampled from ground truth mixPLDS models. Red bars indicate medians and blue boxes the 25% and 75% percentiles. Standard clustering methods (data plotted in black) such as *k*-means, spectral clustering ("specCl"), and subspace clustering ("subCl") are substantially outperformed by the two methods proposed here (data plotted in red). Poisson subspace clustering ("PsubCl") yielded accurate initial cluster estimates that were significantly improved by application of the full mixPLDs model. (B) Misclassification rate as a function of the cluster assignment uncertainty for the mixPLDS model. This shows that the posterior over cluster assignments returned by the mixPLDS model is well calibrated, as neurons with low assignment uncertainty as rarely misclassified.

MixPLDS application II: Ca^{2+} imaging of spinal cord neurons

We tested the mixPLDS model on Ca^{2+} imaging data obtained from an *in vitro*, neonatal mouse spinal cord that expressed the Ca^{2+} indicator GCaMP3 in all motor neurons. When an isolated spinal cord is tonically excited by a cocktail of rhythmogenic drugs (5 μM NMDA, 10 μM 5-HT, 50 μM DA), motor neurons begin to fire rhythmically. In this network state, spatially clustered ensembles of motor neurons fire in phase with each other (Figure 3.6A). Since multiple ensembles that have distinct phase tunings can be visualized in a single imaging field, this data represents a convenient setting for testing our algorithm. The data (90 second long movies) were acquired at 15 Hz from a custom two-photon microscope equipped with a resonant scanner (downsampled from 60 Hz to boost signal-to-noise). The frequency of the rhythmic activity was typically 0.2 Hz. In addition, aggregate motor neuron activity was simultaneously acquired with each movie using a suction electrode attached to ventral root L2. This ventral root recording was used as an external phase reference point to compute phase tuning curves for imaged neurons, which we used to validate our mixPLDS results.

A deconvolution algorithm [Pnevmatikakis et al., 2015] was applied to the recorded Ca^{2+} time series to estimate the spiking activity of 70 motor neurons. The output of the deconvolution, a 70×1140 (neurons $\times$ frames) matrix of posterior expected number of spikes, was used as input to the mixPLDS model. The non-empty bins of the the first 500 out of the 1140 frames of input data (thresholded at 0.1) are shown in Figure 3.6B.

We used a mixPLDS model with $M = 2$ groups with two latent dimensions each, i.e. $d^1 = d^2 = 2$. We imposed the non-negativity constraints $C \geq 0$ on the loading matrix; these were found to be crucial for finding a meaningful clustering of the neurons, as discussed above. The mixPLDS clustering reveals two groups with strongly periodic but phase shifted population activities, as can be seen from the inferred latent factors shown in Figure 3.7A (middle panel, factors of cluster 1 shown in red, factors of cluster 2 in blue). For each cluster, the model learned a stronger (higher variance) latent factor (solid line) and a weaker one (dashed line); we interpret the former as capturing the main activity structure in a cluster and the latter as describing deviations.

Based on the estimated mixPLDS model, we sorted the neurons for visualization into two clusters according to their most likely cluster assignment $\text{argmax}_{s_k=1,2}\, q(s_k)$. Within each cluster, we sorted the neurons according to the ratio of the loading coefficient onto the stronger factor over the loading onto the weaker factor. Replotting the spike raster shown in with this sorting in Figure 3.7A (middle panel) reveals interesting structure. First, it shows that the initial choice of two clusters was well justified for this data set. Second, the sorting reveals that the majority of neurons tend to fire at a preferred phase relative to the oscillation cycle, and the mixPLDS-based sorting corresponds to an increasing ordering of preferred phases. Figure 3.7C shows the loading matrix C of the mixPLDS, which is found to be approximately block diagonal.

On this data set we also have the opportunity to validate the unsupervised clustering by taking into account the simultaneously recorded ventral root data. We computed a phase tuning curve for each neuron against the last 80 time steps of the ventral root recording data (estimated via L_2 regularized generalized linear model estimation, with an exponential-Poisson observation model). For each neuron, we extracted the peak location of this phase tuning curve, which we call the preferred phase. Figure 3.7B shows these preferred phases as a function of (sorted) neuron index, revealing that the two clusters found by the mixPLDS model coincide well with the two modes of the bimodal distribution of preferred phases. Furthermore, within each cluster, the preferred phases are (approximately) increasing, showing that the mixPLDS-sorting of neurons reflects the phase relationship of the neurons relative to the global oscillatory activity reflected in the ventral root activity. We emphasize that this ventral root recording was not used for fitting the mixPLDS and therefore constitutes an independent validation of our results.

We conclude that the mixPLDS model successfully uncovered clustering structure from the recordings that can be validated using the side information from electrophysiological tuning, and furthermore allowed for a meaningful sorting within each cluster capturing neural response properties. In addition, the mixPLDS model leverages the temporal structure in recordings, automatically optimizing for the temporal smoothness level and revealing the main time constants in the data (in the above data set 1.8 and 6.5 sec) as well as main oscillation frequencies (0.2 and 0.45 Hz). Furthermore, either the latent trajectories or the inferred firing rates shown in Figure 3.7A can be used as smoothed proxies for their corresponding population activities for subsequent analyses.

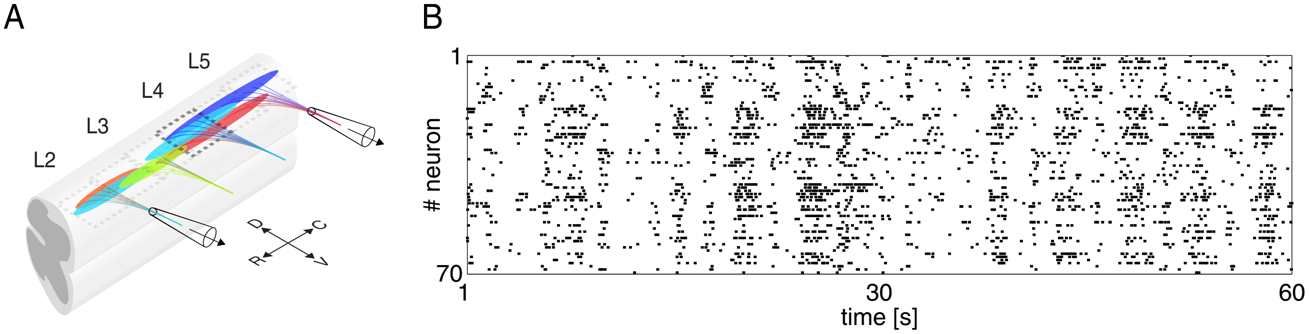

Figure 3.6: **Isolated spinal cord preparation used for evaluating the mix-PLDS model**

(A) Schematic of *in vitro* isolated spinal cord preparation with ventral root recording electrodes shown on segments L2 and L5. (B) 500 frames of spiking data inferred from a fluorescence image sequence containing 70 motor neurons that were used as input for testing the mixPLDS model.

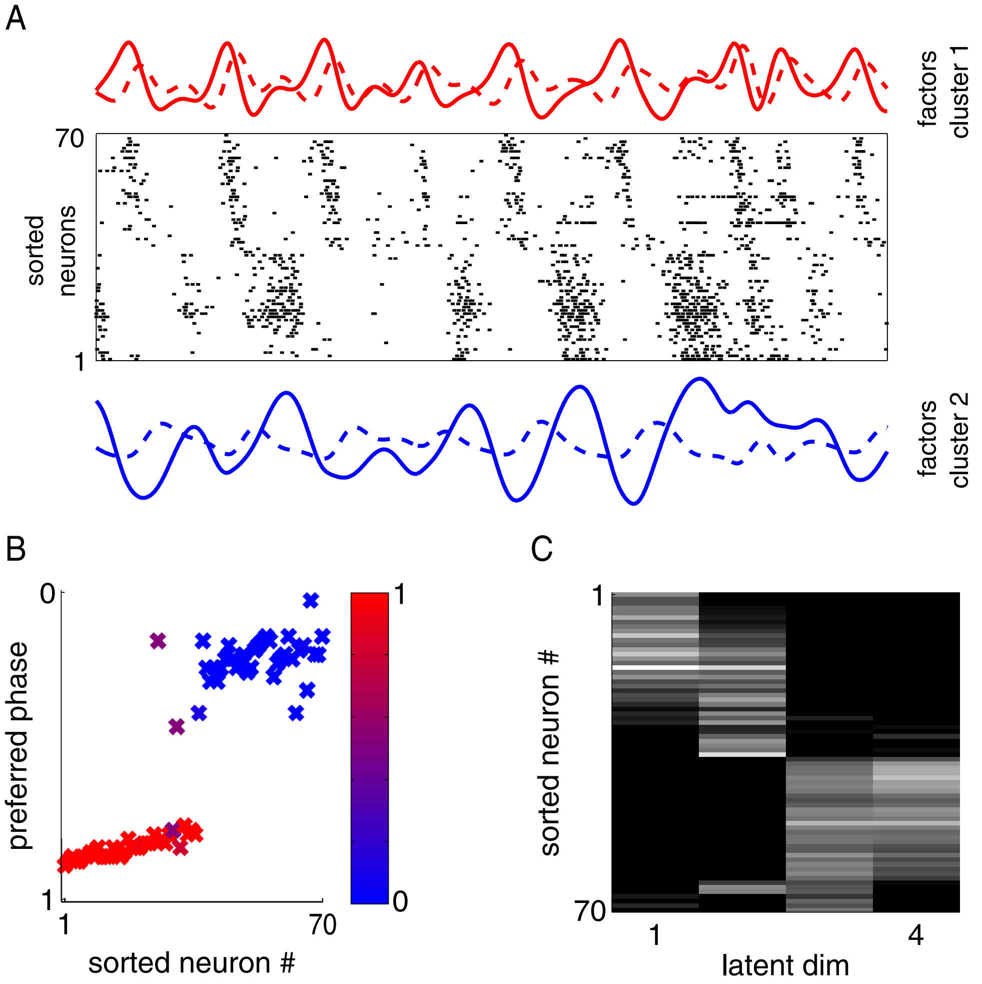

Figure 3.7: **Application of the mixPLDS model to spinal cord imaging data** (A) Same data as in Figure 3.6B but rows are sorted by mixPLDS clusters and factor loadings. Inferred latent factors (red: cluster 1, blue: cluster 2, solid: factor 1, dashed: factor 2) are also shown. (B) Preferred phases shown as a function of (sorted) neuron index and colored by posterior probability of belonging to cluster 1. Clearly visible are two clusters as well as an (approximately) increasing ordering within a cluster. (C) Loading matrix C of the mixPLDS model showing how factors 1,2 (corresponding to cluster 1) and factors 3,4 (corresponding to cluster 2) influence the neurons.

3.2.4 Robust and scalable Bayesian analysis of spatial neural data

A common analytical problem in neuroscience is the interpretation of neural activity with respect to sensory input or behavioral output.[4] This is typically achieved by regressing measured neural activity against known stimuli or behavioral variables to produce a "tuning curve" for each neuron. Unfortunately, because this approach handles neurons individually, it cannot take advantage of simultaneous measurements from spatially adjacent neurons that often have similar tuning properties. At the same time, sharing information between adjacent neurons can errantly degrade measurements of tuning structure across space if there are sharp discontinuities in tuning between nearby neurons. In this section, we develop a computationally efficient block Gibbs sampler that effectively pools information between neurons to de-noise tuning curve estimates while simultaneously preserving sharp discontinuities that might exist in the organization of tuning across space. This method is fully Bayesian and its computational cost scales sub-quadratically with total parameter dimensionality. We demonstrate the robustness and scalability of this approach by applying it to both real and synthetic datasets.

Let us first consider example experimental data where the activity of n neurons is measured across d trials of identical lengths where different stimuli are presented during each trial. We can then model the response $\boldsymbol{y_i} \in R^d$ of neuron i as a function of a stimulus matrix $\boldsymbol{X_i} \in R^{d \times m}$. Each row of $\boldsymbol{X_i}$ corresponds to the stimulus projected onto neuron i, at each of the d trials. In particular, the relationship between the unobserved tuning function $\boldsymbol{\beta_i} \in R^m$ and the observed activity $\boldsymbol{y_i}$ at neuron i in response to stimulus $\boldsymbol{X_i}$ can simply be modeled as:

$$\boldsymbol{y_i} = \boldsymbol{X_i}\boldsymbol{\beta_i} + \boldsymbol{\epsilon_i} \text{ where } \boldsymbol{\epsilon_i} \sim \mathcal{N}(0, \sigma^2 \boldsymbol{I}).$$

The efficient statistical analysis and estimation of the unobserved tuning functions

---

[4] Section 3.2.4 is derived from [Rad et al., 2015].

$\{\boldsymbol{\beta_i}\}$ given the noisy observations $\{\boldsymbol{y_i}\}$, the stimulus set $\{\boldsymbol{X_i}\}$ is the standard tuning curve estimation problem. In this setting, we can use maximum-likelihood estimation to estimate tuning functions one neuron at a time (e.g., $\boldsymbol{\beta_{i,\mathrm{ml}}} := \boldsymbol{(X_i' X_i)^{-1} X_i' y_i}$).

However this model neglects a common feature of many neural circuits: the spatial clustering of neurons sharing a similar information processing function. For example, there are maps of tone frequency across the cortical surface in the auditory system [Issa et al., 2014], visual orientation maps in both cortical [Ohki et al., 2005] and subcortical brain regions [Feinberg & Meister, 2014], and maps respecting the spatial organization of the body (somatotopy) in the motor system [Penfield & Rasmussen, 1950; Romanes, 1964]. As a consequence, neurons in close proximity often have similar tuning functions. In each of these cases, there are typically regions where this rule is violated and largely smooth tuning maps are punctuated by jumps or discontinuities. Therefore simply smoothing in all cases will erode the precision of any sharp borders that might exist. Ideally, we would use an approach to estimate $\{\boldsymbol{\beta_i}\}$ that would smooth out the tuning map more in areas where there is evidence from the data that nearby tuning functions are similar, while letting the data 'speak for itself' and applying minimal smoothing in regions where adjacent neurons have tuning functions that are very dissimilar.

To solve this problem, we propose a multivariate Bayesian extension of Lasso [Tibshirani & Taylor, 2011] and total-variation regularization [Rudin et al., 1992] that uses the following generalized Laplace prior:

$$p(\boldsymbol{\beta}|\lambda, \sigma) \quad \propto \quad \prod_{i \sim j} \Big(\frac{\lambda}{2\sigma}\Big)^m \exp\Big(-\frac{\lambda}{\sigma}\Big\|\boldsymbol{\beta_i} - \boldsymbol{\beta_j}\Big\|_2\Big), \qquad (3.6)$$

where $\|u\|_2 = \sqrt{\sum_{i=1}^m u_i^2}$ and $i \sim j$ if two cells i and j are spatially nearby. This prior allows a diverse and flexible level of similarity between nearby tuning functions. For example, contrary to a $\|\boldsymbol{\beta_i} - \boldsymbol{\beta_j}\|_2^2$ based prior:

$$\prod_{i\sim j}(\frac{\lambda}{2\sigma})^m \exp\Big(-\frac{\lambda}{\sigma}\Big\|\boldsymbol{\beta_i} - \boldsymbol{\beta_j}\Big\|_2^2\Big),$$

in the prior shown in (3.6) large local differences are penalized less, therefore preserving sharp edge features in tuning maps. Intuitively, this prior encourages nearby tuning functions to be similar while allowing for large occasional breaks or outliers in the spatial map of the inferred tuning functions. Moreover, the conditioning of the prior of $\boldsymbol{\beta}$ on σ guarantees the joint log-concavity of the posterior distribution of $(\boldsymbol{\beta}, \sigma)$ (given λ and $\{\boldsymbol{y_i}, \boldsymbol{X_i}\}_{i=1,\cdots,n}$) making it desirable for computational reasons.

Our approach is based on direct and efficient block Gibbs sampling from the posterior. The computational bottleneck of our Gibbs sampler is bypassed using fast linear equation solvers based on sparse banded precision matrices, making it scalable to high dimensional data ($> 10^6$), while not imposing any overly restrictive constraints on the inferred tuning function map that would lead to bias from oversmoothing. With the aid of real experimental data, we demonstrate that this scalable method can dramatically reduce the experimental data required to estimate neural maps.

Further details about the model and our approach to statistical inference can be found in [Rad et al., 2015].

Robust Bayesian analysis application: Ca^{2+} imaging of spinal cord neurons

We will now test the algorithm's performance on real neural imaging data obtained from an isolated mouse spinal cord preparation. In these data, the fluorescent activity sensor GCaMP3 was expressed in motor neurons that innervate leg muscles. After application of a cocktail of rhythmogenic drugs, all motor neurons in the preparation fire in a periodic bursting pattern mimicking that seen during walking [Machado et al., 2015]. Under these conditions, we acquired sequences of fluorescent images and then applied a model-based constrained deconvolution algorithm to infer the timing of neuronal firing underlying each fluorescent activity time series extracted from the pixels corresponding to individual neurons [Pnevmatikakis et al., 2015].

Each mouse leg is controlled by ~ 50 different muscles, each of which is innervated by ~ 50 motor neurons that fire in distinct patterns during locomotor behavior [Krouchev et al., 2006; Akay et al., 2014]. Furthermore, all motor neurons that share common muscle targets are spatially clustered together into "pools" within the spinal cord [Romanes, 1964]. Therefore, during the locomotor-like network state monitored in these data, different spatially-distinct groups of motor neurons are recruited to fire at each moment in time. When the activity of each motor neuron is summarized as a single mean phase tuning value (representing the average phase angle of the ~ 70 firing events detected per neuron, a clear spatial map can be derived (as will be seen in more detail in the following chapter). Such maps appear smooth within pools, and sharply discontinuous between pools.

While phase tuning can be reliably inferred one neuron at a time in these data, fluorescent measurements from each neuron are not always of high quality. As a result, activity events cannot be reliably inferred without dozens of inferred spikes from each neuron [Machado et al., 2015]. Additionally, more neurons could have been observed in less experimental time if phase tuning were measured more efficiently. Therefore we applied our robust and scalable Bayesian information sharing algorithm to these data in an attempt to reduce measurement noise, and decrease the required data necessary to attain precision tuning map measurements.

The ability of our method to recover the preferred phases from only a single detected firing event from each neuron (~ 70 firing events were typically inferred for each neuron) is illustrated in Figure 3.8. Note that panel B produces a map that is very similar to that seen in panel C despite the fact that only a single inferred spike time was available for each neuron. Phase tuning values plotted in panel C were successfully computed one neuron at a time, but 73x as much data was available.

In the subsequent chapter, we will discuss the biological significance of our motor neuron phase tuning results in more detail. Importantly, all results presented in that chapter will have been derived from statistics computed one neuron at a time. We decided to conservatively restrict ourselves to a simpler analysis because sufficient data was available to make the Bayesian approach unnecessary. Indeed, we found that as a function of increased data the optimal choice for the smoothing parameter (λ) fell to zero (i.e. no smoothing) as dozens of spikes/neuron became available.

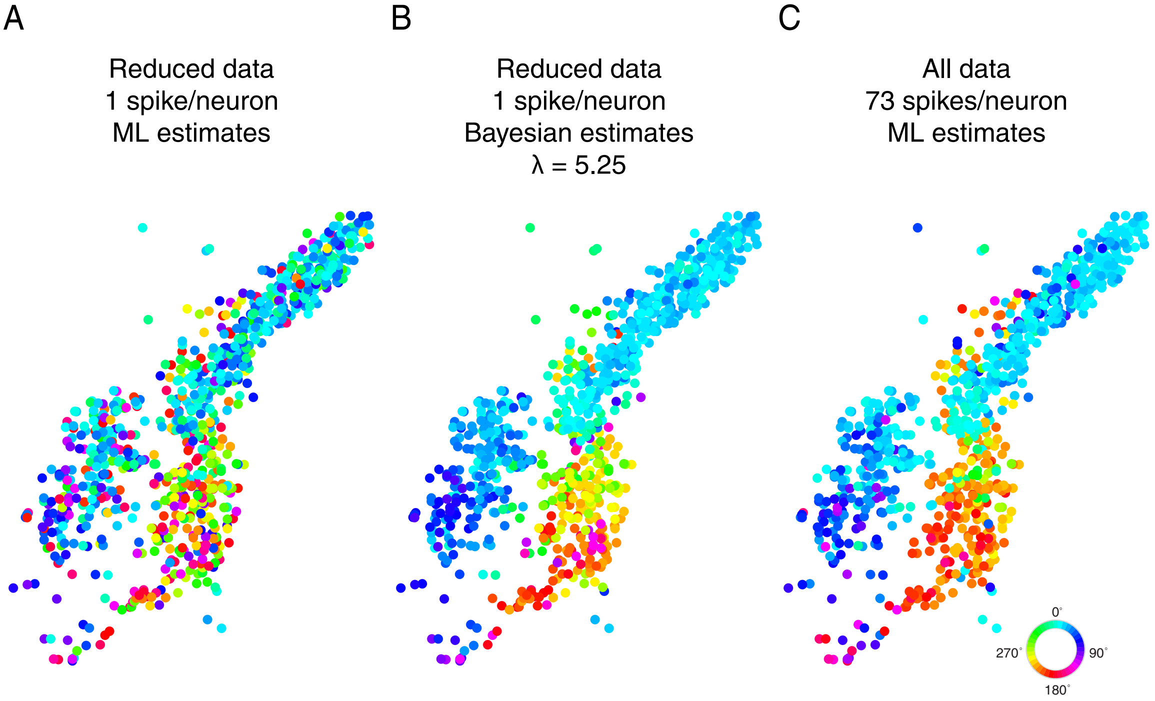

Figure 3.8: **Optimal Bayesian inference of motor neuron phase tuning**

Maps of motor neuron phase tuning obtained from a single isolated spinal cord preparation (n = 695 neurons shown as colored dots). (A) Phase tuning map when only single inferred spikes were used to estimate phase tuning for each neuron. (B) Phase tuning map when information from single inferred spikes could be shared between adjacent neurons according using our Robust Bayesian analysis method to generate a phase tuning map using minimal data. (C) Phase tuning map generated using all available data and maximum likelihood (ML) estimation to produce tuning estimates for each neuron individually. Note similarity to panel (B) but with 73x more data. Phase colorbar shown in inset.

3.3 Discussion

3.3.1 A lack of standardization in the analysis of optical imaging data

While Ca^{2+} imaging methods have been used in neuroscience for decades, because the average dataset is growing increasingly large, data analysis problems are becoming increasingly acute. In this chapter, we discussed a variety of methods and approaches for processing, analyzing, and interpreting these data. However, we have yet to discuss a key problem: the amount of redundant effort involved in rewriting standard algorithms for standard data processing tasks.

At a recent meeting about Ca^{2+} imaging (Simons Foundation Calcium Imaging Data Analysis Workshop, April 2015), many attendees remarked that they each spent a large fraction of time developing data analysis pipelines during their respective experimental imaging projects. While variability between imaging datasets and experimental preparations exists, making some fraction of this work necessary, there is no reason for everything to be rewritten from scratch by every laboratory. This current approach of reinvention is not only inefficient, it also makes interpretation of results difficult. Methods sections of papers generally present data analysis algorithms in a cryptic manner, and source code is rarely provided. Furthermore, not all laboratories possess the technical expertise to implement state-of-the-art algorithms themselves and are consequently forced to resort to the use of older, less effective techniques.

3.3.2 Development of open source data analysis tools

Moving forward, the field should agree on a standard set of algorithms and data analysis procedures for Ca^{2+} imaging data analysis. A standard open source toolbox that contains implementations of commonly used techniques for neuron detection, motion correction, and spike inference should be adopted by experimentalists and used as a platform for computationally-inclined users to build upon. In this vein, two somewhat complimentary projects have emerged over the past year to attempt solving this issue: Sequential IMaging Analysis (SIMA) and Thunder [Kaifosh et al., 2014; Freeman et al., 2014].

SIMA was developed by members of the Losonczy laboratory to implement a standard Ca^{2+} imaging data analysis workflow in Python. Each algorithm within their analysis pipeline is compatible with a standardized set of data structures for reading and manipulating the imaging data. In this way, different algorithms can be mixed and matched at each step of analysis to suit most experimental settings. Since their initial release of the toolbox, dozens of laboratories around the world have begun to use their software.

However, SIMA is still a work in progress. While it contains automated algorithms for neuron identification, none of these approaches will work in all settings. Indeed, even more advanced methods that attempt to solve this problem in a general manner run in to difficulties in some experimental settings [Pnevmatikakis et al., 2015]. Therefore it is hoped that a large number of algorithms will be implemented in toolboxes like SIMA or Thunder so that users can quickly try a variety of approaches on their data and find an approach that works well.

In this spirit, we have implemented the spike inference algorithm that we used in [Machado et al., 2015] for distribution within the SIMA toolbox. As we described earlier in this chapter, one of the principal advances of this new algorithm is that it provides more robust estimates of the underlying model parameters than previous techniques (i.e. [Pnevmatikakis et al., 2015] vs. [Vogelstein et al., 2010]), simplifying usage dramatically. An example that illustrates the functionality of our implementation on simulated fluorescence data can be seen in Figure 3.9.

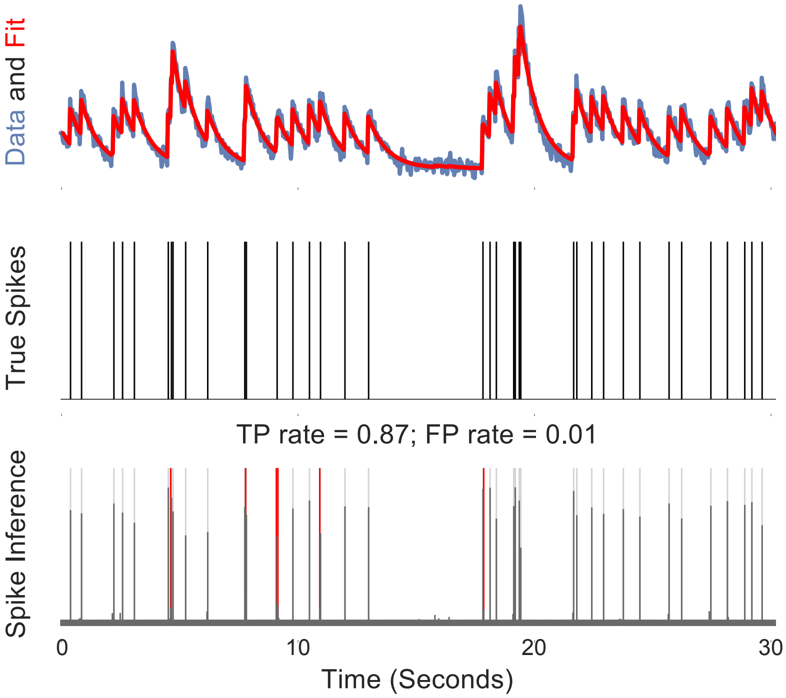

Figure 3.9: **Spike inference implementation for SIMA**

(Top) Simulated fluorescence time series data (blue) with spike inference model fit (red) superimposed. (Middle) True spike train underlying the data shown in the top panel. (Bottom) Spike time histogram inferred by the spike inference algorithm. Dark gray bars represent inferred spikes (proportional to the firing rate in each bin), light gray bars true positive inferred spikes and red bars are false positive inferred spikes.

3.3.3 Spike inference as preprocessing

As we have discussed in this chapter, there are many approaches towards the analysis of large-scale imaging datasets. Because a set of assumptions is inherent in each data analysis procedure, it seems prudent to take a conservative approach, and to only apply data analysis techniques that are specifically necessary to arrive at a particular answer to a biological question.

At the same time, it is important to remember that nearly every question that one could ask using Ca^{2+} imaging methods involves assuming a particular relationship between neuronal activity and Ca^{2+}. We have covered many reasons why this relationship is difficult to measure for a single neuron, and highly variable between neurons. Therefore, it seems that relating fluorescence to spiking is a difficult, but core problem of Ca^{2+} imaging data analysis—often implicitly when "simpler" approaches like peak or onset finding methods are used. The spike inference methods presented here each offer principled approaches towards this problem where the assumptions made about Ca^{2+} fluorescence data are made explicit. Moving forward, once more advanced methods and approaches towards inference validation can be developed, it seems like transforming Ca^{2+} fluorescence data into spike train estimates should be a default preprocessing step so that subsequent analysis can be performed in a more intuitive setting where worries about the vagaries of Ca^{2+} can be forgotten.

4

Measuring the grain of intrinsic locomotor pattern

4.1 Introduction

The mammalian nervous system is charged with the task of moving limbs — a challenge met through the construction of spinal circuits that coordinate interwoven patterns of muscle activity.[1] Spinal motor patterns reflect the activation of selected pools of motor neurons sharing common muscle targets which, in turn, are driven by descending commands, peripheral feedback, and input from spinal premotor interneurons. Many studies have invoked the idea that local spinal circuits alone can sustain motor neuron burst firing in patterns that resemble the rhythmic alternation of antagonist muscles during locomotion [Kiehn & Kjaerulff, 1996; Kudo & Yamada, 1987b; Grillner & Zangger, 1979]. But the basic rules of spinal circuit organization that govern the rhythmicity and alternation of locomotor output remain unclear.

---

[1] Portions of this chapter were derived from work in [Machado et al., 2015].

4.1.1 The organization of motor neurons respects the structure of the limb

One reason that uncertainty about the organization of mammalian locomotor circuits has persisted for so long is because the field has lacked an experimental means for directly relating known information about motor neuron position, identity, and activity to unravel the fundamental principles of locomotor circuit organization. Motor neurons that share common muscle targets are spatially segregated into pools, and at a higher order, motor neuron pools that share common muscle group targets are themselves organized clusters called “columels” [Vanderhorst & Holstege, 1997; McHanwell & Biscoe, 1981; Romanes, 1964; Sürmeli et al., 2011]. The position of each columel within the spinal cord corresponds to the position of its target muscle group within the limb. Dorsal columels target distal musculature, while ventral columels connect to proximal muscle targets (Figure 4.1). Analysis of proprioceptive afferent innervation patterns in a mouse stripped of motor pool-specific genetic identity revealed that this spatial organization appears instrumental in instructing the formation of appropriate sensory-motor neuron connectivity patterns. However, whether position is also involved in the specification of pool-appropriate patterns of descending and interneuronal inputs remains unknown (see Chapter 5) [Sürmeli et al., 2011]. Examining the relevance of motor neuron position to the organization of locomotor circuits requires first obtaining fine-grained measurements of locomotor firing both before and after the correspondence between spatial organization, neuronal identity, and locomotor firing has been perturbed.

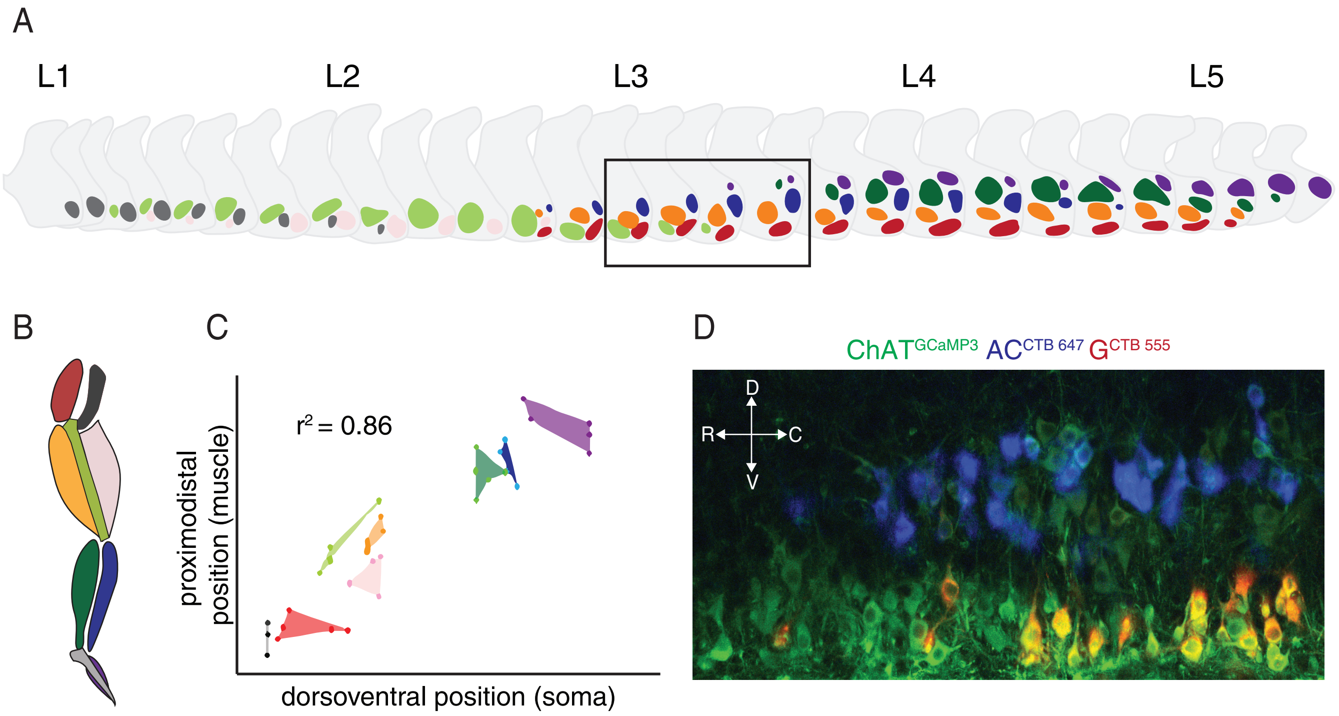

Figure 4.1: **Motor neuron pools are positioned with respect to the limb** (A) Motor neuron cell bodies that innervate different muscles are spatially segregated into rostrocaudally elongated clusters called pools. The position of pools that share common muscle group targets are indicated in color. Light red/gluteal (G), dark gray/proximal hip (PH), orange/hamstring (H), light green/adductors (A), pink/quadriceps (Q), blue/anterior crural (AC), dark green/posterior crural (PC), purple/foot (IF). (B) Cartoon of muscle groups of the leg represented in panel (A). (C) Correlation between proximodistal position of muscle groups along the limb and dorsoventral position of motor neurons within each corresponding pool. Colored convex hulls correspond to muscle groups represented in (A-B). (D) Fluorescence image showing two retrogradely labeled motor neuron pools labeled by CTB. Red G motor neurons can be seen ventrally and blue AC motor neurons are positioned more dorsally. Panels A-C are adapted from [Sürmeli et al., 2011]. Panel C is derived from data obtained in the cat.

4.1.2 Isolated mammalian spinal cord can produce patterned motor output

Attempts to delineate the spinal circuitry of mammalian locomotion have focused largely on connections among interneurons with presumed roles in pattern generation. One long-held view proposes that the premotor circuits that direct the alternation of antagonist flexor and extensor muscles exhibit an interdependence that is achieved through reciprocal interneuronal connections [Brown, 1914; Zhang et al., 2014; McCrea & Rybak, 2008; Talpalar et al., 2011]. Specifically, these models argue that rhythm generation is grounded in an opponency between neuronal populations controlling limb muscles with antagonist functions. These models rely on a symmetric, mutually inhibitory interaction between two interneuron sub-circuits that govern firing in motor pools innervating antagonist flexor and extensor muscles, respectively. This mutual inhibition helps ensure rhythmic, inverse firing patterns in the two subcircuits, providing a foundation for the alternating activation of antagonist motor pools observed experimentally. However, measurements during the spontaneous silencing ("deletion") of certain bursts during intrinsic locomotor firing appear inconsistent with symmetric models. When flexor motor neurons fail to burst, sustained firing in extensor motor neurons can result.

These observations that rhythmic flexor or extensor motor output can occur without activation of their antagonist pair have called into question the obligate role of reciprocal connectivity implied by symmetric models [Burke et al., 2001; Pearson & Duysens, 1976; Zhong et al., 2012]. Since spinal interneurons should be capable of distinguishing the identity of flexor and extensor motor neurons, we reasoned that new insight into the organization of locomotor circuits might emerge from a focus on the recognition and selection of motor pools by premotor interneurons, rather than on the intricacies of interneuron interconnectivity.

To clarify the organization of these networks we needed to characterize the correspondence between locomotor firing pattern and limb muscle target for motor neurons in the absence of descending command and feedback control. Beginning in the late 1980s (e.g. [Kudo & Yamada, 1987b]), this has been achieved by isolating neonatal rodent spinal cord preparations in artificial cerebrospinal fluid (ACSF) and applying rhythmogenic agonists including NMDA, 5-HT, and DA. To monitor the aggregate activity of motor neurons, ventral root recordings are then obtained simultaneously from multiple lumbar spinal segments. This approach revealed rhythmic bursting activity and alternation along the rostrocaudal axis (Figure 4.2A-B)—mirroring an observed a rostrocaudal bias in the position of flexor and extensor motor neuron pools [Kiehn & Kjaerulff, 1996; Kudo & Yamada, 1987b; Yakovenko et al., 2002]. As a consequence of this observation, motor neuron activity in this preparation has been termed "fictive locomotion."

However, the detailed relationship between this *in vitro* motor neuron firing pattern and actual locomotor firing is difficult to determine using only ventral root recordings, as each root contains axons arising from many pools [Vanderhorst & Holstege, 1997]. To remedy this issue, peripheral nerve [Meehan et al., 2012], muscle [Kiehn & Kjaerulff, 1996], and intracellular recordings [Lafreniere-Roula & McCrea, 2005] can be performed. Each of these approaches is capable of revealing muscle specific activation patterns (Figure 4.2C-D), however they are not able to resolve questions about the organization of locomotor firing that relate to population activity across space. For example, how much variance in activity exists within a single motor pool? Is variance in motor firing pattern organized across space? Or do flexor and extensor-like firing patterns coexist in discrete pools at each segment, in contrast to previous reports of a "wave" of motor neuron activity that spreads across motor pool borders [O'Donovan et al., 2008]? To address these questions, we developed a new cellular-resolution approach that allows the activity of a large fraction of all limb-innervating motor neurons to be related to their positions in the spinal cord.

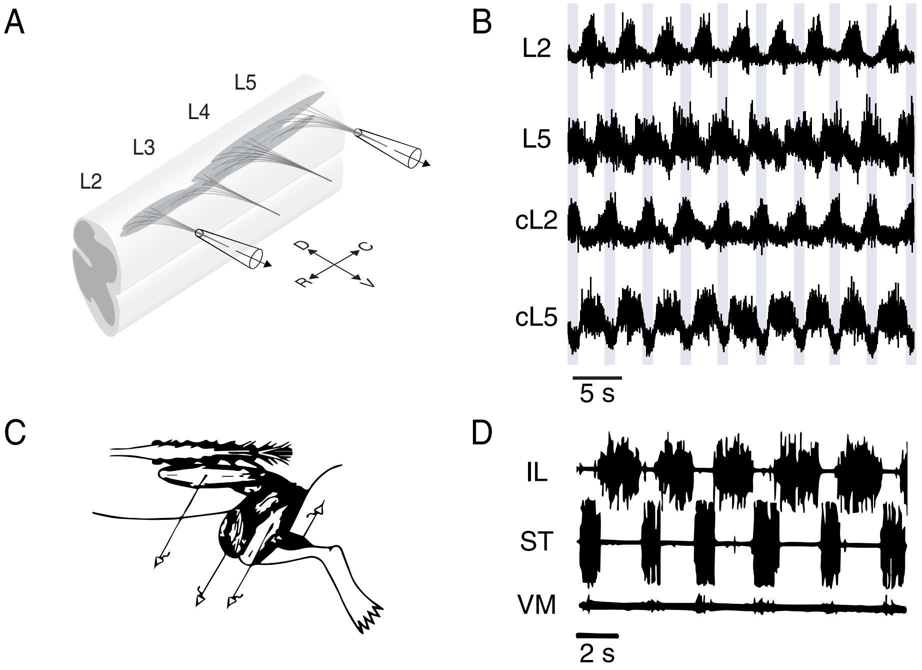

Figure 4.2: **Isolated mammalian spinal cord can produced patterned motor output**

(A) Schematic isolated mouse spinal cord preparation with suction electrodes positioned on lumbar ventral roots L2 and L5. (B) Representative dataset obtained following the application of 5 μM NMDA, 10 μM 5-HT, 50 μM DA. Recordings (DC-1 kHz) were obtained from ventral roots on both the ipsi- and contralateral sides of the preparation, displaying characteristic alternation. (C) Schematic of isolated rat spinal cord preparation with attached hindlimb and intramuscular recording electrodes. (D) Representative recordings obtained from the iliopsoas (IL), semitendinosis (ST), and vastus medialis (VM) muscles after 30 μM 5-HT was applied to evoke rhythmic activity. Panels C-D are adapted from [Kiehn & Kjaerulff, 1996].

4.1.3 Measuring the fundamental grain of motor pattern

We coupled two-photon imaging of a genetically encoded Ca^{2+} indicator with spike inference (as described in 3) to measure the firing of hundreds of target-defined motor neurons in an isolated neonatal mouse spinal cord preparation induced to locomotor-like activity [Bonnot et al., 2002; Kwan et al., 2009]. This approach permitted us to examine the relationship between motor neuron settling position, locomotor firing pattern, and muscle target identity. While the existence of motor neuron pools has been long known [Romanes, 1964], our optical assay permitted us to enumerate the number of firing patterns within and between motor pools as well as their precise manifestation across space.

Our analysis of wild type preparations revealed that motor pools innervating muscles with synergistic functions at a joint fired synchronously with a characteristic phase, and flexor pools were activated in a spatially-organized sequence that conforms to the order of activation of their target limb muscles in certain behavioral contexts *in vivo* [Akay et al., 2014; Grillner, 1981]. Instead of finding only a single flexor and extensor-like pattern (as in Figure 4.2), we found multiple flexor and extensor patterns reminiscent of *in vivo* patterns of muscle recruitment during locomotion (as in Figure 4.3). These results indicate that spinal premotor circuits possess the capacity to direct the temporal activation of motor neurons in a manner that reflects the functions of their target limb muscles [Krouchev et al., 2006; Rasmussen et al., 1978].

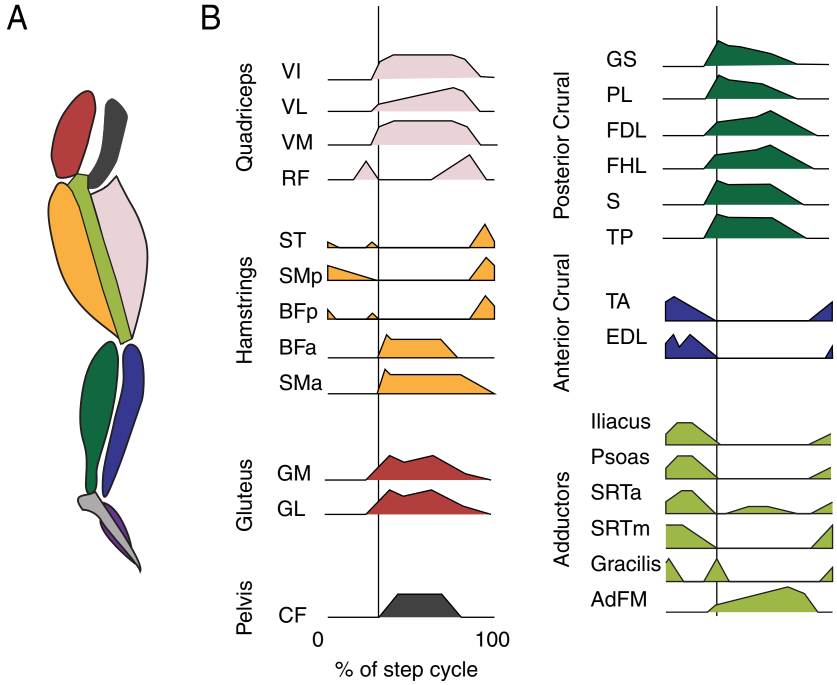

Figure 4.3: **EMG recordings obtained during locomotion in the cat reveal temporal sequencing in leg muscle recruitment**

(A) Cartoon of color coded muscle groups in the hindlimb. (B) Step cycle-averaged EMG traces obtained from hindlimb muscles. Data were obtained from cats during forward, level walking at approximately 0.6 m/s. The height of each EMG trace corresponds to increased recruitment normalized to its peak. 0% corresponds to the onset of swing phase. The time of swing/stance transition is indicated by the vertical line. Panel B was adapted from [Yakovenko et al., 2002], which aggregated EMG data taken from many publications.

4.2 Results

4.2.1 Motor neuron firing phase at cellular resolution

To specify in detail the influence of local premotor circuits in determining locomotor firing pattern, we analyzed the activity of motor neurons innervating individual muscle groups under conditions in which descending and peripheral sensory input has been eliminated. To achieve this, Ca^{2+}-sensitive fluorescence signals were monitored in hindlimb-innervating motor neurons in isolated neonatal (postnatal day 2 to 5) mouse spinal cord preparations induced to a state of locomotor-like activity by glutamate and monoamine receptor agonists (5 μM NMDA, 10 μM 5-HT, 50 μM DA) (Figure 4.4A-D; Kudo and Yamada, 1987). Motor neuron expression of the Ca^{2+} indicator GCaMP3 was achieved by crossing mice carrying a floxed ROSA-CAG-lsl-GCaMP3 allele [Zariwala et al., 2012] with $Olig2 :: Cre$ or $ChAT :: Cre$ motor neuron driver lines [Lowell et al., 2006; Sürmeli et al., 2011].

Twelve to twenty-four hours prior to imaging, groups of synergist muscles were injected with Alexa 555- or 647-conjugated cholera toxin B subunit (CTB) to mark the target identity of motor neurons. Two-photon microscopy was used to acquire GCaMP3 fluorescence image sequences each lasting 90 s, assessing 22 to 64 sagittally-oriented imaging fields (512 μm x 512 μm) that spanned lumbar segments L2 to L6. Concurrent recordings of rhythmic activity from lumbar ventral roots L1, or more typically L2, provided a reference signal for assessing motor neuron burst firing, with the locomotor cycle defined as the interval between adjacent peaks of L1 or L2 activity (L1 or L2 peaks $= 0°$). Electrodes placed on caudal lumbar segments L4 or L5 and contralateral L2 (Figure 4.2B, Figure 4.4B) provided a means of determining whether the alternating burst firing characteristic of locomotor activity was evident in each preparation [Kiehn & Kjaerulff, 1996; Kudo & Yamada, 1987b].

To characterize differences in the locomotor burst firing of motor neurons that innervate different target muscles we defined firing features through the analysis of Ca^{2+}-sensitive fluorescence from motor neuron cell bodies. But slow Ca^{2+} extrusion and noise in fluorescence measurements obscure prominent burst features such as duration and the phase of peak firing [Helmchen & Tank, 2005]. To address this problem we used a model-based statistical algorithm that infers the spike train most likely to underlie each somatic fluorescence time series [Pnevmatikakis et al., 2015]. This algorithm fits fluorescence data using a model of spike-related fluorescence fluctuations that assumes each action potential results in a fluorescence transient with instantaneous rise and exponential decay, in the added presence of Gaussian noise (see Section 8.6). For each somatic fluorescence time series, the algorithm yielded a relative estimate of the number of spikes in each imaging frame. These normalized spike counts were assembled into histograms that display the rhythmic burst firing of each motor neuron during the image sequence (black bars in Figure 4.4E). To quantify burst timing, the mean phase of each burst was calculated, and the median phase value was defined as a neuron's phase tuning (Figure 4.4D,F).

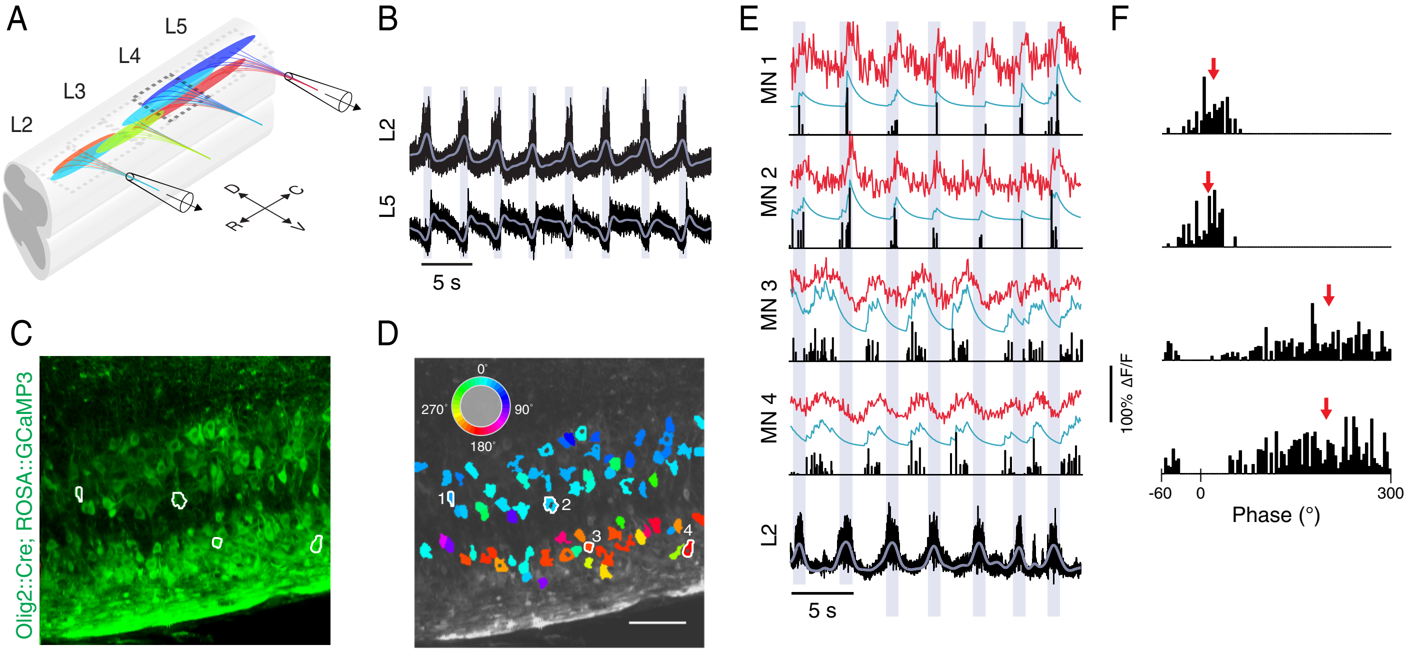

Figure 4.4: **Measuring locomotor firing from motor neuron Ca^{2+} sensitive fluorescence**

(A) Schematic of the neonatal whole-cord preparation used for imaging. LMC motor pools and their corresponding roots are shown in color. (B) Ventral root recordings (DC to 1 kHz) obtained from L2 and L5 roots during agonist-induced locomotor firing. (C) Single imaging field containing GCaMP3-expressing motor neurons (green). (D) ROIs for motor neurons in (C) colored according to phase tuning. Scale bars in (D) and (G) are 100 μm. Phase color map is inset. (E) Fluorescence time courses (red) for four motor neurons from (C) along with spike inference model fit (cyan) and inferred spiking (black bars). (F) Inferred spike counts from a full 90 s image sequence are plotted across the locomotor cycle (L2 root signal peaks = 0°) for the four motor neurons in (E), with the phase tuning of each neuron indicated (red arrows).

4.2.2 Reproducibility and consistency in locomotor firing

In each spinal cord preparation, motor neurons are spread across many imaging fields, and as such, neuron-by-neuron comparisons of phase tuning require that values are stable over time. To assess tuning stability, we imaged a subset of fields in each preparation at time points separated by 20 to 220 minutes. But even if tuning is stable, errors intrinsic to the measurement of burst phase from inferred spiking will result in variation in tuning estimates between time points. We estimated this error by measuring the tuning of motor neurons imaged during antidromic activation, when all neurons fire in synchrony. The distribution of the resulting tuning values indicated that two separate estimates of the same underlying tuning would differ on average by 10.1° (further details presented in Section 8.8). In comparison, temporally separated estimates of motor neuron firing during agonist-induced locomotor-like activity exhibited a median difference of only 12.0° ($n = 1714$ neuron pairs; Figure 4.5A-D). Moreover, the slope of a linear regression fit indicated an incremental deviation of tuning values of only 2.8° per hour. Finally, the mean burst frequency of each experimental preparation was consistent across preparations (0.25 Hz, s.d. = 0.062 Hz, $n = 15$ spinal cords; Figure 4.6). Together, these findings establish that the phase tuning of LMC motor neurons in individual preparations is relatively stable over the duration of data collection. Thus, phase tuning estimates are both accurate and stable, enabling assessment of the relative tuning of motor neurons that innervate different limb muscles.

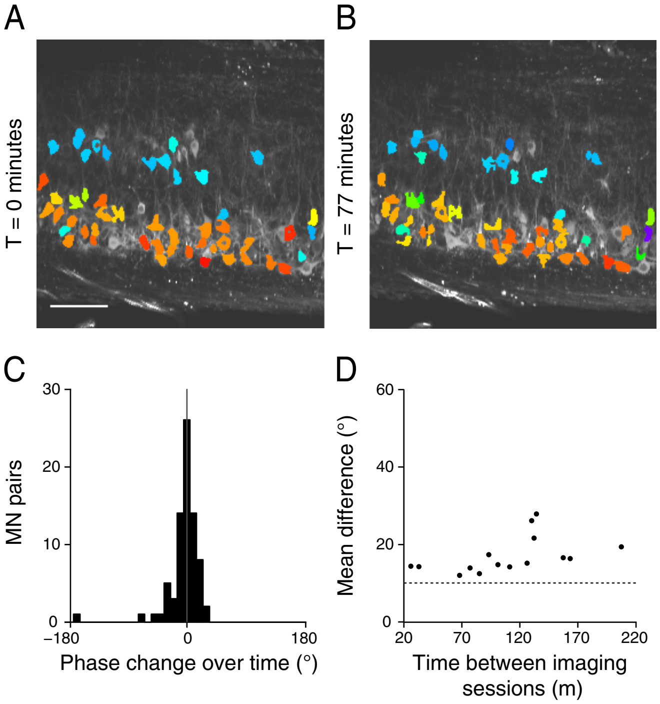

Figure 4.5: **Stability of phase tuning over time**

(A-B) Phase tuning for motor neurons measured twice during an experiment (0 and 77 minutes later) to assess phase tuning stability. (C) Distribution of tuning changes for all motor neurons (76 pairs) imaged in the preparation shown in (A-B). Mean change = −2°, standard deviation = 21°. (D) Mean tuning difference versus the interval between measurements for 15 mice (1714 neurons total). Dotted line indicates predicted mean difference assuming stable phase tuning.

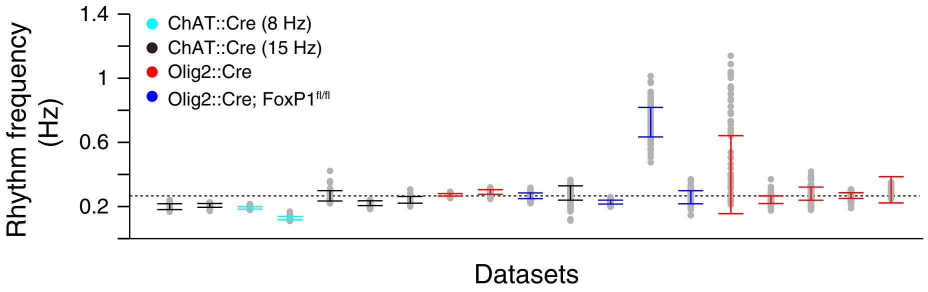

Figure 4.6: **Consistency of burst frequency across preparations**

Average burst frequency during agonist-induced locomotor firing is shown for each preparation. Dots are median frequency values derived from single image sequences. Bars denote medians ± median absolute deviations across all image sequences from a single preparation. For wild type preparations, mean burst frequency across all preparations = 0.25 Hz, s.d. = 0.062 Hz, n = 15 spinal cords. In $FoxP1^{MN\Delta}$ preparations, mean = 0.37 Hz, s.d. = 0.24 Hz, n = 4 spinal cords. Burst frequency distributions from wild type and $FoxP1^{MN\Delta}$ preparations were statistically indistinguishable (p = 0.66, Wilcoxon rank sum test).

4.2.3 Synergy group-specific locomotor firing

Pools of motor neurons that innervate muscles with similar functions at an individual joint form functional synergy groups that are spatially clustered within the spinal cord [McHanwell & Biscoe, 1981; Romanes, 1964; Vanderhorst & Holstege, 1997]. We therefore examined if the phase tuning of motor neurons segregates with synergy group identity. In each spinal cord preparation we analyzed between 400 and 1400 limb-innervating motor neurons that exhibited phasic firing (mean = 818 motor neurons; Figure 4.9A-C; see Section 8.10 and [Berens, 2009; Zar, 1999]). From these measurements we constructed spatial tuning maps in which the position of each motor neuron in three-dimensional space was noted in a color scaled according to its tuning value (Figure 4.8). Spatial tuning maps revealed numerous motor neurons with tuning values close to the reference ventral root activity peak (L1 or L2 = 0°), and many others with near antiphase (≈ 180°) tuning, at each lumbar segmental level (Figure 4.10). We observed that motor neurons with similar tuning values were arranged in rostrocaudally-elongated clusters that formed relatively sharp boundaries with other neuronal clusters that had distinct tuning values. These spatially coherent clusters were reminiscent in shape and spatial extent to motor pool synergy groups, suggesting a direct correspondence between synergy group identity and firing phase. These findings contrast with prior reports of a wave-like rostrocaudal propagation of motor neuron activity across the rostral LMC during locomotor firing [O'Donovan et al., 2008], which could reflect a lack of cellular resolution in earlier Ca^{2+} imaging-based measurements.

To probe further the correspondence between identity and firing phase we measured the phase tuning of motor neurons that had been assigned to particular synergy groups (Figure 4.7). CTB was injected into four muscle groups: the intrinsic foot (IF), anterior crural (AC), quadriceps (Q), and gluteal (G) muscles, and the tuning of retrogradely-labeled motor neurons was measured. Identified IF and AC motor neuron populations exhibited unimodal tuning distributions whereas Q and G motor neuron populations displayed bimodal distributions (Figure 4.11). Among Q motor neurons, the more lateral, presumptive rectus femoris (RF) motor neurons were tuned near 0°, whereas more medial, presumptive vastus (V) motor neurons were tuned close to 180° [De Marco Garcia & Jessell, 2008; Vanderhorst & Holstege, 1997] (Figure 4.11C). Similarly, for G motor neurons, a more rostral, presumptive tensor fasciae latae (TFL) cluster was tuned near 0°, whereas a caudal cluster containing the three remaining gluteal motor pools (GM) was tuned around 180° (Figure 4.11D). These results are consistent with functional definitions of RF and TFL as hip flexors, and V and GM muscles as knee and hip extensors, respectively [Platzer & Spitzer, 2003]. The alignment of six synergy groups with phasically homogeneous clusters seen in tuning maps supports the view that phase tuning is spatially organized in register with synergy group identity.

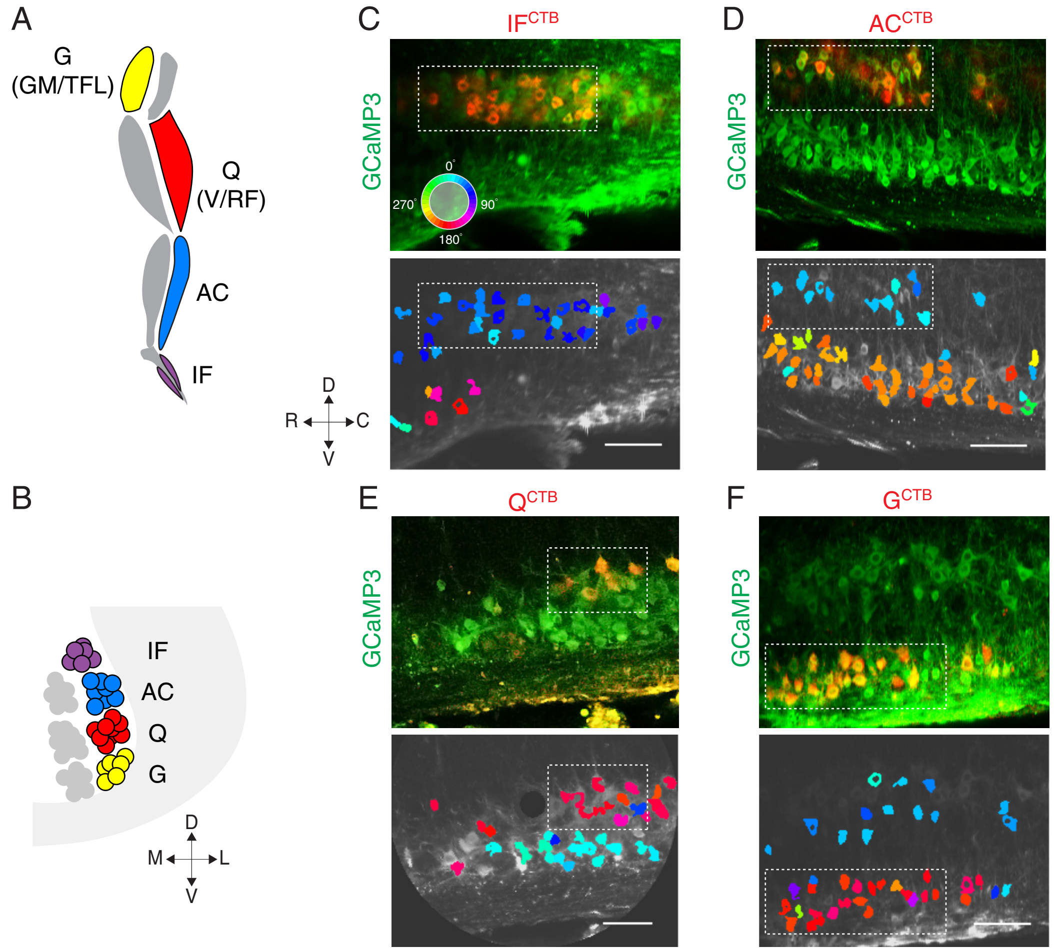

Figure 4.7: **Uniformity in phase tuning across identified synergy groups** (A) Schematic leg showing the position of all muscle groups characterized using CTB. (B) Top: transverse spinal cord section showing the position of corresponding motor pools. (C) Top: sagittal image showing position of CTB-labeled IF neurons (red). Bottom: ROIs for motor neurons with significantly phasic activity colored according to phase tuning using the color scale indicated. Dotted line denotes a region containing CTB-labeled IF motor neurons. (D-F) Same format as (C) but for three additional muscle groups: (D) Anterior crural (AC), (E) Quadriceps (Q), and (F) Gluteal (G). Scale bar in each image is 100 μm.

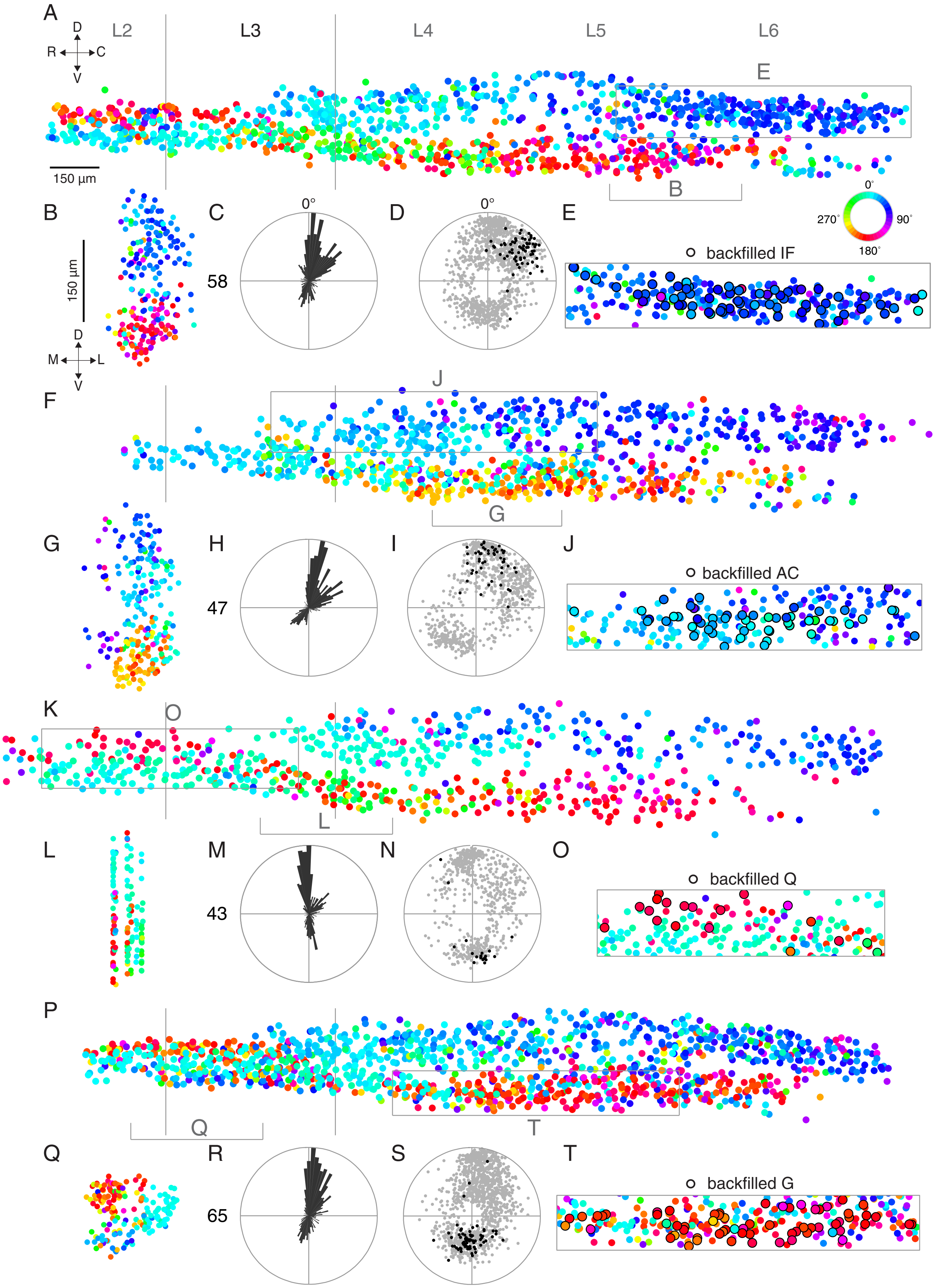
A
D
R
C
V
L2
L3
L4
L5
L6
E
150 µm
B
C
0°
58
D
0°
E
0°
270°
90°
180°
backfilled IF
150 µm
D
M
L
V
J
F
G
G
H
47
I
J
backfilled AC
K
O
L
L
M
43
N
O
backfilled Q
P
Q
T
Q
R
65
S
T
backfilled G

Figure 4.8 *(preceding page)*: **Spatial maps of motor neuron phase tuning across the LMC**

(A,F,K,P) Maps showing phase tuning of motor neurons within the spinal cord as viewed from the lateral side. Data were obtained from two different preparations (1177 neurons in (A), 827 neurons in (F), 670 neurons in (K), and 1264 neurons in (P)). Boundaries of the antidromically-activated segment are indicated by vertical lines. Labels of other segments were drawn assuming equal segment widths. (B,G,L,Q) Transverse projections for the rostrocaudal extent indicated in (A) and (F), respectively. (C,H,M,R) Polar histogram showing the phase tuning of neurons mapped in (A,F,K,P), respectively. The maximal number of neurons within a single bin is shown to the left of each histogram. (D,I,N,S) Polar plot indicating the phase tuning of all motor neurons mapped in (A,F,K,P), respectively, in gray. CTB-labeled intrinsic foot (IF; D), anterior crural (AC; J), quadriceps (Q; O), and gluteal (G; T) motor neurons are shown in black. The radial position of each point represents the circular spread of its phase tuning. (E,J,O,T) Magnification of the boxed areas in (A,F,K,P), respectively, show CTB-labeled neurons in detail.

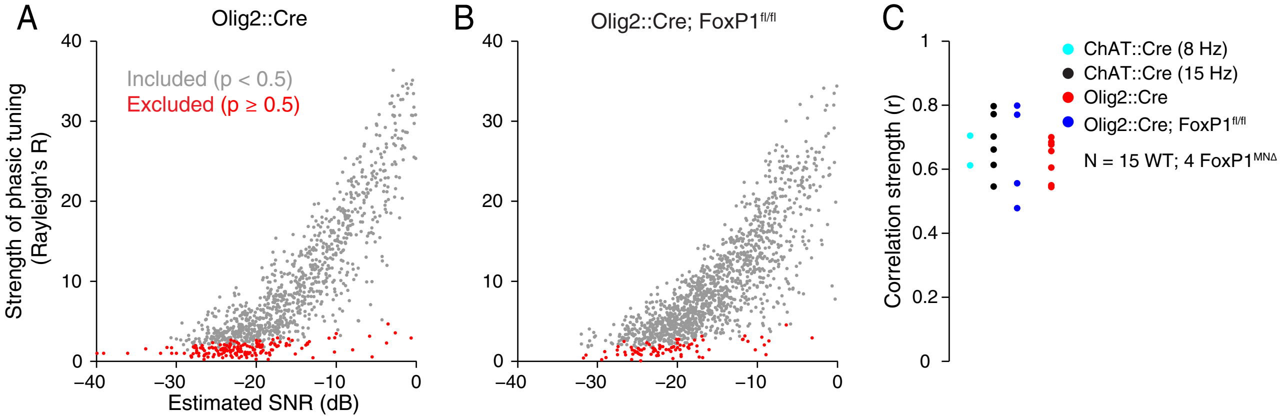

Figure 4.9: **Correlation between signal quality and phase tuning strength** (A) Correlation between estimated signal-to-noise ratio (SNR) and the R statistic from Rayleigh's test of circular uniformity for all imaged motor neurons in a single $Olig2 :: Cre$ mouse. Red points denote imaged motor neurons that were excluded from further analysis because they had Rayleigh's test P values > 0.5. (B) Same format as (A) in a $FoxP1^{MN\Delta}$ preparation. (C) The correlation between R and SNR was high in all wild type preparations (Pearson correlation = 0.54-0.80, mean = 0.66, n = 15 wild type spinal cords) indicating that much of the pattern of motor neuron firing is captured by its phase tuning. This correlation seen in wild type data was statistically indistinguishable from the correlation measured in $FoxP1^{MN\Delta}$ data (Pearson correlation = 0.48-0.80, mean = 0.65, n = 4 spinal cords; comparison to wild type: p = 0.94, two-sample, two-tailed t-test).

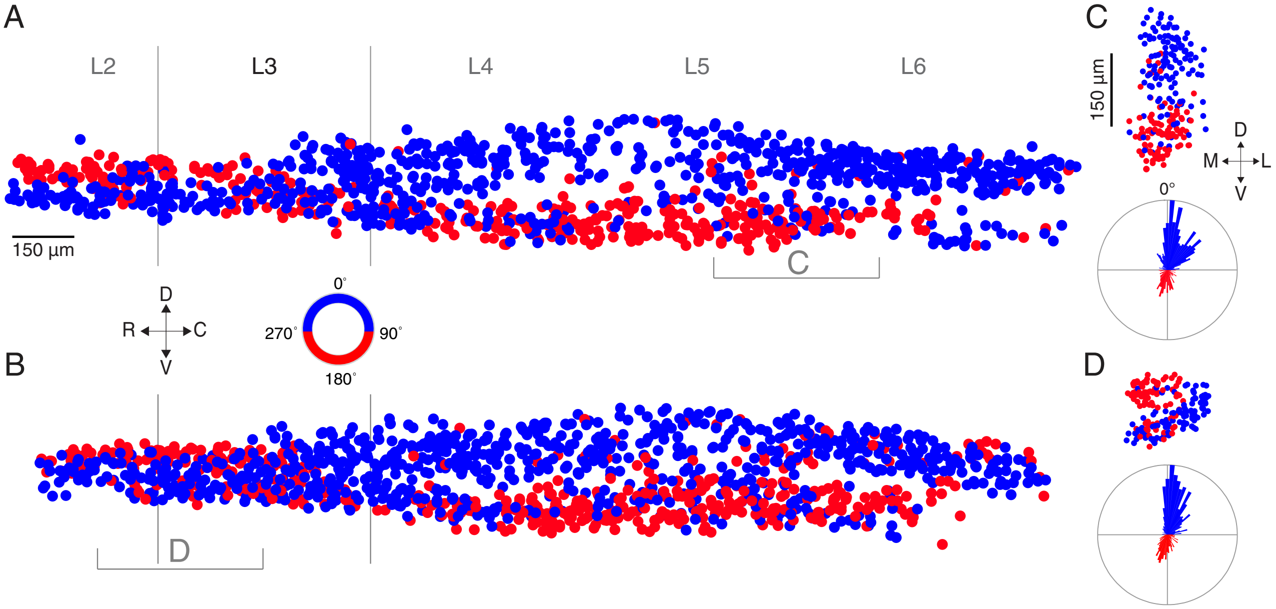

Figure 4.10: **Antiphase firing patterns coexist along the rostrocaudal axis** Maps of motor neuron activity matching the format and data from (A-E and P-T) of the previous figure, but with phase tuning represented using only two colors: blue = tuning closer to 0° and red = tuning closer to 180°.

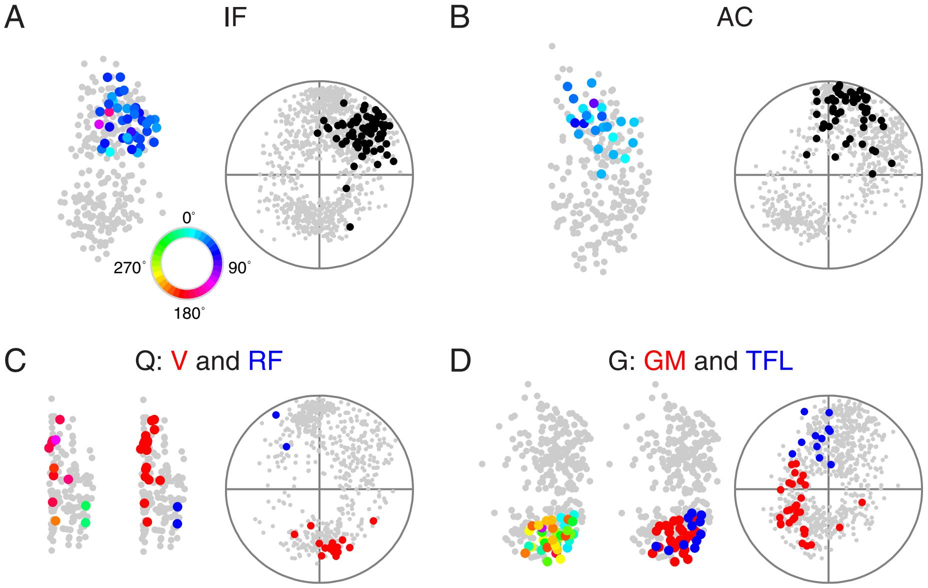

Figure 4.11: **Spatial organization of CTB-labeled motor neurons**

Transverse projections (left) from rostrocaudal segments of individual spinal cords with the phase tuning of CTB-labeled intrinsic foot (IF; A), anterior crural (AC; B), quadriceps (V/RF; C), and gluteal (GM/TFL; D) motor neurons indicated in color. For each cord, polar plots (right) show the phase tuning of all motor neurons (gray), and all IF (A), AC (B), Q (C), and G (D) motor neurons identified by CTB-labeling (black). The radial position of each point represents the circular spread around the phase tuning. Middle subplots in C and D are similar to the adjacent transverse projections, except CTB-labeled neurons are color coded red and blue according to their assignment via k-means clustering into one of two groups: vastus (V) and rectus femoris (RF) in (C), gluteus (GM) and tensor fasciae latae (TFL) in (D).

4.2.4 Structure in synchronous firing patterns within and between motor pools

If locomotor firing is synergy group-specific then covariation in burst firing phase from cycle to cycle might be stronger within than between groups. To test this possibility we evaluated burst phase covariation using a synchrony index that reflects the across-cycle consistency of phase differences between pairs of motor neurons (Figure 4.12A-C) [Mormann et al., 2000]. We observed higher synchrony among motor neurons assigned to the same synergy group by CTB labeling (Figure 4.12D, mean index ± standard error of the mean (s.e.m.) $= 0.51 \pm 0.007$, n = 517 pairs; $p < 10^{-10}$, Wilcoxon test, see Extended Experimental Procedures), and lower synchrony among motor neurons assigned to different synergy groups (Figure 4.12D, mean index ± s.e.m. $= 0.33 \pm 0.026$, n = 68 pairs; p = 4.2 x 10^{-7}, Wilcoxon test; comparing with synergist pairs p = 4.4 x 10^{-10}, Wilcoxon test; p = 4.7 x 10^{-6} after controlling for differences in proximity). Thus synergist motor neurons are preferentially synchronized.

We also assessed the degree of phase synchrony for synergist motor neuron pairs as a function of their separation. Synchrony indices did not vary significantly with proximity along the rostrocaudal axis (Spearman correlation (ρ) = -0.07, p = 0.12; Figure 4.12E). In contrast, we detected a shallow proximity-dependence along the dorsoventral axis (ρ = -0.09, p = 0.04; Figure 4.12F), which may reflect slightly elevated synchrony among motor neurons within the pools that comprise each synergy group. Nevertheless, as a whole these findings indicate that the major determinant of synchrony in motor neuron burst phase is synergy group membership.

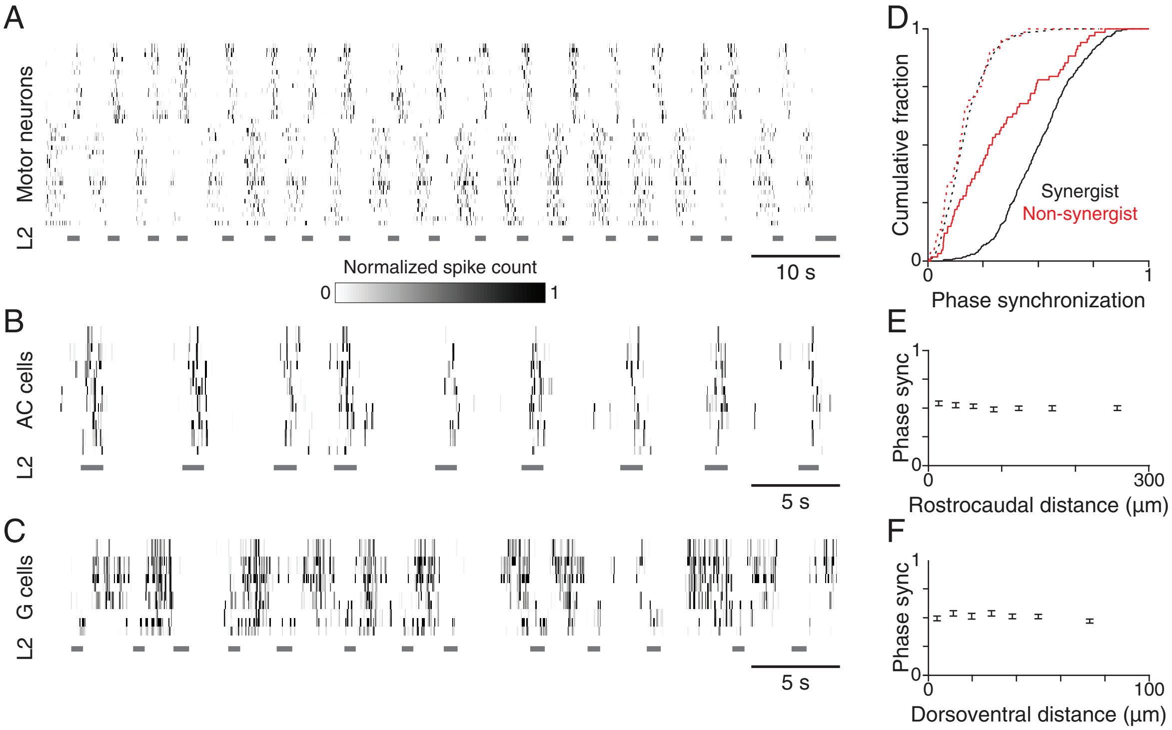

Figure 4.12: **Assessment of synchrony in locomotor firing**

(A) Normalized spike histograms of 44 simultaneously imaged motor neurons, illustrating synchronized firing across locomotor cycles. The normalized spike count computed for each imaging frame is indicated by a grayscale tick mark horizontally spanning the frame duration. Wide gray bars at bottom denote periods of elevated L2 ventral root activity. (B) Spike histograms for 8 simultaneously imaged AC motor neurons. (C) Spike histograms for 6 simultaneously imaged G motor neurons. (D) Cumulative histograms of phase synchronization indices computed for pairs of identified motor neurons within the same (black) or between different (red) synergy groups. Phase synchronization was computed with (dotted) and without (solid) circular permutation of one spike histogram relative to the other. (E-F) Phase synchronization of normalized, unpermuted spike histograms for identified neurons within the same synergy group versus proximity along the rostrocaudal (E) or dorsoventral (F) axes. Pairs of motor neurons were divided into 7 equally sized groups according to pairwise distance, data are plotted along the x-axis according to the mean pairwise distance for each group, and error bars = mean ± s.e.m.

4.2.5 Positional order and the sequential activation of flexor synergy groups

Walking is characterized by the sequential activation of limb muscles, with a precision in recruitment that reflects their biomechanical function [Rossignol, 1996]. In mice, and in some cases in cats, flexor muscles are activated in a sequence that follows the order of their target muscles along the proximodistal axis of the limb [Akay et al., 2014; Grillner, 1981; Krouchev et al., 2006; Rasmussen et al., 1978].

To examine the degree to which the order of muscle recruitment can be imposed by local spinal circuits we characterized the sequential activation of flexor synergy groups innervating different limb joints. Normalized spike histograms were used to derive an average firing rate across the locomotor cycle for individual motor neurons within defined synergy groups (Figure 4.13A-F, gray time series in lower panels; Figure 4.7). Because Q and G motor neurons display bimodal tuning we used k-means clustering ($k = 2$) to separate the cycle-averaged firing rates of both groups, yielding distinct RF and V pools at different mediolateral positions within the Q population, and rostrocaudally distinct TFL and GM pools within the G population (Figure 4.11C,D). Synergy group averages of cycle-averaged firing rates showed that the phase of peak firing and burst duration were consistent across preparations (Figure 4.13A-F, upper panels; color time series in lower panels).

Strikingly, we found that the order at which firing rates attained 50% of their eventual maxima, a measure of burst onset, correlated with the ventrodorsal position of motor neurons within the LMC, and thus the proximodistal position of their target muscles (Figure 4.13G,H). The synergy group-averaged firing of the ventral-most motor neurons innervating the hip flexor TFL muscle had an onset at a cycle phase of $-43.8 \pm 20.9^\circ$ (median ± standard error of median, n = 34 neurons). The firing of more dorsally positioned motor neurons innervating RF, a hip flexor with a more distal origin and insertion than TFL, had an onset at -33.0 ± 4.4° (n = 38). The firing of still more dorsally positioned motor neurons innervating ankle flexor AC muscles had an onset at -13.2 ± 2.2° (n = 106). Finally, the dorsal-most motor neurons, which innervate toe flexor IF muscles, had an onset at 19.2 ± 2.6° (n = 72). The correlations of both burst onset phase and peak firing phase with position were strong (onset: $\rho = 0.70$, $p < 10^{-10}$); peak: $\rho = 0.69$, $p < 10^{-10}$); Figure 4G,H). Thus local spinal circuits appear able to impose a motor neuron activation order reflective of that observed in certain locomotor contexts *in vivo*.

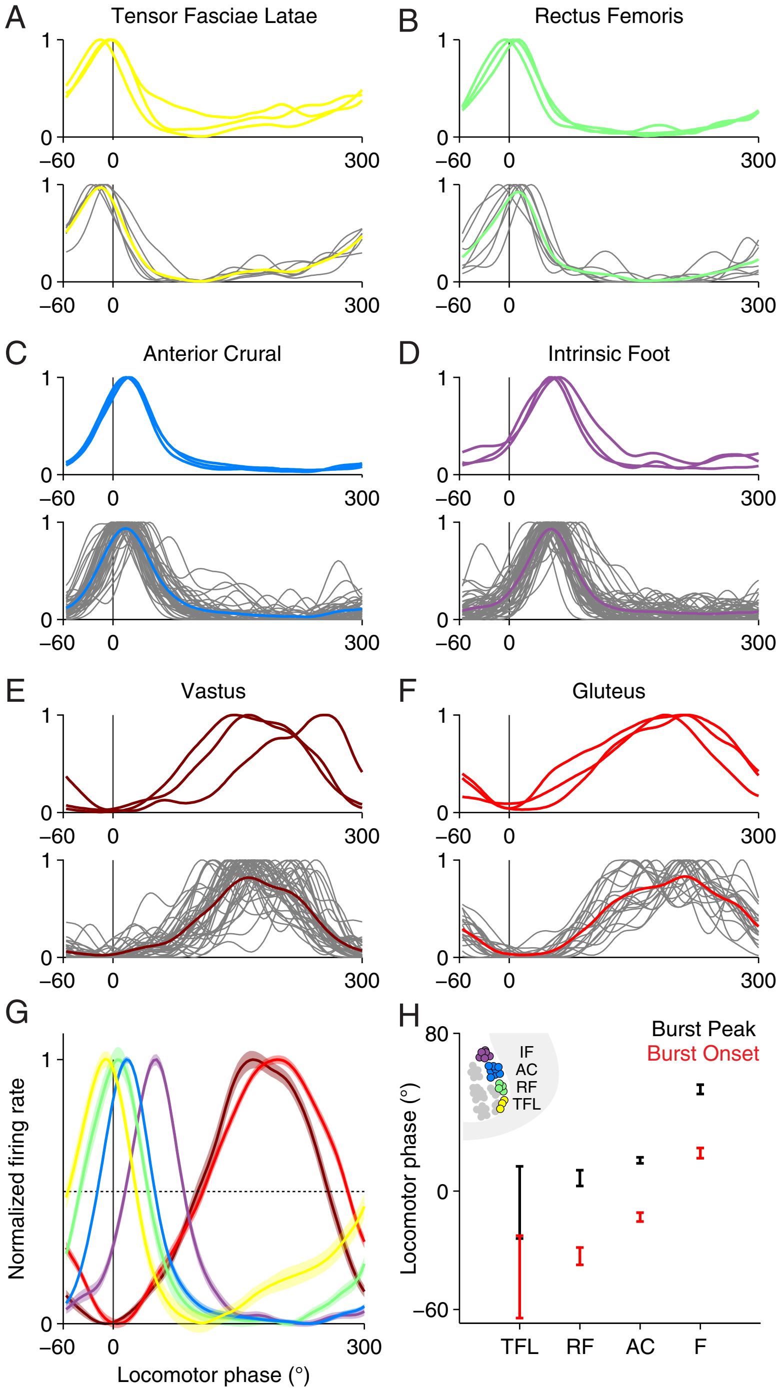
A
Tensor Fasciae Latae
B
Rectus Femoris
C
Anterior Crural
D
Intrinsic Foot
E
Vastus
F
Gluteus
1
0
−60
0
300
G
Normalized firing rate
Locomotor phase (°)
H
80
0
−60
Locomotor phase (°)
Burst Peak
Burst Onset
IF
AC
RF
TFL
TFL
RF
AC
F

Figure 4.13 *(preceding page)*: **Cycle-averaged firing of identified motor neurons reveals sequential recruitment of flexor synergy groups**

(A-F) Bottom: cycle-averaged firing rates from individual CTB-labeled motor neurons (gray) imaged in a single preparation. Colored traces represent their means. Top: Mean cycle-averaged firing rates from CTB-labeled motor neurons in each of three different preparations for each of the six different synergy groups analyzed. (G) Synergy group-averaged firing rates ± s.e.m. for identified motor neurons pooled across preparations. Colors correspond to those used in A-F. (H) Median burst peak and burst onset times ± standard error of the median for four flexor synergy groups ordered by dorsoventral position (inset).

4.2.6 Locomotor firing intensity varies as a function of motor pool identity

In addition to measuring the phase tuning and burst duration of motor neurons during locomotor firing, we wondered if the number of spikes emitted by a given neuron over the locomotor cycle varied systematically as a function of its muscle target identity. Since our fast spike inference algorithm yields spike histograms that are only proportional to the absolute number of spikes in each bin, and the multiplicative factor that would relate spike histograms to the true firing rate is unknown and different for each neuron, we needed to use a new approach to infer firing rates.

Therefore, we used a different spike inference algorithm that estimated firing rate information, in addition to inferring the timing of spiking activity. Because this approach [Pnevmatikakis et al., 2013] estimates sequences of spike times, as opposed to "spike histograms," we can compute the number of inferred spikes/second across each 90 s imaging session in order to produce a firing rate estimate for each neuron.

In order to determine whether these firing rate values made sense, we first looked to see whether the firing rate of motor neurons declined over time. In contrast to phase tuning, which appears stable for hours, fewer motor neurons exhibited strong phasic modulation (and therefore met the Rayleigh test statistic threshold necessary to appear in our phase tuning maps) at the end of an experiment than at the beginning. This effect could be explained if the firing rate of individual motor neurons declined as a function of preparation health–consistent with earlier observations that motor neuron firing decreases when the spinal cord is exposed to hypoxic conditions [Wilson et al., 2003].

Indeed, in both of the experimental datasets that we analyzed, we saw a significant, linear decrease in estimated neuronal firing over time (Figure 4.14A,B,D,E). In one preparation, we found that firing rates decreased at a rate of -0.0041 Hz/minute, and in the second preparation rates decreased by -0.0049 Hz/minute. These results support our hypothesis that the firing rates of individual motor neurons decrease as a function of time and preparation viability. Together with our earlier validation of this firing rate estimation method (from Chapter 3), we therefore have confidence in our ability to estimate firing rate from our motor neuron imaging data.

Next, we used these firing rate estimates to examine whether neurons innervating flexor, extensor, and foot muscles had systematically different median firing rates over the locomotor cycle. We performed this analysis in two ways: either by using CTB labeled populations of neurons, or by classifying neurons as flexor, extensor, or foot-like on the basis of their phase tuning ($|phase| < 10°$ was defined as flexor-like, $|phase| > 140°$ was defined as extensor-like, and $80° > phase > 40°$ was defined as foot-like firing). To verify that this simple classification scheme would actually isolate neurons in spatially segregated populations that contain flexor, extensor, and foot motor pools, we simply plotted cluster identity in color on top of our motor neuron position maps (Figure 4.15). This approach reveals a close correspondence between the position of identified extensor (Figure 4.15A), and foot motor neurons (Figure 4.15D) and our neuron classification scheme (Figure 4.15C,F).

We then examined the median firing rates of classified flexor, extensor, and foot-like neurons. We found that foot-like firing neurons had the lowest median firing rates (prep 1 = $0.73 \pm .05$ Hz; prep 2 = $.42; \pm .05$ Hz; median ± standard error of the median), flexor-firing neurons fired at more intermediate rates (prep 1 = $0.91 \pm .03$ Hz; prep 2 = $0.74 \pm .04$ Hz), and extensor motor neurons had the highest firing rates (prep 1 = $0.85 \pm .04$ Hz; prep 2 = $1.24 \pm .06$ Hz) (Figure 4.14C,F). In both preparations, foot-classified neurons had significantly lower firing rates than both flexor and extensor classified neurons ($p < 0.005$ for all individual comparisons; Wilcoxon rank sum test). The difference in median firing between the flexor and extensor classes was only significant in preparation 2 ($p < 10^{-7}$; $p > 0.5$ in preparation 1). Importantly, members of each of the three phase classes were imaged at each time point during each experiment, making it unlikely that these results arose as a consequence of firing rates declining over the duration of each experiment (Figure 4.14B,E).

This primary effect that we saw between foot-classified neurons and those with other phase tunings also holds for CTB-labeled foot-innervating motor neurons (Figure 4.14F; Figure 4.15D,E). The median firing rate of all motor neurons was $0.73 \pm .018$ Hz in preparation 2. In contrast, the CTB-labeled foot flexor motor neurons identified in that preparation fired at $0.35 \pm .014$ Hz (significantly lower than the distribution of all neurons; $p < 0.005$). The median of the CTB-labeled foot motor neuron rate distribution was indistinguishable from that of the foot-classified neuron distribution ($p > 0.5$).

Similarly, we also observed that CTB-labeled gluteus motor neurons (G; an extensor muscle) fired at a significantly higher median rate than the distribution of all active motor neurons (1.26 ± 0.08 for backfilled G neurons vs. $0.81 \pm .019$ Hz for all neurons; $p < 10^{-6}$). However, the distribution of G motor neurons was also statistically different from the distribution of all extensor-classified neurons ($p < 0.005$)—perhaps reflecting the fact that different extensor motor pools each have their own distinct firing rate distributions. Together these results indicate that different motor synergy groups not only fire at different times during locomotor firing, but at different intensities as well.

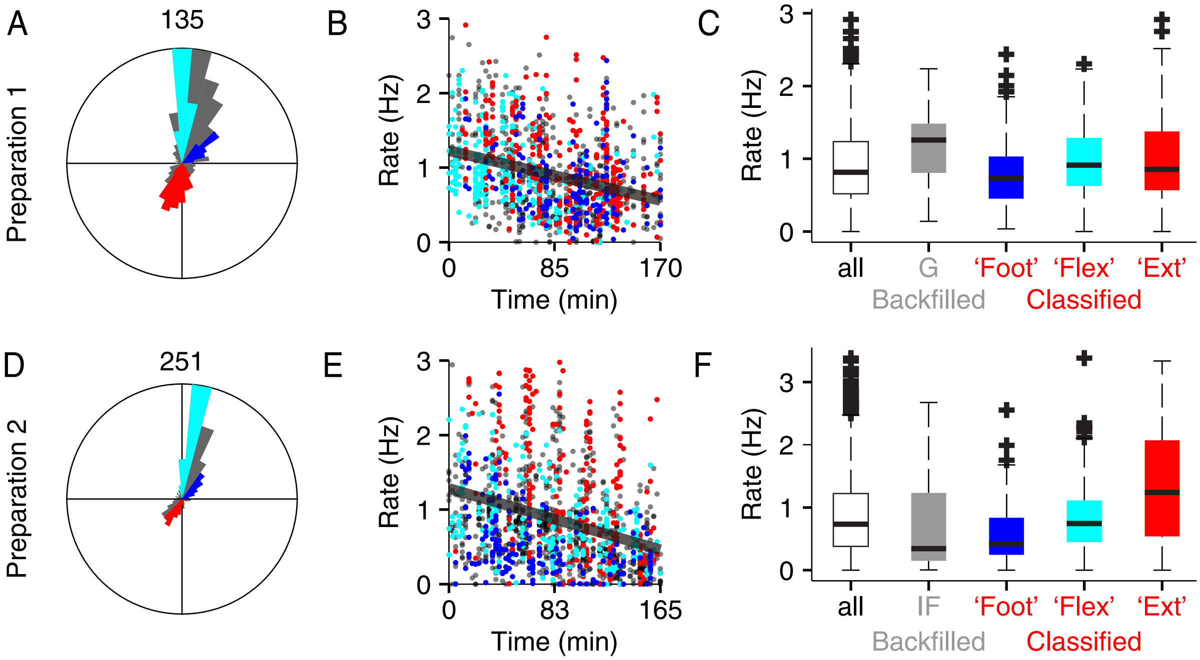

Figure 4.14: **Mean firing rates during fictive locomotion vary as a function of pool identity**

(A,D) Histogram of all phasic neurons (Rayeligh test P < 0.5) from two preparations (n = 1264 neurons in preparation 1; n = 1396 neurons in preparation 2). Colors correspond to neurons identified as belonging to one of three clusters on the basis of their phase tuning: cyan points denote flexor-like firing, red points denote extensor-like firing, and blue points denote foot-like firing. Phase criteria for assignment to each class is indicated in the text. (B,E) Firing rate of each phasic neuron (dots) in each preparation as a function of time imaged. Colored dots were assigned to one of the three clusters defined in (A,D). (C,F) Box plot displaying mean firing rate distributions for all phasic neurons (all), backfilled neurons (gluteus/G in C; foot/IF in F), or for each of the three identified clusters defined in (A,D). Horizontal bars within boxes represent medians and edges of boxes represent the 25th and 75th percentile mean rate value for each cell type. "+" points represent outlier neurons.

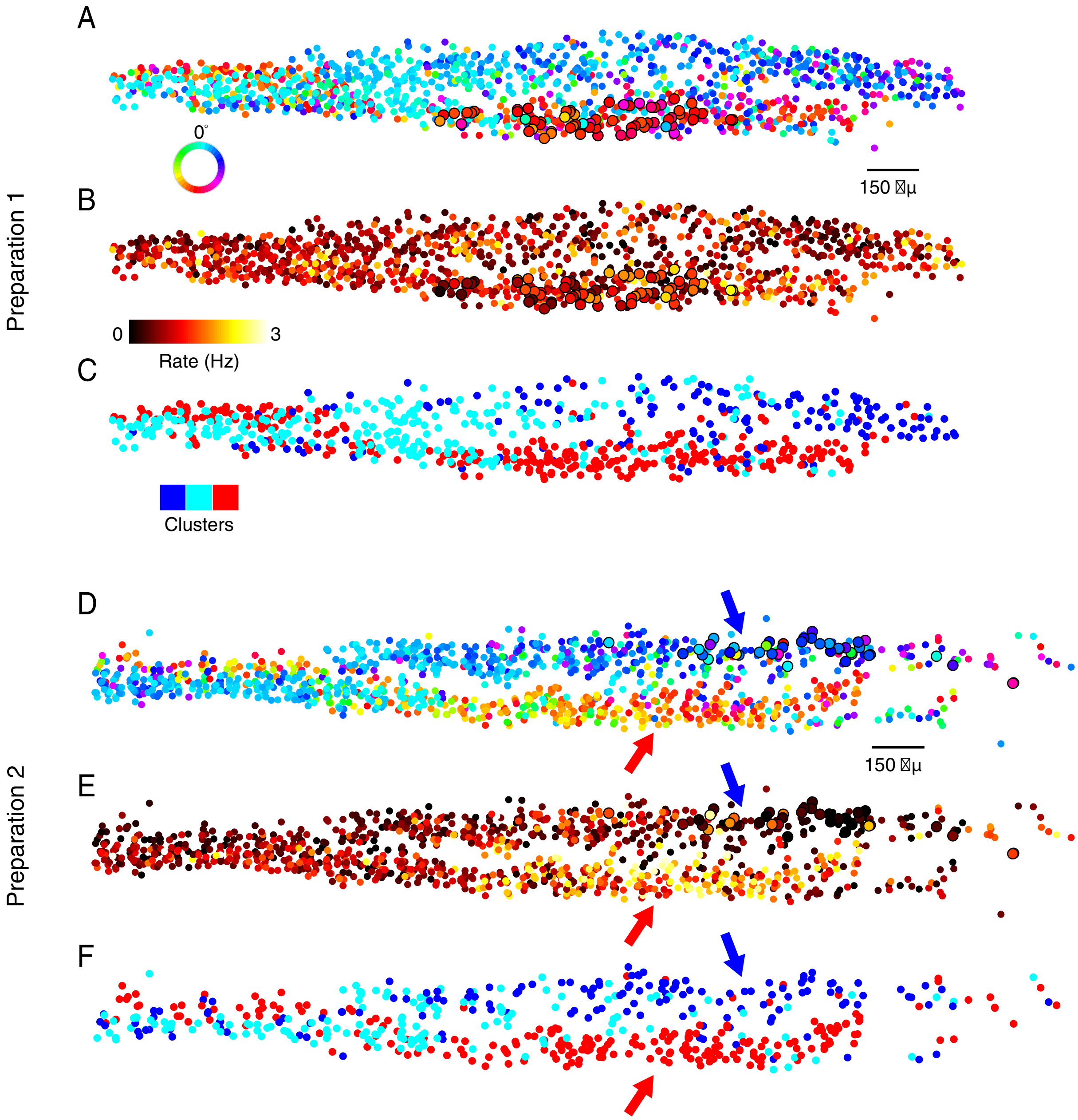
A
0°
150 µ
B
Preparation 1
0
3
Rate (Hz)
C
Clusters
D
150 µ
E
Preparation 2
F

Figure 4.15 *(preceding page)*: **Spatial maps of mean firing rate reveal the organization of motor neuron activation intensity across space**

(A,D) Phase tuning maps from two datasets analyzed in this firing rate analysis. Phase tuning was computed using results from the fast spike inference algorithm (as in Figure 4.8). Numbers above each histogram indicate the maximal number of neurons in a single histogram bin. (B,E) The estimated mean firing rate is displayed for each phasic neuron. Brighter colors indicate higher firing rates. Firing rate estimation was accomplished using Markov Chain Monte Carlo-based spike inference methods [Pnevmatikakis et al., 2013]. (C,F) Cluster identities were assigned according to mean phase tuning, as described in the legend of Figure 4.14. (Arrows in D-F) Indicated regions show the position of high firing rate extensor motor neurons (red arrows) and low firing rate foot motor neurons (blue arrows).

4.3 Discussion

The temporal features of motor neuron firing observed in neonatal spinal cord *in vitro* exhibit distinctions from, and commonalities with, the pattern of activation of their muscle targets in adults *in vivo*. Such a comparison indicates the sufficiency of local circuits in conferring aspects of locomotor pattern, as well as their inherent limitations.

4.3.1 Elements of in vivo locomotor pattern retained in an isolated preparation

We note differences between motor neuron firing patterns observed *in vitro* when compared with the activation of corresponding target muscles *in vivo*, with such discrepancies implicating descending commands or sensory feedback in shaping locomotor pattern.

Included among the discrepancies are differences in the number and duration of motor bursts. We observed that TFL and RF motor neurons burst only once per locomotor cycle *in vitro*, yet their target muscles exhibit dual burst activity in many locomotor contexts *in vivo* [Rossignol, 1996; Yakovenko et al., 2002]. This difference likely reflects the influence of sensory feedback, inducing a second phase of motor neuron bursting per cycle, or shifting the firing phase of a subset of neurons within the TFL and RF pools [Loeb, 1985; Perret & Cabelguen, 1980]. A second distinction is that flexor motor neurons exhibit relatively brief bursts in vitro, whereas flexor muscle activation in vivo can occupy a much greater proportion of the locomotor cycle. Studies in cat and mice in vivo suggest that the duration of muscle activation is also governed by sensory feedback, in part through the regulation of muscle offset timing [Akay et al., 2014; Lam & Pearson, 2001]. Together, these findings suggest that premotor circuits are sufficient to produce a basic dynamical template of locomotor activity that is subject to refinement through sensory feedback.

Nevertheless, conserved features emerge from a comparison of locomotor patterns in vitro and in vivo, most clearly in the timing of recruitment of motor neurons that innervate synergist muscles acting on different joints. Our findings indicate that local circuits are sufficient to direct the activation of motor neurons innervating synergistic flexor muscles, in a ventrodorsal sequence that matches the proximodistal positioning of their muscle targets. EMG recordings from mouse hindlimb muscles during walking document the activation of hip, knee, and ankle flexor muscles in a similar proximodistal order [Akay et al., 2014]. Even in cat, certain locomotor conditions reveal an analogous proximal to distal activation sequence that extends from hip to toe synergy groups [Rasmussen et al., 1978; Grillner, 1981; Krouchev et al., 2006], despite considerable task-dependent variability in the order of muscle recruitment [Rossignol, 1996; Yakovenko et al., 2002]. The mouse motor neuron activation sequence observed in vitro implies that premotor interneurons are able to recognize and select from motor synergy groups governing different limb joints.

Two-photon Ca^{2+} imaging reveals aspects of the organization of locomotor firing across the LMC that could not have been discerned from motor nerve or muscle recordings, which conflate the activity of individual motor neurons and pools. The combined cellular and high spatial resolution afforded by imaging revealed that motor neurons exhibit abrupt changes in firing at the boundaries between synergy groups. The spatial resolution and broad coverage provided by our datasets were critical in exposing spatially extended synchrony. Cellular resolution estimation of neuronal firing was also necessary to delineate the precision of flexor firing that dominates among $FoxP1^{MN\Delta}$ motor neurons (see Chapter 5).

4.3.2 Locomotor pattern complexity in the isolated neonatal rodent preparation

At first glance, the heterogeneous firing patterns across different flexor synergy groups appear inconsistent with a recent analysis of ventral root recordings from isolated neonatal rat spinal cord [Dominici et al., 2011]. This prior study concluded that locomotor output from neonatal preparations is well-approximated by two alternating rhythmic patterns, in contrast to the greater complexity observed in EMG recordings from behaving adults. This discrepancy prompted us to perform an analysis similar to that of Dominici et al. but using the cycle-averaged firing rates of the many motor neurons recorded in individual neonatal spinal cords. Non-negative matrix factorization reveals that four components are needed to explain $\sim 90\%$ of the variance in locomotor firing across the neonatal LMC, as in adult EMG (Figure 4.16A-E). Similar results were obtained using principal components analysis (Figure 4.16F). Thus the complexity of locomotor output from the isolated neonatal rodent spinal cord preparation is similar to that generated in adults in vivo, contrary to the conclusion of Dominici et al.

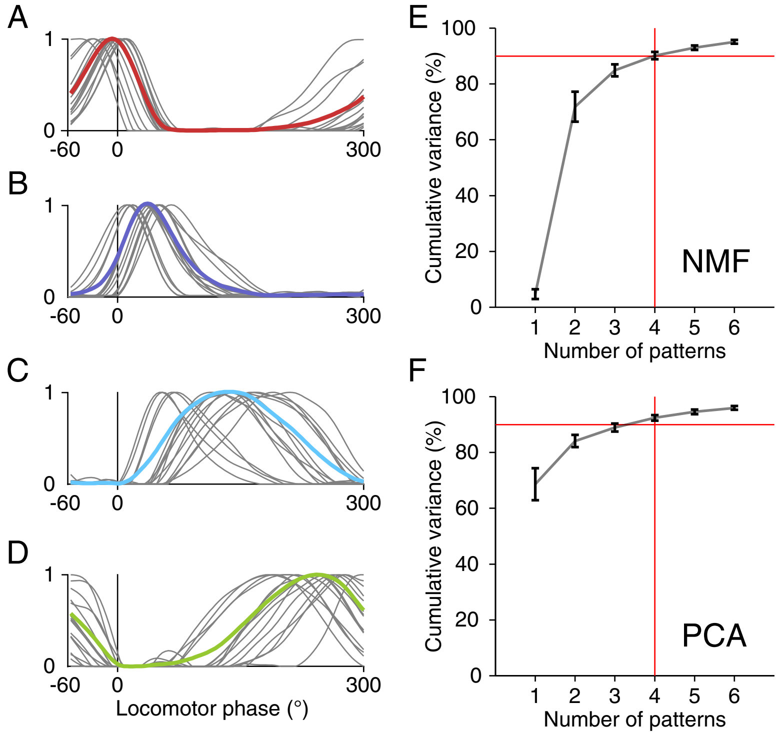

Figure 4.16: **Basic patterns extracted from *in vitro* neonatal mouse locomotor firing**

(A-D) Components resulting from non-negative matrix factorization (NMF) on the cycle-averaged firing rates from 15 wild type datasets each decomposed into 4 components. Gray lines represent components from individual datasets, colored lines represent means across all datasets. (E) Cumulative variance (± s.d., n = 15 preparations) explained by adding additional components. Red lines indicate the number of components necessary to account for approximately 90% of the cumulative variance.

4.3.3 Future applications of this assay

Our imaging studies emphasize the inadequacy of monitoring ventral root activity as a viable means of probing the logic of mammalian locomotor circuitry. Interpretations of *in vitro* ventral root recordings have typically relied upon the notion that lumbar L2 and L5 root activity peaks reflect, respectively, the phases of flexor and extensor motor neuron firing. Yet our findings document that at each lumbar segment there are sizable populations of motor neurons that exhibit distinct flexor or extensor firing patterns. The basis of this discrepancy remains to be resolved, but most obviously could reflect quantitative differences in the number of flexor and extensor motor neurons at different segmental levels [Yakovenko et al., 2002] and/or differences in motor neuron firing frequency. Whatever its basis, our findings illustrate that a reliance on ventral root activity peaks ignores the extent of diversity in motor neuron activities present at individual segmental levels of the spinal cord.

Moving forward, there are many applications for the assay presented here. Since this approach permits the measurement of cellular-resolution activity patterns from a large fraction of all limb innervating motor neurons to be measured during locomotor firing, simply applying it to existing mouse strains that manipulated spinal interneuron circuits will likely lead to fundamentally new interpretations of previously described knockout phenotypes that have been described over the last decade [Lanuza et al., 2004; Gosgnach et al., 2006; Crone et al., 2008; Zhang et al., 2008] (Figure 1.5).

While ablating any of these genetically defined subpopulations of neurons has an impact on locomotor pattern output, recording from only two ventral roots is an inadequate readout. In this chapter, we have shown a high degree of structure in motor output that goes far beyond simple flexor-extensor alternation. The standard ventral root recording assay can only assay deficits to alternation, burst robustness, and burst frequency. Indeed, each of those phenotypes can be observed in the data presented in Figure 1.5. It seems highly unlikely that, given the structure that we know exists at the level of single motor neuron firing, that there is nothing else to be learned from these mutants.

In the next chapter, we will explore the locomotor firing of motor neurons in a mutant mouse where the transcription factor FoxP1 has been selectively deleted from all limb-innervating motor neurons. In the context of that manipulation, it will be useful to consider why many of our observations would have been qualitatively different had we lacked the spatial and cellular resolution afforded by the assay described in this chapter.

5

Flexor primacy in intrinsic locomotor firing

5.1 Introduction

The locomotor activity characterization in the previous chapter served as a reference for analyzing how reversion of lumbar motor neuron identity to an ancestral state might change locomotor pattern.[1] In this chapter, we present evidence in support of the concept of flexor primacy: the idea that the basic organization of flexor circuits predates the emergence of extensor circuits, and therefore that modern flexor circuits may have emerged by co-opting ancient axial circuits. Under this view, the reversion of lateral motor column (LMC) neurons to an ancestral-like state might lead to their recruitment of flexor-defining premotor inputs. To assess this possibility, we genetically inactivated the FoxP1 transcription factor to convert limb-innervating motor neurons to an HMC-like ground state [Dasen et al., 2008; Kusakabe & Kuratani, 2005; Rousso et al., 2008]. In *FoxP1* mutant preparations we find that virtually all limb-innervating motor neurons – those innervating extensor as well as flexor limb muscles – are activated with the precise temporal features of flexor motor neurons. Our observations show that the subtype identity of motor neurons profoundly influences the

---

[1] Portions of this chapter were derived from work in [Machado et al., 2015].

pattern of motor output. They also lend credence to the idea that a flexor-like motor pattern emerged during vertebrate evolution without reliance on a functionally opponent extensor premotor circuit.

5.1.1 The diversification of motor neuron identity across evolution

The identities, muscle targets and functional specialization of motor neurons have diversified greatly during vertebrate evolution, providing a potential means of addressing the influence of motor neuron identity on locomotor pattern. Within this broad evolutionary context certain physiological studies have raised the possibility that mammalian flexor networks evolved by co-opting a core axial motor circuit responsible for swimming in ancestral aquatic vertebrates. In primitive vertebrates, the body undulations that underlie swimming reflect the wave-like recruitment of motor neurons innervating segmentally-arrayed axial muscles [Grillner & Wallen, 1985].

A similar wave-like pattern of motor neuron activation is evident from ventral root recordings at thoracic levels in the isolated neonatal rat spinal cord during locomotor-like activity [Falgairolle & Cazalets, 2007], as can be seen in Figure 5.1. In the adapted data, suction electrode recordings were simultaneous obtained from up to 16 ventral roots during drug-induced fictive locomotion. When the mean phase tuning of each thoracic segment was aggregated across experiments and plotted with a common phase reference point (ventral root L2), a caudo-rostral wave in activity becomes apparent (Figure 5.1B). Since limb innervating LMC motor neurons do not reside at thoracic segments, this thoracic wave must reflect the firing of median (MMC) and hypaxial (HMC) motor column neurons that innervate trunk (epaxial) and body wall (hypaxial) muscles, respectively.

Intriguingly, the activity of rostral lumbar segments, which are known to fire in a flexor-like phase, form a caudal continuation of this thoracic activity wave, whereas more caudal extensor-related segments burst in antiphase. This continuity of thoracic and flexor firing may reflect the reappropriation of axial circuits for flexor pattern generation, and thus argues for the evolutionary primacy of the flexor system. In support of this view, there is experimental data indicating that the developmental programs controlling the growth of hypaxial musculature in mammals may be shared with those that regulate the development of generic axial musculature in primitive jawless vertebrates like lampreys (Figure 5.2).

In contrast to all extant jawed vertebrates (which belong to the infraphylum *Gnathostomata*), lampreys lack paired appendages. They also lack a clear distinction between dorsal epaxial and ventral hypaxial muscles which are typically separated from each other along the dorsoventral axis of a gnathostome by a connective tissue called the horizonatal myoseptum (Figure 5.2 B,D). This distinction between lampreys and gnathostomes prompted developmental researchers to wonder whether the muscles of lampreys were more similar to epaxial or hypaxial muscles in other vertebrates [Kusakabe & Kuratani, 2005]. Because expression of gnathostome transcription factor *Pax3* is restricted to hypaxial muscles at late developmental stages, and because *Pax3* appears necessary for both limb and hypaxial muscle development [Franz et al., 1993], Kusakabe and Kuratani examined whether the lamprey homolog of *Pax3*, called *LampPax3/7*, was expressed in lamprey musculature (Figure 5.2 A,C). They found that it was present, suggesting an evolutionary linkage between ancestral axial and modern hypaxial muscles.

As we will see in section 5.1.2, this insight will prove valuable in interpreting complementary studies of hypaxial (HMC) verses epaxial (MMC) motor neuron development. Together, these results permit us to argue that a reversion of limb-innervating (LMC) motor neurons to an HMC-like state is tantamount to an ancestral reversion, wherein we can examine the impact of motor neuron identity on locomotor circuit organization and activity patterning.

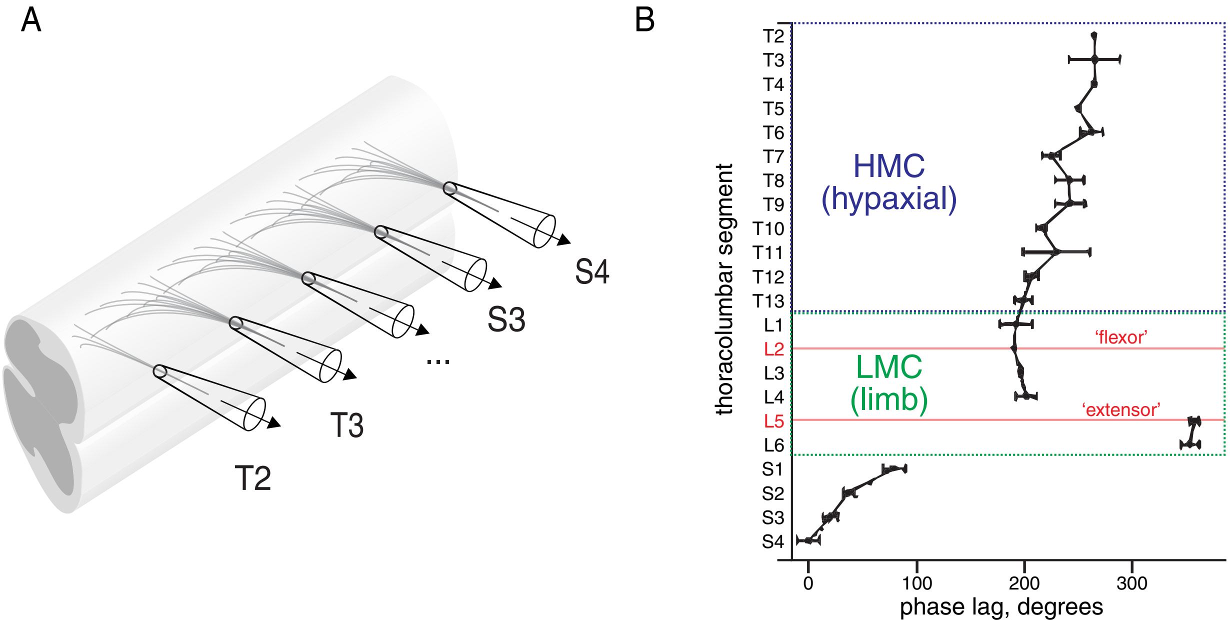

Figure 5.1: **Continuity of thoracic and flexor firing in the isolated rat spinal cord**

(A) Ventral root recordings were simultaneously obtained from up to 16 thoracic, lumbar, and sacral segments in order to accumulate phase tuning information from each segment. (B) Mean phase tuning of each ventral root signal relative to L2. Data represented as means ± s.e.m. Adapted from [Falgairolle & Cazalets, 2007].

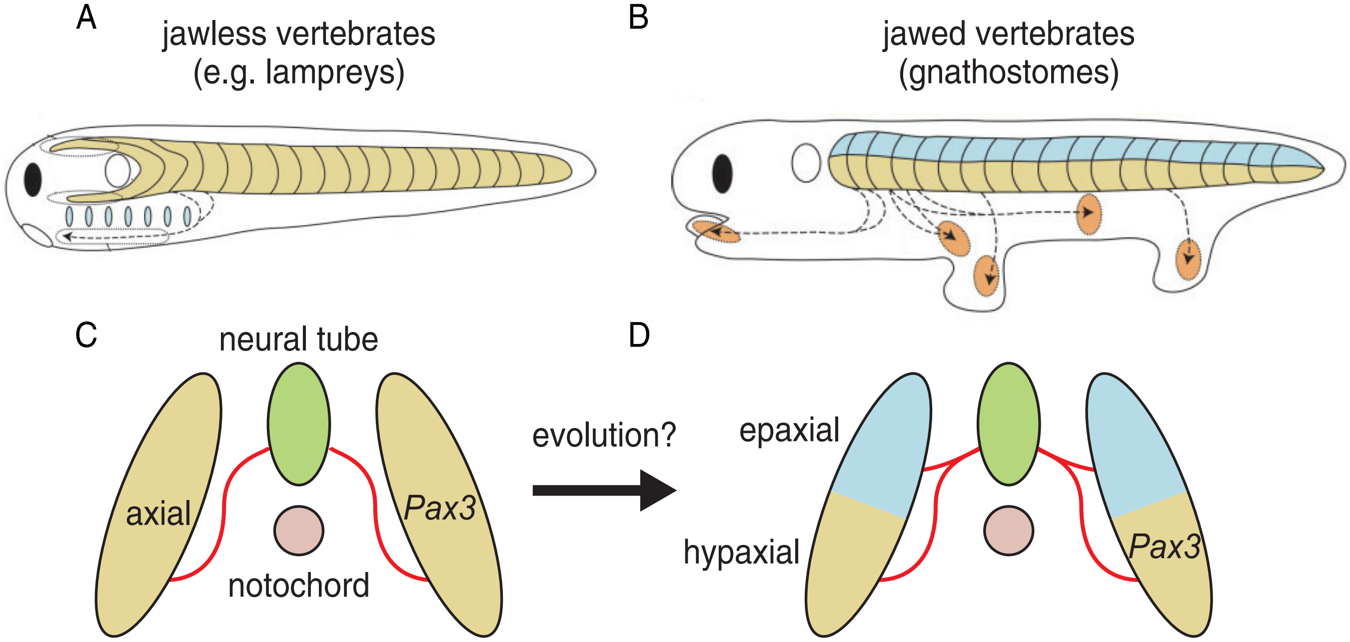

Figure 5.2: **Hypaxial musculature shares common developmental programs with primitive axial muscles**

(A-B) Lateral view of a lamprey and a jawed vertebrate (gnathostomes, e.g. mammals) showing the position of hypaxial (yellow) and epaxial (blue) musculature. (C) Transverse view of a lamprey. Axial musculature (yellow) is innervated by motor neurons in the spinal cord (green) and expresses *LampPax3/7*, the lamprey homolog of mammalian *Pax3*. (D) Transverse view of a jawed vertebrate. Axial musculature in gnathostomes can be morphologically divided into dorsal epaxial (blue), and ventral hypaxial (yellow) muscles. At late developmental stages, *Pax3* expression is restricted to hypaxial musculature, where its presence is necessary for normal limb and hypaxial muscle development. Adapted from [Kusakabe & Kuratani, 2005].

5.1.2 In the absence of FoxP1, motor neuron identity is reverted to an ancestral state

Given that hypaxial – but not epaxial musculature – continues to rely on ancestral axial developmental programs [Kusakabe & Kuratani, 2005], previous work also investigated whether similar results might hold for the development of motor neurons. Simply mapping the results from [Kusakabe & Kuratani, 2005] onto motor neuron development would predict that the development of hypaxial-innervating (HMC) neurons would represent a default state that can be elaborated upon to produce epaxial (MMC) or limb-innervating (LMC) motor neurons. Indeed, [Agalliu et al., 2009] demonstrated that the development of MMC motor neurons was dependent on the graded expression of Wnt genes along the dorsoventral axis of the spinal cord. Similarly, [Dasen et al., 2008; Rousso et al., 2008] demonstrated that a rostrocaudal FGF pathway was necessary to pattern Hox expression and instruct LMC and PGC development. As predicted, in the absence of either Wnt or Hox activity, motor neuron identity defaults to an HMC-like state (Figure 5.3A), further supporting the idea that the HMC-like state represents an ancestral motor neuron identity.

Additionally, in mutant mice where *FoxP1*, a necessary Hox cofactor, has been inactivated [Dasen et al., 2008], no motor neuron progenitors assume either an LMC or PGC-like genetic identity. Instead, all non-MMC motor neurons are reverted to an atavistic HMC-like state. Despite this, reverted motor neurons in lumbar segments still form functional synaptic contacts with limb muscles (Figure 5.3B). We took advantage of this ancestral reversion of limb-innervating motor neurons in order to examine the contribution of motor neuron identity in the organization of spinal interneuron circuits that mediate locomotor behaviors.

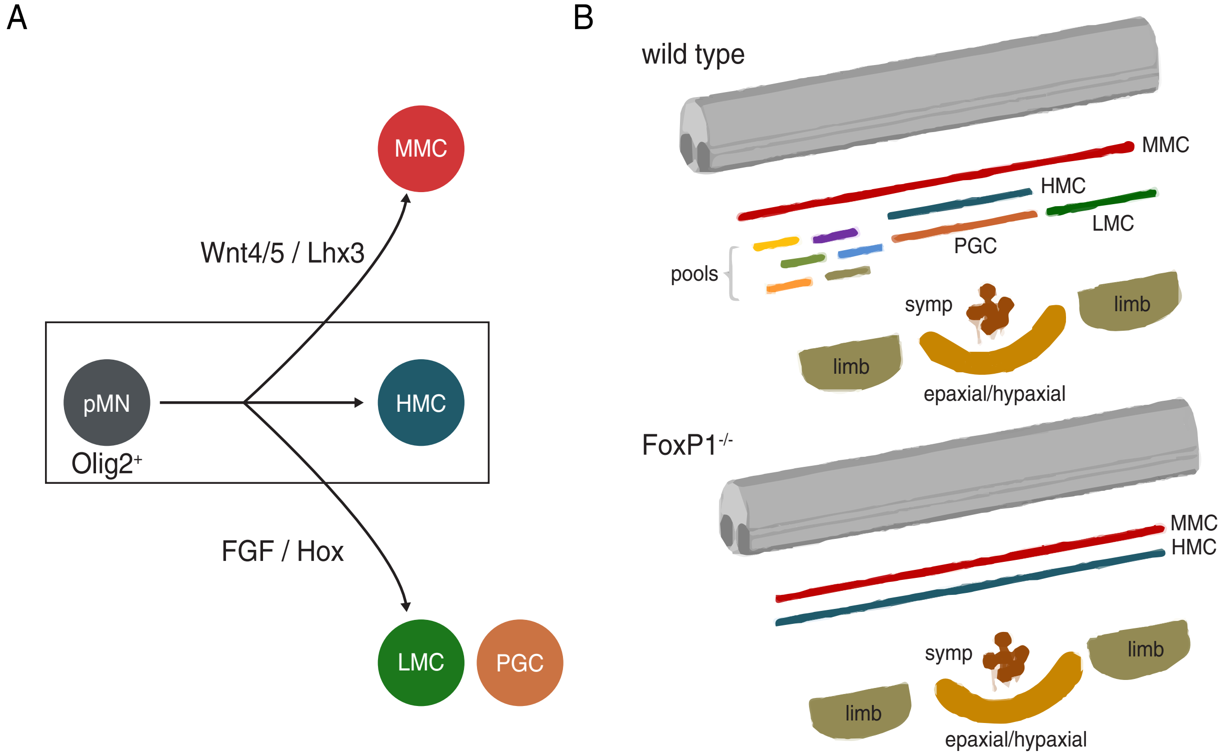

Figure 5.3: **In the absence of FoxP1, motor neuron identity is reverted to a default, HMC-like ground state**

(A) During development, motor neuron progenitors (pMN) expressing *Olig2* diversify into members of one of four columns that each share different types of muscle targets: MMC (epaxial; red), HMC (hypaxial; blue), PGC (sympathetic; orange), and LMC (limb muscles; green). Development of MMC neurons is dependent on Wnt signaling. FGF signaling and Hox transcription factor activity is required for development of LMC and PGC neurons. (B) Top: The position of each motor column is noted in a wild type mouse spinal cord. LMC motor neurons also have muscle-specific pool identities (colored pools). Bottom: After FoxP1 inactivation, PGC and LMC motor neurons are reverted to a generic HMC-like state. Panel (A) adapted from [Agalliu et al., 2009]. Panel (B) adapted from [Dasen et al., 2008].

5.1.3 The recognition of motor neurons by interneurons

The issue of spinal circuit organization as a function of changes to motor neuron identity has been examined previously. In particular, [Sürmeli et al., 2011] examined whether patterns of proprioceptive sensory input onto motor neurons were perturbed in mutant mice where *FoxP1* had been selectively removed from all motor neurons. In the absence of such a genetic manipulation, proprioceptive sensory afferents arising from a particular muscle contact their homonymous motor pool, as well as synergist motor pools that reside in similar dorsoventral positions [Eccles et al., 1957; Kudo & Yamada, 1987a] (Figure 5.4A). This specificity in sensory afferent targeting with respect to pool identity and neuronal position urged a consideration of the mechanisms by which afferents found their appropriate postsynaptic motor neuron targets.

When *FoxP1* was removed from motor neurons (termed $FoxP1^{MN\Delta}$ mice), muscles were still fully innervated, but the position of the identity-stripped motor neurons that shared common pool targets was scrambled. Therefore, this experimental manipulation effectively decoupled the issue of motor neuron position from that of identity. In this context, [Sürmeli et al., 2011] found that proprioceptive afferents formed synaptic partners with motor neurons at similar dorsoventral positions in both wild type and $FoxP1^{MN\Delta}$ mice. This result suggests that the dorsoventral position of a motor neuron, independent of its genetic status, is sufficient for the formation of functional sensory contacts (Figure 5.4B).

In this chapter, we examine the impact of this same genetic perturbation on interneuron-motor neuron connectivity, finding that, in contrast to sensory inputs, space is not sufficient for the maintenance of normal locomotor firing patterns.

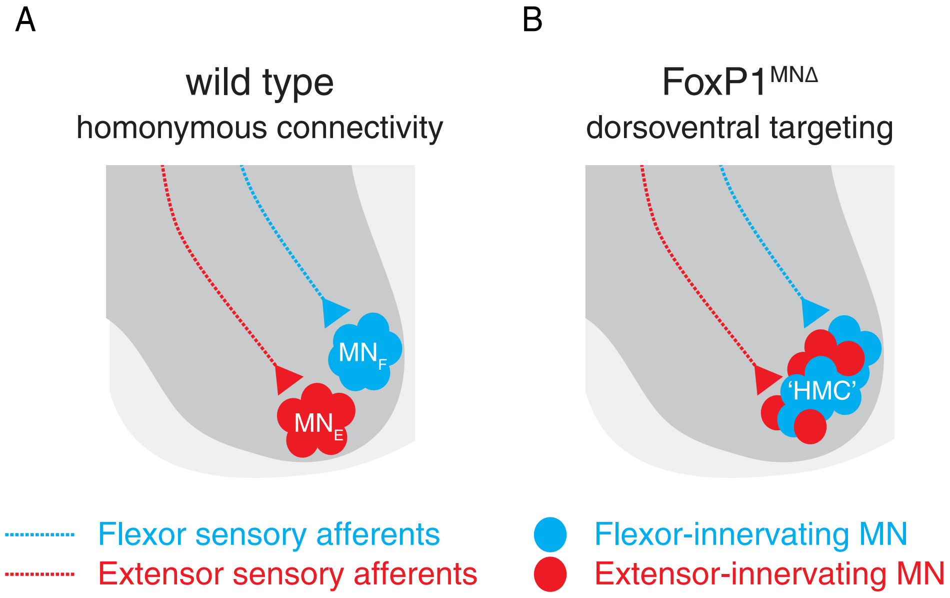

Figure 5.4: **Sensory afferents find postsynaptic motor neuron targets using positional information**

(A) Proprioceptive 1a afferents target homonymous motor neurons in wild type mice. (B) In $FoxP1^{MN\Delta}$ mice, where motor neurons have been stripped of their pool specific genetic identities, 1a afferents form synaptic contacts with the motor neurons that now occupy the dorsoventral positions that their homonymous pool targets would have occupied in wild type mice.

5.2 Results

5.2.1 Locomotor firing after reversion of motor neuron identity

Are locomotor firing patterns modified by reverting motor neuron identity to an ancestral-like state? To test this possibility, mice harboring a conditional *FoxP1* allele were crossed with an $Olig2 :: Cre$ driver line to generate motor neuron selective $FoxP1^{MN\Delta}$ mutants [Dasen et al., 2008]. In $FoxP1^{MN\Delta}$ mice, motor neurons fail to acquire LMC columnar and pool-specific identities and instead assume many of the functional features of thoracic HMC neurons. Transfated motor neurons in $FoxP1^{MN\Delta}$ mice fail to exhibit a stereotypic relationship between neuronal position and muscle target (Figure 5.5), yet both flexor and extensor muscles are still innervated. As a consequence, muscles co-contract, limbs are rigid and normal locomotion is precluded [Sürmeli et al., 2011].

To assess the impact of the reversion of motor neuron identity on locomotor firing, we first monitored lumbar ventral root activities. Induction of locomotor-like activity in isolated $FoxP1^{MN\Delta}$ preparations elicited rhythmic root activity at frequencies similar to those in wild type mice (Figure 4.6; $p = 0.66$, Wilcoxon test). However, the normal ipsilateral alternation between L2 and L5 roots was no longer detected, and both roots fired in near-synchrony (Figure 5.6A-C), even though alternation between contralateral roots was still evident (data not shown). Ventral root activity measurements revealed that phase differences between T9-10 and L2 ventral root activity peaks were similar in wild type and $FoxP1^{MN\Delta}$ preparations (Figure 5.6D-F; $p = 0.85$, two-sample, two-tailed t-test). Thus, the reversion of motor neuron columnar fate abolishes rostrocaudal alternation in motor neuron burst firing. Nevertheless, rostral lumbar ventral root activity still provides a valid phase reference.

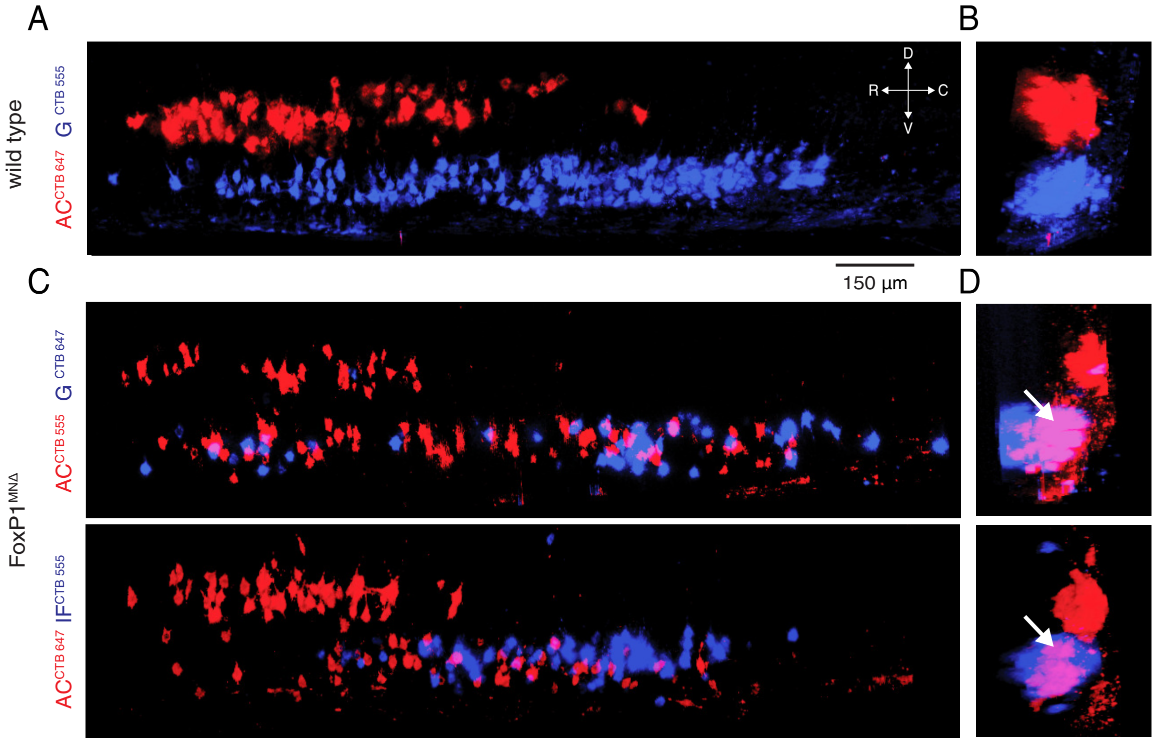

Figure 5.5: **Spatial organization of CTB-labeled $FoxP1^{MN\Delta}$ motor neurons** (A) Maximum intensity projection across a sagittally-oriented lumbar spinal cord image stack from a wild type mouse. Identified anterior crural (AC) motor neurons (red) are confined to a dorsal band above identified gluteal (G) motor neurons (blue). (B) Transverse projection across the stack used in (A). (C-D) Maximum intensity projections across two sagittal image stacks from two different $FoxP1^{MN\Delta}$ mice showing labeled AC, G, and intrinsic foot (IF) motor neurons. Arrows in (D) denote ventrally positioned AC motor neurons.

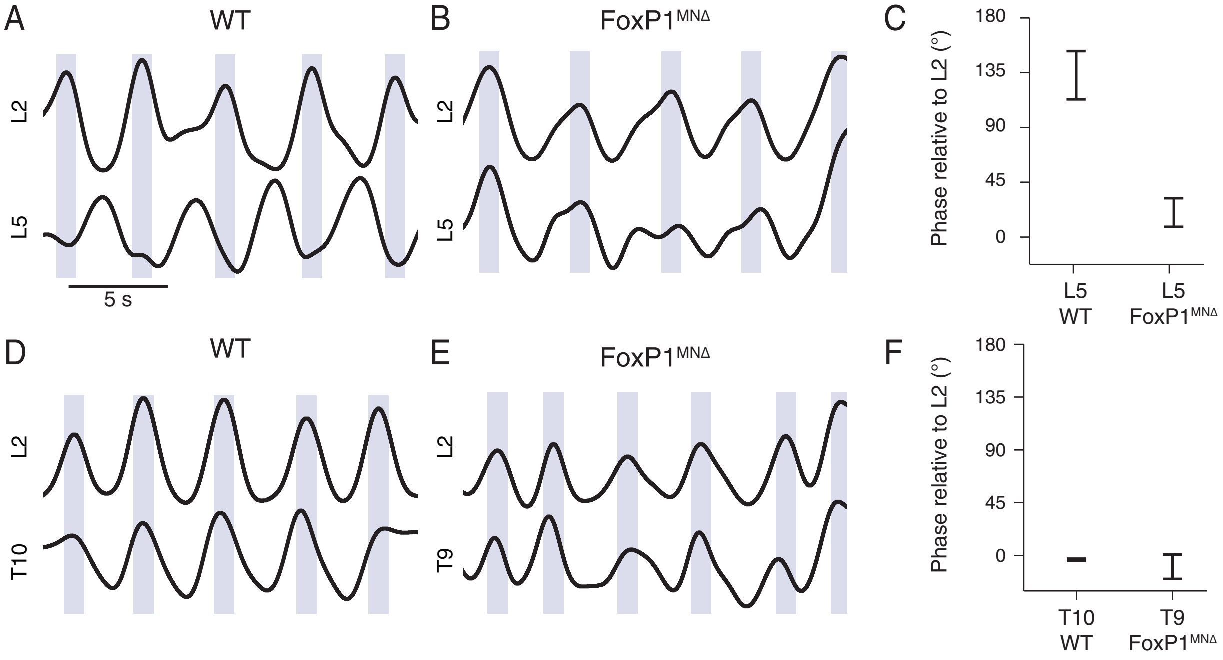

Figure 5.6: **Ventral root activity in wild type and $FoxP1^{MN\Delta}$ preparations** (A-B; D-E) Filtered ventral root recordings from wild type (A,D) and $FoxP1^{MN\Delta}$ mutant mice (B,E). (C) Phase differences between ventral root peaks measured between L5 and ipsilateral L2. Error bars represent the means ± s.e.m. computed for 45 90 s recordings from a wild type mouse (left) and 24 recordings from a $FoxP1^{MN\Delta}$ mouse (right). (F) Phase differences between ventral root peaks measured between thoracic segments and ipsilateral L2. Error bars represent the means ± s.e.m. computed for 16 90 s recordings from a wild type mouse (left) and 28 recordings from a $FoxP1^{MN\Delta}$ mouse (right).

5.2.2 Loss of motor neuron identity induces flexor-like locomotor firing

To probe the cellular origins of changes in lumbar locomotor activity, we performed GCaMP3 fluorescence imaging of motor neurons and ventral root recording in $FoxP1^{MN\Delta}$ preparations. Motor neuron phase tuning maps (200-900 motor neurons/map; mean = 656 motor neurons) revealed substantial differences from tuning in wild type preparations (Figure 5.7; $p = 0.0002$, K-S test). Motor neurons exhibited rhythmic firing at a common phase, close to 0° (Figure 5.7C,H,M), with only ~2% (29/1413) of $FoxP1^{MN\Delta}$ motor neurons bursting at phase values close to 180° (Figure 5.8). This anomalous minority likely reflects the redundant functions of FoxP4 and thus the preservation of LMC identity in a small fraction of limb-innervating motor neurons [Dasen et al., 2008].

To exclude the possibility that motor neurons targeting certain muscles remain silent in $FoxP1^{MN\Delta}$ preparations, we analyzed the activity of identified motor neurons. $FoxP1^{MN\Delta}$ motor neurons retrogradely labeled by CTB injection into intrinsic foot (IF; toe flexors), anterior crural (AC; ankle flexors), gluteal (G; hip extensor/flexor), and gastrocnemius (GS, ankle extensor) muscles exhibited highly overlapping tuning distributions (IF: -3 ± 21°, mean ± s.d., n = 46 neurons; AC: 20 ± 26°, n = 88; G: 13 ± 23°, n = 8; GS: -19 ± 28°, n = 33) in marked contrast to wild type preparations. In particular, we noted a profound conversion of extensor (G and GS) motor neuron firing to a flexor-like phase (Figure 5.7D,E,N,O). In addition, IF motor neurons now fired slightly earlier than AC neurons, the inverse of their wild type relationship. We conclude that the loss of FoxP1 erodes the normal synergy group-specific patterns of motor neuron burst firing and promotes flexor monotony.

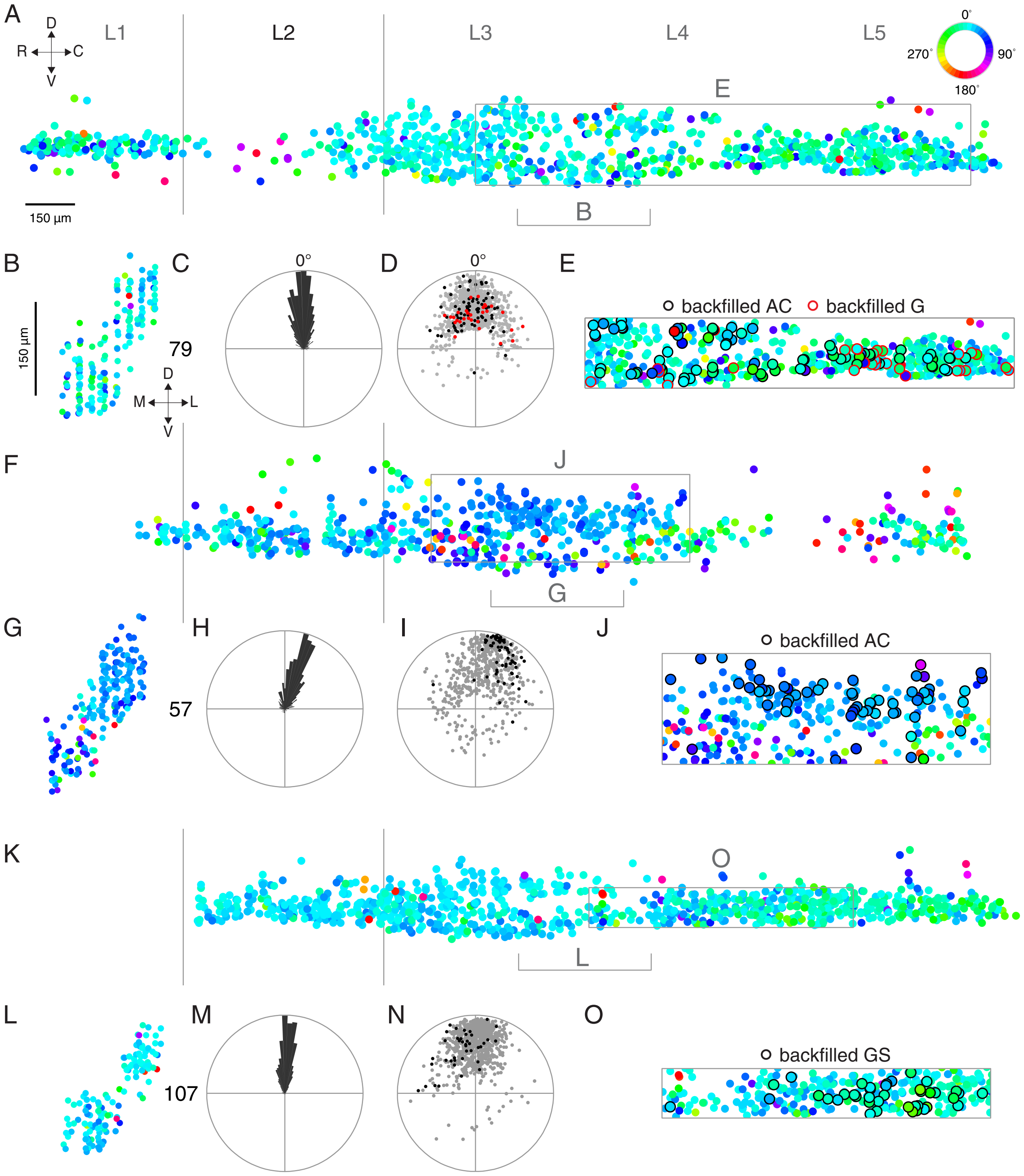
A
D
R
C
V
L1
L2
L3
L4
L5
0°
270°
90°
180°
E
150 µm
B
B
150 µm
C
0°
79
D
M
L
V
D
0°
E
backfilled AC
backfilled G
F
J
G
G
H
57
I
J
backfilled AC
K
O
L
L
M
107
N
O
backfilled GS

Figure 5.7 *(preceding page)*: **Uniform motor neuron phase tuning in $FoxP1^{MN\Delta}$ cords**

(A,F,K) Map showing phase tuning of motor neurons within three $FoxP1^{MN\Delta}$ spinal cords as viewed from the lateral side (927 neurons in (A), 630 neurons in (F), and 859 neurons in (K)). Segmental boundaries of the antidromically-activated segment are indicated by vertical lines. Labels of other segments were drawn assuming equal segment widths. (B,G,L) Transverse projection for the rostrocaudal extent indicated in (A,F,K). (C,H,M) Polar histogram showing phase tuning of neurons mapped in (A,F,K). The maximal number of neurons within a single bin is shown to the left of the histogram. (D) Polar plot indicating the phase tuning of all motor neurons mapped in (A) plotted in gray with the tunings of all CTB-labeled anterior crural (AC, black) and gluteal (G, red) motor neurons from the same preparation superimposed. Similar plots for AC motor neurons and gastrocnemius (GS) motor neurons taken from plots (A) and (F) are shown in (I) and (N), respectively. The radial position of each point in (D,I,N) represents circular spread around its phase tuning. (E,J,O) Boxed area in (A,F,K) with CTB-labeled motor neurons indicated.

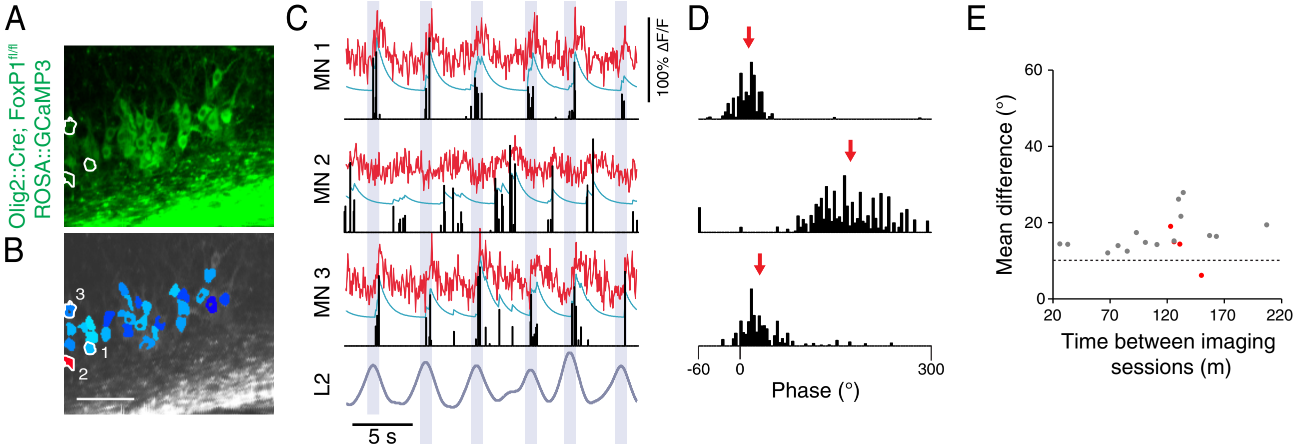

Figure 5.8: **A minority of $FoxP1^{MN\Delta}$ MN fire out of phase with the dominant pattern**

(A) Single imaging field from a $FoxP1^{MN\Delta}$ spinal cord containing GCaMP3-expressing motor neurons (green). Scale bar is 100 μm. (B) ROIs for motor neurons in (A) colored according to phase tuning using the same color scale as (A,F,K) in Figure 5.7. (C) Fluorescence time courses (red) for three motor neurons from (B) along with spike-induced fluorescence model fit (cyan) and inferred spikes (black bars). (D) Inferred spike counts from a full 90 s image sequence plotted across the locomotor cycle for the three motor neurons in (C), with the phase tuning of each neuron indicated (red arrows). (E) Mean tuning difference versus the interval between measurements for 4 $FoxP1^{MN\Delta}$ mice (red) superimposed on values from 15 wild type mice (gray). Dotted line indicates predicted mean difference assuming stable phase tuning.

5.2.3 Motor neuron firing is precisely flexor-like in $FoxP1^{MN\Delta}$ preparations

We also examined the precision with which motor neurons adopted flexor-like firing in $FoxP1^{MN\Delta}$ preparations. Cycle-averaged firing rates of wild type motor neurons could be separated into two sets using k-means clustering (Figure 5.96A,B), revealing well-separated sets within individual preparations (clustering index mean ± s.e.m. = 3.99 ± 0.26, n = 12 spinal cords), and across different preparations (clustering index = 3.85, n = 5967 neurons). One set of firing rates was characterized by brief bursts (86.7 ± 24.0° duration, mean ± s.d., n = 4212 neurons) with phase tunings early in the locomotor cycle (13.7 ± 27.5°). The second set exhibited prolonged bursts (165.7 ± 46.5° duration, n = 1755 neurons) tuned later in the locomotor cycle (166.2 ± 46.1°). We found that 99.4% (175/176) of identified motor neurons innervating AC and IF muscles were included within the early firing set. This finding suggests that early- and late-firing sets are comprised of flexor and extensor motor neurons, respectively (Figure 5.9C,D).

An equivalent analysis of $FoxP1^{MN\Delta}$ motor neurons revealed that the cycle-averaged firing rates for virtually all neurons precisely matched those of wild type flexor motor neurons, both in phase tuning and burst duration (Figure 5.10A-D). k-means clustering failed to identify well-separated sets, either in individual $FoxP1^{MN\Delta}$ preparations (clustering index mean ± s.e.m. = 0.48 ± 0.14, n = 4), or among neurons aggregated across different $FoxP1^{MN\Delta}$ preparations (cluster index = 0.27, n = 1413 neurons). Cluster separation was significantly less than for wild type firing rates (p = 2.1 x 10-6, one-tailed unpaired t-test). Collectively, $FoxP1^{MN\Delta}$ motor neurons exhibited distributions of phase tuning (mean ± s.d. = 12.0 ± 42.2°; Figure 5.106B) and burst duration (90.7 ± 29.3°) that were similar to those of the early firing wild type set that comprises flexor motor neurons.

Consistent with this, analysis of phase tuning and burst duration distributions from $FoxP1^{MN\Delta}$ mice revealed that firing exhibited 21-fold greater similarity to that of wild type flexors than that of extensors. Overlaps between the joint phase tuning and burst duration distributions were computed for motor neurons from each $FoxP1^{MN\Delta}$ cord (n = 4) and either the early or late firing sets of motor neurons aggregated from all wild type cords. This computation quantified the similarity in firing between $FoxP1^{MN\Delta}$ motor neurons and wild type motor neurons assigned to either set. Overlap with the early firing wild type set (62 ± 3%) was significantly larger than with the late firing wild type set (3 ± 0.4%; p = 9.1 x 10-5, one-tailed paired t-test). Moreover, distributions for CTB-labeled $FoxP1^{MN\Delta}$ motor neurons (Figure 5.10C,D) overlapped much more heavily with the early firing wild type set (AC and IF overlap = 71%, GM and GS = 43%) than with the late firing wild type set (AC and IF = 3%, GM and GS = 5%; $p = 10^{-5}$, Monte Carlo test). Taken together, our results indicate that almost all hindlimb-innervating motor neurons fire in a precisely flexor-like pattern after genetic reversion of motor neuron columnar identity.

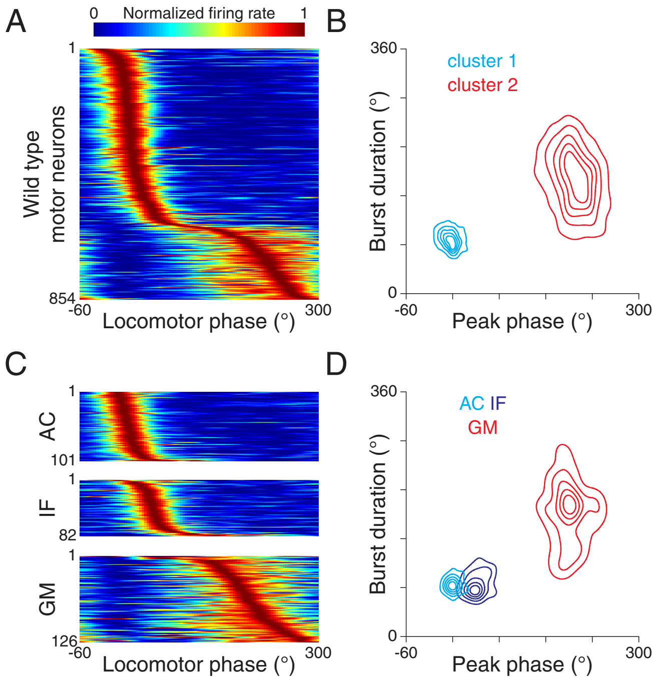

Figure 5.9: **Divergence in cycle-averaged firing between flexor and extensors motor neurons**

(A) Cycle-averaged firing rates for 854 motor neurons obtained from one wild type preparation. (B) Kernel density plots of the joint distribution of peak firing phase and burst duration for 5967 motor neurons pooled across 14 preparations and clustered into two groups. (C) Cycle-averaged firing rates for identified anterior crural (AC), intrinsic foot (IF), and gluteal extensor (GM) motor neurons, pooled across all wild type preparations. (D) Kernel density plots of the joint distribution of peak phase and burst duration for identified wild type motor neurons.

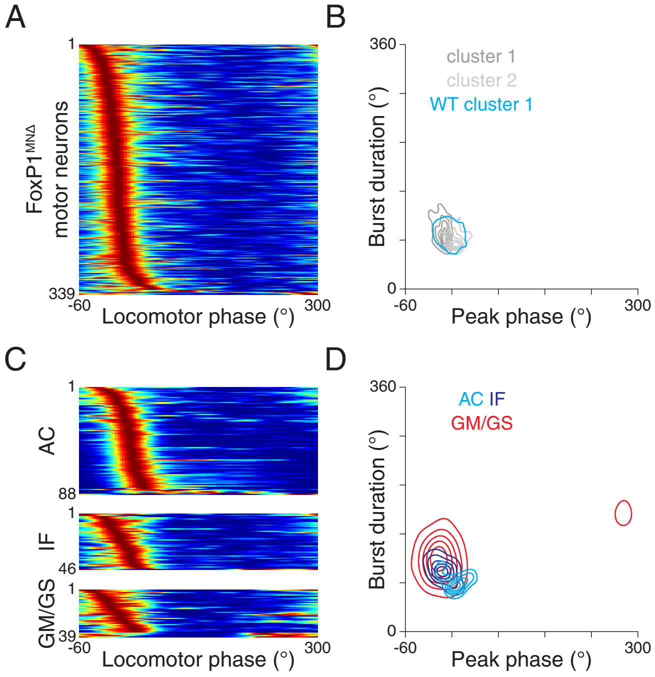

Figure 5.10: **Prevalence of flexor-like firing in $FoxP1^{MN\Delta}$ motor neurons**
(A) Cycle-averaged firing rates for 339 motor neurons from one $FoxP1^{MN\Delta}$ preparation. (B) Kernel density plots of the joint distribution of peak phase and burst duration for 1413 imaged $FoxP1^{MN\Delta}$ motor neurons pooled across 4 mice and clustered into two groups. Overlaid in cyan is the 1/6th of maximum contour from cluster 1 derived from wild type data shown in Figure 5.9 (B). (C) Cycle-averaged firing rates for identified anterior crural (AC), intrinsic foot (IF), gluteal (GM) or gastrocnemius (GS) motor neurons in $FoxP1^{MN\Delta}$ mice, pooled across 4 $FoxP1^{MN\Delta}$ preparations. (D) Kernel density plots of the joint distribution of peak phase and burst duration for $FoxP1^{MN\Delta}$ motor neurons retrogradely labeled from AC, IF, GM, and GS muscles.

5.3 Discussion

Our analysis reveals that the subtype identity of motor neurons determines the temporal features of locomotor pattern. Most critically, the reversion of LMC neurons to an ancestral HMC-like columnar character induces essentially all limb-innervating motor neurons to fire in a flexor-like pattern, a strong indication of the primacy of flexor pattern generation. This finding has relevance for the current organizational state of mammalian locomotor circuits.

5.3.1 Relating our in vitro results to the in vivo behavior of $FoxP1^{MN\Delta}$ mice

In [Sürmeli et al., 2011], EMG recordings were obtained from flexor and extensor muscles during treadmill walking in adult $FoxP1^{MN\Delta}$ mice (Figure 5.11). These recordings revealed synchronous activation of ankle flexor and extensors, in paired large and small amplitude bursts (Figure 5.11D). This result is consistent with our *in vitro* observations that most $FoxP1^{MN\Delta}$ motor neurons fire in the flexor phase while a small minority fire in extensor phase, and that both motor neuron types innervate each of the muscle groups we injected. That is, every muscle would receive strong input during the flexor phase, and much weaker input during the extensor phase, leading to both large and small activity peaks during each locomotor cycle.

Though the undulatory nature of the locomotor behavior in $FoxP1^{MN\Delta}$ mice was to some extent reminiscent of undulatory swimming, it was also idiosyncratic. We hesitate to assert that this phenotype may be directly related to the motor neuron activation patterns we observed in $FoxP1^{MN\Delta}$ preparations because of the possibility that the undulation reflects a behavioral compensation driven by descending or peripheral input that combats the loss of proper spinal locomotor patterning. Nevertheless, the similarity between our *in vitro* results and those observed by [Sürmeli et al., 2011] suggests that the dominance of the flexor pattern may persist under adult, *in vivo* conditions.

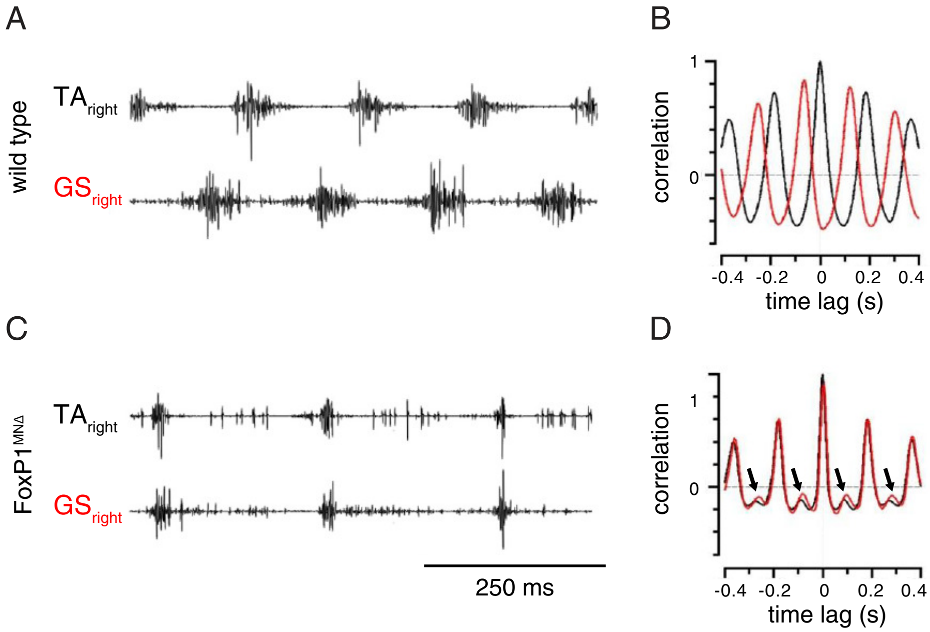

Figure 5.11: **Behavior of $FoxP1^{MN\Delta}$ mice *in vivo***

(A,C) EMG recordings from right ankle flexor (tibialis anterior, TA) and right ankle extensor (gastrocnemius, GS) muscles from wild type and $FoxP1^{MN\Delta}$ mice during swimming. (B,D) Autocorrelograms of muscle burst patterns of right TA with itself (black), and right GS (red) in wild type and $FoxP1^{MN\Delta}$ mice. Arrows denote secondary peaks of activity in autocorrelogram. Adapted from [Sürmeli et al., 2011].

5.3.2 The recognition of flexor and extensor motor neurons

What explains the finding that essentially all limb-innervating motor neurons fire in a flexor-like pattern after $FoxP1^{MN\Delta}$-mediated reversion of motor neuron identity? One possibility is that LMC neurons have an active role in the differentiation or function of pattern-generating circuits (Figure 5.12, middle panel). The reversion of motor neuron identity may undermine the formation of extensor circuits, leaving, by default, a monophasic flexor system. Mechanistically, LMC neurons could be the source of a secreted signal that instructs the assembly of extensor circuits. In fact there is precedent for the secretion by LMC motor neurons of a signal, retinoic acid, which drives the diversification of limb-innervating motor neurons [Sockanathan & Jessell, 1998]. Alternatively, synaptic feedback from LMC motor neurons may be necessary for extensor pattern generation. Recruitment of Renshaw inhibitory or equivalent excitatory interneurons by motor neuron axon collaterals might influence ongoing interneuron network activity [Alvarez & Fyffe, 2007; Machacek & Hochman, 2006; ODonovan et al., 2010].

A second scenario is suggested by the apparent ability of premotor interneurons to discriminate flexor and extensor motor neurons (Figure 5.12, right panel). The ancestral similarity of flexor LMC and HMC motor neurons may lead to the expression of shared surface recognition features on these two motor neuron classes, permitting flexor but not extensor premotor interneurons to form connections with ancestrally-reverted motor neurons. In this view, normal premotor activity would be preserved in $FoxP1^{MN\Delta}$ spinal cord, but extensor premotor interneurons would fail to recognize HMC-like motor neurons. The finding that a small minority of motor neurons with extensor-like firing are still present indicates that extensor premotor circuits are at least in part preserved. Moreover, the scattered distribution of the few extensor-tuned motor neurons in $FoxP1^{MN\Delta}$ preparations implies that premotor interneurons are able to select individual target motor neurons with precision.

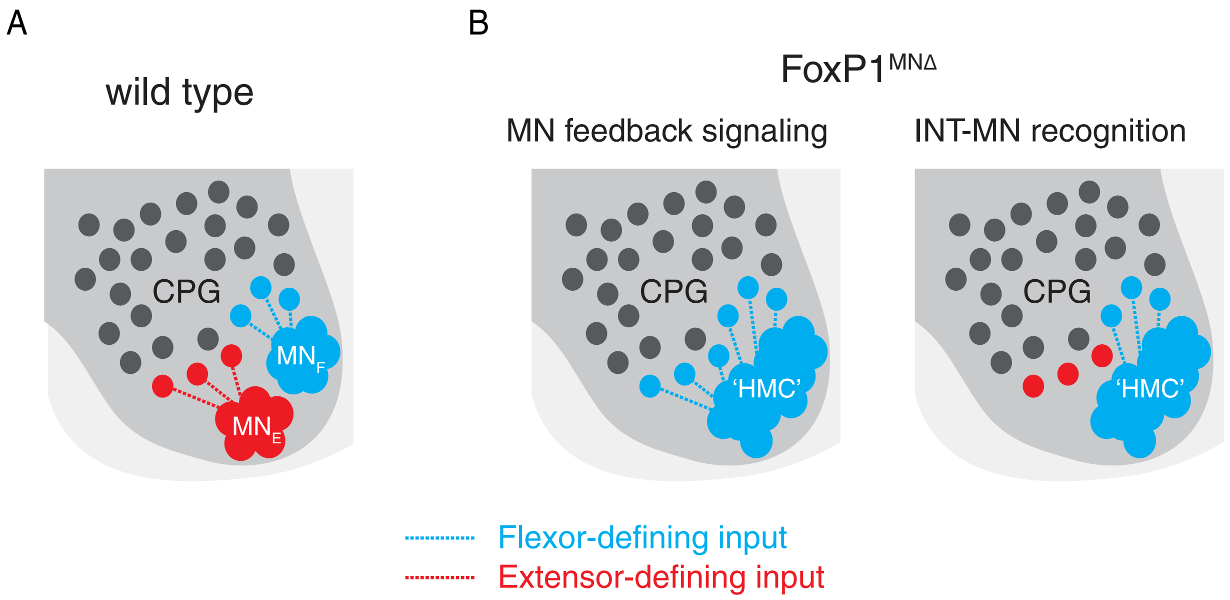

Figure 5.12: **Motor neuron recognition in wild type and $FoxP1^{MN\Delta}$ mice** (A) Interneuron-motor neuron connectivity in wild type circuits. (B) Two possibilities to explain the dominance of flexor firing in $FoxP1^{MN\Delta}$ mice. Left: Modified interneuron identity or activity. Right: Modified interneuron-motor neuron connectivity.

5.3.3 The evolutionary primacy of flexor pattern generation

Whether extensor pattern generation is diminished or HMC-like motor neurons recruit only flexor interneuronal input, the prevalence of flexor firing in $FoxP1^{MN\Delta}$ preparations provides strong support for the evolutionary primacy of flexor pattern generation. In mammals the phasic continuity evident between limb flexor and thoracic ventral root activity, and the similarity between wave-like patterns in mammalian thoracic and primitive vertebrate motor output, are consistent with the idea that flexor pattern generation emerged by co-opting a primitive swim circuit. This implies that paired flexor and extensor patterns did not emerge jointly at the evolutionary onset of limb-based locomotion. In the direct ancestors of tetrapods, the extensor system may have evolved as a later elaboration of spinal circuitry, to promote ground repulsion through limb extension.

That the basic organization of modern flexor circuits predates the evolutionary emergence of extensor circuits further implies that the generation of flexor-like pattern can occur without opponent input from extensor premotor circuits. This view concurs with the subordinate nature of extensor pattern generation suggested by certain observations. Notably, locomotor firing in mice and cats is subject to brief and sporadic periods of quiescence, termed ‘deletions’, that persist for several cycles. Flexor burst deletions are accompanied by a corresponding period of tonic extensor motor neuron firing, whereas flexor motor neuron bursting continues unabated during extensor burst deletions [Duysens, 1977; Duysens, 2006; Zhong et al., 2012]. Other studies have suggested that the rhythm of locomotor firing is directed by populations of interneurons that burst exclusively in flexor phase and in turn drive pattern forming circuits [Brownstone & Wilson, 2008; Pearson & Duysens, 1976], which could at least partly explain how flexor dominance is imposed. Taken together with our findings, these results suggest that the late addition of extensor pattern, coupled with the need for flexor-extensor coordination, led to an asymmetric dependence in pattern generating circuits, with flexor circuits having a dominant role.

Locomotor firing persists after the loss of any single cardinal interneuron population ([Lanuza et al., 2004; Gosgnach et al., 2006; Crone et al., 2008; Zhang et al., 2008]; also shown in Figure 1.5), suggesting that the generation of locomotor firing may be achieved through a diverse array of interneuron network architectures. Moreover, modeling studies have shown that locomotor-like activity patterns can be read out from neural networks permitted considerable flexibility in their connectivity, as long as the network outputs are weighted appropriately [Sussillo & Abbott, 2009]. In this context, and with a new emphasis on motor neuron recognition, it is conceivable that interneuronal connectivity is only weakly constrained, whereas output connections with motor synergy groups are precisely specified.

6

Functionally defining premotor interneuron circuits

6.1 Introduction

In the data presented in previous chapters, we found striking diversity in locomotor firing that went beyond simple flexor-extensor alternation in wild type mice. Our analysis of $FoxP1^{MN\Delta}$ mice revealed that motor neuron subtype identity was necessary for the emergence of appropriate locomotor firing patterns. One interpretation of this result is that interneurons identify their post-synaptic motor neuron targets on the basis of their pool-specific gene expression patterns. Therefore homogenizing motor neuron identity recruits homogenous patterns of premotor input. This idea implies that there are distinguishable sets of interneurons that each have different motor pool preferences.

In order to look for such functional diversity in the premotor interneuron network, we developed methods for characterizing the activity arising from axons of a subset of inhibitory spinal interneurons (those derived from the $En1^+$ V1 domain) surrounding flexor versus extensor motor neuron pools. These experiments are also designed to test another prediction implied by most models of locomotor circuits: that motor neurons should receive inhibition exclusively in a reciprocal phase to their firing pattern [Brown, 1914; McCrea & Rybak, 2008; Endo & Kiehn, 2008; Talpalar et al., 2011]. That is, unless uncharacterized non-reciprocal inhibitory interneurons play a significant role during locomotion [Brownstone & Bui, 2010], flexor motor neurons should receive inhibition only in the extensor phase, and vice versa.

6.1.1 The functional organization of spinal interneurons is unknown

Before we present our approach towards the measurement interneuronal firing, let us first review what is already known about the activity of spinal interneurons during locomotor activity. In the introduction we considered the development of spinal interneuron circuits from four domains of progenitor cells, termed V0-V3. We also considered previous genetic perturbation studies that examined the effect on locomotor firing of removing each neuronal lineage (see Figure 1.5). These perturbation experiments were difficult to interpret, in part, due to the fact that the ventral root recording assay is intrinsically low dimensional, but also because there is not thought to be a clear one-to-one mapping between the V0-V3 domains and functional elements of locomotor circuits.

In recent years, monosynaptic rabies tracing has been presented as a means of identifying a set of functionally related interneurons for study: those that share common motor pool targets [Tripodi et al., 2011]. In brief, monosynaptic rabies tracing requires the injection of two viral vectors into a muscle of interest: a replication-deficient rabies vector carrying the gene for a fluorescent protein, and a second “helper virus” that expresses the rabies glycoprotein gene. After muscle injection, both the rabies virus and the helper virus infect a fraction of the motor neurons innervating the injected muscle. However, because the retrograde spread of rabies infection is dependent on the presence of the glycoprotein gene delivered by the helper virus, the modified rabies virus can jump to presynaptic interneurons only one time (here we will refer to these last-order premotor interneurons as simply "premotor interneurons"). Despite some technical complications with this approach [Zampieri et al., 2014], a number of papers have used this approach to at least coarsely map the spatial distribution of spinal interneurons that share common motor pool targets (Figure 6.1; [Tripodi et al., 2011; Goetz et al., 2015]).

This approach revealed that limb-innervating motor pools each receive input from broad, largely overlapping, spatial distributions of interneurons that span many spinal segments. The differences seen in the spatial extent of pre-flexor versus pre-extensor interneuron distributions were mostly seen in the dorsomedial cord—presumably reflecting differential sensory inputs [Tripodi et al., 2011]. In contrast to limb-innervating pools, epaxial (MMC) and hypaxial (HMC) motor pools receive differential amounts of contralateral interneuron input [Goetz et al., 2015]. Importantly, the spatial distribution of inhibitory premotor interneurons was shown to look nearly identical to the distribution of all premotor interneurons. Together, these findings reveal the distributed, overlapping nature of premotor interneuron populations that are presumably involved in different functions during motor behavior.

Given that interneurons monosynaptically connected to different pools appear to be intermingled with other ventral interneurons, what is known about the activity of spinal interneurons during locomotor firing? A series of recent papers used two-photon Ca^{2+} imaging to examine the phase tuning of interneuron somata present at rostral lumbar segments in isolated mouse spinal cord preparations across small spatial scales (Figure 6.2; [Kwan et al., 2009; Kwan et al., 2010]). These experiments revealed a flexor bias in the phase tuning of most interneurons (perhaps owing to the rostral position of the imaging measurements), as well as a lack of spatial microstructure in these firing patterns (Figure 6.2A-D). Importantly, when analysis was restricted to only genetically defined subsets of interneurons known to be excitatory, the flexor bias in phase tuning was still apparent (Figure 6.2E). These results showing that a flexor-like pattern is stronger than an extensor-like pattern are consistent with extracellular recording data obtained from decerebrate cats [Cuellar et al., 2009] and isolated rat spinal cord preparations [Tresch & Kiehn, 1999].

In the context of these results, we are prompted to ask two questions: are the inhibitory interneurons in this region firing in an antiphase pattern, as would be predicted by half-center models? And are the firing patterns of the interneurons that are monosynaptically connected to motor neurons different?

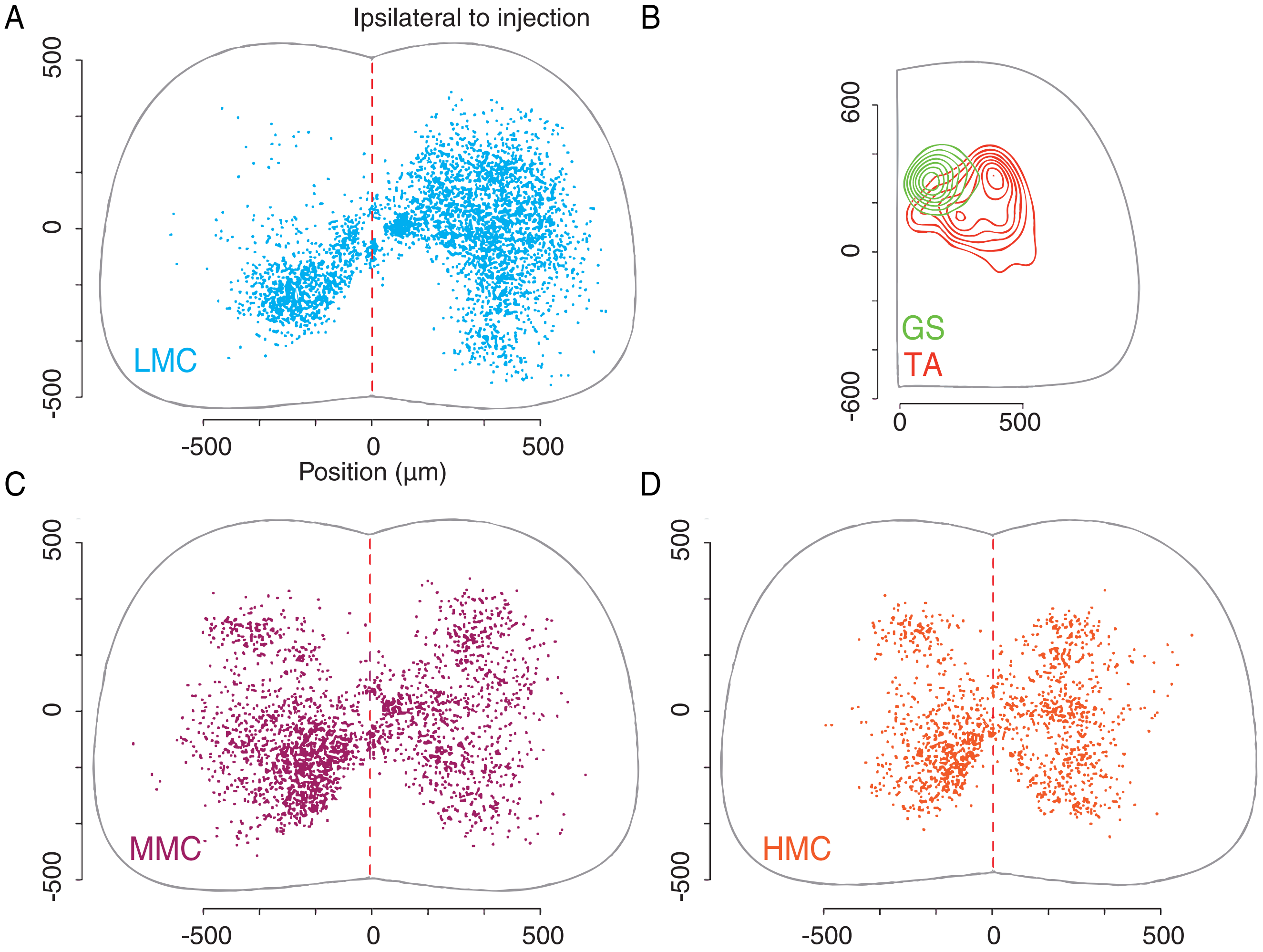

Figure 6.1: **Spatial distributions of interneurons that are presynaptic to different types of motor neurons**

(A) Spatial distribution of interneurons that are monosynaptically connected to quadriceps motor neurons after muscle injection of rabies virus into the quadriceps muscle (knee extensor). (B) Contour map showing a mediolateral separation in the spatial distribution of interneurons that are presynaptic to the gastrocnemius (GS; extensor) and tibialis anterior muscles (TA; ankle flexor). (C-D) Distribution of interneurons that are presynaptic to dorsal epaxial (MMC; panel C) or ventral hypaxial motor neurons (HMC). In each panel, the right hand side is ipsilateral to the muscle that was injected with rabies virus. Panels A,C, and D from [Goetz et al., 2015]. Panel B adapted from [Tripodi et al., 2011].

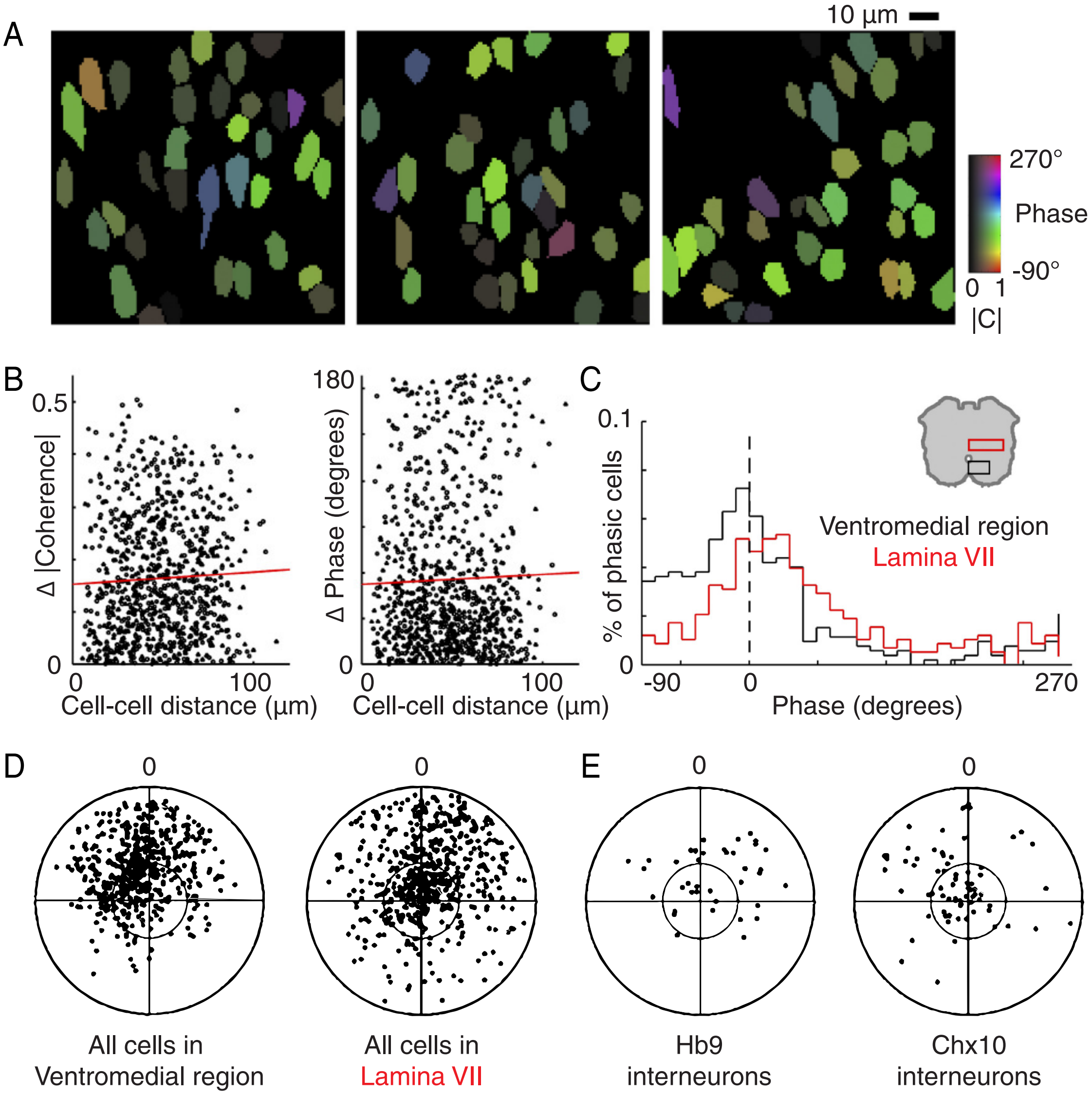

Figure 6.2: **The firing of spinal interneurons is not organized with respect to space at fine spatial scales**

(A) Phase tuning of ventral spinal interneurons of unknown genetic provenance measured in three different spinal cord preparations. (B) Phase tuning preference and strength (coherence with respect to ventral root L2) do not correlate with cell-cell distance. (C-D) Phase tuning distributions for imaged spinal interneurons with respect to ventral root L2. (E) Phase tuning distributions for identified excitatory interneurons belonging to either the Hb9 or Chx10 (V2a) populations. Figure adapted from [Kwan et al., 2010].

6.1.2 En1-derived inhibitory interneurons are heterogeneous and spatially organized

In contrast to the evidence just discussed arguing that functional subnetworks are highly intermingled within spinal locomotor circuits, recent work from Jay Bikoff in the Jessell laboratory indicates the presence of a high degree of diversity in the genetic identity of En1-derived V1 inhibitory interneurons. Specifically, a microarray screen designed to find transcription factors that were specifically enriched in V1 interneurons revealed a number of genes that were expressed in only spatially restricted subsets of the parental V1/$En1^+$ population (Figure 6.3). While the functional consequences of this result are not yet clear, it alone begs the question of whether functionally distinct spinal interneuron microcircuits are organized across space. If this were true, biases in activity during locomotor firing might be observable, even in isolated preparations.

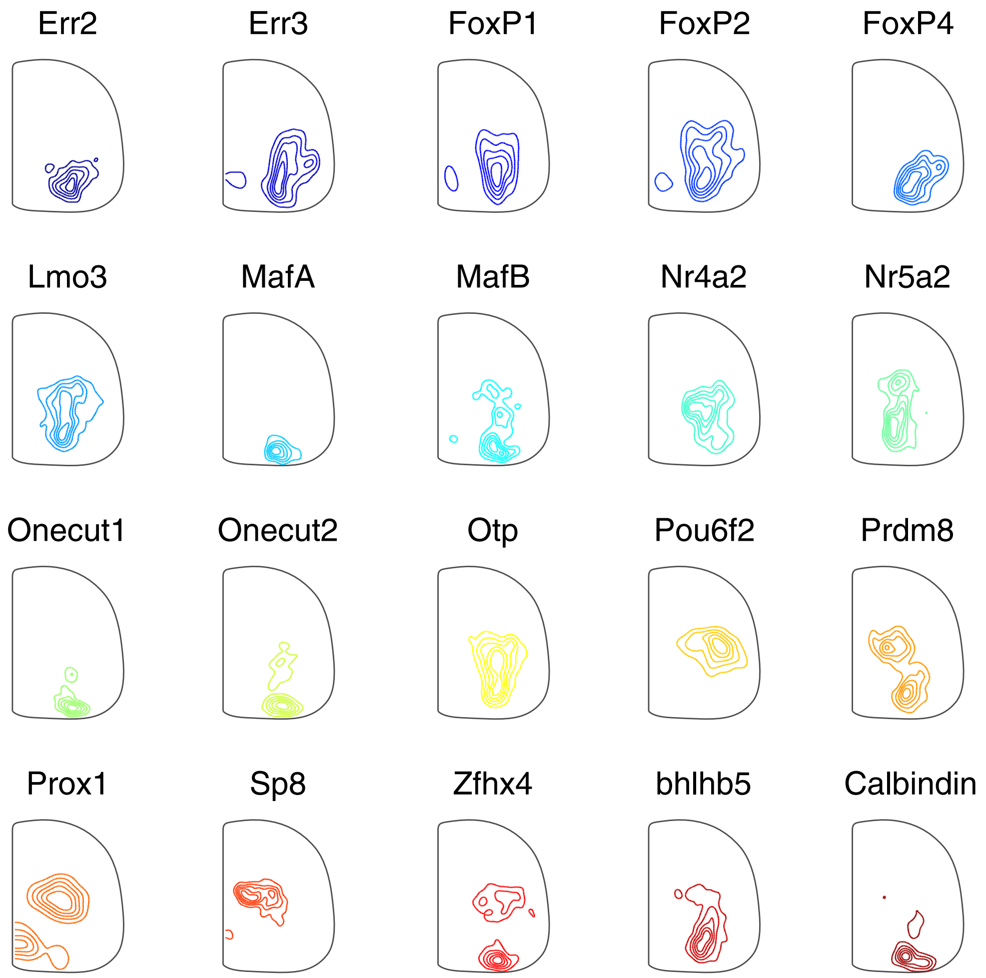

Figure 6.3: **En1-derived inhibitory interneurons are heterogeneous and spatially organized**

Spatial distributions of En1-derived inhibitory interneurons at postnatal day 0. Each panel represents the spatial distribution of lumbar interneurons expressing both the transcription factor En1 and the gene indicated. Data provided by Jay Bikoff from the Jessell Laboratory.

6.1.3 Premotor interneuron activity must be measured with respect to pool target

New work towards elucidating the architecture of spinal motor circuits must contend with two issues. First, as we saw in the monosynaptic rabies tracing data, even functionally unrelated interneurons that have antagonist motor pool targets are positioned in largely overlapping spatial distributions. Second, spinal locomotor circuits are highly redundant and distributed. This has been appreciated by dozens of papers, perhaps most notably [Kjaerulff & Kiehn, 1996]. However, in the past year two studies revealed that even thoracic networks appear to be involved in locomotor firing.

The first of these studies recorded intracellularly from motor neurons positioned at mid-thoracic segment T7 during drug induced fictive locomotion [Beliez et al., 2015]. Importantly, application of the rhythmogenic agonists was restricted to lumbar segments by creating a barrier between lumbar and thoracic segments that restricted the rostral diffusion of drugs. Nevertheless, robust oscillatory firing was observed in intracellularly recorded motor neurons, suggesting that lumbar locomotor circuits provided ascending rhythmic drive to thoracic segments (Figure 6.4A).

Consistent with these observations, a second study measured the locomotor firing of interneurons at thoracic segments in an *ex vivo* turtle carapace-spinal cord preparation [Guzulaitis et al., 2014]. Because thoracic segments reside inside the turtle's shell where there is no musculature, no motor neurons are present. Surprisingly, interneurons at thoracic segments were robustly active during fictive scratching behavior—and they fired in phase with ipsilateral flexor muscles (Figure 6.4B).

Together, these new observations underscore the fact that interneuron activity must be measured with respect to motor pool target. It seems likely that the "last order" interneurons are spatially intermingled with all other locomotor-related interneurons. Because of this possibility that there is a lack of spatial structure in interneuron activity, and because rhythmogenic drugs might induce firing in interneurons that do not even normally fire during locomotor tasks [Brocard et al., 2013], we developed a new approach for measuring interneuron activity with respect to motor pool target, and found activity patterns that are inconsistent with a push-pull scheme for controlling motor neuron firing.

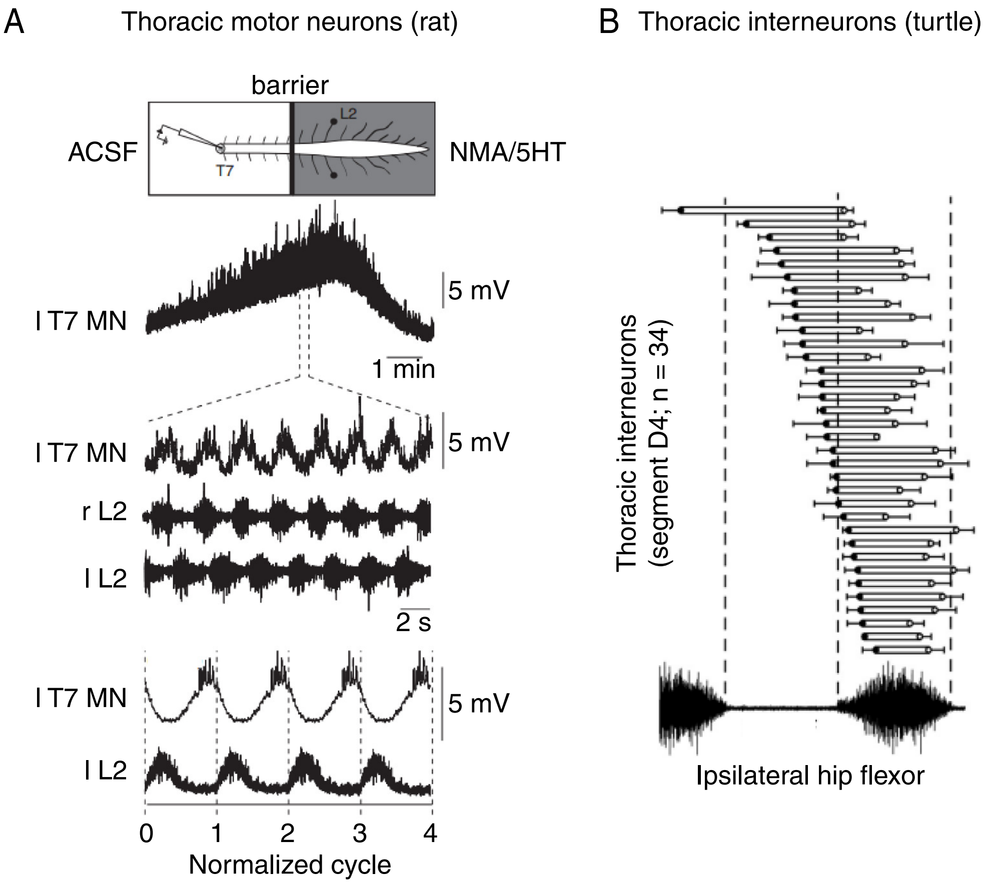

Figure 6.4: **Thoracic neurons are phasically active during rhythmic limb movements**

(A) Intracellular recording from a thoracic motor neuron (from segment T7) in an isolated neonatal rat spinal cord preparation where rhythmogenic drugs have been applied solely to the lumbar segments. These observations indicate the presence of ascending connections from lumbar locomotor circuits to thoracic motor neurons. (B) Intracellular recordings reveal the cycle-averaged firing of 34 thoracic spinal interneurons (from segment D4) in a turtle carapace-spinal cord preparation during fictive scratching behavior. Importantly, thoracic neurons were rhythmically active despite the lack of any motor neurons at those segments in the turtle. Panel A adapted from [Beliez et al., 2015]. Panel B adapted from [Guzulaitis et al., 2014].

6.1.4 Controlling the firing of motor neurons with different patterns of presynaptic input

Let us now consider the different strategies by which presynaptic input can drive a motor neuron to fire in a periodic bursting pattern that are schematized in Figure 6.5A. As we considered earlier, half-center models dating back to [Brown, 1914] argue that reciprocal patterns of excitation and inhibition are responsible for the membrane potential dynamics observed in motor neurons during rhythmic motor behaviors (see the fourth trace in Figure 6.5A). Recently, a series of papers [Endo & Kiehn, 2008; Petersen et al., 2014; Berg et al., 2007] has applied conductance decomposition techniques to intracellular recording data obtained from motor neurons to try and infer patterns of presynaptic input and thus test which of the four strategies might be used rhythmic motor firing.

In [Petersen et al., 2014] and [Berg et al., 2007], intracellular recordings were obtained from motor neurons in the turtle during tactile-induced shell scratching behavior. During this rhythmic locomotor activity, their measurements of synaptic input onto motor neurons revealed striking periods of concurrent excitatory and inhibitory input—in conflict with traditional half-center like models (Figure 6.5A-C). When similar methods were applied to the drug-induced isolated neonatal mouse spinal cord preparation, a very different result was observed: reciprocal patterns of excitation and inhibition (Figure 6.5D; [Endo & Kiehn, 2008]). Additionally, an asymmetry was seen between flexor and extensor motor neurons. Inhibitory inputs appeared to be much stronger than excitatory inputs onto extensor motor neurons (akin to the "inhibition driven" scenario in 6.5A). A similar result was not seen in flexor motor neurons. The differences between these two studies has been largely interpreted as evidence that the [Berg et al., 2007] findings do not hold in mice and other mammals [Grillner & Jessell, 2009].

But there are also technical reasons suggesting that perhaps the two circuits might actually behave similarly, despite the evidence to the contrary. First, standard methods for conductance decomposition ([Monier et al., 2008]) depend on the assumption that the total input to the neuron consists of three components: excitatory, inhibitory, and constant leak conductances. Owing to the fact that motor neurons are very large and not at all electrotonically compact, it is unlikely that an injected holding current (or command potential in voltage-clamp mode) will actually have an effect over the entire spatial extent of the neuron ([Spruston et al., 1993; Williams & Mitchell, 2008], Carl Schoonover, personal communication). Therefore, the assumption of constant leak conductance over time is unlikely to be true under all circumstances. Second, it has been observed that the presence of gap junctions can confound conductance decomposition analysis [Berg & Ditlevsen, 2013]. This is significant because in the P0-P4 age range where the [Endo & Kiehn, 2008] experiments were conducted, it is known that strong coupling exists between motor neurons [Personius et al., 2007]. On the other hand, some elements of the findings from [Endo & Kiehn, 2008], particularly the differences seen between flexor and extensor motor neurons, warrant further consideration. [Berg et al., 2007] and [Petersen et al., 2014] only investigated the inputs onto flexor motor neurons in their preparation. It is therefore possible that the flexor-extensor asymmetry observed in [Endo & Kiehn, 2008] holds in turtles and that antiphase inhibition plays a more dominant role in controlling the firing of turtle extensor motor neurons.

In addition, the turtle and mouse studies are in agreement in another respect: both [Petersen et al., 2014] and [Endo & Kiehn, 2008], provide evidence that reciprocal inhibition is present in their preparation (Figure 6.5C,E). Indeed, the idea that reciprocal “push-pull” inhibition could give rise to alternating patterns of motor firing is not controversial. The outstanding question is not whether reciprocal inhibition is sufficient, but rather we would like to know what control scheme is actually dominant during normal motor behaviors. In this chapter, we will address this question by first enumerating the types of inhibitory interneuron firing patterns across the lumbar spinal cord, and then examine which patterns appear in the inhibitory interneuron processes that surround flexor and extensor motor pools.

In this chapter, we will present two novel approaches for addressing these questions using Ca^{2+} imaging: a wide-field imaging assay, and an approach for imaging the axons of interneurons surrounding identified motor neuron pools. But first, we must make a note of caution: the conclusions presented in this chapter should be interpreted as more preliminary than the others presented in this thesis. Nevertheless, we found that in contrast to our hypothesis, inhibitory interneuron activity does not dramatically change in areas of neuropil surrounding flexor versus extensor motor pools. Additionally, the activity of interneurons surrounding flexor motor neurons looks mostly flexor-like—not exclusively extensor-like as predicted.

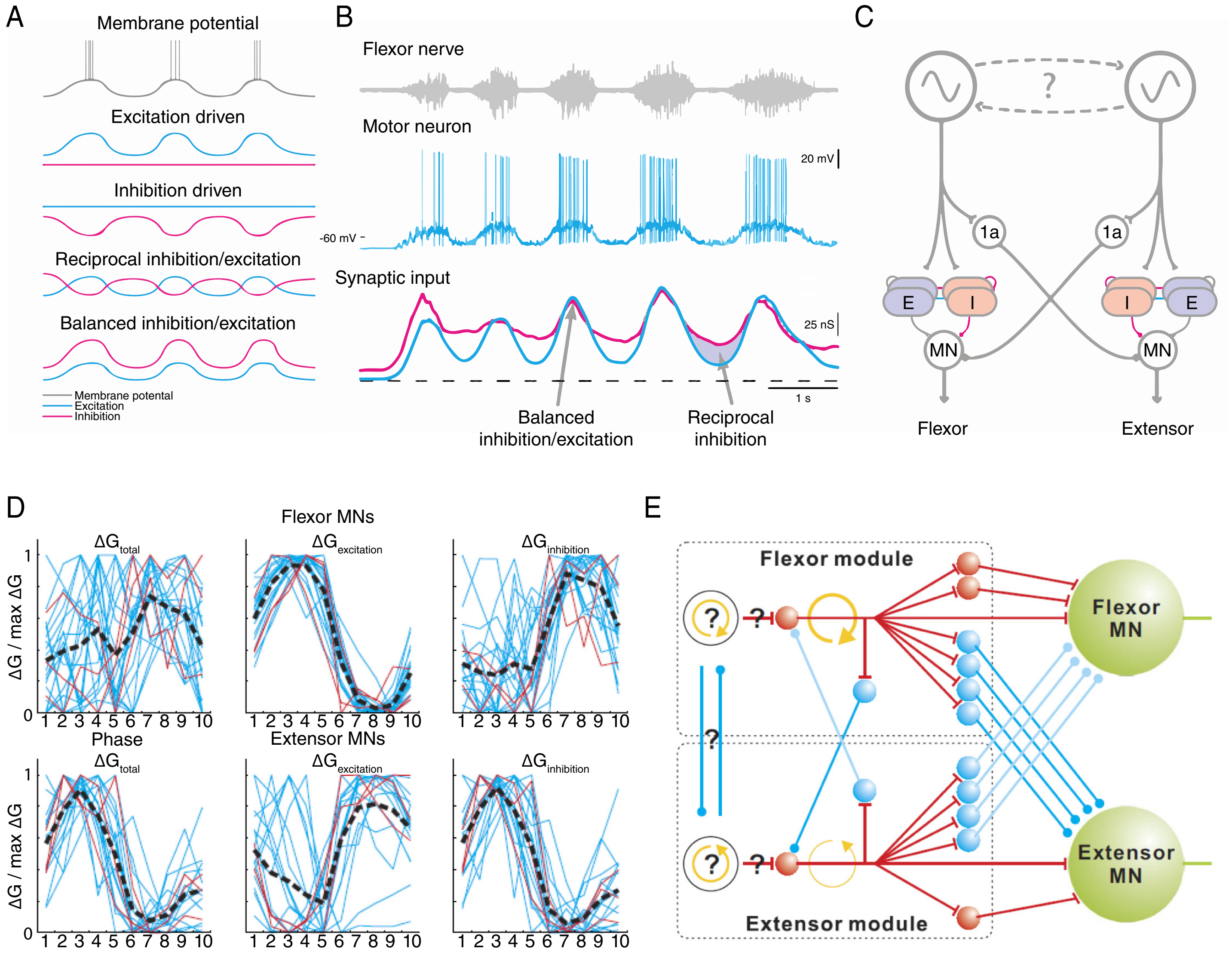
A
Membrane potential
Excitation driven
Inhibition driven
Reciprocal inhibition/excitation
Balanced inhibition/excitation
Membrane potential
Excitation
Inhibition
B
Flexor nerve
Motor neuron
20 mV
-60 mV
Synaptic input
25 nS
1 s
Balanced inhibition/excitation
Reciprocal inhibition
C
?
1a
1a
E
I
I
E
MN
MN
Flexor
Extensor
D
Flexor MNs
ΔG total
ΔG excitation
ΔG inhibition
ΔG / max ΔG
1
0
1 2 3 4 5 6 7 8 9 10
Phase
Extensor MNs
ΔG total
ΔG excitation
ΔG inhibition
ΔG / max ΔG
1
0
1 2 3 4 5 6 7 8 9 10
E
Flexor module
?
?
?
Flexor MN
Extensor MN
Extensor module

Figure 6.5 *(preceding page)*: **Different patterns of presynaptic input could underlie motor neuron firing during locomotion**

(A) Four possible strategies for producing a periodic membrane potential (top) with different combinations of excitatory (blue) and inhibitory (red) input. (B) Conductance decomposition performed on an intracellular recording taken from a turtle flexor motor neuron during tactile induced scratching behavior (nerve activity in gray, top; motor neuron activity in blue, middle; conductance decomposition shown on bottom to show inferred presynaptic input). (C) Model illustrating possible circuit basis for observations shown in (B). (D) Results from applying conductance decomposition methods to data obtained from mouse flexor (top row) and extensor (bottom row) motor neurons. The left panel shows the normalized time course of conductance changes over a step cycle (dotted line = mean, solid lines = individual motor neurons). The step cycle has been discretized into 10 bins: the first 5 bins correspond to the time of flexor motor neuron firing, the second 5 bins to extensor firing. The middle panel shows only the normalized time course of excitatory conductances. The right panel shows the normalized time course of inhibitory conductances. (E) Model presented to explain data shown in (D). Panels A-C adapted from [Petersen et al., 2014]. Panels D-E adapted from [Endo & Kiehn, 2008].

6.2 Results

6.2.1 A wide-field imaging approach for quantifying locomotor pattern complexity

We first set out to enumerate the dominant patterns of En1-derived inhibitory interneuron activity present in the ventral spinal cord. Because of the distributed nature of locomotor circuits, the relevant networks span cubic millimeters of space. Because of this fact, and due to small relative size of interneuron somata, we decided to first develop a wide-field imaging assay to measure the dominant activity patterns that might exist within inhibitory interneurons across the ventrolateral spinal cord.

In the next section, we will use wide-field epifluorescence microscopy to examine isolated spinal cord preparations that express the Ca^{2+} indicator GCaMP6F selectively in En1-derived interneurons. Because of a lack of optical sectioning ability, and due to the low magnification of the objective used (4x), this technique cannot reveal the activity of individual neurons. However, we can simultaneously monitor neural activity across imaging fields that are approximately 2 mm^2 in size. By computing the phase tuning for individual pixels, that are each likely contain multiple neurons we can derive large-scale, but low-resolution, maps of locomotor firing activity across nearly the whole lumbar cord from single imaging fields. We can also apply non-negative matrix factorization (NMF) algorithms to these data in order to decompose them into multiple spatially-distinct components and thus reveal the types of locomotor firing patterns that seem to predominate in the activity present in the inhibitory network. This large-scale approach will let us assess the heterogeneity of firing pattern across space in a reasonably unbiased way, such that we can appropriately focus our high-resolution imaging efforts on areas of interest.

To first demonstrate the efficacy of this approach, we have applied it to wide-field imaging data obtained from a ChAT::Cre; ROSA::GCaMP3 mouse with retrogradely labeled quadriceps (Q) and intrinsic foot (IF) synergist groups (Figure 6.6A). By examining the phase tuning of individual pixels within this data, we can produce a phase map that clearly resembles that seen in our two-photon imaging data (Figure 6.6B-C). Importantly, adjacent pixels tend to share similar phase tunings and regions known to contain superficially positioned flexor or extensor motor neurons appear to fire as expected. However, regions that contain multiple motor pools with different tunings (see the middle of panel Figure 6.6B) appear less smooth. This is likely because the average phase tuning of a pixel that contains many neurons with multiple phase tunings cannot be well-described by a single value.

To overcome this limitation of our phase maps, we can apply NMF in order to try and decompose the whole dataset into a linear combination of time-varying activity patterns, and spatial weights corresponding to the pixels where each activity pattern resides. Based on our analysis of motor neuron firing in isolated preparations, such an approach should reveal three dominant patterns: a flexor-like pattern, a phase-lagged foot-like pattern, and an antiphase extensor-like pattern. As a sanity check that our approach is working, the spatial footprints of each of these activity vectors should correspond to the known anatomical position of flexor, extensor, and foot motor pools. Importantly, because both the spatial and temporal patterns extracted by NMF are constrained to be positive, pairs of patterns cannot cancel each other out and can therefore be interpreted independently.

The results from this analysis can be seen in Figure 6.6D-G. By applying NMF to the data (k components = 5, 3 components shown, MATLAB function *nmfnnls* from [Li & Ngom, 2013]), we were able to extract three spatially distinct sets of pixels corresponding to the three temporal patterns shown in panel G. NMF 1 resembles a flexor-like pattern, NMF 2 resembles late-flexor/foot-like activity, and NMF 3 is an extensor-like pattern. The two components that were not shown are more difficult to interpret and appeared to resemble mixtures of firing signals and baseline fluorescence drift. We examined the residual movie (i.e. data - 5 component NMF reconstruction) and found that it lacked clear spatial or temporal structure, suggesting that $k = 5$ components is sufficient to explain this dataset.

Because we lack cellular resolution in this assay, these results are consistent with intuition. The fact that small pixel weights are imposed on some dorsal regions in NMF 3 (the extensor component) likely reflects contributions from deep, medially positioned extensor motor pools that were too deep to resolve with cellular resolution in our two-photon assay.

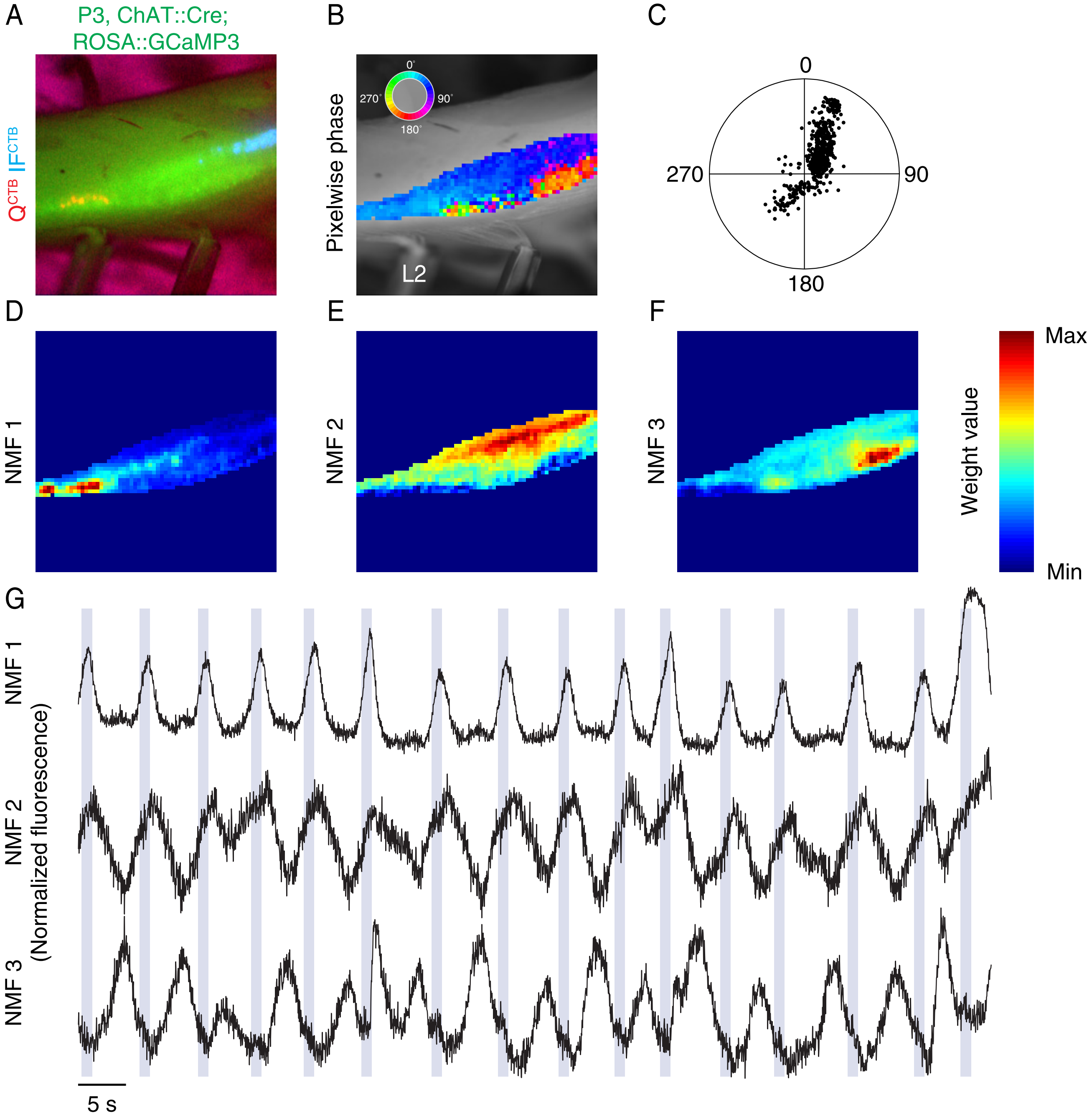
A
P3, ChAT::Cre;
ROSA::GCaMP3
QCTB IFCTB
B
Pixelwise phase
0°
270°
90°
180°
L2
C
0
270
90
180
D
NMF 1
E
NMF 2
F
NMF 3
Max
Weight value
Min
G
NMF 1
NMF 2
NMF 3
(Normalized fluorescence)
5 s

Figure 6.6 *(preceding page)*: **Non-negative matrix factorization reveals pool-like structure in wide-field motor neuron imaging datasets**

(A) Sagittally-oriented mouse spinal cord expressing GCaMP3 (Ai38 reporter)in motor neurons under 4x magnification. Quadriceps (Q) and intrinsic foot (IF) motor neurons were retrogradely labeled with CTB as shown in red and blue, respectively. (B) Phase was computed relative to ventral root L2 peak for all bright green pixels (indicating GCaMP expression). The phase tuning of each pixel is indicated in color and is superimposed on the mean intensity projection of the image time series (imaging rate = 30 Hz). (C) The phase tuning of each pixel is shown in polar space. The radial position of each pixel represents the strength of its tuning. (D-F) The image time series analyzed in (B) was decomposed into 5 components using non-negative matrix factorization (NMF). The weights associated with three NMF components are shown in (D-F). The time series corresponding to each of the NMF components shown is plotted in panel (G) relative to detected L2 bursts (blue bars). The size of the imaging field is 1.95 mm^2.

6.2.2 The large-scale structure of inhibitory interneuron activity

In the context of the motor neuron results, we can now apply this wide-field imaging technique towards the analysis of inhibitory En1 interneuron activity and have confidence that we will be able to successfully describe features of inhibitory interneuron firing across space. We decided to focus on acquiring imaging data in the sagittal plane in order to characterize the kinds of activity we can see in regions surrounding different motor pools. Because GCaMP fluorescence signals can be detected from both neuronal processes as well as somata, fluorescence activity averaged across a CTB-labeled motor pool obtained from a mouse expressing GCaMP solely in inhibitory interneurons is likely to, in part, reflect the activity of interneuronal axons that contact that motor pool (this assumption is validated using two-photon microscopy in Section 6.2.3 of this chapter).

In these experiments, we drove GCaMP6F expression in En1-derived inhibitory interneurons by looking at the progeny arising from En1::Cre mice crossed to either Ai95/ROSA::GCaMP6F or Ai93/TIGRE::GCaMP6F;ROSA::TTA mice obtained from the Allen Institute [Madisen et al., 2015]. Qualitatively similar results were obtained from both mice despite the fact that GCaMP expression was found in only a subset of En1 neurons when using the Ai93 reporter. This is likely a consequence of the fact that the Ai93 reporter is double conditional: GCaMP expression is dependent both the Cre as well as the TTA system. However, reporter expression within GCaMP$^+$ neurons was visibly brighter in Ai93 preparations.

Results from our wide-field imaging assay applied towards the study of En1 neurons (using the Ai93 reporter) can be seen in Figure 6.7A-B. As can be seen from the pixelwise phase map (panels B-C), this preparation displayed striking uniformity in the average phase tuning of individual pixels across lumbar segments. Even in regions on top of the CTB labeled gluteal (G) motor neurons (red), no apparent difference can be seen versus in the more dorsal region containing retrogradely labeled foot motor neurons (IF; blue). Importantly, the phase tuning value that is shared across space appears to correspond to late-flexor phase—the peak value typically seen in foot motor neurons. The results from applying our NMF analysis to the data similarly show a lack of firing pattern diversity. While three spatially distinct components were extracted D-F), in each case, the corresponding activity exhibited periodic activity that appears in phase with the flexor-related L2 ventral root signal (Figure 6.7G). This observation of a dominant flexor-like firing pattern appear at odds with the idea that flexor motor pools should be mostly receiving extensor-like inhibition during locomotor firing.

Largely similar results can be seen in another preparation that was oriented at a slightly different angle such that fluorescence emitted from the most ventrolateral regions of the gray matter can be seen (Figure 6.8A-C). The pixelwise phase map reveals that, much like in the previous figure, most of the ventral spinal cord has peak activity during the flexor phase. However, it appears that a band of pixels in the ventral cord has extensor tuning. To examine this more closely, we can examine three NMF components that were found (Figure 6.8D-F). As suggested by the pixelwise phase tuning map, many of the dorsal pixels can be explained by two flexor-like modes. In contrast, NMF 3 clearly shows a ventrally-positioned extensor component that is positioned where Renshaw cells are known to be located.

Since Renshaw cells are En1-derived interneurons that receive input from motor neurons directly, it would make sense that we would be able to resolve extensor pattern in that region of the cord as we know that extensor motor pools providing input to Renshaw cells reside in those segments. Our hypothesis that this extensor-like pattern actually comes from Renshaw cells is supported by the fact that antidromic stimulation of ventral roots before induction of locomotor firing robustly evoked fluorescence in a similar spatial region (data not shown). This observation of extensor-firing putative Renshaw cells does not help us explain flexor-extensor alternation because Renshaw neurons are known to provide recurrent feedback onto the same motor neurons that provide them input and a pharmacological blockade of their input from motor neurons does not appear to abolish flexor-extensor alternation [Talpalar et al., 2011].

A third example of locomotor firing can be seen in Figure 6.9A-D. The imaging field shown from this preparation is caudal to the other wide-field images shown. The blue IF pool which resides in L5/L6 ends in the region where the spatial footprint of NMF component 3 peaks (Figure 6.9D). While no ventral root data is shown for this preparation, it can be clearly seen that the rostrally positioned NMF components fire synchronously and in short bursts (Figure 6.9B-C). In contrast, NMF component 3 is positioned at segments L6/S1 and fires in an antiphase, broadly-tuned pattern—much like extensor motor neurons.

As a whole, these results are surprisingly inconsistent with the idea that the dominant mode of inhibition is to be active out of phase with motor neuron activity. While we were able to detect extensor-like patterns, we found such patterns in both caudal regions where we expect Renshaw cells to reside, as well as in sacral segments. This flexor bias in inhibitory interneuron activity appears roughly consistent with measurements from identified excitatory interneurons [Kwan et al., 2010]. These observations suggest that excitatory and inhibitory interneuron firing are likely to be highly similar across the spinal network. But what about the subset of interneurons that actually form connections with flexor and extensor motor neurons? To examine this question, we will now use two-photon imaging to measure locomotor firing pattern in inhibitory processes that surround different retrogradely labeled motor pools.

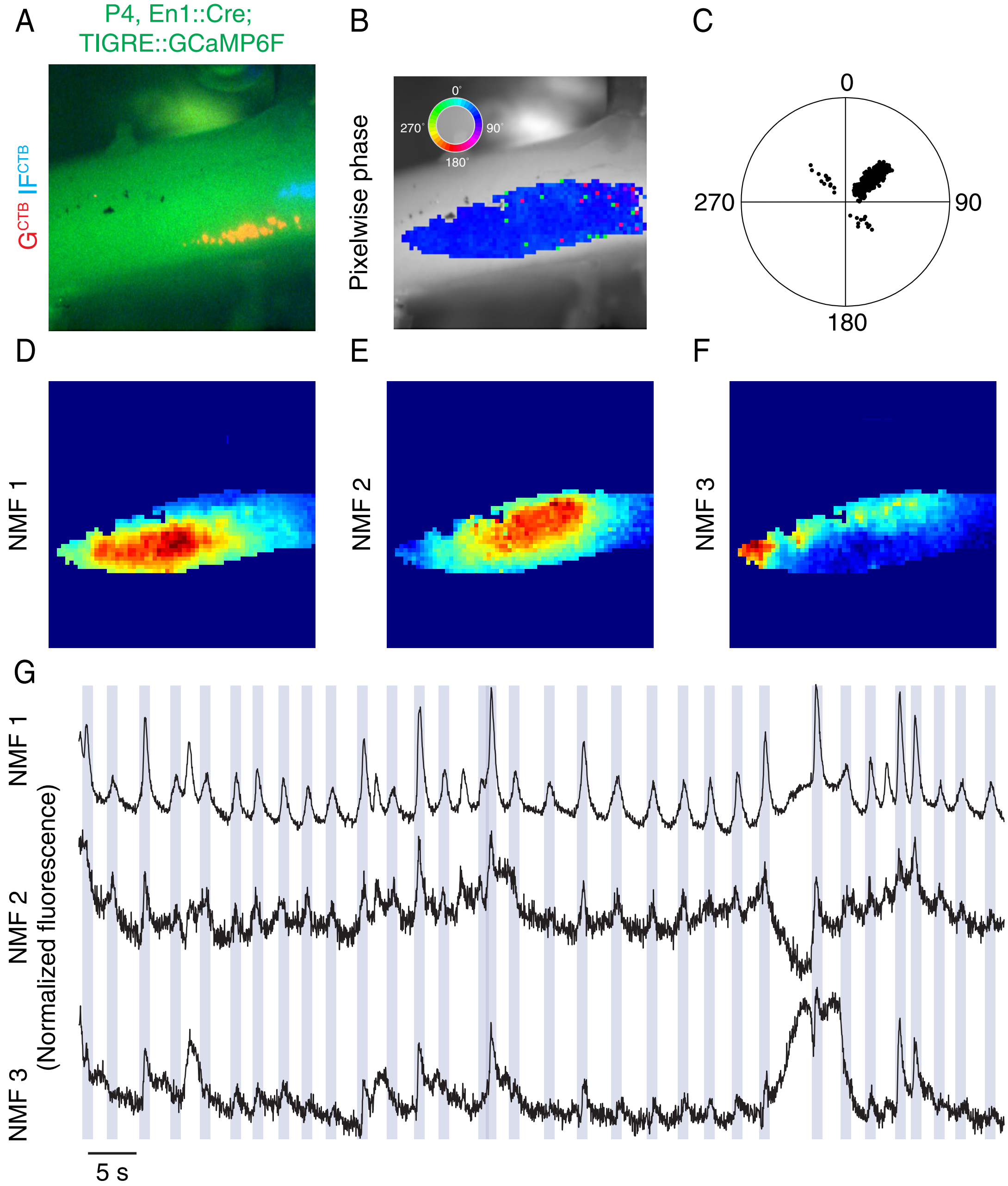
A
P4, En1::Cre;
TIGRE::GCaMP6F
GCTB IFCTB
B
Pixelwise phase
0°
90°
180°
270°
C
0
90
180
270
D
NMF 1
E
NMF 2
F
NMF 3
G
NMF 1
NMF 2
NMF 3
(Normalized fluorescence)
5 s

Figure 6.7 *(preceding page)*: **Homogeneity in En1-derived inhibitory motor neuron activity across lumbar segments**

(A) Sagittally-oriented mouse spinal cord expressing GCaMP6F (Ai93 reporter) in En1-derived V1 inhibitory interneurons under 4x magnification and epifluorescence illumination. Gluteus (G) and intrinsic foot (IF) motor neurons were retrogradely labeled with CTB as shown in red and blue, respectively. (B) Phase was computed relative to ventral root L2 peak for all bright green pixels (indicating GCaMP expression in interneurons). The phase tuning of each pixel is indicated in color and is superimposed on the mean intensity projection of the image time series (imaging rate = 30 Hz). (C) The phase tuning of each pixel is shown in polar space. The radial position of each pixel represents the strength of its tuning. (D-F) The image time series analyzed in (B) was decomposed into 5 components using non-negative matrix factorization (NMF). The weights associated with three NMF components are shown in (D-F). The time series corresponding to each of the NMF components shown is plotted in panel (G) relative to detected L2 bursts (blue bars).

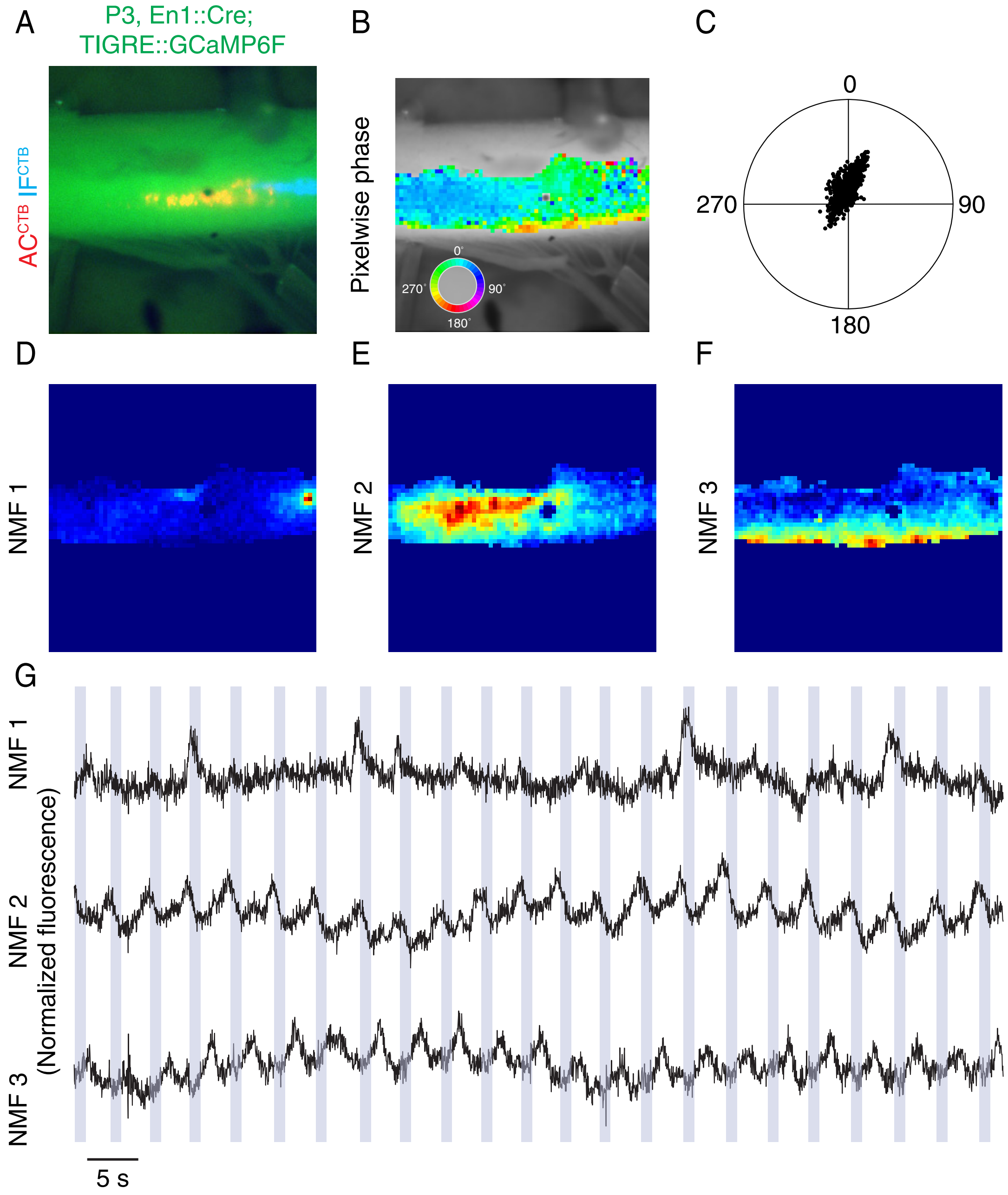
A
P3, En1::Cre;
TIGRE::GCaMP6F
AC^CTB
IF^CTB
B
Pixelwise phase
0°
90°
180°
270°
C
0
90
180
270
D
NMF 1
E
NMF 2
F
NMF 3
G
NMF 1
NMF 2
NMF 3
(Normalized fluorescence)
5 s

Figure 6.8 *(preceding page)*: **Extensor-like activity in putative Renshaw cells** (A) Sagittally-oriented mouse spinal cord expressing GCaMP6F (Ai95 reporter) in En1-derived V1 inhibitory interneurons under 4x magnification and epifluorescence illumination. Gluteus (G) and intrinsic foot (IF) motor neurons were retrogradely labeled with CTB as shown in red and blue, respectively. (B) Phase was computed relative to ventral root L2 peak for all bright green pixels (indicating GCaMP expression in interneurons). The phase tuning of each pixel is indicated in color and is superimposed on the mean intensity projection of the image time series (imaging rate = 30 Hz). (C) The phase tuning of each pixel is shown in polar space. The radial position of each pixel represents the strength of its tuning. (D-F) The image time series analyzed in (B) was decomposed into 10 components using non-negative matrix factorization (NMF). The weights associated with three NMF components are shown in (D-F). The time series corresponding to each of the NMF components shown is plotted in panel (G) relative to detected L2 bursts (blue bars).

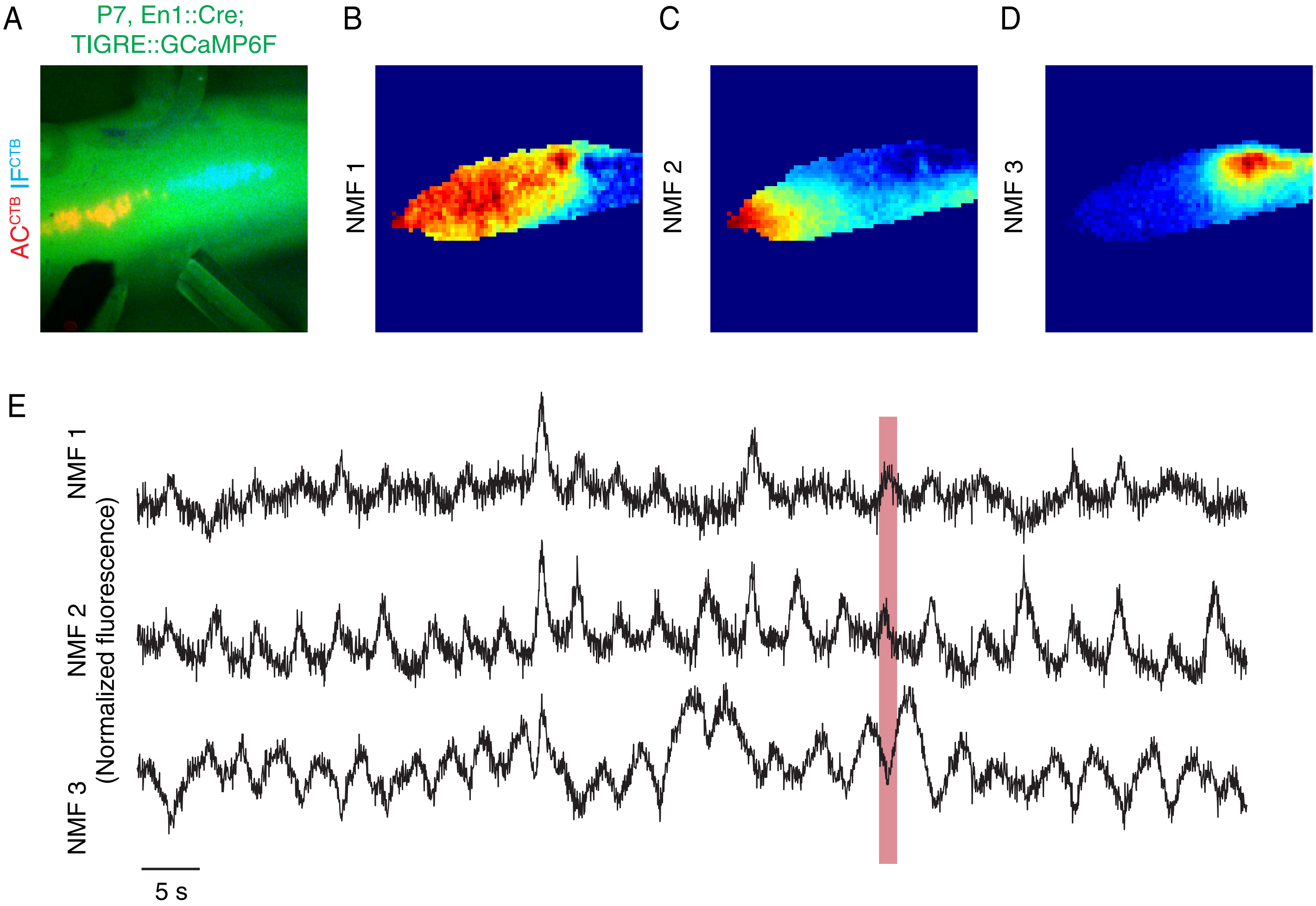

Figure 6.9: **Extensor-dominant activity in rostral sacral segments**

(A) Sagittally-oriented mouse spinal cord expressing GCaMP6F (Ai93 reporter) in En1-derived V1 inhibitory interneurons under 4x magnification and epifluorescence illumination. Gluteus (G) and intrinsic foot (IF) motor neurons were retrogradely labeled with CTB as shown in red and blue, respectively. (B-D) An image time series acquired from the field in (A) at 30 Hz and was decomposed into 5 components using non-negative matrix factorization (NMF). The weights associated with three NMF components are shown in (B-D). The time series corresponding to each of the NMF components shown is plotted in panel (E). Note the more caudal position of this imaging field relative to those shown from previous preparations: it stretches to rostral S1.

6.2.3 The structure of inhibitory interneuron activity as a function of pool target

Our wide-field imaging data revealed a clear asymmetry in the activity of ventrolateral inhibitory interneurons present in lumbar spinal segments. Instead of seeing a mixture of flexor-like and extensor-like patterns, we observed that inhibitory interneuron activity appears to be dominated by a flexor-like firing pattern. However, these data lacked the spatial resolution necessary to determine whether or not this result was the consequence of biased firing in interneuron somata, processes, or both.

In order to address this question, we used two-photon microscopy to examine fluorescent activity arising from interneuron cell bodies and processes that surround CTB-labeled flexor and extensor motor neurons. Example imaging fields taken from two preparations with retrogradely labeled anterior crural motor neurons (AC, ankle flexors) can be seen in Figure 6.10A-B. The panels in the third column of the figure show the pixelwise phase tuning of the most phasically active pixels in each movie with phase tuning denoted in color (peak ventral root L2 activity was defined as 0°). These same tuning values are also represented in the polar plots shown in the fourth column. As can be seen from the first example dataset shown in the top row of the figure, phasic pixels with flexor-like tuning values appear to surround an AC cell body. In contrast, the bottom two rows show that there are interneuron cell bodies surrounding AC motor neurons with both flexor-like and extensor-like tunings.

These results are consistent with our wide-field imaging data: in both cases a clear bias towards flexor-like firing can be seen. While the bias towards flexor activity is not absolute and some pixels with extensor-like tuning were also detected, the fact that we do not see a significant bias in the opposite direction towards antiphase inhibition is inconsistent half-center models. Additionally, this data serves to validate our assumption that some of the wide-field signals that we measured may have arisen from fluorescence fluctuations in neuronal processes verses just somata.

To further illustrate the fact that both flexor and extensor-like signals can be extracted from the inhibitory neuropil surrounding flexor motor neurons, we again applied non-negative matrix factorization. Because we were interested in determining whether a given pixel was active in a flexor-like pattern or an extensor-like pattern we used a constrained NMF algorithm that favored solutions where the spatial footprints of NMF components tended to be sparse (i.e. we encouraged small weights on pixels to be pushed to zero using MATLAB function *sparsenmfnnls* from [Li & Ngom, 2013]; k components = 3). When this approach is applied to an example imaging field obtained from a region surrounding flexor motor neurons, we were able to successfully extract both flexor-like and extensor-like activity modes (Figure 6.11A-F).

We then applied the same NMF analysis to data acquired from a preparation with labeled gluteal motor neurons (G; hip extensor). Half-center models would predict that flexor-like inhibitory inputs would converge on extensor-like motor neurons. In contrast, if the same principle of in phase inhibition seen around flexor motor neurons were to hold, we might expect to see extensor-biased inhibitory activity. As can be seen from Figure 6.11G-J, the pixelwise phase tuning map reveals a broad distribution of phase tunings. However, applying sparse NMF to these data only reveals flexor-like firing patterns, as would be expected from the half-center model and [Endo & Kiehn, 2008].

Together these results from our two-photon imaging assay appear to support the findings we saw in our wide-field imaging assay. Inhibitory interneuron activity appears to be dominated by a flexor-like pattern across the ventrolateral extent of the lumbar spinal cord–even in the regions surrounding flexor and extensor motor pools.

While we cannot rule out the fact that there are strongly different patterns of input onto distal motor neuron dendrites than onto perisomatic regions, our results still appear inconsistent with an exclusively “push-pull” scheme of reciprocal inhibition suggested by half-center models to explain flexor-extensor alternation. Our observations that the types of interneuron firing patterns do not appreciably change as one looks at regions around extensor motor neurons instead of flexor motor neurons might also hint at some asymmetry in the circuit mechanisms for controlling the firing of extensor versus flexor motor neuron firing, as also argued in [Endo & Kiehn, 2008].

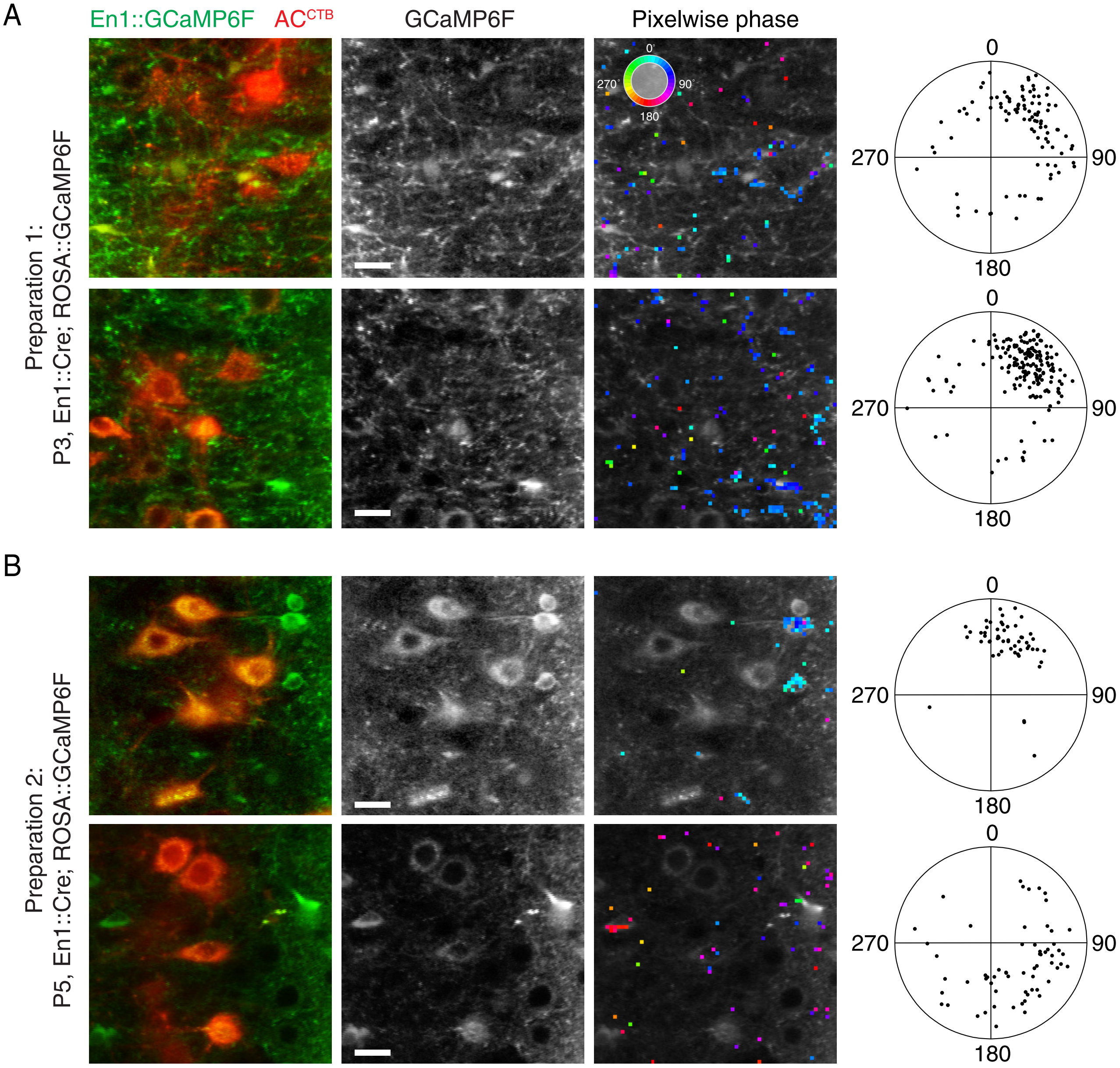
A
En1::GCaMP6F
AC^CTB
GCaMP6F
Pixelwise phase
0°
270°
90°
180°
Preparation 1:
P3, En1::Cre; ROSA::GCaMP6F
0
270
90
180
B
Preparation 2:
P5, En1::Cre; ROSA::GCaMP6F

Figure 6.10 *(preceding page)*: **Flexor-biased inhibitory interneuron activity surrounds flexor motor neuron somata**

(A) Left Panels: Mean intensity projection across two image time sequences acquired from an Ai93 GCaMP6F; En1::Cre spinal cord preparation extracted at postnatal day 3. GCaMP6F (green) can be seen in axons, while retrogradely labeled anterior crural (ankle flexor; AC) motor neurons can be seen in red. Middle panels: Mean intensity projection of only the green GCaMP6F channel. Right Panels: Phase tuning of the most phasic subset of pixels is shown in color. Polar plots: each dot represents the phase tuning of a pixel from the adjacent panel. (B) Format matches (A) except maps were taken from a second preparation that relied on the Ai95 reporter, instead of the Ai93 reporter, to express GCaMP6F. The second preparation was extracted at postnatal day 5. Scale bar shown in middle panels 20 μm. 0° in phase tuning plots was defined as the time of peak L2 ventral root activity.

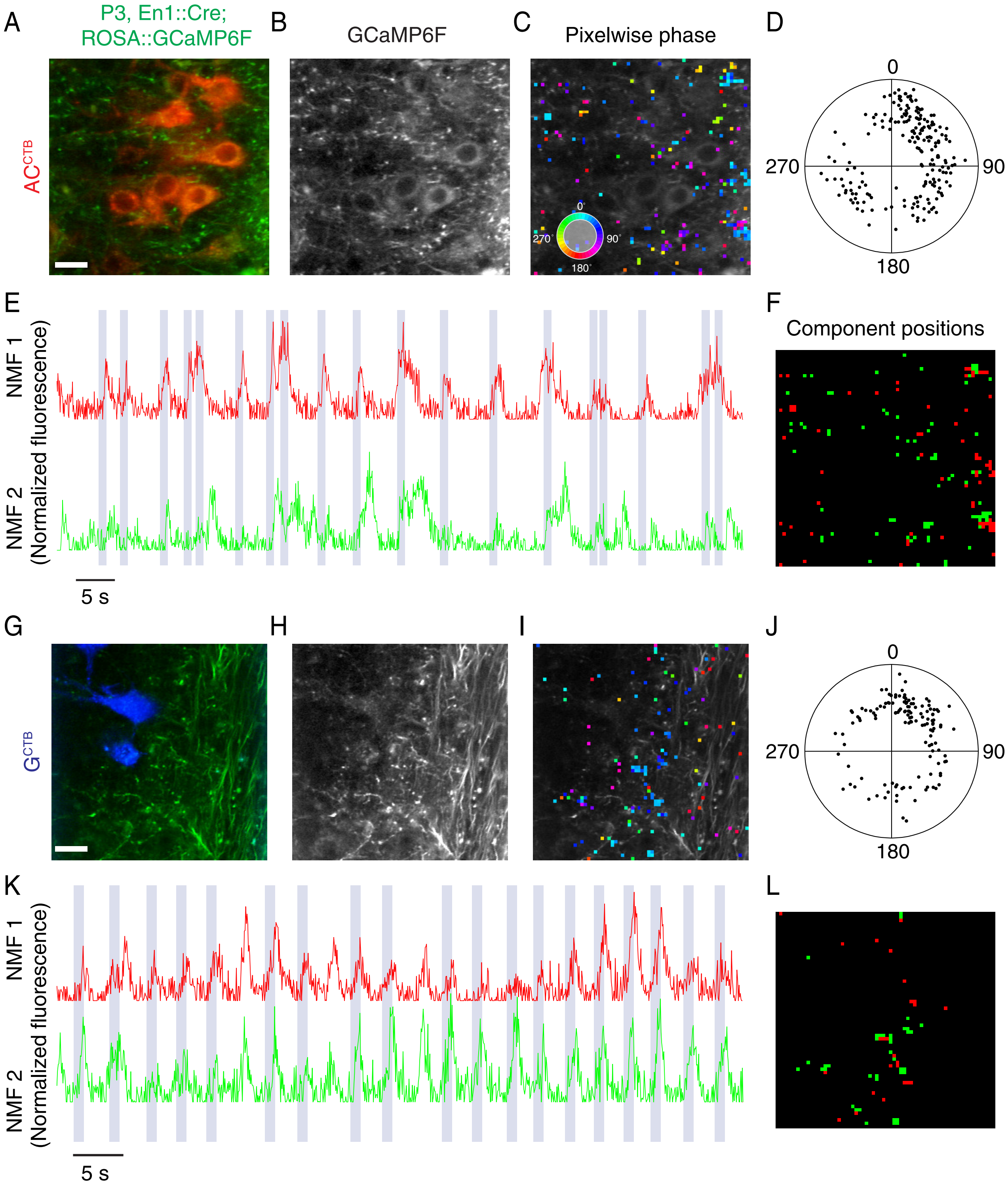
A
P3, En1::Cre;
ROSA::GCaMP6F
AC^{CTB}
B
GCaMP6F
C
Pixelwise phase
0°
90°
180°
270°
D
0
90
180
270
E
NMF 1
NMF 2
(Normalized fluorescence)
5 s
F
Component positions
G
G^{CTB}
H
I
J
0
90
180
270
K
NMF 1
NMF 2
(Normalized fluorescence)
5 s
L

Figure 6.11 *(preceding page)*: **Non-negative matrix factorization reveals antiphase inhibitory interneuron activity around both flexor and extensor motor neurons**

(A) Mean intensity projection across two image time sequences acquired from an Ai95 GCaMP6F; En1::Cre spinal cord preparation extracted at postnatal day 3. GCaMP6F (green) can be seen in axons, while retrogradely labeled anterior crural (ankle flexor; AC) motor neurons can be seen in red. (B) Mean intensity projection of only the green GCaMP6F channel. (C) Phase tuning of the most phasic subset of pixels is shown in color. (D) each dot represents the phase tuning of a pixel from the adjacent panel. (E) Two extracted NMF components (red and green lines; sparse NMF was used to find k = 3 components) relative to detected L2 bursts (blue bars). (F) Spatial extent of each NMF component. Red corresponds to NMF component 1, green to NMF component 2. (G-L) Format matches (A-F) except maps were taken from a second preparation where CTB was used to label gluteal motor neurons (blue; hip extensor). This preparation used the Ai93 reporter, instead of the Ai95 reporter, to express GCaMP6F and was extracted at postnatal day 4. Scale bar shown in middle panels 20 μm.

6.3 Discussion

6.3.1 A lack of spatial and temporal structure in inhibitory interneuron activity

These interneuron imaging experiments demonstrate a new approach for functionally mapping the types of inhibitory inputs that motor neurons in different pools might receive during locomotor firing. The fact that we failed to to see homogeneous antiphase firing amongst inhibitory interneuron axons surrounding a given pool prompts a reconsideration of the kinds of circuits that could be mediating flexor-extensor alternation. While we do not dispute the idea that reciprocal inhibition may play a role, these observations suggest that it may not be the only type of inhibition impinging upon motor neurons during locomotor firing.

Our motor neuron imaging data suggests that the activity during a locomotor state may be more complex than a collection of reciprocal flexor-extensor patterns suggested by models assuming that there is a dedicated flexor-extensor circuit for the control of each limb joint. Our interneuron imaging results are similarly inconsistent with such models as there appears to be little diversity in the activity patterns of inhibitory interneurons across space.

6.3.2 Constraining new models of locomotor circuits

As we considered in the introduction of this chapter, in both *in vivo* preparations as well as in the drug-induced locomotor preparation, it is possible that many rhythmically active ventral interneurons are neither necessary or even related to the production of motor output. Because of this, it is difficult to unambiguously interpret the gross patterns of interneuron activity that we observed in our wide-field data. Nevertheless, these observations appear similar to other measurements from spinal interneurons described in the literature, particularly studies from the decerebrate cat [Cuellar et al., 2009; Pérez et al., 2009], and isolated mouse spinal cord [Zhong et al., 2012].

In the Figure 6.12, data adapted from [Pérez et al., 2009] shows an apparent rostrocaudal "wave" of interneuron activity in the cat during fictive scratching behavior. This interneuron activity appears to be flexor-like, both in terms of its activation time as well as in the duration of each burst of activity. The similarity between these results and ours may be coincidental, but in either case, it suggests that interneuron activity in mammalian spinal circuits might be largely dominated by a single pattern of activity that arises through a combination of network factors and cell-intrinsic mechanisms [Brocard et al., 2013; Zhong et al., 2007].

The model constructed in [Pérez et al., 2009] to explain their observations is consistent with this idea, except it still relies on a half-center like readout layer to connect the interneuron networks that fire in the wave-like patterns to motor pools (similar to the one shown in Figure 6.5E). In contrast, [Petersen et al., 2014] presents the connections between the CPG and motor neurons as more complex. In addition to reciprocal inhibition between motor pools, there is also a recurrent network of both excitatory and inhibitory interneurons that are presynaptic to each motor pool (Figure 6.5C). Given that we observe clear on-phase inhibitory interneuron activity surrounding each motor pool, our observations appear more consistent with the [Petersen et al., 2014] model as it permits both on- and off-phase inhibition to each motor neuron. However, we also observed a surprising lack of diversity in the firing patterns of inhibitory interneurons, suggesting that both CPG and downstream premotor networks might actually be interconnected into a single dense, and distributed network (as suggested for CPG networks alone in [Guzulaitis et al., 2014]). With enough neurons and connections, it seems possible that a single network might be effectively multi-layer, in

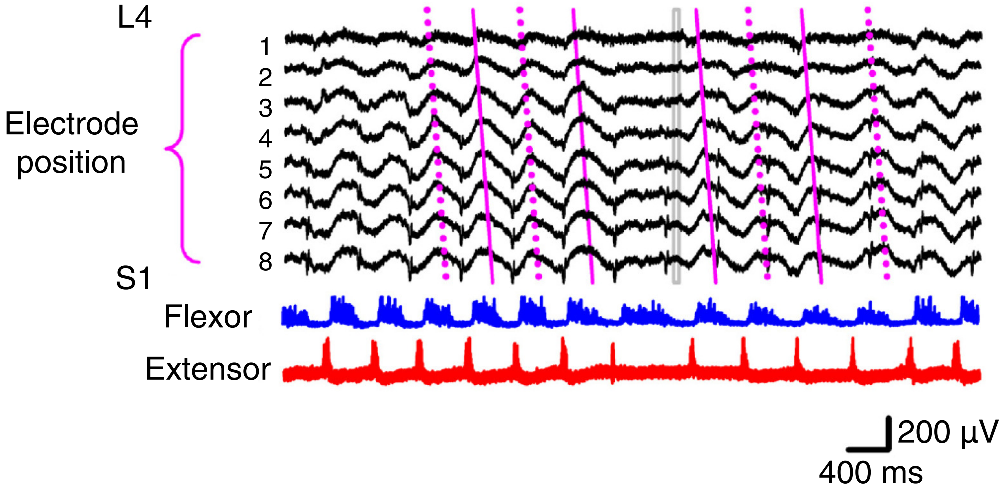

Figure 6.12: **Flexor-like wave of interneuron activity observed during fictive scratching in the cat**

(Top) Extracellular field recordings obtained from lumbar spinal segments in decerebrate cats revealed sinusoidal activity from dorsal horn and intermediate zone interneurons. The phase of this pattern changed as a function of rostrocaudal position. (Bottom) Simultaneous nerve recordings obtained from the tibialis anterior muscle (flexor) and the gastrocnemius muscle (extensor). Figure adapted from [Pérez et al., 2009].

that motor output would be robust to local perturbations to interneuron activity. Clearly there must be differences in the types of inputs seen to flexor versus extensor motor neurons, but there might also be much shared common input onto all pools from this dense, rhythmically active, network.

6.3.3 The role of reciprocal inhibition in flexor-extensor alternation

Our results suggest that both on-phase and off-phase inhibitory inputs onto motor neurons may exist during locomotor activity. Reciprocal inhibition may still play a necessary role in mediating flexor-extensor alternation, but may be only one of many inhibitory elements involved. Given the importance the nervous system must place on controlling motor output, it would be reasonable to redundantly employ a number of circuit mechanisms for enforcing that muscles do not inappropriately co-contract. In isolated spinal cord preparations that lack sensory feedback it would also make sense that reciprocal inhibition, which is classically defined with respect to proprioceptive inputs, might play a less dominant role. Similarly, because our imaging assays are biased towards observing superficially positioned interneurons, rather than to see microcircuits that receive sensory input, it makes sense that our use of new methods might reveal previously unappreciated aspects of the circuit. In future experiments, many questions regarding the organization of these interneuron networks will hopefully be resolved more clearly—perhaps by combining the imaging assays introduced in this chapter with recently developed non-toxic rabies tracing techniques [Reardon et al., in preparation].

7

General discussion

7.1 Motor pattern as a readout of computation in the nervous system

In this thesis, we explored the structure of motor neuron and interneuron firing at cellular resolution. Because these experiments were performed in spinal cord preparations that were isolated from descending or peripheral inputs, we were able to test the intrinsic capacity of local spinal circuits to generate patterned motor output. These measurements yielded insight into the structure and function of the neural circuitry underlying locomotor behavior, but they also provide an important context for considering the functional roles of unobserved sensory and descending signals. In particular, descending commands from motor cortex and the brainstem do not exist in isolation. The structure of such commands is derived in part from feedback arising in spinal circuits, permitting these inputs to engage with the ongoing dynamics present in their target spinal circuits in order to successfully "command" motor output. In this way, we can consider knowledge of intrinsic spinal cord network dynamics as necessary for deciphering the logic of upstream motor circuits–especially in non-primates where monosynaptic cortical input onto motor neurons is either sparse, or non-existent [Lemon & Griffiths, 2005].

At another level, spinal locomotor circuits represent an ideal test case for testing new ideas and hypotheses about how to generally approach the study of recurrent neural networks. Unlike most other recurrent circuits in the mammalian central nervous system, the computational goal of spinal locomotor circuits is intuitively clear: to produce patterned motor output. This simple fact along with the positioning of these networks at both the sensory and motor periphery has been exploited for decades in neuroscience, yet in recent decades much basic work about neural circuits has been conducted in other systems. Owing to the intuitive tractability of spinal circuits, a renewed focus on the spinal cord as a model system by the circuit neuroscience community at large might be warranted.

7.2 Defining the grain of intrinsic locomotor pattern

Our measurements of motor neuron activity permitted us to infer new constraints on the types of interneuron circuits that could mediate the coordinated firing of motor neurons during locomotor behaviors. We found sharp discontinuities in motor neuron phase tuning at the borders between synergy groups. This observation falsifies the possibility that “locomotor” firing in isolated preparations is the consequence of a sequential wave-like recruitment of motor neurons across space with disregard to motor pool borders. In combination with our analysis of $FoxP1^{MN\Delta}$ mice, this type of structure implies that the cohort of interneurons that is presynaptic to a given motor neuron is dependent on motor neuron identity.

The observation that locomotor firing in $FoxP1^{MN\Delta}$ mice collapsed to a nearly homogeneous flexor-like firing pattern suggests an even more specific linkage between motor neuron identity and firing pattern: a default, hypaxial-like, identity recruits interneurons that drive a specifically flexor-like pattern of firing. In addition to suggesting the evolutionary primacy of flexor circuits, this result argues that future studies should focus on the mechanisms that match spinal interneurons with different motor pool targets.

Another major conclusion of this work is that the isolated neonatal rodent spinal cord preparation produces a more complicated locomotor pattern than was previously appreciated in the literature (e.g. in [Dominici et al., 2011]). Therefore, a more detailed interrogation of firing in motor neurons and interneurons in this preparation is warranted. In Chapter 6, we explored a novel approach for examining the activity of genetically defined interneurons with respect to different motor pool targets. However, that assay represents only a single approach. Here we will briefly consider other possible avenues for exploration that have become recently possible due to the development of new genetic and optical tools for both measuring and perturbing neural activity.

7.3 Future directions

7.3.1 Simultaneous measurement of motor neurons and interneurons

In Chapter 6, we measured Ca^{2+}-sensitive fluorescent transients that arose from interneuron axons around retrogradely labeled motor neuron cell bodies. To relate these data to our measurements of motor neuron recruitment during locomotor firing, we computed phase tuning values with respect to ventral root L2. This approach suffers from two primary shortcomings. First, because we do not simultaneously measure the cellular resolution activity of motor neurons and interneurons, we must rely on separate motor neuron imaging experiments to interpret the phasic activation patterns that we observe in axons. Second, our measurements might be contaminated by dendrites, cell bodies, or axons of passage as GCaMP expression is not restricted to axons and synapses. Based on histological and anatomical evidence, the regions around motor pools appear to mostly contain processes rather than cell bodies in En1::Cre mice, but it would be better to only measure fluorescence directly from presynaptic terminals.

Both of these problems could be solved by using two newly developed tools. In particular, a synaptophysin-GCaMP fusion protein has been developed [Pech et al., 2015]. This would permit exclusive measurement of fluorescent transients in presynaptic terminals. Using a transgenic mouse or conditional viral vector expressing this indicator might work particularly well in the isolated spinal cord preparation. A complimentary approach to this would be to use a postsynaptic activity sensor like the intensity-based glutamate-sensing fluorescent reporter, iGluSnFR [Marvin et al., 2013]. In theory, iGluSnFR could be expressed sparsely in motor neurons and a red-shifted GECI or synaptophysin-GCaMP is expressed in a subset of interneurons in the same preparation. Such an approach has been tested in *C. elegans* [Marvin et al., 2013] and in the mouse retina [Borghuis et al., 2013]. Importantly, *Cre* dependent reporter mice that express iGluSnFR have already been developed by the Allen Brain Institute [Madisen et al., 2015].

A third approach for imaging interneurons that are presynaptic to defined motor pools would rely on the use of new highly efficient, nearly-non-toxic, virulent rabies strains developed by TR Reardon and A Murray in the Jessell laboratory [Reardon et al., in preparation]. Earlier in this thesis, we described our successful usage of SAD-B19 rabies containing GCaMP6 to image interneurons and motor neurons. However, we were not able to use this approach for transynaptic tracing because the poor efficiency of the retrograde spread from the muscle into motor neurons meant that muscle injections of virus yielded few infected motor neurons. Next, the presynaptic jump from these “starter” motor neurons into interneuron network was also inefficient due to the efficiency of the SAD-B19 virus strain and because we used a conditional Rosa::Rabies-SAD-B19-Glycoprotein mouse rather than a viral vector to selectively drive glycoprotein expression in motor neurons (as the AAV based approaches took too long for us to carry out a physiology experiment in the P1-P5 age range).

New strains of virus developed from the virulent N2C strain of rabies appear to have improved transynaptic spreading efficiency by $\sim$50x and also massively reduced toxicity issues [Reardon et al., in preparation]. Injecting this vector into the leg muscles of a hypothetical Rosa::Rabies-N2C-Glycoprotein; ChAT::Cre mouse would permit direct and exclusive measurement of activity from interneurons that are presynaptic to muscles of interest. Mixing the rabies virus with CTB conjugated to Alexa 647 would allow disambiguation of motor neurons from interneurons. Finally, expressing tdTomato in different subtypes of interneurons using already developed Flp lines would allow subtypes of excitatory and inhibitory premotor interneurons to be identified in the same preparation.

Through the use of these three approaches, it seems likely that comprehensive activity measurements of interneuron activity can be obtained and related to the postsynaptic motor neuron firing patterns that we described in detail in this thesis. However, the isolated neonatal spinal cord preparation is obviously limited in its ability to tell us about how spinal locomotor circuits might operate in adult, *in vivo* conditions. Unfortunately, because the spinal cord moves with respect to the vertebral column during behavior, *in vivo* fluorescent imaging at cellular resolution during locomotion is technically difficult. Even if a robust method for *in vivo* imaging of the ventral horn could be developed, it would only permit the measurement of activity of network activity from at best, a fraction of a single spinal segment.

An simpler *in vivo* approach to complement our large-scale measurements of activity in the neonatal preparation could come through the use of the new photoactivatable calcium integrator protein, CaMPARI [Fosque et al., 2015]. In principle, this indicator can be used in a similar manner to immediate early gene expression, except with a much more clear relationship between reporter intensity and neural activity. CaMPARI is an engineered fusion protein made from the photoconvertible EosFP (which irreversibly converts from a red to a green fluorophore following photoactivation) and Calmodulin. Consequently, a neuron expressing CaMPARI can be photoactivated during behavior, and if it is active, it will be irreversibly photoconverted to red. This permits histological methods to be used to map the spatial organization of neuronal activity during the specific epoch of a behavioral task where the photoconversion light source was activated, as illustrated in Figure 7.1.

This approach seems ideal for the characterization of intact spinal circuits in adult mice during behavior. As long as light fibers or LEDs can be surgically implanted such that the ventral spinal cord can be exposed to 405 nm light, interneurons activated during locomotor tasks can be mapped. For example, the photoconversion light source could be triggered by an EMG recording from a hindlimb extensor muscle. In this way, the 3D spatial distribution of interneurons activated concurrently with that muscle could be mapped *in vivo* and potentially across the whole spinal cord and brainstem. While photoconversion takes many seconds of exposure to the excitation light source, the light could be applied potentially dozens of times during detected muscle contraction to yield robust photoconversion in the activated neurons.

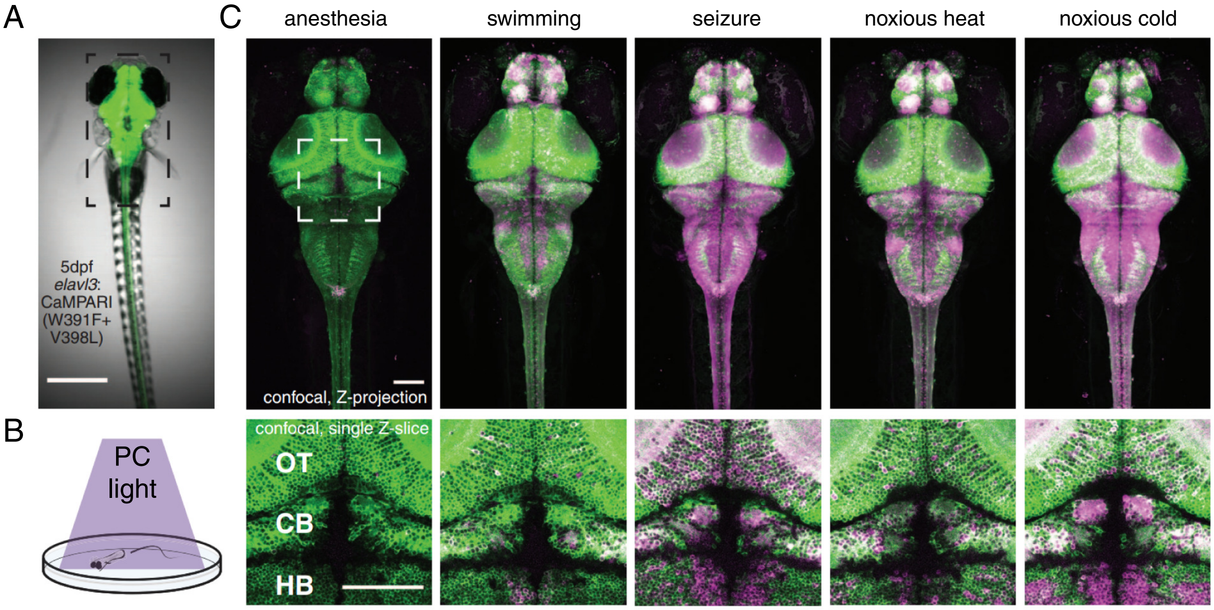

Figure 7.1: **Photoactivatable calcium integrators permit whole-brain activity characterization using histological methods**

(A) Pan-neuronal CaMPARI expression in a transgenic zebrafish larva (5 days post fertilization). (B) Experimental setup with a freely moving zebrafish and photoconversion (PC) light source. (C) Confocal images of zebrafish larvae exposed to 10 seconds of PC light during different behavioral conditions. Scale bar is 500 μm in (A) and 100 μm in (C). Figure adapted from [Fosque et al., 2015].

7.3.2 New methods for the induction and manipulation of locomotor firing

In addition to employing new approaches for measuring spinal network activity during locomotor firing, the work presented in this thesis could be extended by simply repeating the motor neuron and imaging assays developed here during electrical and optogenetic perturbations. Importantly, locomotor firing was induced in each of the *in vitro* experiments described in this thesis using the same pharmocological cocktail: 5 μM NMDA, 10 μM 5-HT, 50 μM DA. However, other combinations of NMDA, 5-HT, NE, and/or DA [Beliez et al., 2014], dorsal root stimulation [Taccola, 2011], and even ventral root stimulation [ODonovan et al., 2010] can evoke similarly "locomotor-like" network activity.

While most stimulation protocols appear to generate roughly similar patterns of activity as measured from ventral roots [Beliez et al., 2014], one study electrically stimulated dorsal roots with rhythmically patterned stimuli as opposed to the standard sequence of square-wave pulses (Figure 7.2A-B; [Taccola, 2011]). Under conditions of rhythmic dorsal root stimulation that attempted to mimic real proprioceptive feedback, the observed locomotor output was considerably more robust and long lasting. Obtaining motor neuron firing maps using the imaging methods developed here during different types of patterned electrical stimulation might reveal how incoming sensory information is interpreted and integrated by spinal locomotor circuits.

In addition to the use of electrical stimulation, patterned optical stimulation of defined interneuron populations would also be a useful technique. [Hägglund et al., 2013] demonstrated the viability of this approach by expressing the light-gated cation channel channelrhodopsin in excitatory interneurons. When different subsets of interneurons were activated with light, simultaneous ventral root recordings revealed that locomotor firing was not necessarily all-or-nothing (Figure 7.2C). Instead, it appeared that some light stimuli evoked locomotor firing in only a subset of motor pools. However, because ventral root or nerve recordings were only obtained from 2-4 sites at a time in this study, it was not possible to know precisely which pools were activated. If imaging were used instead (with red-shifted opsins as to not interfere with imaging), the precise spatiotemporal footprint of motor neuron activation could be assessed systematically as a function of light stimulus.

Another source of ideas for perturbation experiments that could be performed in the isolated neonatal spinal cord preparation is the zebrafish. In contrast to mammalian spinal cord development, the critical step of zebrafish development where spinal networks transition from spontaneous bouts of asynchronous activity to rhythmic locomotor-like firing occurs over a period of ∼2 hours (Figure 7.3; [Warp et al., 2012]). Therefore, questions about the role of activity during development can be directly tested by using GCaMP3 to monitor the activity of nearly all spinal neurons during that interval of development, and then repeating the experiment under conditions where the interneuron activity has been optically perturbed.

Owing to differences in development, as well as the larger size of mammalian circuits, this particular experiment is not feasible in the neonatal mouse preparation. However, it might be possible to perform a conceptually similar experiment by taking advantage of the fact that flexor-extensor alternation does not appear to arise until around the time of birth [Nishimaru & Kudo, 2000]. Given that isolated preparations are viable for upwards of 12 hours in the E18.5-P0 age window, it might be possible to observe the emergence of flexor-extensor alternation *in vitro*. If this were seen, perturbation experiments similar to [Warp et al., 2012; Hägglund et al., 2013] could be employed to clarify our understanding of the circuits responsible for alternation.

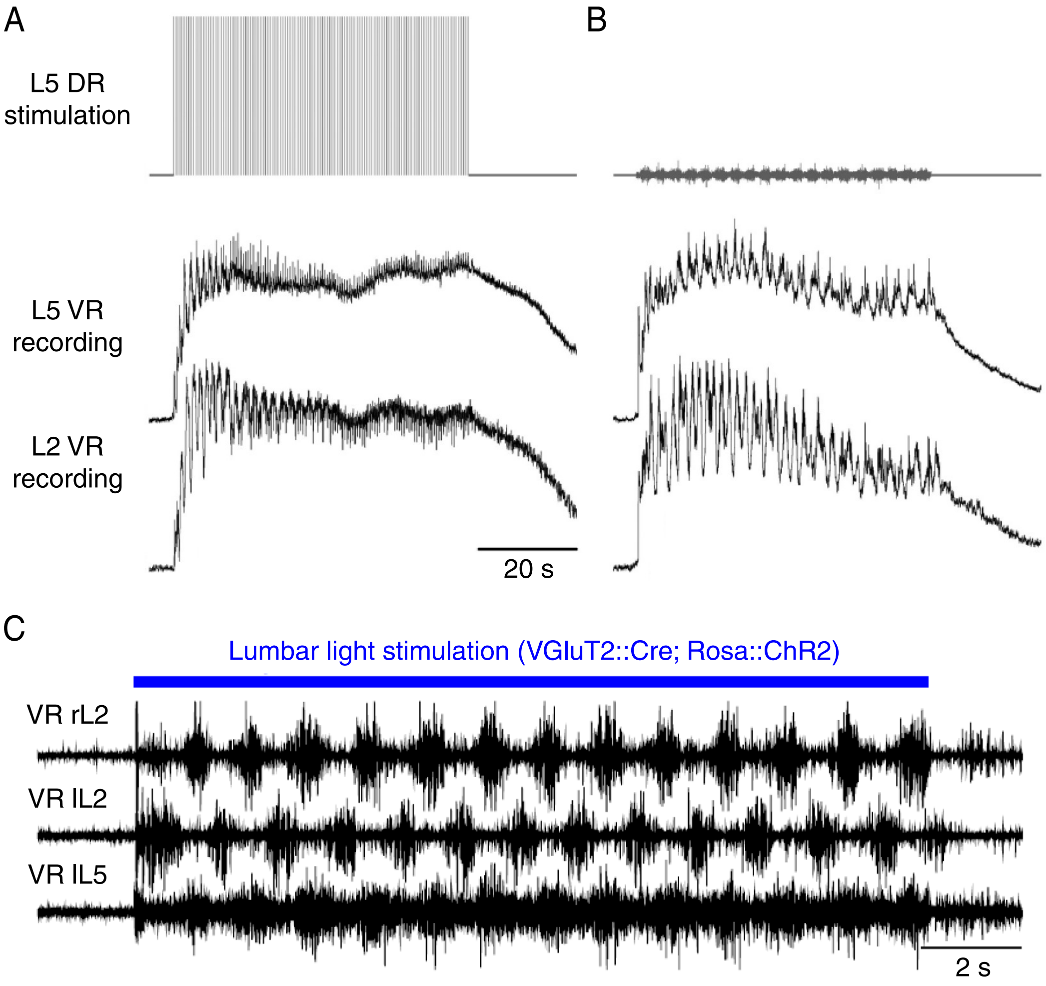

Figure 7.2: **Methods for evoking and perturbing locomotor-like network activity: optogenetics and patterned electrical stimulation**

(A) Activity evoked by sustained square-wave stimulation of dorsal root (DR) L5. (B) Activity evoked via patterned, locomotor-like, stimulation of dorsal root L5. (C) Activity evoked via channelrhodopsin photoactivation of VGluT2 expressing interneurons in the lumbar spinal cord. Panels (A-B) were adapted from [Taccola, 2011]. Panel (C) was adapted from [Hägglund et al., 2013].

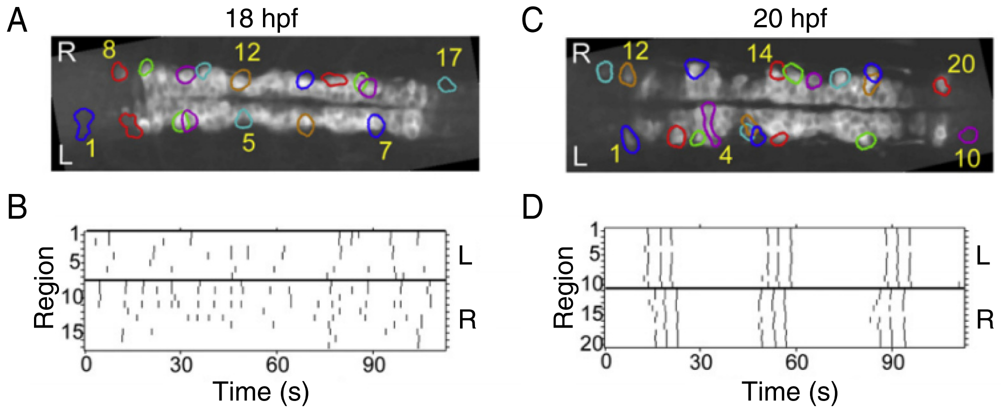

Figure 7.3: **Measuring and perturbing network activity in the embryonic zebrafish during development**

(A) Imaging field of GCaMP3 expressing spinal neurons obtained from a paralyzed zebrafish embryo at 18 hours post-fertilization (hpf). (B) Detected fluorescence events from regions denoted in (A). (C) Imaging field from same zebrafish obtained two hours later at 20 hpf. (D) Detected fluorescence events from regions in (C). Figure was adapted from [Warp et al., 2012].

7.4 Conclusions

While we have only begun to elucidate the mechanisms underlying motor neuron firing in the isolated spinal cord preparation, this thesis prompts a reconsideration of the way forward. Many previous studies have demonstrated that the pattern generating circuits in the thoracolumbar spinal cord are both redundant and distributed across many spinal segments [Kjaerulff & Kiehn, 1996; Beliez et al., 2015; Guzulaitis et al., 2014]. However, because most previous work relied on intrinsically low-dimensional methods for reading out motor and interneuron pattern, it has been difficult to understand how spinal interneuron activity might be organized across a local region containing even just a few hundred neurons. Here we have introduced a new assay for measuring the nearly complete pattern of motor neuron activity as well as a complimentary approach for measuring interneurons with respect to defined patterns of motor output. Moving forward, future studies should be pursued using similarly high-dimensional recording methods for interrogating and perturbing these neural circuits.

At a more conceptual level, our findings argue that the isolated mouse spinal cord preparation represents an opportunity to dissect pattern generating circuits one synapse at a time—rather than all at once. As we considered in Chapter 6, in both *in vivo* preparations as well as in the drug-induced locomotor preparation, it is likely that many rhythmically active ventral interneurons are neither necessary or even related to the production of motor output. As a consequence, the activity of individual interneurons must be interpreted with respect to their position within the broader locomotor circuit. Given our lack of knowledge about the precise organization of motor circuits, a logical place to begin is to consider the population of interneurons that are presynaptic to functionally distinct motor pools. Once we have characterized those patterns in detail, it might be more clear how to interpret the activity of interneurons that are not monosynaptically connected to motor neurons. In parallel, developmental studies of the mechanisms mediating appropriate interneuron-motor neuron activity must be performed to gain knowledge of the principles that define spinal interneuron connectivity. Once we can discern the differences in premotor activity and connectivity that underlie different locomotor firing patterns, we will be able to more clearly consider the kinds of network commands that might be used by descending systems to sculpt motor behavior.

8

Experimental procedures

All experiments and procedures were performed according to NIH guidelines and approved by the Institutional Animal Care and Use Committee of Columbia University.[1]

8.1 Retrograde labeling of motor neurons

Motor neurons were retrogradely labeled *in vivo* at P1-P3 via intramuscular injections of cholera toxin B subunit (CTB) conjugated to Alexa 555 or 647 (0.1% w/v in PBS; obtained from Life Technologies) [Sürmeli et al., 2011]. This approach was used to label up to two different muscle groups in the same mouse. Imaging experiments were conducted 24-48 h after tracer injection. Injected hindlimbs were dissected under fluorescence guidance after each experiment to verify that the diffusion of injected CTB conjugate was restricted to the targeted muscle group.

8.2 Spinal cord isolation

Mice, aged 2-5 days postnatal, were rapidly decapitated and the vertebral column was removed and pinned ventral side up in a Sylgard-lined (Dow Corning) dissection

---

[1] Sections 8.1 to 8.13 of this chapter were derived from work in [Machado et al., 2015].

dish perfused with ACSF (125 mM $NaCl$, 25 mM $NaHCO_3$, 1.25 mM NaH_2PO_4, 2.5 mM KCl, 2 mM $CaCl_2$, 1 mM $MgCl_2$, and 25 mM D-glucose, 315 mOsm, equilibrated with 95% O_2 and 5% CO_2) held at 4° C with a feedback control system (ECO RE 415 S, Lauda) that cooled a brass holder encircling the dissection dish (G. Johnson, Columbia University). A ventral laminectomy was performed and dorsal and ventral roots were disconnected from their respective dorsal root ganglia and surrounding connective tissue. The isolated spinal cord was then transferred to a custom recording chamber mounted under a two-photon microscope and allowed to equilibrate for at least 30 minutes. The temperature of the ACSF in the recording chamber was held constant at $24-25°$ C using an inline heater (Warner). ACSF was recirculated throughout the experiment using a peristaltic pump (Gilson) with a flow rate of 9-10 mL/min.

8.3 Ventral root recording and stimulation

After equilibration, spinal cords were pinned with the left lateral side positioned upwards. Suction electrodes were mounted on custom miniature manipulators that attached to the edges of the recording chamber. These electrodes were positioned around ventral roots L1 or L2 and L4 or L5 on both the left and right sides of the cord. Additional suction electrodes used for stimulation were placed on dorsal roots L4 or L5. By stimulating dorsal roots at different intensities (8-20 μA), we were able to evoke monosynaptic responses (assessed based on latency) between homonymous pairs of dorsal and ventral roots as well as longer latency polysynaptic responses between heteronymous pairs of roots [Mentis et al., 2011]. These measurements were used to verify that electrodes were positioned correctly on the relevant roots and that we could resolve signals from each one. Electrodes were also positioned on ventral roots L3 or L4 for antidromic motor neuron stimulation. Collectively, these electrodes served to stabilize the preparation mechanically, minimizing flow-induced motion artifacts during imaging. Ventral root activity was recorded (DC-4 kHz) using a multichannel amplifier and signal conditioner (CyberAmp 380, Molecular Devices), digitized at 10 kHz (Digidata 1440A, Molecular Devices), and recorded in Clampex (v. 10.3, Molecular Devices).

8.4 Two-photon microscopy

We used a Prairie Technologies Ultima microscope constructed using an Olympus BX-51 chassis with a 20x objective (1.0 numerical aperture, 2 mm working distance; XLUMPLFLN, Olympus) to acquire all fluorescence images (256x256 pixels/frame). Excitation light was controlled with an electro-optical modulator (Model 302 RM, Con-Optics). We excited GCaMP3 and $CTB - Alexa^{555}$ at 940 nm (Chameleon Ultra II laser; Coherent), separated emitted fluorescence with a 560 nm dichroic (Chroma), and collected through separate emission filters (525/50 for GCaMP3 and 595/50 for $CTB - Alexa^{555}$). $CTB - Alexa^{647}$ was excited at 780 nm, and its fluorescence was separated with a 640 nm dichroic (Chroma) and collected through a 660/40 emission filter (Chroma). We detected fluorescence using two non-descanned multi-Alkali photomultiplier tubes (Hamamatsu R3896, used for $CTB - Alexa^{555}$ and $CTB - Alexa^{647}$ imaging) and one GaAsP detector (Hamamatsu 7422PA-40, used for GCaMP3 imaging). We delivered 100-200 mW (at 940 nm excitation) and 100-300 mW (at 780 nm) to the back aperture of the objective during image acquisition. In 17 of 19 preparations from the motor neuron imaging project, the two-photon laser was raster scanned across the preparation at 60 Hz using a resonant galvanometer. These signals were downsampled to 15 Hz to increase the signal-to-noise ratio. In the remaining 2 of 19 preparations, the laser was scanned at 8 Hz with conventional 6 mm galvanometers in a spiral trajectory.

At the beginning of each motor neuron imaging experiment, ventral root L3 or L4 was stimulated via a suction electrode to activate motor neurons antidromically [Bonnot et al., 2005; Lev-Tov & O'Donovan, 1995]. Using square pulses (0.2

ms duration), we drove motor neurons to fire in a rhythmic pattern that resembled activity observed during agonist-induced locomotor firing [Cazalets et al., 1996; Hochman & Schmidt, 1998]. The antidromic stimulus consisted of ten 1.5 s long bursts, where each burst consisted of 9-25 pulses. These burst stimuli were delivered at a frequency of 0.22 Hz, approximating the 0.25 Hz average burst frequency we observed during agonist-induced locomotor firing. An identical stimulus waveform was used in every experiment. Stimulus intensity was 60 μA, approximately 5 times greater than the minimum intensity needed to evoke an antidromic response (cf. [Bonnot et al., 2005]). This supramaximal stimulus intensity was chosen to yield a maximal number of responsive neurons, such that larger stimulation intensities would not recruit more neurons or change the observed pattern of antidromic activation. The region containing responsive motor neurons was first identified through the BX-51 epifluorescence path using a 4x Olympus objective (UPlanFL, 0.13 numerical aperture) and an EM-CCD (Hamamatsu C9100-13; 30 ms exposure per frame). We then acquired two-photon image sequences from 4-8 imaging fields within this region during stimulation.

The membrane voltage of motor neurons during antidromic stimulation in a nearly identical experimental preparation, together with earlier intracellular recordings from motor neurons, suggest that motor neurons reliably spike following each antidromic stimulation pulse when stimulated at suprathreshold intensities (G.Z. Mentis, personal communication; [Bonnot et al., 2005; Brock et al., 1952]). In rare instances, individual antidromic pulses sometimes induce multiple spikes, but there is no indication that the overall shape of induced bursts during antidromic stimulation would be, on average, biased such that our validation procedure would errantly validate our phase tuning estimation methods. Furthermore, our observation of phase stability over time across hundreds of motor neurons suggests that even if some bias were to exist in our phase tuning measurements, it is at least consistent over time.

After optically recording antidromic responses, we applied a rhythmogenic agonist cocktail (5 μM NMDA, 10 μM 5-HT, 50 μM DA) to induce locomotor firing. One hour after application, we began acquiring image sequences in fields collectively spanning the three-dimensional extent of the lateral motor column within the mediolateral depth imageable in our preparation. To choose these imaging fields, we first manually chose 6-8 overlapping fields that collectively spanned 2370-3330 μm along the rostrocaudal axis of the lumbar spinal cord, or approximately the whole rostrocaudal extent of the LMC. Starting from the position of each of these fields, we then chose 6-8 imaging fields equally spaced across 120-140 μm along the mediolateral axis, starting at the most lateral extent of the motor column and descending medially. Imaging fields were then visited consecutively in a pseudo-random order, and image sequences were acquired from each field for 90 s. A subset of fields were imaged a second time (6-28 locations; mean = 15) to assess stability in phase tuning over time.

8.5 Image segmentation and preprocessing

Fluorescence image sequences were preprocessed in ImageJ using custom scripts. The centroid of each motor neuron soma was manually identified, and a 15 x 15 pixel (30 x 30 μm) square region of interest (ROI) centered upon each of these centroids was defined. Fluorescence from these ROIs over time (data arrays of size 15 x 15 x T time steps) were then imported into MATLAB and processed further with custom scripts. Motor neuron somata contained in ROIs were manually matched to CTB-labeled somata apparent in static images acquired under 780 nm and 940 nm excitation from the same imaging fields. All subsequent analysis described here was performed in MATLAB.

Within each square ROI, we then found a set of pixels, called the spatial filter, which corresponded to a single motor neuron soma. First, we took each data array and decomposed it using a low-rank approximate PCA method for which we specified the decomposition rank to be 5 [Rokhlin et al., 2009]. We then defined the z-scores of the first decomposition component to be our initial spatial filter and thresholded the filter such that all positive pixel weights were set to be 1, and all negative weights were set to 0. Finally, we smoothed the filter (MATLAB function bwmorph using the "majority" option) and decomposed it into connected components, retaining only the largest component (all other components were set to 0). If the largest component contained fewer than 5% of the total pixels in the 15x15 pixel square, which is much smaller than the average motor neuron soma area, we discarded that data array from further analysis. The spatial filters chosen from all data arrays taken from the same image sequence were subsequently compared to determine if any pixels had been assigned to the spatial filters of multiple neurons. Pixels that were assigned to multiple spatial filters were re-assigned to belong to only the spatial filter arising from the nearest filter centroid. Each pixel time series in the data array was then multiplied by its corresponding spatial filter weight and summed to yield a one-dimensional fluorescence time series for each soma. Fluorescence time series were scaled to be between zero and one (for use with our spike inference algorithm) or in terms of $\Delta F/F$ for plotting. $\Delta F/F$ was defined as $(f - f_0)/f_0$), where f_0 was the 10th percentile value of f). Fluorescence time series were temporally aligned with ventral root recordings using frame acquisition times extracted from the voltage drive signal to the electro-optical modulator, which were recorded in Clampex.

8.6 Spike inference

We used new model-based fluorescence deconvolution methods [Pnevmatikakis et al., 2015] to estimate the spike train underlying each fluorescence time series. Intracellular Ca^{2+} concentration c was approximated by a first-order autoregressive model:

$$c(t) = \gamma c(t-1) + s(t) \tag{8.1}$$

where s is the number of spikes that the neuron fired during the t-th time bin, $t = 1, \ldots, T$, and γ is related to the time constant,τ, of the Ca^{2+} indicator by $\gamma = 1 - \Delta/\tau$, where the frame rate of acquisition in Hz is defined as $1/\Delta$. Each fluorescence time series f was then modeled as:

$$f(t) = \alpha c(t) + b + \epsilon_t \sim N(0, \sigma^2) \tag{8.2}$$

where α is a non-negative scalar and ϵ represents stationary Gaussian noise. This first-order model assumes an instantaneous transient rise time because the rise time of GCaMP3 in Ai38 reporter mice is roughly the same as our 67 ms/frame image acquisition rate [Zariwala et al., 2012]. The baseline signal amplitude, b, was estimated by taking the 10^{th} percentile value of each fluorescence time series and was not optimized further by the spike inference algorithm. This approach worked well with our data, because each motor neuron was active for a large fraction of its fluorescence time series.

To estimate τ, we used image sequences collected during antidromic stimulation. We assumed that the binned spike train, s, underlying each fluorescence time series, f, could be approximated by the antidromic stimulus. Using this assumption, both the s and f are known. We then estimated a single τ for each antidromic image sequence using the fluorescence time series from all responsive motor neurons within it (neuron selection criteria described in Quantification of phase estimation error below). This calculation used the Multivariate Output-Error State-sPace (MOESP) systems identification method [Verhaegen & Verdult, 2007] implemented in the n4sid function in the MATLAB System Identification Toolbox. The median τ across all antidromic image sequences collected from a given cord was used as τ for spike inference from motor neurons from that cord. τ varied as a function of Cre driver strain used and ranged from 0.67 - 1.10 seconds.

Next, we estimated the noise power σ^2 by assuming that the autocovariance function of each fluorescence signal f at lag t, $C_f(t)$, satisfies the following equation:

$$C_f(1) = \gamma C_f(0) - \sigma^2\gamma \tag{8.3}$$

An alternative and more robust approach towards the estimation of σ^2 comes from examining the power spectral density (PSD) of f, as presented in [Pnevmatikakis et al., 2015]. This method is somewhat less dependent on parametric model assumptions about the data. Due to the slow decay dynamics of the Ca^{2+} indicator, the AR process acts typically as a low pass filter on incoming spikes, and therefore the noiseless Ca^{2+} trace has very low power in the high frequency range. Since the noise is assumed to be white, its PSD is flat across all frequencies. To estimate σ^2 we can therefore compute the PSD of f and average its value at the range of high frequencies (e.g. in the range $[(F_s/4, F_s/2])$, where $F_s = 1/\Delta$, the imaging frame rate in Hz.

While equality (8.3) is only strictly true when neuronal spiking follows Poisson statistics, we were able to use our antidromic data to verify that this approach is approximately correct for our data. We achieved this by computing true σ^2 values directly from Gaussian fits to residual error histograms. Residual error was computed by subtracting fluorescence data taken during antidromic stimulation from the convolution of the antidromic stimulus and the calcium decay kernel (as defined in (8.2)). True σ^2 values closely matched those estimated using equation (8.3).

Given these parameter estimates for γ and σ^2 , we then employed a constrained non-negative deconvolution algorithm [Pnevmatikakis et al., 2015] that inferred the most likely c and s underlying each fluorescence time series:

$$\begin{aligned} &\underset{\mathbf{c},\mathbf{s}}{\text{minimize}} \quad \mathbf{1}_T^\top \mathbf{s}, \\ &\text{subject to:} \quad \mathbf{s} \geq 0, \quad s(t) = c(t) - \gamma c(t-1), \quad \|\mathbf{f} - \mathbf{c} - b\mathbf{1}_T\| \leq \sigma\sqrt{T}. \end{aligned} \tag{8.4}$$

In order to find the most likely sparse spiking pattern that is sufficient to explain each fluorescence trace without overfitting, the convex program (8.4) was solved using the CVX computational package [Grant et al., 2008] or a non-negative least angle regression algorithm [Pnevmatikakis et al., 2015]. The runtime of both algorithms increased linearly with the number of time steps in the fluorescence data. The magnitude of s at each time step represents a relative estimate of number of spikes that occurred during each imaging frame. Each s value was then normalized by the maximum s for each neuron.

We also used our spike inference algorithm to estimate the signal-to-noise ratio (SNR) for each neuron in our motor neuron imaging dataset. This quantity was defined as:

$$10 \; log_{10} \frac{\|\mathbf{c}\|}{\sigma^2 T}, \tag{8.5}$$

Our spike inference algorithm yielded spike histograms consisting of a sequence of numbers between zero and one, each proportional to an estimate of neuronal firing rate at a given imaging frame. A more accurate, but less efficient, spike inference method returns continuously valued spike times, permitting the temporal pattern of multiple spikes within individual imaging frames to be detected and also providing uncertainty estimates (i.e. error bars) for all model parameters and spike inference output [Pnevmatikakis et al., 2013]. In order to test whether the simpler algorithm that we used in the analysis presented in this paper errantly biased our conclusions, fluorescence data from two preparations were additionally analyzed with a different spike inference algorithm that used this more complex algorithm. We found that both methods yielded quantitatively similar results.

8.7 Validating the use of a linear model of Ca^{2+} dynamics

To test whether the linear model used to relate c to s defined in section 8.6 was adequate for relating fluorescence to spiking in our motor neuron imaging dataset, we tested whether fluorescence may be better described as a nonlinear function of c denoted $n(t)$:

$$n(t) = \frac{1}{1 + \exp(-\beta_0 - \beta_1 c[t])}, \tag{8.6}$$

so that observed fluorescence is now given by:

$$f(t) = \alpha n(t) + b + \epsilon_t, \tag{8.7}$$

where α,b and ϵ are defined as in the linear model (equation (8.2)). Such a model can account for nonlinearity, such as that produced by the saturation of Ca^{2+} indicator binding. We compared the ability of these two models to predict the structure of actual fluorescence data acquired during antidromic stimulation. Model parameters underlying the sigmoidal nonlinearity (β_0, β_1) and for scaling the data (a, b) could be directly computed in this setting because the relationship between actual spiking and fluorescence was known. For a given set of antidromic spike times $[a_1, a_2, \ldots, a_K]$, we created the binned spike train s by assigning each spike time to a correct bin and scaling it depending on how close it was to the end of the bin:

$$s(t) = \sum_{\substack{i: a_i \in [(t-1)\Delta, t\Delta) \\ i=1,\ldots,K}} \exp(-\frac{t\Delta - t_i}{\tau}), \tag{8.8}$$

where $\tau = -\Delta/(\gamma - 1)$ and γ was derived using the system identification approach described in section 8.6. We then computed c (termed the linear prediction in this context) given the binned antidromic stimulus, s, and the linear relationship defined in equation (8.2). To generate the nonlinear prediction, we first computed the parameters $(\beta_0, beta_1, a, b)$ underlying the maximum likelihood nonlinearity by solving:

$$\min_{\beta_0,\beta_1,\alpha,b} \sum_{t=1}^{T} (f[t] - n[t])^2. \tag{8.9}$$

With these parameters, we were able to use the binned antidromic stimulus, s, and the relationship between n and s to produce our nonlinear prediction of fluorescence data during the spike train s. To assess the goodness of fit of each model, we computed the Pearson correlation between each the each model prediction and our fluorescence data recorded during antidromic stimulation, f, termed $corr(linear, f)$ and $corr(nonlinear, f)$. In nearly all cases, the difference between the models $corr(nonlinear, f) - corr(linear, f)$ was close to zero, suggesting the sufficiency of the linear model for use in spike inference.

8.8 Ventral root burst identification and phase estimation

Raw ventral root recordings were first symmetrically band-pass filtered (1 Hz-1 kHz). To make root activity peaks clearer, we filtered each resulting time series $s(t)$ by replacing its value at each time step with the standard deviation of $s(t)$ from 5 ms prior to 5 ms after that time step, and ignoring the first and last 5 ms of the time series [Ahrens et al., 2012]. Finally, we convolved the result with a Gaussian kernel ($\sigma = 0.5s$) to eliminate most local maxima and thus permit reliable peak detection. Locomotor cycles were defined as the epochs between adjacent L1 or L2 peaks. Angle gradations ($0° - 360°$) were uniformly distributed within each cycle. Little variation was observed between datasets referenced to L1 recordings and those referenced to L2 recordings, consistent with previous observations [Falgairolle & Cazalets, 2007; Kwan et al., 2009]. Circular statistics on phase measurements were implemented using the Circular Statistics toolbox [Berens, 2009; Zar, 1999].

To quantify burst firing phase, each nonzero spike count value was assigned to a cycle phase based on its relative proximity to the root peaks immediately surrounding it (i.e. the locomotor cycle in which it fell). For each motor neuron, the circular mean of these phase values, weighted by the corresponding size of each inferred spike count, was computed at each locomotor cycle. Spikes arising from locomotor cycles that were greater than 10 s long or less than 2.5 s long (approximately 0.5x and 2.0x the average locomotor burst frequency, respectively) were excluded from the phase computation, as burst cycles of those lengths tended to arise from rare failures in peak detection or transient interruptions in rhythmic network activity. A motor neurons phase tuning was defined as the median of the resulting values, which approximated the average phase of burst firing. We chose to quantify mean burst phase instead of onset or offset, after evaluating each statistic for all identified ankle flexor motor neurons recorded during locomotor firing and finding that the variance across the population was slightly higher for both onset and offset.

The mean burst frequency of the locomotor rhythm was quantified for each imaging field by computing the inter-burst interval time between adjacent L1 or L2 peaks and taking the inverse of these mean inter-burst interval times. The average frequency for each preparation was quantified by taking the median across all recordings.

8.9 Quantification of phase estimation error

Inferred spiking calculated from fluorescence collected during across four consecutive antidromic bursts bursts was used to measure the error of phase tuning estimates. These four bursts, which each consisted of 16-24 pulses over 1.5 seconds, equating to an average pulse rate of 10-17 Hz, were chosen because the observed fluorescence responses well approximated those seen during agonist-induced locomotor firing. We analyzed only those motor neurons imaged during antidromic stimulation that had a summed squared residual error value below an empirically determined threshold set such that only neurons unambiguously responding to the stimulus were included (n = 9 - 98 neurons per cord, mean = 26 neurons per cord, 367 neurons total; N = 14 spinal cords). The summed squared residual error was computed for each neuron by subtracting the normalized fluorescence data from the convolution of the antidromic stimulus underlying the fluorescence data (binned into a histogram with the bin width equal to the imaging frame rate) with an exponentially decaying kernel, $k(t) = e^{-t/\tau}$, where τ was estimated using our system identification approach described above.

We computed the phase tuning of each qualifying neuron following the same procedure used for neurons recorded during locomotor firing, except here the midpoint of each antidromic stimulus burst was defined as 0° in each cycle. Since the antidromic stimulus was assumed to be equal to the motor neuron spike train, in addition to being a phase reference the midpoint of each antidromic burst is also the true phase for each cell. The estimated phase tuning values here thus represent the errors associated with estimating phase from fluorescence.

We compared the phase tuning error distributions obtained from the use of our spike inference method to those obtained from a simpler method, termed peak detection. In our peak detection algorithm, we symmetrically band-pass filtered the fluorescence data from 0.1 Hz to 1 Hz with a 4th order Butterworth filter, and then found the maxima of the filtered time series using the findpeaks MATLAB function with a minimum peak height of 0.2 times the standard deviation of the filtered time series. We also used the mean difference of the phase tuning error distributions to derive a baseline value for assessing the stability of phase tuning over time. This mean difference represents the expected difference between phase tuning measurements taken at different time points under the assumption that phase tuning does not change. The mean difference was estimated by taking $2/\sqrt{\pi}$ times the standard deviation of the observed antidromic error in each dataset.

8.10 Generation of spatial maps of phase tuning

A subset of all imaged motor neurons were included in the spatial maps of phase tuning. Neurons were selected by performing Rayleighs test of circular uniformity on the normalized spike histogram of each neuron. Motor neurons yielding p-values ≥ 0.5 were excluded, effectively eliminating the noisiest neurons while retaining broadly tuned cells with weak signals but reliable phase tuning estimates. As imaging fields were partially overlapping, individual neurons were sometimes found in multiple image sequences. These duplicate neurons were located by finding pairs of neuron centroids located within 20 μm of each other, where each centroid was from an overlapping pair of imaging fields. Only one copy of each duplicate neuron was retained. Maps created from data obtained from both *Olig2::Cre* and *ChAT::Cre* expressing mice were quantitatively indistinguishable.

Since the variation in spinal cord thickness across segments caused the central canal to not lie straight, we corrected the positional coordinates of imaged neurons to compensate. We first fit a smoothing spline to the three dimensional positional coordinates of motor neurons using the fit function in MATLAB with the smoothness parameter set to 10^{-9}. Then, we used the smoothing spline to generate a new rostrocaudal coordinate for each neuron, given by the distance from the origin to the neurons original rostrocaudal position as measured along the smoothing spline. The mediolateral and dorsoventral coordinates were also re-centered around the fitted smoothing spline by subtracting off the position of the smoothing spline in the original coordinate space from each original mediolateral and dorsoventral neuronal position.

To functionally identify the boundaries of certain spinal segments in these maps, epifluorescence image sequence data acquired during antidromic stimulation (4x magnification) were used. For each pixel in the imaging field, we computed the standard deviation of fluorescence across time and overlaid resulting values on their corresponding positions within epifluorescence images showing CTB-labeled cells. The resulting image showed the region of the lumbar spinal cord that had high standard deviation values indicating that it was responsive to the antidromic stimulus. We manually registered this image to our large-scale spatial maps of phase tuning by using the rostrocaudal position of CTB-labeled motor neurons. We then defined the boundaries of the antidromically activated segment as the rostral and caudal edges of the region containing responsive cells. In one case in which the caudal boundary was obscured by the position of the ventral root in epifluorescence images, we used the center position of the ventral root as the caudal segmental boundary.

8.11 Phase synchronization

Phase synchronization was computed using normalized spike histograms yielding a Rayleigh test p-value < 0.05. This more stringent criterion was used to restrict our analyses to neurons whose somatic fluorescence was recorded with a high signal-to-noise ratio. Spike histograms, treated as time series vectors, were first band-pass filtered between 0.1 and 1 Hz (4th order symmetric Butterworth filter, MATLAB functions butter and filtfilt), in order to focus on the degree of synchronization at the frequency of locomotor firing (mean ± s.d. $= 0.25 \pm 0.06$ Hz, n = 15 spinal cords). Filtered histograms were then expressed in terms of instantaneous phase by taking their Hilbert transform (MATLAB function hilbert) and converting complex values to phase angles. The first and last tenths of the resulting instantaneous phase vectors were removed. To compute phase synchronization for a pair of N-element instantaneous phase vectors, we first computed their relative phase by subtracting them, yielding $\phi = [\phi_1 \ldots \phi_N]$. Phase synchronization is then the scalar R given by [Mormann et al., 2000]:

$$R = \left| \frac{1}{N} \sum_{j=1}^{N} e^{i\phi_j} \right| \tag{8.10}$$

To test for the significance of synchrony within and between synergy groups, we used a Wilcoxon test to compare phase synchrony index distributions with their equivalent calculated after circular permutation of one time series from each pair. Because cycle periods vary, circular permutation should reduce synchrony to a level approaching that expected by chance if the two time series were independent. Circular permutation was performed by picking a random element in one of the time series, removing the series of elements coming before it, and concatenating them to the end of the remaining time series. We also used the Wilcoxon test to compare phase synchrony index distributions within and between synergy groups. Here, we performed the test both with and without a control for differences in the proximity of neuron pairs within versus between synergist groups. In the controlled case, we first identified, for each pair of non-synergist motor neurons, the pair of synergist motor neurons not previously identified whose proximity was most similar. The Wilcoxon test was then used to compare phase synchrony index distributions for non-synergist and identified synergist pairs.

8.12 Cycle-triggered firing rates

Cycle-triggered firing rates were computed for cells whose spike histograms yielded a Rayleigh test p-value < 0.05. The firing rate vectors were computed by generating a 100-bin histogram of inferred spike counts according to their locomotor phase, then convolving these histograms with a Gaussian kernel ($\sigma = 4$ bins). Burst duration was measured from cycle-averaged firing rates by identifying the last histogram bin before, and first histogram bin after, the peak value at which the spike count is $\leq$ half of the peak value. Burst duration was the fraction of the histograms domain, expressed in degrees, between these two bins. The last and first histogram bins were considered to be adjacent, as implied by the cyclic nature of the histograms domain.

After k-means clustering (k = 2) was performed on cycle-averaged firing rates, a clustering index was calculated to quantify the separation between the resulting two clusters. The clustering index was measured in terms of the phase of peak firing and burst duration measured from cycle-averaged firing rates. To compute this index, we first generated a two-element vector for each cycle-averaged firing rate in which the first element was peak phase and the second element was burst duration. We then computed the two-dimensional vector mean (centroid) for vectors assigned to each cluster, resulting in the cluster centroids $c_1 = [c_1^1 \; c_2^1]$ and $c_2 = [c_1^2 \; c_2^2]$. We then measured the root-mean-squared distance between all vectors and their centroid for each cluster, resulting in the cluster root-mean-squared distances r_1 and r_2. The clustering index, CI, was defined as:

$$CI = \frac{2\sqrt{(c_1^1 c_1^2)^2 + (c_2^1 c_2^2)^2}}{r^1 + r^2}. \tag{8.11}$$

The overlap between joint distributions of peak phase and burst duration was measured by first estimating a kernel density function (using the MATLAB function kde2d obtained from the MathWorks file exchange) defined across a grid to describe each joint distribution. These density functions were normalized to ensure they integrated to one. The overlap of two density functions was found by finding the lower of the two densitys values at each grid point, then summing all of those lower values. Fold difference in similarity for the joint distribution of $FoxP1^{MN\Delta}$ motor neurons was computed by dividing its overlap with the early firing wild type set with that of the late firing wild type set. We tested for differences in overlap between CTB-labeled $FoxP1^{MN\Delta}$ motor neurons and early or late firing wild type clusters using a Monte Carlo approach. The joint peak phase and burst duration distributions for CTB-labeled $FoxP1^{MN\Delta}$ motor neurons were bootstrap resampled 100,000 times and overlap with both wild type clusters was computed each time. P-values measuring overlap differences were calculated as:

$$\frac{1 + \#\text{ of bootstraps for which overlap with the late firing cluster was higher}}{100,001} \tag{8.12}$$

8.13 Analysis of motor pattern complexity

All cycle-triggered firing rates for neurons with Rayleigh test p-values < 0.05 from each dataset were stored in matrices, denoted R, of size $100 \times n$, where $n =$ number of neurons in the current dataset and 100 is the number of bins in our cycle-averaged firing rates. Each of these matrices was then approximately factorized using non-negative matrix factorization (using the MATLAB function nnmf; [Lee & Seung, 1999]). This method finds a pattern matrix P, and a weight matrix W, such that $R \approx PW$ with all entries in P (size $100 \times k$) and W (size $k \times n$) constrained to be non-negative. k defines the number of patterns to use in the decomposition.

We factorized the R matrix for each dataset using this approach with $k = 1 - 6$. To guard against poor initial initializations for P and W leading to poor estimates, we set the 'replicates' option to 10, so each factorization operation was repeated that many times with the lowest-error replicate returned by the algorithm. As in [Dominici et al., 2011], variance explained in the data by the P and W matrices resulting from NMF at each k value was given by:

$$\text{Variance Explained} = 1 - SSE/SST \tag{8.13a}$$

$$\text{where:} \tag{8.13b}$$

$$SSE = \sum_{i=1}^{n} \sum_{j=1}^{100} \mathrm{L}_{i,j}{}^2 \tag{8.13c}$$

$$\mathrm{L} = R - PW \tag{8.13d}$$

$$SST = \sum_{i=1}^{n} \sum_{j=1}^{100} R_{i,j} - \bar{R}_j{}^2 \tag{8.13e}$$

$$\tag{8.13f}$$

In addition, we performed a similar analysis using principal components analysis implemented by the MATLAB function princomp. The amount of variance explained by each principal component was simply returned by that function in the latent argument.

Bibliography

[Adrian, 1966] Adrian, L. (1966). Thomas graham brown. 1882-1965. *Biographical Memoirs of Fellows of the Royal Society*, (pp. 23–33).

[Agalliu et al., 2009] Agalliu, D., Takada, S., Agalliu, I., McMahon, A. P., & Jessell, T. M. (2009). Motor neurons with axial muscle projections specified by Wnt4/5 signaling. *Neuron*, 61(5), 708–720.

[Ahrens et al., 2012] Ahrens, M. B., Li, J. M., Orger, M. B., Robson, D. N., Schier, A. F., Engert, F., & Portugues, R. (2012). Brain-wide neuronal dynamics during motor adaptation in zebrafish. *Nature*, 485(7399), 471–477.

[Akay et al., 2014] Akay, T., Tourtellotte, W. G., Arber, S., & Jessell, T. M. (2014). Degradation of mouse locomotor pattern in the absence of proprioceptive sensory feedback. *Proceedings of the National Academy of Sciences*, 111(47), 16877–16882.

[Alstermark et al., 2010] Alstermark, B., Hultborn, H., Jankowska, E., & Pettersson, L.-G. (2010). Anders lundberg (1920–2009). *Experimental brain research*, 200(3-4), 193–195.

[Alvarez & Fyffe, 2007] Alvarez, F. J. & Fyffe, R. E. (2007). The continuing case for the renshaw cell. *The Journal of Physiology*, 584(1), 31–45.

[Arthur & Vassilvitskii, 2007] Arthur, D. & Vassilvitskii, S. (2007). k-means++: The advantages of careful seeding. In *Proceedings of the Eighteenth Annual ACM-SIAM Symposium on Discrete Algorithms* (pp. 1027–1035).: Society for Industrial and Applied Mathematics.

[Azim et al., 2014] Azim, E., Jiang, J., Alstermark, B., & Jessell, T. M. (2014). Skilled reaching relies on a v2a propriospinal internal copy circuit. *Nature*, 508(7496), 357–363.

[Bargmann & Marder, 2013] Bargmann, C. I. & Marder, E. (2013). From the connectome to brain function. *Nature Methods*, 10(6), 483–490.

[Beliez et al., 2014] Beliez, L., Barrière, G., Bertrand, S. S., & Cazalets, J.-R. (2014). Multiple monoaminergic modulation of posturo-locomotor network activity in the newborn rat spinal cord. *Frontiers in Neural Circuits*, 8.

[Beliez et al., 2015] Beliez, L., Barrière, G., Bertrand, S. S., & Cazalets, J.-R. (2015). Origin of thoracic spinal network activity during locomotor-like activity in the neonatal rat. *The Journal of Neuroscience*, 35(15), 6117–6130.

[Berens, 2009] Berens, P. (2009). CircStat: a MATLAB toolbox for circular statistics. *Journal of Statistical Software*, 31(10), 1–21.

[Berg et al., 2007] Berg, R. W., Alaburda, A., & Hounsgaard, J. (2007). Balanced inhibition and excitation drive spike activity in spinal half-centers. *Science*, 315(5810), 390–393.

[Berg & Ditlevsen, 2013] Berg, R. W. & Ditlevsen, S. (2013). Synaptic inhibition and excitation estimated via the time constant of membrane potential fluctuations. *Journal of Neurophysiology*, 110(4), 1021–1034.

[Bonnot et al., 2005] Bonnot, A., Mentis, G. Z., Skoch, J., & O'Donovan, M. J. (2005). Electroporation loading of calcium-sensitive dyes into the CNS. *Journal of Neurophysiology*, 93(3), 1793–1808.

[Bonnot et al., 2002] Bonnot, A., Whelan, P. J., Mentis, G. Z., & O'Donovan, M. J. (2002). Spatiotemporal pattern of motoneuron activation in the rostral lumbar and the sacral segments during locomotor-like activity in the neonatal mouse spinal cord. *Journal of Neuroscience*, 22(3), RC203.

[Borghuis et al., 2013] Borghuis, B. G., Marvin, J. S., Looger, L. L., & Demb, J. B. (2013). Two-photon imaging of nonlinear glutamate release dynamics at bipolar cell synapses in the mouse retina. *The Journal of Neuroscience*, 33(27), 10972–10985.

[Bouyer & Rossignol, 2003] Bouyer, L. & Rossignol, S. (2003). Contribution of cutaneous inputs from the hindpaw to the control of locomotion. i. intact cats. *Journal of Neurophysiology*, 90(6), 3625–3639.

[Boyd & Vandenberghe, 2004] Boyd, S. & Vandenberghe, L. (2004). *Convex Optimization*. Cambridge University Press.

[Brocard et al., 2013] Brocard, F., Shevtsova, N. A., Bouhadfane, M., Tazerart, S., Heinemann, U., Rybak, I. A., & Vinay, L. (2013). Activity-dependent changes in extracellular ca 2+ and k+ reveal pacemakers in the spinal locomotor-related network. *Neuron*, 77(6), 1047–1054.

[Brock et al., 1952] Brock, L. G., Coombs, J. S., & Eccles, J. C. (1952). The recording of potentials from motoneurones with an intracellular electrode. *Journal of Physiology*, 117(4), 431–460.

[Brown, 1914] Brown, T. G. (1914). On the nature of the fundamental activity of the nervous centres; together with an analysis of the conditioning of rhythmic activity in progression, and a theory of the evolution of function in the nervous system. *The Journal of Physiology*, 48(1), 18–46.

[Brown, 1916] Brown, T. G. (1916). Die reflexfunktionen des zentralnervensystems mit besonderer berücksichtigung der rhythmischen tätigkeiten beim säugetier. *Ergebnisse der Physiologie*, 15(1), 480–790.

[Brownstone & Bui, 2010] Brownstone, R. M. & Bui, T. V. (2010). Spinal interneurons providing input to the final common path during locomotion. *Progress in Brain Research*, 187, 81.

[Brownstone & Wilson, 2008] Brownstone, R. M. & Wilson, J. M. (2008). Strategies for delineating spinal locomotor rhythm-generating networks and the possible role of hb9 interneurones in rhythmogenesis. *Brain Research Reviews*, 57(1), 64–76.

[Buesing et al., 2014] Buesing, L., Machado, T. A., Cunningham, J. P., & Paninski, L. (2014). Clustered factor analysis of multineuronal spike data. In *Advances in Neural Information Processing Systems* (pp. 3500–3508).

[Burke et al., 2001] Burke, R., Degtyarenko, A., & Simon, E. (2001). Patterns of locomotor drive to motoneurons and last-order interneurons: clues to the structure of the cpg. *Journal of Neurophysiology*, 86(1), 447–462.

[Byron et al., 2009] Byron, M. Y., Cunningham, J. P., Santhanam, G., Ryu, S. I., Shenoy, K. V., & Sahani, M. (2009). Gaussian-process factor analysis for low-dimensional single-trial analysis of neural population activity. In *Advances in Neural Information Processing Systems* (pp. 1881–1888).

[Cajal, 1909] Cajal, S. R. y. (1909). Histologie du système nerveux de l'homme et des vertébrés, vol. 1maloine.

[Cazalets et al., 1996] Cazalets, J. R., Borde, M., & Clarac, F. (1996). The synaptic drive from the spinal locomotor network to motoneurons in the newborn rat. *Journal of Neuroscience*, 16(1), 298–306.

[Chen et al., 2013] Chen, T.-W., Wardill, T. J., Sun, Y., Pulver, S. R., Renninger, S. L., Baohan, A., Schreiter, E. R., Kerr, R. A., Orger, M. B., Jayaraman, V., et al. (2013). Ultrasensitive fluorescent proteins for imaging neuronal activity. *Nature*, 499(7458), 295–300.

[Churchland et al., 2012] Churchland, M. M., Cunningham, J. P., Kaufman, M. T., Foster, J. D., Nuyujukian, P., Ryu, S. I., & Shenoy, K. V. (2012). Neural population dynamics during reaching. *Nature*, 487(7405), 51–56.

[Cowley & Schmidt, 1997] Cowley, K. & Schmidt, B. (1997). Regional distribution of the locomotor pattern-generating network in the neonatal rat spinal cord. *Journal of Neurophysiology*, 77(1), 247–259.

[Creed et al., 1932] Creed, R. S., Denny-Brown, D., Eccles, J. C., Liddell, E. G. T., & Sherrington, C. S. (1932). Reflex activity of the spinal cord.

[Crivici & Ikura, 1995] Crivici, A. & Ikura, M. (1995). Molecular and structural basis of target recognition by calmodulin. *Annual Review of Biophysics and Biomolecular Structure*, 24(1), 85–116.

[Crone et al., 2008] Crone, S. A., Quinlan, K. A., Zagoraiou, L., Droho, S., Restrepo, C. E., Lundfald, L., Endo, T., Setlak, J., Jessell, T. M., Kiehn, O., et al. (2008). Genetic ablation of V2a ipsilateral interneurons disrupts left-right locomotor coordination in mammalian spinal cord. *Neuron*, 60(1), 70–83.

[Cuellar et al., 2009] Cuellar, C. A., Tapia, J. A., Juárez, V., Quevedo, J., Linares, P., Martínez, L., & Manjarrez, E. (2009). Propagation of sinusoidal electrical waves along the spinal cord during a fictive motor task. *The Journal of Neuroscience*, 29(3), 798–810.

[Dai et al., 2005] Dai, X., Noga, B. R., Douglas, J. R., & Jordan, L. M. (2005). Localization of spinal neurons activated during locomotion using the c-fos immunohistochemical method. *Journal of neurophysiology*, 93(6), 3442–3452.

[Dasen et al., 2008] Dasen, J. S., De Camilli, A., Wang, B., Tucker, P. W., & Jessell, T. M. (2008). Hox repertoires for motor neuron diversity and connectivity gated by a single accessory factor, FoxP1. *Cell*, 134(2), 304–316.

[Dasen & Jessell, 2009] Dasen, J. S. & Jessell, T. M. (2009). Chapter six hox networks and the origins of motor neuron diversity. *Current Topics in Developmental Biology*, 88, 169–200.

[Dasen et al., 2005] Dasen, J. S., Tice, B. C., Brenner-Morton, S., & Jessell, T. M. (2005). A hox regulatory network establishes motor neuron pool identity and target-muscle connectivity. *Cell*, 123(3), 477–491.

[De Marco Garcia & Jessell, 2008] De Marco Garcia, N. V. & Jessell, T. M. (2008). Early motor neuron pool identity and muscle nerve trajectory defined by postmitotic restrictions in Nkx6.1 activity. *Neuron*, 57(2), 217–231.

[Dominici et al., 2011] Dominici, N., Ivanenko, Y. P., Cappellini, G., dAvella, A., Mondì, V., Cicchese, M., Fabiano, A., Silei, T., Di Paolo, A., Giannini, C., et al. (2011). Locomotor primitives in newborn babies and their development. *Science*, 334(6058), 997–999.

[Duysens, 1977] Duysens, J. (1977). Reflex control of locomotion as revealed by stimulation of cutaneous afferents in spontaneously walking premammillary cats. *Journal of Neurophysiology*, 40, 737–751.

[Duysens, 2006] Duysens, J. (2006). How deletions in a model could help explain deletions in the laboratory. *Journal of Neurophysiology*, 95(1), 562–565.

[Eccles et al., 1957] Eccles, J., Eccles, R. M., & Lundberg, A. (1957). The convergence of monosynaptic excitatory afferents on to many different species of alpha motoneurones. *The Journal of Physiology*, 137(1), 22–50.

[Elhamifar & Vidal, 2013] Elhamifar, E. & Vidal, R. (2013). Sparse subspace clustering: Algorithm, theory, and applications. *Pattern Analysis and Machine Intelligence, IEEE Transactions on*, 35(11), 2765–2781.

[Endo & Kiehn, 2008] Endo, T. & Kiehn, O. (2008). Asymmetric operation of the locomotor central pattern generator in the neonatal mouse spinal cord. *Journal of Neurophysiology*, 100(6), 3043–3054.

[Falgairolle & Cazalets, 2007] Falgairolle, M. & Cazalets, J.-R. (2007). Metachronal coupling between spinal neuronal networks during locomotor activity in newborn rat. *The Journal of Physiology*, 580(1), 87–102.

[Feinberg & Meister, 2014] Feinberg, E. H. & Meister, M. (2014). Orientation columns in the mouse superior colliculus. *Nature*.

[Fosque et al., 2015] Fosque, B. F., Sun, Y., Dana, H., Yang, C.-T., Ohyama, T., Tadross, M. R., Patel, R., Zlatic, M., Kim, D. S., Ahrens, M. B., et al. (2015). Labeling of active neural circuits in vivo with designed calcium integrators. *Science*, 347(6223), 755–760.

[Franz et al., 1993] Franz, T., Kothary, R., Surani, M., Halata, Z., & Grim, M. (1993). The splotch mutation interferes with muscle development in the limbs. *Anatomy and Embryology*, 187(2), 153–160.

[Freeman et al., 2014] Freeman, J., Vladimirov, N., Kawashima, T., Mu, Y., Sofroniew, N. J., Bennett, D. V., Rosen, J., Yang, C.-T., Looger, L. L., & Ahrens, M. B. (2014). Mapping brain activity at scale with cluster computing. *Nature Methods*, 11(9), 941–950.

[Frigon & Gossard, 2009] Frigon, A. & Gossard, J.-P. (2009). Asymmetric control of cycle period by the spinal locomotor rhythm generator in the adult cat. *The Journal of Physiology*, 587(19), 4617–4628.

[Garaschuk et al., 2006] Garaschuk, O., Milos, R.-I., & Konnerth, A. (2006). Targeted bulk-loading of fluorescent indicators for two-photon brain imaging in vivo. *Nature Protocols*, 1(1), 380.

[Gerhard et al., 2013] Gerhard, F., Kispersky, T., Gutierrez, G. J., Marder, E., Kramer, M., & Eden, U. (2013). Successful reconstruction of a physiological circuit with known connectivity from spiking activity alone. *PLoS Computational Biology*, 9(7), e1003138.

[Ghahramani et al., 1996] Ghahramani, Z., Hinton, G. E., et al. (1996). *The EM algorithm for mixtures of factor analyzers.* Technical report, Technical Report CRG-TR-96-1, University of Toronto.

[Goetz et al., 2015] Goetz, C., Pivetta, C., & Arber, S. (2015). Distinct limb and trunk premotor circuits establish laterality in the spinal cord. *Neuron*, 85(1), 131–144.

[Gosgnach et al., 2006] Gosgnach, S., Lanuza, G. M., Butt, S. J., Saueressig, H., Zhang, Y., Velasquez, T., Riethmacher, D., Callaway, E. M., Kiehn, O., & Goulding, M. (2006). V1 spinal neurons regulate the speed of vertebrate locomotor outputs. *Nature*, 440(7081), 215–219.

[Goulding, 2009] Goulding, M. (2009). Circuits controlling vertebrate locomotion: moving in a new direction. *Nature Reviews Neuroscience*, 10(7), 507–518.

[Grant et al., 2008] Grant, M., Boyd, S., & Ye, Y. (2008). CVX: Matlab software for disciplined convex programming.

[Greenberg, 2015] Greenberg, D. (2015). Spike detection with biophysical models for calcium indicator proteins. In *Calcium Imaging Data Analysis Workshop*.

[Grewe et al., 2010] Grewe, B. F., Langer, D., Kasper, H., Kampa, B. M., & Helmchen, F. (2010). High-speed in vivo calcium imaging reveals neuronal network activity with near-millisecond precision. *Nature Methods*, 7(5), 399–405.

[Grillner, 1981] Grillner, S. (1981). *Handbook of Physiology, The Nervous System II*, chapter Control of locomotion in bipeds, tetrapods, and fish. American Physiological Society.

[Grillner et al., 1995] Grillner, S., Deliagina, T., El Manira, A., Hill, R., Orlovsky, G., Wallén, P., Ekeberg, Ö., & Lansner, A. (1995). Neural networks that coordinate locomotion and body orientation in lamprey. *Trends in Neurosciences*, 18(6), 270–279.

[Grillner et al., 1970] Grillner, S., Hongo, T., & Lund, S. (1970). The vestibulospinal tract. effects on alpha-motoneurones in the lumbosacral spinal cord in the cat. *Experimental brain research*, 10(1), 94–120.

[Grillner & Jessell, 2009] Grillner, S. & Jessell, T. M. (2009). Measured motion: searching for simplicity in spinal locomotor networks. *Current opinion in neurobiology*, 19(6), 572–586.

[Grillner & Wallen, 1985] Grillner, S. & Wallen, P. (1985). Central pattern generators for locomotion, with special reference to vertebrates. *Annual Review of Neuroscience*, 8(1), 233–261.

[Grillner & Zangger, 1979] Grillner, S. & Zangger, P. (1979). On the central generation of locomotion in the low spinal cat. *Experimental Brain Research*, 34(2), 241–261.

[Grosenick et al., 2015] Grosenick, L., Marshel, J. H., & Deisseroth, K. (2015). Closed-loop and activity-guided optogenetic control. *Neuron*, 86(1), 106–139.

[Gutierrez et al., 2013] Gutierrez, G. J., O?Leary, T., & Marder, E. (2013). Multiple mechanisms switch an electrically coupled, synaptically inhibited neuron between competing rhythmic oscillators. *Neuron*, 77(5), 845–858.

[Guzulaitis et al., 2014] Guzulaitis, R., Alaburda, A., & Hounsgaard, J. (2014). Dense distributed processing in a hindlimb scratch motor network. *The Journal of Neuroscience*, 34(32), 10756–10764.

[Hägglund et al., 2013] Hägglund, M., Dougherty, K. J., Borgius, L., Itohara, S., Iwasato, T., & Kiehn, O. (2013). Optogenetic dissection reveals multiple rhythmogenic modules underlying locomotion. *Proceedings of the National Academy of Sciences*, 110(28), 11589–11594.

[Harvey et al., 2012] Harvey, C. D., Coen, P., & Tank, D. W. (2012). Choice-specific sequences in parietal cortex during a virtual-navigation decision task. *Nature*, 484(7392), 62–68.

[Helmchen & Tank, 2005] Helmchen, F. & Tank, D. W. (2005). A single-compartment model of calcium dynamics in nerve terminals and dendrites. *Imaging in Neuroscience and Development*, (pp. 265–275).

[Henneman et al., 1965] Henneman, E., Somjen, G., & Carpenter, D. O. (1965). Functional significance of cell size in spinal motoneurons. *Journal of Neurophysiology*, 28(3), 560–580.

[Hochman & Schmidt, 1998] Hochman, S. & Schmidt, B. J. (1998). Whole cell recordings of lumbar motoneurons during locomotor-like activity in the in vitro neonatal rat spinal cord. *Journal of Neurophysiology*, 79(2), 743–752.

[Horikawa et al., 2010] Horikawa, K., Yamada, Y., Matsuda, T., Kobayashi, K., Hashimoto, M., Matsu-ura, T., Miyawaki, A., Michikawa, T., Mikoshiba, K., & Nagai, T. (2010). Spontaneous network activity visualized by ultrasensitive ca^{2+} indicators, yellow cameleon-nano. *Nature Methods*, 7(9), 729–732.

[Hultborn, 1972] Hultborn, H. (1972). Convergence on interneurones in the reciprocal ia inhibitory pathway to motoneurones. *Acta Physiologica Scandinavica*, 85(s375), 1–42.

[Issa et al., 2014] Issa, J. B., Haeffele, B. D., Agarwal, A., Bergles, D. E., Young, E. D., & Yue, D. T. (2014). Multiscale optical ca^{2+} imaging of tonal organization in mouse auditory cortex. *Neuron*, 83(4), 944–959.

[Jessell, 2000] Jessell, T. M. (2000). Neuronal specification in the spinal cord: inductive signals and transcriptional codes. *Nature Reviews Genetics*, 1(1), 20–29.

[Jessell et al., 2011] Jessell, T. M., Sürmeli, G., & Kelly, J. S. (2011). Motor neurons and the sense of place. *Neuron*, 72(3), 419–424.

[Jones et al., 2011] Jones, J. G., Tansey, E., & Stuart, D. G. (2011). Thomas graham brown (1882–1965): Behind the scenes at the cardiff institute of physiology. *Journal of the History of the Neurosciences*, 20(3), 188–209.

[Jones et al., 2007] Jones, L. M., Fontanini, A., Sadacca, B. F., Miller, P., & Katz, D. B. (2007). Natural stimuli evoke dynamic sequences of states in sensory cortical ensembles. *Proceedings of the National Academy of Sciences*, 104(47), 18772–18777.

[Kaifosh et al., 2014] Kaifosh, P., Zaremba, J. D., Danielson, N. B., & Losonczy, A. (2014). Sima: Python software for analysis of dynamic fluorescence imaging data. *Frontiers in Neuroinformatics*, 8.

[Keshri et al., 2013] Keshri, S., Pnevmatikakis, E., Pakman, A., Shababo, B., & Paninski, L. (2013). A shotgun sampling solution for the common input problem in neural connectivity inference. *arXiv preprint arXiv:1309.3724*.

[Kiehn & Kjaerulff, 1996] Kiehn, O. & Kjaerulff, O. (1996). Spatiotemporal characteristics of 5-ht and dopamine-induced rhythmic hindlimb activity in the in vitro neonatal rat. *Journal of Neurophysiology*, 75(4), 1472–1482.

[Kjaerulff & Kiehn, 1996] Kjaerulff, O. & Kiehn, O. (1996). Distribution of networks generating and coordinating locomotor activity in the neonatal rat spinal cord in vitro: a lesion study. *The Journal of Neuroscience*, 16(18), 5777–5794.

[Krouchev et al., 2006] Krouchev, N., Kalaska, J. F., & Drew, T. (2006). Sequential activation of muscle synergies during locomotion in the intact cat as revealed by cluster analysis and direct decomposition. *Journal of Neurophysiology*, 96(4), 1991–2010.

[Kudo & Yamada, 1987a] Kudo, N. & Yamada, T. (1987a). Morphological and physiological studies of development of the monosynaptic reflex pathway in the rat lumbar spinal cord. *The Journal of Physiology*, 389(1), 441–459.

[Kudo & Yamada, 1987b] Kudo, N. & Yamada, T. (1987b). N-methyl-d, l-aspartate-induced locomotor activity in a spinal cord-indlimb muscles preparation of the newborn rat studied in vitro. *Neuroscience Letters*, 75(1), 43–48.

[Kusakabe & Kuratani, 2005] Kusakabe, R. & Kuratani, S. (2005). Evolution and developmental patterning of the vertebrate skeletal muscles: perspectives from the lamprey. *Developmental Dynamics*, 234(4), 824–834.

[Kwan et al., 2009] Kwan, A. C., Dietz, S. B., Webb, W. W., & Harris-Warrick, R. M. (2009). Activity of Hb9 interneurons during fictive locomotion in mouse spinal cord. *The Journal of Neuroscience*, 29(37), 11601–11613.

[Kwan et al., 2010] Kwan, A. C., Dietz, S. B., Zhong, G., Harris-Warrick, R. M., & Webb, W. W. (2010). Spatiotemporal dynamics of rhythmic spinal interneurons measured with two-photon calcium imaging and coherence analysis. *Journal of Neurophysiology*, 104(6), 3323–3333.

[Lafreniere-Roula & McCrea, 2005] Lafreniere-Roula, M. & McCrea, D. A. (2005). Deletions of rhythmic motoneuron activity during fictive locomotion and scratch provide clues to the organization of the mammalian central pattern generator. *Journal of Neurophysiology*, 94(2), 1120–1132.

[Lallemend & Ernfors, 2012] Lallemend, F. & Ernfors, P. (2012). Molecular interactions underlying the specification of sensory neurons. *Trends in Neurosciences*, 35(6), 373–381.

[Lam & Pearson, 2001] Lam, T. & Pearson, K. G. (2001). Proprioceptive modulation of hip flexor activity during the swing phase of locomotion in decerebrate cats. *Journal of Neurophysiology*, 86(3), 1321–1332.

[Lanuza et al., 2004] Lanuza, G. M., Gosgnach, S., Pierani, A., Jessell, T. M., & Goulding, M. (2004). Genetic identification of spinal interneurons that coordinate left-right locomotor activity necessary for walking movements. *Neuron*, 42(3), 375–386.

[Lee & Seung, 1999] Lee, D. D. & Seung, H. S. (1999). Learning the parts of objects by non-negative matrix factorization. *Nature*, 401(6755), 788–791.

[Lee & Jessell, 1999] Lee, K. J. & Jessell, T. M. (1999). The specification of dorsal cell fates in the vertebrate central nervous system. *Annual review of Neuroscience*, 22(1), 261–294.

[Lemon & Griffiths, 2005] Lemon, R. N. & Griffiths, J. (2005). Comparing the function of the corticospinal system in different species: organizational differences for motor specialization? *Muscle and Nerve*, 32(3), 261–279.

[Lev-Tov & O'Donovan, 1995] Lev-Tov, A. & O'Donovan, M. J. (1995). Calcium imaging of motoneuron activity in the en-bloc spinal cord preparation of the neonatal rat. *Journal of Neurophysiology*, 74(3), 1324–1334.

[Li et al., 2015] Li, N., Chen, T.-W., Guo, Z. V., Gerfen, C. R., & Svoboda, K. (2015). A motor cortex circuit for motor planning and movement. *Nature*, 519(7541), 51–56.

[Li & Ngom, 2013] Li, Y. & Ngom, A. (2013). The non-negative matrix factorization toolbox for biological data mining. *Source Code for Biology and Medicine*, 8(1), 1–15.

[Llinas et al., 1972] Llinas, R., Blinks, J., & Nicholson, C. (1972). Calcium transient in presynaptic terminal of auid giant synapse: Detection with aequorin. *Science*, 176(4039), 1127–1129.

[Lloyd, 1943] Lloyd, D. P. (1943). Neuron patterns controlling transmission of ipsilateral hind limb reflexes in cat. *Journal of Neurophysiology*, 6(4), 293–315.

[Loeb, 1985] Loeb, G. E. (1985). Motoneurone task groups: coping with kinematic heterogeneity. *Journal of Experimental Biology*, 115(1), 137–146.

[Lowell et al., 2006] Lowell, B., Olson, D., & Yu, J. (2006). Development and phenotype of ChAT-IRES-Cre mice. *MGI Direct Data Submission:[MGI Ref ID J: 114556]*.

[Machacek & Hochman, 2006] Machacek, D. W. & Hochman, S. (2006). Noradrenaline unmasks novel self-reinforcing motor circuits within the mammalian spinal cord. *The Journal of Neuroscience*, 26(22), 5920–5928.

[Machado et al., 2015] Machado, T., Pnevmatikakis, E., Paninski, L., Jessell, T., & Miri, A. (2015). Primacy of flexor locomotor pattern revealed by ancestral reversion of motor neuron identity. *Cell*.

[Macke et al., 2011] Macke, J. H., Buesing, L., Cunningham, J. P., Byron, M. Y., Shenoy, K. V., & Sahani, M. (2011). Empirical models of spiking in neural populations. In *Advances in Neural Information Processing Systems* (pp. 1350–1358).

[Madisen et al., 2015] Madisen, L., Garner, A. R., Shimaoka, D., Chuong, A. S., Klapoetke, N. C., Li, L., van der Bourg, A., Niino, Y., Egolf, L., Monetti, C., et al. (2015). Transgenic mice for intersectional targeting of neural sensors and effectors with high specificity and performance. *Neuron*, 85(5), 942–958.

[Mante et al., 2013] Mante, V., Sussillo, D., Shenoy, K. V., & Newsome, W. T. (2013). Context-dependent computation by recurrent dynamics in prefrontal cortex. *Nature*, 503(7474), 78–84.

[Marder, 2011] Marder, E. (2011). Variability, compensation, and modulation in neurons and circuits. *Proceedings of the National Academy of Sciences*, 108(Supplement 3), 15542–15548.

[Marder & Bucher, 2007] Marder, E. & Bucher, D. (2007). Understanding circuit dynamics using the stomatogastric nervous system of lobsters and crabs. *Annual Review of Physiology*, 69, 291–316.

[Marvin et al., 2013] Marvin, J. S., Borghuis, B. G., Tian, L., Cichon, J., Harnett, M. T., Akerboom, J., Gordus, A., Renninger, S. L., Chen, T.-W., Bargmann, C. I., et al. (2013). An optimized fluorescent probe for visualizing glutamate neurotransmission. *Nature Methods*, 10(2), 162–170.

[McCrea & Rybak, 2008] McCrea, D. A. & Rybak, I. A. (2008). Organization of mammalian locomotor rhythm and pattern generation. *Brain Research Reviews*, 57(1), 134–146.

[McHanwell & Biscoe, 1981] McHanwell, S. & Biscoe, T. (1981). The localization of motoneurons supplying the hindlimb muscles of the mouse. *Philosophical Transactions of the Royal Society of London. B, Biological Sciences*, 293(1069), 477–508.

[Meehan et al., 2012] Meehan, C. F., Grondahl, L., Nielsen, J. B., & Hultborn, H. (2012). Fictive locomotion in the adult decerebrate and spinal mouse in vivo. *The Journal of Physiology*, 590(2), 289–300.

[Mentis et al., 2011] Mentis, G. Z., Blivis, D., Liu, W., Drobac, E., Crowder, M. E., Kong, L., Alvarez, F. J., Sumner, C. J., & O'Donovan, M. J. (2011). Early functional impairment of sensory-motor connectivity in a mouse model of spinal muscular atrophy. *Neuron*, 69(3), 453–467.

[Mishchenko et al., 2011] Mishchenko, Y., Vogelstein, J. T., Paninski, L., et al. (2011). A bayesian approach for inferring neuronal connectivity from calcium fluorescent imaging data. *The Annals of Applied Statistics*, 5(2B), 1229–1261.

[Monier et al., 2008] Monier, C., Fournier, J., & Frégnac, Y. (2008). In vitro and in vivo measures of evoked excitatory and inhibitory conductance dynamics in sensory cortices. *Journal Neuroscience Methods*, 169(2), 323–365.

[Moore, 1965] Moore, G. E. (1965). Cramming more components onto integrated circuits. *Electronics*, 38(8).

[Mormann et al., 2000] Mormann, F., Lehnertz, K., David, P., & E Elger, C. (2000). Mean phase coherence as a measure for phase synchronization and its application to the EEG of epilepsy patients. *Physica D: Nonlinear Phenomena*, 144(3), 358–369.

[Moult et al., 2013] Moult, P. R., Cottrell, G. A., & Li, W.-C. (2013). Fast silencing reveals a lost role for reciprocal inhibition in locomotion. *Neuron*, 77(1), 129–140.

[Nakai et al., 2001] Nakai, J., Ohkura, M., & Imoto, K. (2001). A high signal-to-noise Ca^{2+} probe composed of a single green fluorescent protein. *Nature Biotechnology*, 19(2), 137–141.

[Ng et al., 2002] Ng, A. Y., Jordan, M. I., Weiss, Y., et al. (2002). On spectral clustering: Analysis and an algorithm. *Advances in Neural Information Processing Systems*, 2, 849–856.

[Nikolenko et al., 2008] Nikolenko, V., Watson, B. O., Araya, R., Woodruff, A., Peterka, D. S., & Yuste, R. (2008). Slm microscopy: scanless two-photon imaging and photostimulation with spatial light modulators. *Frontiers in Neural Circuits*, 2.

[Nishimaru & Kudo, 2000] Nishimaru, H. & Kudo, N. (2000). Formation of the central pattern generator for locomotion in the rat and mouse. *Brain Research Bulletin*, 53(5), 661–669.

[O'Donovan et al., 2008] O'Donovan, M. J., Bonnot, A., Mentis, G. Z., Arai, Y., Chub, N., Shneider, N. A., & Wenner, P. (2008). Imaging the spatiotemporal organization of neural activity in the developing spinal cord. *Developmental Neurobiology*, 68(6), 788–803.

[ODonovan et al., 2010] ODonovan, M. J., Bonnot, A., Mentis, G. Z., Chub, N., Pujala, A., & Alvarez, F. J. (2010). Mechanisms of excitation of spinal networks by stimulation of the ventral roots. *Annals of the New York Academy of Sciences*, 1198(1), 63–71.

[O'Donovan et al., 1993] O'Donovan, M. J., Ho, S., Sholomenko, G., & Yee, W. (1993). Real-time imaging of neurons retrogradely and anterogradely labelled with calcium-sensitive dyes. *Journal of Neuroscience Methods*, 46(2), 91–106.

[Ohki et al., 2005] Ohki, K., Chung, S., Ch'ng, Y. H., Kara, P., & Reid, R. C. (2005). Functional imaging with cellular resolution reveals precise micro-architecture in visual cortex. *Nature*, 433(7026), 597–603.

[Okatan et al., 2005] Okatan, M., Wilson, M. A., & Brown, E. N. (2005). Analyzing functional connectivity using a network likelihood model of ensemble neural spiking activity. *Neural Computation*, 17(9), 1927–1961.

[Osakada et al., 2011] Osakada, F., Mori, T., Cetin, A. H., Marshel, J. H., Virgen, B., & Callaway, E. M. (2011). New rabies virus variants for monitoring and manipulating activity and gene expression in defined neural circuits. *Neuron*, 71(4), 617–631.

[Packer et al., 2014] Packer, A. M., Russell, L. E., Dalgleish, H. W., & Häusser, M. (2014). Simultaneous all-optical manipulation and recording of neural circuit activity with cellular resolution in vivo. *Nature Methods*.

[Pearson & Duysens, 1976] Pearson, K. & Duysens, J. (1976). Function of segmental reflexes in the control of stepping in cockroaches and cats. *Advances in Behavioral Biology*.

[Pearson, 2004] Pearson, K. G. (2004). Generating the walking gait: role of sensory feedback. *Progress in brain research*, 143, 123–129.

[Pech et al., 2015] Pech, U., Revelo, N. H., Seitz, K. J., Rizzoli, S. O., & Fiala, A. (2015). Optical dissection of experience-dependent pre-and postsynaptic plasticity in the drosophila brain. *Cell Reports*, 10(12), 2083–2095.

[Penfield & Rasmussen, 1950] Penfield, W. & Rasmussen, T. (1950). The cerebral cortex of man; a clinical study of localization of function.

[Pérez et al., 2009] Pérez, T., Tapia, J. A., Mirasso, C. R., García-Ojalvo, J., Quevedo, J., Cuellar, C. A., & Manjarrez, E. (2009). An intersegmental neuronal architecture for spinal wave propagation under deletions. *The Journal of Neuroscience*, 29(33), 10254–10263.

[Perret & Cabelguen, 1980] Perret, C. & Cabelguen, J.-M. (1980). Main characteristics of the hindlimb locomotor cycle in the decorticate cat with special reference to bifunctional muscles. *Brain Research*, 187(2), 333–352.

[Personius et al., 2007] Personius, K. E., Chang, Q., Mentis, G. Z., O'Donovan, M. J., & Balice-Gordon, R. J. (2007). Reduced gap junctional coupling leads to uncorrelated motor neuron firing and precocious neuromuscular synapse elimination. *Proceedings of the National Academy of Sciences*, 104(28), 11808–11813.

[Petersen et al., 2014] Petersen, P. C., Vestergaard, M., Jensen, K. H., & Berg, R. W. (2014). Premotor spinal network with balanced excitation and inhibition during motor patterns has high resilience to structural division. *The Journal of Neuroscience*, 34(8), 2774–2784.

[Platzer & Spitzer, 2003] Platzer, W. & Spitzer, G. (2003). *Color Atlas of Human Anatomy, Volume 1: Locomotor System.* Thieme Verlag, Stuttgart New York.

[Pnevmatikakis et al., 2013] Pnevmatikakis, E. A., Merel, J., Pakman, A., & Paninski, L. (2013). Bayesian spike inference from calcium imaging data. In *Signals, Systems and Computers, 2013 Asilomar Conference on* (pp. 349–353).: IEEE.

[Pnevmatikakis et al., 2015] Pnevmatikakis, E. A., Soudry, D., Gao, Y., Machado, T. A., , Pfau, D., Reardon, T., Mu, Y., Lacefield, C., Poskanzer, K., Ahrens, M., Peterka, D., Bruno, R., Jessell, T. M., Yuste, R., & Paninski, L. (2015). Simultaneous denoising, deconvolution, and demixing of calcium imaging data. *Under review.*

[Pratt & Jordan, 1987] Pratt, C. A. & Jordan, L. M. (1987). Ia inhibitory interneurons and renshaw cells as contributors to the spinal mechanisms of fictive locomotion. *Journal of Neurophysiology*, 57(1), 56–71.

[Rad et al., 2015] Rad, K. R., Machado, T., Jessell, T., & Paninski, L. (2015). Robust and scalable bayesian analysis of spatial neural data.

[Rasmussen et al., 1978] Rasmussen, S., Chan, A., & Goslow, G. (1978). The cat step cycle: electromyographic patterns for hindlimb muscles during posture and unrestrained locomotion. *Journal of Morphology*, 155(3), 253–269.

[Reddy et al., 2008] Reddy, G. D., Kelleher, K., Fink, R., & Saggau, P. (2008). Three-dimensional random access multiphoton microscopy for functional imaging of neuronal activity. *Nature Neuroscience*, 11(6), 713–720.

[Renshaw, 1941] Renshaw, B. (1941). Influence of discharge of motoneurons upon excitation of neighboring motoneurons. *Journal of Neurophysiology*, 4(2), 167–183.

[Rexed, 1952] Rexed, B. (1952). The cytoarchitectonic organization of the spinal cord in the cat. *Journal of Comparative Neurology*, 96(3), 415–495.

[Ridgway & Ashley, 1967] Ridgway, E. & Ashley, C. (1967). Calcium transients in single muscle fibers. *Biochemical and Biophysical Research Communications*, 29(2), 229–234.

[Rochefort et al., 2008] Rochefort, N. L., Jia, H., & Konnerth, A. (2008). Calcium imaging in the living brain: prospects for molecular medicine. *Trends in Molecular Medicine*, 14(9), 389–399.

[Rokhlin et al., 2009] Rokhlin, V., Szlam, A., & Tygert, M. (2009). A randomized algorithm for principal component analysis. *SIAM Journal on Matrix Analysis and Applications*, 31(3), 1100–1124.

[Romanes, 1964] Romanes, G. (1964). The motor pools of the spinal cord. *Progress in Brain Research*, 11, 93–119.

[Rossignol, 1996] Rossignol, S. (1996). Neural control of stereotypic limb movements. *Comprehensive Physiology*.

[Rousso et al., 2008] Rousso, D. L., Gaber, Z. B., Wellik, D., Morrisey, E. E., & Novitch, B. G. (2008). Coordinated actions of the forkhead protein foxp1 and hox proteins in the columnar organization of spinal motor neurons. *Neuron*, 59(2), 226–240.

[Rudin et al., 1992] Rudin, L., Osher, S., & Fatemi, E. (1992). Nonlinear total variation based noise removal algorithms. *Physica D: Nonlinear Phenomena*, (pp. 259–268).

[Seung et al., 2000] Seung, H. S., Lee, D. D., Reis, B. Y., & Tank, D. W. (2000). Stability of the memory of eye position in a recurrent network of conductance-based model neurons. *Neuron*, 26(1), 259–271.

[Sherrington, 1906] Sherrington, C. S. (1906). Observations on the scratch-reflex in the spinal dog. *The Journal of Physiology*, 34(1-2), 1–50.

[Sherrington, 1913] Sherrington, C. S. (1913). Reflex inhibition as a factor in the co-ordination of movements and postures. *Quarterly Journal of Experimental Physiology*, 6(3), 251–310.

[Shimomura, 1995] Shimomura, O. (1995). A short story of aequorin. *Biological Bulletin*, (pp. 1–5).

[Shimomura et al., 1962] Shimomura, O., Johnson, F. H., & Saiga, Y. (1962). Extraction, purification and properties of aequorin, a bioluminescent protein from the luminous hydromedusan, aequorea. *Journal of Cellular and Comparative Physiology*, 59(3), 223–239.

[Smetters et al., 1999] Smetters, D., Majewska, A., & Yuste, R. (1999). Detecting action potentials in neuronal populations with calcium imaging. *Methods*, 18(2), 215–221.

[Smith & Brown, 2003] Smith, A. & Brown, E. (2003). Estimating a state-space model from point process observations. *Neural Computation*, 15(5), 965–991.

[Smith & Häusser, 2010] Smith, S. L. & Häusser, M. (2010). Parallel processing of visual space by neighboring neurons in mouse visual cortex. *Nature Neuroscience*, 13(9), 1144–1149.

[Sockanathan & Jessell, 1998] Sockanathan, S. & Jessell, T. M. (1998). Motor neuron–derived retinoid signaling specifies the subtype identity of spinal motor neurons. *Cell*, 94(4), 503–514.

[Spruston et al., 1993] Spruston, N., Jaffe, D. B., Williams, S. H., & Johnston, D. (1993). Voltage-and space-clamp errors associated with the measurement of electrotonically remote synaptic events. *Journal of Neurophysiology*, 70(2), 781–802.

[Stepien & Arber, 2008] Stepien, A. E. & Arber, S. (2008). Probing the locomotor conundrum: descending the 'v' interneuron ladder. *Neuron*, 60(1), 1–4.

[Stevenson & Kording, 2011] Stevenson, I. H. & Kording, K. P. (2011). How advances in neural recording affect data analysis. *Nature Neuroscience*, 14(2), 139–142.

[Sürmeli et al., 2011] Sürmeli, G., Akay, T., Ippolito, G. C., Tucker, P. W., & Jessell, T. M. (2011). Patterns of spinal sensory-motor connectivity prescribed by a dorsoventral positional template. *Cell*, 147(3), 653–665.

[Sussillo & Abbott, 2009] Sussillo, D. & Abbott, L. F. (2009). Generating coherent patterns of activity from chaotic neural networks. *Neuron*, 63(4), 544–557.

[Svoboda & Yasuda, 2006] Svoboda, K. & Yasuda, R. (2006). Principles of two-photon excitation microscopy and its applications to neuroscience. *Neuron*, 50(6), 823–839.

[Swanson, 2012] Swanson, L. W. (2012). *Brain architecture: understanding the basic plan*. Oxford University Press.

[Taccola, 2011] Taccola, G. (2011). The locomotor central pattern generator of the rat spinal cord in vitro is optimally activated by noisy dorsal root waveforms. *Journal of Neurophysiology*, 106(2), 872–884.

[Takeoka et al., 2014] Takeoka, A., Vollenweider, I., Courtine, G., & Arber, S. (2014). Muscle spindle feedback directs locomotor recovery and circuit reorganization after spinal cord injury. *Cell*, 159(7), 1626–1639.

[Talpalar et al., 2013] Talpalar, A. E., Bouvier, J., Borgius, L., Fortin, G., Pierani, A., & Kiehn, O. (2013). Dual-mode operation of neuronal networks involved in left-right alternation. *Nature*, 500(7460), 85–88.

[Talpalar et al., 2011] Talpalar, A. E., Endo, T., Löw, P., Borgius, L., Hägglund, M., Dougherty, K. J., Ryge, J., Hnasko, T. S., & Kiehn, O. (2011). Identification of minimal neuronal networks involved in flexor-extensor alternation in the mammalian spinal cord. *Neuron*, 71(6), 1071–1084.

[Tian et al., 2009] Tian, L., Hires, S. A., Mao, T., Huber, D., Chiappe, M. E., Chalasani, S. H., Petreanu, L., Akerboom, J., McKinney, S. A., Schreiter, E. R., et al. (2009). Imaging neural activity in worms, flies and mice with improved gcamp calcium indicators. *Nature Methods*, 6(12), 875–881.

[Tibshirani & Taylor, 2011] Tibshirani, R. & Taylor, J. (2011). The solution path of the generalized lasso. *Annals of Statistics*, 39(3), 1335–1371.

[Tipping & Bishop, 1999] Tipping, M. & Bishop, C. (1999). Mixtures of probabilistic principal component analyzers. *Neural Computation*, 11(2), 443–482.

[Tresch & Kiehn, 1999] Tresch, M. C. & Kiehn, O. (1999). Coding of locomotor phase in populations of neurons in rostral and caudal segments of the neonatal rat lumbar spinal cord. *Journal of Neurophysiology*, 82(6), 3563–3574.

[Tresch & Kiehn, 2000] Tresch, M. C. & Kiehn, O. (2000). Motor coordination without action potentials in the mammalian spinal cord. *Nature Neuroscience*, 3(6), 593–599.

[Tripodi et al., 2011] Tripodi, M., Stepien, A. E., & Arber, S. (2011). Motor antagonism exposed by spatial segregation and timing of neurogenesis. *Nature*, 479(7371), 61–66.

[Tsien, 1988] Tsien, R. Y. (1988). Fluorescence measurement and photochemical manipulation of cytosolic free calcium. *Trends in Neurosciences*, 11(10), 419–424.

[Vanderhorst & Holstege, 1997] Vanderhorst, V. & Holstege, G. (1997). Organization of lumbosacral motoneuronal cell groups innervating hindlimb, pelvic floor, and axial muscles in the cat. *The Journal of Comparative Neurology*, (382), 46–76.

[Varga et al., 2011] Varga, Z., Jia, H., Sakmann, B., & Konnerth, A. (2011). Dendritic coding of multiple sensory inputs in single cortical neurons in vivo. *Proceedings of the National Academy of Sciences*, 108(37), 15420–15425.

[Verhaegen & Verdult, 2007] Verhaegen, M. & Verdult, V. (2007). *Filtering and system identification: a least squares approach*. Cambridge university press.

[Vogelstein et al., 2010] Vogelstein, J. T., Packer, A. M., Machado, T. A., Sippy, T., Babadi, B., Yuste, R., & Paninski, L. (2010). Fast nonnegative deconvolution for spike train inference from population calcium imaging. *Journal of Neurophysiology*, 104(6), 3691–3704.

[Warp et al., 2012] Warp, E., Agarwal, G., Wyart, C., Friedmann, D., Oldfield, C. S., Conner, A., Del Bene, F., Arrenberg, A. B., Baier, H., & Isacoff, E. Y. (2012). Emergence of patterned activity in the developing zebrafish spinal cord. *Current Biology*, 22(2), 93–102.

[Williams & Mitchell, 2008] Williams, S. R. & Mitchell, S. J. (2008). Direct measurement of somatic voltage clamp errors in central neurons. *Nature Neuroscience*, 11(7), 790–798.

[Wilson et al., 2003] Wilson, R., Chersa, T., & Whelan, P. (2003). Tissue po 2 and the effects of hypoxia on the generation of locomotor-like activity in the in vitro spinal cord of the neonatal mouse. *Neuroscience*, 117(1), 183–196.

[Yakovenko et al., 2002] Yakovenko, S., Mushahwar, V., VanderHorst, V., Holstege, G., & Prochazka, A. (2002). Spatiotemporal activation of lumbosacral motoneurons in the locomotor step cycle. *Journal of Neurophysiology*, 87(3), 1542–1553.

[Yuste et al., 2005] Yuste, R., MacLean, J. N., Smith, J., & Lansner, A. (2005). The cortex as a central pattern generator. *Nature Reviews Neuroscience*, 6(6), 477–483.

[Zampieri et al., 2014] Zampieri, N., Jessell, T. M., & Murray, A. J. (2014). Mapping sensory circuits by anterograde transsynaptic transfer of recombinant rabies virus. *Neuron*, 81(4), 766–778.

[Zar, 1999] Zar, J. H. (1999). *Biostatistical Analysis*. Pearson Education India.

[Zariwala et al., 2012] Zariwala, H. A., Borghuis, B. G., Hoogland, T. M., Madisen, L., Tian, L., De Zeeuw, C. I., Zeng, H., Looger, L. L., Svoboda, K., & Chen, T.-W. (2012). A Cre-dependent GCaMP3 reporter mouse for neuronal imaging in vivo. *The Journal of Neuroscience*, 32(9), 3131–3141.

[Zhang et al., 2014] Zhang, J., Lanuza, G. M., Britz, O., Wang, Z., Siembab, V. C., Zhang, Y., Velasquez, T., Alvarez, F. J., Frank, E., & Goulding, M. (2014). V1 and v2b interneurons secure the alternating flexor-extensor motor activity mice require for limbed locomotion. *Neuron*, 82(1), 138–150.

[Zhang et al., 2008] Zhang, Y., Narayan, S., Geiman, E., Lanuza, G. M., Velasquez, T., Shanks, B., Akay, T., Dyck, J., Pearson, K., Gosgnach, S., et al. (2008). V3 spinal neurons establish a robust and balanced locomotor rhythm during walking. *Neuron*, 60(1), 84–96.

[Zhao et al., 2011] Zhao, Y., Araki, S., Wu, J., Teramoto, T., Chang, Y.-F., Nakano, M., Abdelfattah, A. S., Fujiwara, M., Ishihara, T., Nagai, T., et al. (2011). An expanded palette of genetically encoded Ca^{2+} indicators. *Science*, 333(6051), 1888–1891.

[Zhong et al., 2007] Zhong, G., Masino, M. A., & Harris-Warrick, R. M. (2007). Persistent sodium currents participate in fictive locomotion generation in neonatal mouse spinal cord. *The Journal of Neuroscience*, 27(17), 4507–4518.

[Zhong et al., 2012] Zhong, G., Shevtsova, N. A., Rybak, I. A., & Harris-Warrick, R. M. (2012). Neuronal activity in the isolated mouse spinal cord during spontaneous deletions in fictive locomotion: insights into locomotor central pattern generator organization. *The Journal of Physiology*, 590(19), 4735–4759.